Steuerungs- und Regelungstechnik

Alexander Warsewa

Energy-based modeling and decentralized observers for adaptive structures

Band 59

Berichte aus dem
Institut für Systemdynamik
Universität Stuttgart

isys

Energy-based modeling and decentralized observers for adaptive structures

Von der Fakultät
Konstruktions-, Produktions- und Fahrzeugtechnik
der
Universität Stuttgart

zur Erlangung der Würde eines
Doktor-Ingenieurs (Dr.-Ing.) genemigte Abhandlung

Vorgelegt von

Alexander Warsewa

geboren in Filderstadt

Hauptberichterin:	Prof. Dr.-Ing. Cristina Tarín
Mitberichter:	PD Dr.-Ing. habil. Paul Kotyczka

Tag der mündlichen Prüfung: 26. April 2021

Institut für Systemdynamik der Universität Stuttgart

2021

Berichte aus dem
Institut für Systemdynamik
Universität Stuttgart

Band 59

Alexander Warsewa

Energy-based modeling and decentralized observers for adaptive structures

D 93 (Diss. Universität Stuttgart)

Shaker Verlag
Düren 2021

Bibliographic information published by the Deutsche Nationalbibliothek
The Deutsche Nationalbibliothek lists this publication in the Deutsche Nationalbibliografie; detailed bibliographic data are available in the Internet at http://dnb.d-nb.de.

Zugl.: Stuttgart, Univ., Diss., 2021

Printed in Germany.

ISBN 978-3-8440-8040-7
ISSN 1863-9046

Shaker Verlag GmbH • Am Langen Graben 15a • 52353 Düren
Phone: 0049/2421/99011-0 • Telefax: 0049/2421/99011-9
Internet: www.shaker.de • e-mail: info@shaker.de

Vorwort

»Du meine Güte«, staunte Smeik. »Was ist das denn?«
[...]
»Nichts.«
»Wie: nichts?«
»Es ist nichts von Bedeutung«
[...]
»Raus mit der Sprache, Doktor – was ist das?«
»Das ist, äh, eine Doktorarbeit.«
»Eine Doktorarbeit?« lachte Smeik. »Jetzt bin ich aber erleichtert. Ich dachte schon, es sei eine schreckliche Krankheit.«
»Das ist eine Doktorarbeit gewissermaßen auch.«[1]

Zum schlussendlich erfolgreichen Abschluss meiner Promotion haben viele Menschen einen wertvollen Beitrag geleistet. Mein besonderer Dank gilt Cristina Tarín für die angenehme Betreuung meiner Arbeit, ihre Wertschätzung und das mir entgegengebrachte Vertrauen. Ohne Ihre Kompromissbereitschaft und Ihr offenes Ohr bei Schwierigkeiten gäbe es diese Doktorarbeit nicht. Auch Oliver Sawodny danke ich für die Ermöglichung von Teilzeit, die Wertschätzung meines Beitrags zum SFB und seinen Einsatz für ein Gemeinschaftsgefühl am Institut. Paul Kotyczka danke ich für die Übernahme des Mitberichts, die gründliche Lektüre meiner Arbeit und das konstruktive und wohlwollende Feedback. Bernd Bertsche für seine Bereitschaft mir als Vorsitzender des Prüfungsausschusses im Covid-19-Format neben Luftreinigern die Prüfung abzunehmen.

Ohne tolle Kolleg:innen ist die Arbeit etwas trostlos und deshalb danke ich neben allen anderen besonders meinen SFB-Mitstreiter:innen am ISYS – Michael Böhm, Julia Wagner, Marius Oei, Andreas Gienger, Philipp Arnold und Spasena Dakova – für den prima Austausch und viele motivierende Worte. Bei meinem Projektpartner Flavio Guerra bedanke mich für die entspannte und produktive Zusammenarbeit! Mit meinen Bürokollegen Dominik Esslinger und Martin Oberdorfer habe ich mich immer sehr wohl gefühlt. Dominik war mir ein hervorragendes Vorbild was die zeitnahe Fertigstellung meiner Dissertation angeht. Martin hat für den nötigen Ernst bei der Arbeit ... nein. Es hat Spaß gemacht mit dir das Büro zu teilen, zu kochen und ab und an zu bouldern! Gerlind Preisenhammer und Corina Hommel waren mit ihrer geduldigen und freundlichen Art stets eine große Hilfe bei allen organisatorischen Aufgaben. Joachim Endler und Sven Gutekunst haben meinen Dank für ihre Unterstützung in Sachen Versuchsaufbauten und IT. Michael Zeitz für seine wertvolle Rückmeldung zu manchem Probevortrag. Bei Marion Fleischer bedanke ich mich für die Pflege unserer Büropflanze und ihre beeindruckende Auswahl Weihnachtsplätzchen. Die

[1] Moers, Walter: „Rumo & Die Wunder im Dunkeln“, 8. Auflage. Piper Verlag GmbH, München, 2009, S. 142

Kantine „Rolands“ sei hier noch erwähnt für die Erweiterung meines Repertoires an vegetarischen Gerichten um „geschmorte Möhre à la Currywurst“.

Eine große Stütze während dieser nicht unbedingt leichten Zeit waren mir Jonas Poehlmann, Laura Faul, Asuka Okawa, Carolin Kraft, Sophia Größchen, Marie Graef, Anna Donat, Dominic Hillerkuss und Ruben Danner. Ihr wunderbaren Menschen, ich liebe euch!

Zu guter Letzt möchte ich noch meine persönliche Meinung zum SFB 1244 zum Ausdruck bringen. Die grundlegende Idee den Energie- und Ressourcenverbrauch des Bauwesens zu senken vertrete ich voll und ganz. Die jetzigen Lösungsansätze und -beispiele sind mir allerdings noch zu konform mit einem Narrativ des Wirtschaftswachstums und eignen sich am meisten für den hochverdichteten urbanen Raum der Industrienationen. Ich würde es begrüßen, wenn zukünftige Entwicklungen in dieser Hinsicht breiter aufgestellt sind.

Tübingen, im April 2021 Alexander Warsewa

Abstract

Responsible for a major amount of global waste production, greenhouse gas emission, energy and resource consumption, the construction sector is far from being considered a green industry. To reduce its future environmental impact, it is of utmost importance to save materials and energy on construction of new structures. Adaptive structures constitute a novel technological remedy that enables crossing the limits of classical lightweight construction. With the ability of an adaptive structure to change its shape or structural properties in reaction to external loads, it can utilize the load-carrying capacity of its elements in a near-optimal way. This requires, however, active and reliable control of the state of the structure – in this context its deformation and vibrations – which is considered a challenging task.

This thesis is concerned with two associated problem complexes. On the one hand, suitable dynamic modeling of adaptive structures and on the other hand, approaches for state estimation as a prerequisite for control. For system description, the theory of port-Hamiltonian systems is employed. Due to its modularity, the energy-based approach is especially suitable for complex systems of heterogeneous nature. The systems also exhibit convenient properties that can be exploited for both state estimation and control. Regarding the state estimation problem, a decentralized approach with local observers is proposed.

Port-Hamiltonian modeling of adaptive structures begins with the introduction of models for structural components. This includes the classical beam elements as well as a disk and plate element for two-dimensional continua. The coupling of hydraulic actuators with the mechanical structure is also discussed. For the spatial discretization of the infinite-dimensional systems, the structure-preserving partitioned finite element method (PFEM) is employed and compared to classical FEM. In order to automatically assemble complex system from individual elements, a port-based approach is introduced that works with algebraic constraints.

Decentralization of the observers for state estimation is conducted on the level of the dynamic models. If a system model of the overall structure is available, local models can be derived from it by means of transformations. Otherwise, decentralized structures can also be composed of individual modules, without the need to know the global system model in advance. In both cases, Luenberger observers can be designed for local state estimation in a way that the observers themselves constitute a port-Hamiltonian system. The presented methods are assessed and compared to each other with the help of simulation models of adaptive structure and using an experimental platform that represents a scaled version of an adaptive high-rise building.

Aim of this thesis was to demonstrate and harness the potential of energy-based methods for the application to adaptive structures. With the presented methods and approaches, an appropriate basis was successfully developed, which can be consequently built on.

Kurzfassung

Das Bauwesen ist verantwortlich für einen erheblichen Anteil am weltweiten Massenmüllaufkommen, CO2-Ausstoß, Energie- und Ressourcenverbrauch. Um dem entgegenzusteuern, ist es von entscheidender Bedeutung, beim Bau neuer Strukturen mit weniger Material und Energie auszukommen. Adaptive Strukturen stellen einen neuen technologischen Lösungsansatz dar, welcher es ermöglicht die Grenzen des klassischen Leichtbaus zu überschreiten. Indem ein adaptives Tragwerk seine Form oder strukturellen Eigenschaften an wechselnde äußere Lasten anpasst, kann die Tragfähigkeit der Strukturelemente nahezu optimal ausgenutzt werden. Dafür ist jedoch eine aktive und zuverlässige Regelung des Gebäudezustands – hier Verformungen und Schwingungen des Tragwerks – notwendig, was eine besondere Herausforderung darstellt.

In der vorliegenden Arbeit werden zwei zugehörige Problematiken thematisiert. Zum einen geeignete dynamische Modellierung adaptiver Tragwerke und zum anderen, die für die Regelung erforderliche Schätzung des Systemzustands. Zur Systembeschreibung wird die Port-Hamilton-Modellierung eingesetzt. Der energiebasierte Ansatz eignet sich durch seine Modularität besonders für komplexe Systeme heterogener Natur und weist günstige Eigenschaften für den Regler- und Beobachterentwurf auf. Bezüglich der Zustandsschätzung wird ein dezentraler Ansatz mit lokalen Beobachtern verfolgt.

Zunächst werden verteilparametrische Port-Hamilton-Modelle für Tragwerkskomponenten adaptiver Strukturen vorgestellt. Dazu gehören Balkenmodelle und ein Scheiben- und Plattenmodell für zweidimensionale Kontinua. Weiterhin wird auf hydraulische Aktorik und deren Kopplung mit der mechanischen Struktur eingegangen. Zur Ortsdiskretisierung der unendlichdimensionalen Systeme wird die strukturerhaltende partitionierten Finite-Elemente-Methode (PFEM) angewandt und ein Vergleich mit klassischer FEM angestellt. Um automatisch komplexe Systeme aus Einzelelementen zusammenzusetzen, wird ein Port-basierter Ansatz vorgestellt.

Die Dezentralisierung der Zustandsschätzung erfolgt auf Basis der dynamischen Modelle. Ist ein Systemmodell der Gesamtstruktur vorhanden, können lokale Modelle mittels Transformation von diesem abgeleitet werden. Andererseits können dezentrale Strukturen auch aus Einzelmodulen aufgebaut werden, ohne dass ein Gesamtsystem bekannt ist. In beiden Fällen können lokale Luenberger-Beobachter so entworfen werden, dass diese ebenfalls Port-Hamilton-Systeme darstellen. Die Methoden werden sowohl mit Simulationsmodellen, als auch anhand einer Experimentalplattform, welche eine skalierte Version eines adaptiven Hochhaustragwerks darstellt, überprüft und miteinander verglichen.

Ziel dieser Arbeit war es, das Potential energiebasierter Methoden für die Anwendung auf adaptive Strukturen aufzuzeigen und nutzbar zu machen. Mit den vorgestellten Ansätzen und Methoden wurde erfolgreich eine entsprechende Basis geschaffen, auf die konsequent weiter aufgebaut werden kann.

Contents

1 Introduction

1.1 General context and motivation

Scarcity of resources and pollution of the environment are pressing issues related to both technological development and the growth in global human population. Construction industry is responsible for a major amount of energy and resource consumption and contributes heavily to waste production and greenhouse gas emission [5, 35, 89, 127]. At the same time, development and implementation of new technologies to address these problematic aspects have been comparatively limited in this sector [12]. An increasing tendency for the occurrence of catastrophic incidents, such as heat waves, flooding or hurricanes, further aggravates the situation and calls for timely reactions. Both in terms of technology, as in terms of radically new conceptions of how urban development is to take place in the future.

A key in reducing the environmental impact of the built environment is to lower its *embodied energy*, i. e. the energy required for the production of construction materials and during the construction process [22]. As energy and resource demand for building operation decrease, this will become increasingly relevant. Developing lightweight construction is a logical consequence of this observation. The limits of classical lightweight construction are dictated by the required stability of the building in face of extreme loads. This is especially problematic for high-rise structures.

Introducing *adaptive structures* that can react to a changing environment and to loads of varying characteristics is an effective means to push these limits, enabling *ultra-lightweight* construction [119]. With the ability to actively manipulate structural properties (e. g. stiffness, length or damping), an adaptive structure can utilize the load-bearing capability of its elements in a near-optimal way. This new type of ultra-lightweight construction therefore does not rely on specialized materials or shape and topology optimization, but on the adaptivity itself. While this requires more operational energy, the technology comes with a big potential to reduce both embodied and whole-life energy. The taller or more slender a building or the wider the span of structure, the more monetary cost can be saved when building the adaptive version instead of the passive one [115]. Similar projections are made with respect to the negative environmental impact.

As it is the case for most promising technologies, the conception, design and implementation of adaptive structures brings forth many challenges. Among the most relevant ones is efficient and, above all, reliable structural control. Especially the active manipulation of the load distribution requires knowledge of the state of the structure, i. e. its deformation and velocity, in real-time. A considerable amount of integrated and external sensors are needed for the accurate state estimation of an adaptive structure. For large-scale structures, these are distributed over considerable physical distances. The requirements for control go beyond those of e. g. structural health-monitoring [45] for damage detection and lifespan extension. Rather than extracting statistical features from measurement data collected over relatively long

periods of time, the use of real-time data for model-based reconstruction of the system state is the matter of interest.

The more complex and the larger a structure, the more expedient it becomes to break it down into modules of smaller size. Instead of processing sensor data and computing the control input on a central unit, these operations can then be handled in a decentralized manner. One major advantage of a decentralized approach is its modularity. Complex functions can be realized by combining simple units, analogous to the cells in a human body forming tissues and entire organs. This makes it easier to introduce redundancies, reuse, exchange and recycle modules, opening up possibilities for truly flexible designs. Accessing only physically close sensors and actuators reduces the amount of data that needs to be transferred and thereby potentially also complexity and cost. Modules may also be interconnected for networked operation.

Design, conceptualization, construction and operation of adaptive structures require a much closer collaboration between architects and engineers than usual and involve a higher number of engineering disciplines. Model-based state estimation and control of these structures requires dynamic simulation models with components from different domains (think of e. g. smart materials, hydraulic or piezoelectric actuators). However, each discipline or domain developed its own specific terminology and set of tools, which makes interdisciplinary modeling a demanding task.

Energy-based approaches for modeling and control were developed with heterogeneous and complex systems in mind. Dynamic processes in physical systems are governed by the exchange, conversion and dissipation of energy – regardless of their domain. Recognizing this fact allows for a unified and domain-independent description in which energy acts as the *lingua franca*. In port-based modeling, individual elements of a system are interconnected at power ports, through which they can exchange energy in terms of power flows. The theory of port-Hamiltonian systems combines these ideas with powerful concepts from other engineering disciplines. A port-Hamiltonian system is passive by definition, i. e. its energy can only be increased via external supply of power and is otherwise conserved or dissipated. This property can be exploited for control.

Thus, coming back to adaptive structures, port-Hamiltonian systems offer ways to deal with the outlined problems resulting from interdisciplinary and complexity. Within the energy-based formulation, different physical domains (e. g. electrical, mechanical or thermodynamic) can be handled in the same way. Conservation of favorable system properties, such as passivity, on interconnection makes for a modular approach that is suitable for robust decentralized state estimation and control.

1.2 The CRC 1244

This thesis is a product of work in the collaborative research center 1244 (CRC 1244) "adaptive skins and structures for the built environment of tomorrow", financed by the German research foundation (Deutsche Forschungsgemeinschaft, DFG)[1]. Since the CRC 1244 is occasionally referenced in the following, it shall be briefly introduced here. The project is an interdisciplinary collaboration of fourteen different institutes located at the University of Stuttgart. Further collaboration partners are the Fraunhofer Institute for Building Physics (IBP) and two architecture professorships in the cities of Hamburg and Bremen. A network of ties to numerous researchers worldwide fosters the international proliferation of the developments in the CRC.

The CRC 1244 constitutes four principal areas of research that are further divided into numerous sub-projects:

A) Design and planning methodology

B) System technology and design

C) Integrative components

D) Economic and ecological aspects

It is also endeavored to excite public interest and a discussion of the ideas beyond a scientific context. For this purpose, a high-rise demonstrator is being constructed on campus of the University of Stuttgart with the intention to present the results of the project to a broader audience. The demonstrator is introduced in detail in Chapter 8. This thesis is mainly situated in area "B", but also contributes to "A" and "C". Modeling and control of adaptive skins is not considered, as this would go beyond the scope of this work. However, transfer of the methods to adaptive skins is considered both possible and expedient.

1.3 Aim and focus of this thesis

Aim of this thesis is to pave a way for energy-based methods – in particular port-Hamiltonian systems theory – in the emerging field of adaptive structures. The two main topics covered in the following are the modeling of these complex and heterogeneous structures on the one hand and methods for decentralized state estimation on the other. This provides a solid basis for active structural control with the powerful framework of port-Hamiltonian systems at ones disposal.

While many of the aspects and approaches covered in this thesis are certainly original, an equally important goal was to show which existing methods are suitable for the

[1] Project homepage: `https://www.sfb1244.uni-stuttgart.de/en/`

purpose at hand. Rather than focusing entirely on the development of new methods, available methods are assessed and expanded in the specific context of adaptive structures.

Based on the experience of working in an interdisciplinary project, it is refrained from attempting to generalize the approaches as much as possible and from using mathematical language specific to certain disciplines. Instead, the mathematical content is presented in a preferably easily understandable and accessible way. Well-established methods from other disciplines such as the finite element method (FEM) are referenced when appropriate and compared to port-Hamiltonian approaches. References to more specific works that demand a certain background are, however, also frequently provided for those striving to delve deeper. The author hopes that this encourages and eases an exchange between collaborating scientists and engineers from different disciplines.

1.4 State of the art

As different topics are covered in this thesis, the review of the state of the art is divided into several sections. Firstly, past and recent developments in the fields of active structural control and adaptive structures are presented in Section 1.4.1. This is complemented by an overview of decentralized state estimation in this context in Section 1.4.2. In Section 1.4.3, the origins of port-Hamiltonian systems theory and its development and emerging application areas up to the time this thesis was written are summarized. Finally, a brief conclusion is drawn, highlighting where potential for further development is seen.

1.4.1 Active and adaptive structural control

The concept of control of civil structures was first introduced by Yao in the 1970s [141] as an alternative safety measure. Since then the main research in this area has been devoted to finding solutions for the protection against extreme load situations such as earthquakes and storms. Technologies and devices for vibration control are commonly divided into four categories – passive, active, semi-active and hybrid – according to the degree to which they can be actively manipulated. Passive systems such as seismic isolation systems or energy dissipation devices are already well accepted in practice as means to mitigate structural oscillations [121]. Figure 1.1 shows parts of a base isolation system and a prominent example of a tuned mass damper (TMD). The latter is installed in the Taipei 101 building in Taiwan and has a mass of 600 t.

The inability of passive devices to adapt to different loading conditions or structural changes led to the investigation of active devices such as electromagnetic or hydraulic actuators, which directly exert forces to counteract critical loads. Systems that have

(a) Base isolation system of an electric converter station in New Zealand [33]

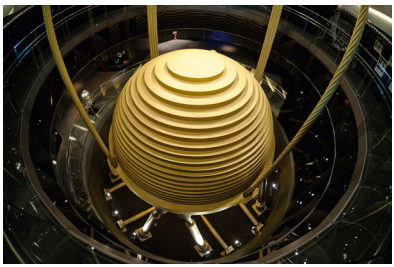

(b) Tuned mass damper installed in the Taipei 101 tower [32]

Figure 1.1: Examples of passive devices for structural control

been under research to date include the active versions of base isolation and TMDs, active tendon systems, distributed actuators and active coupled building systems [47, 106]. Practical implementation and acceptance of active structural control approaches has been hampered by their high power demand and increased system complexity [47, 121].

Semi-active devices combine the advantages of active control with a low energy demand whereas hybrid systems are combinations of active or semi-active control systems with passive dampers. Both active and semi-active systems have made it past the experimental stage with many actual realizations – most of them in Japan [121]. The Kajima Technical Research Institute was the first full-scale building equipped with a hydraulic semi-active damping system [77]. Ikeda [63] comments on the effectiveness of active and semi-active systems installed in Japan and highlights their importance. An overview over recent developments in Europe is given by Basu et al. [14].

A relatively new area of application for active and adaptive structural control systems is lightweight construction with the goal to save resources and reduce emissions [119, 120] as described in Section 1.1. Passive dampers or active tuned mass dampers (ATMDs) can principally be used for this purpose, but their effectiveness is limited, because they add additional weight to the structure. Instead, the development of novel active control concepts as well as the manipulation of static structural properties (e. g. stiffness) is required for this use case. The latter constitutes a less developed field of research [70].

An early example is a study of Noak et al. [96], where the stiffness of a steel beam is actively controlled by a hydraulic actuator. Control of the flexural stiffness of multi-layer beams is studied by Gandhi and Kang [48]. The stiffness of polymer layers changes with temperature. The same effect is achieved with electroactive polymers in [58]. Bleicher et al. [16] use pneumatic muscles to control the vibration of a lightweight

footbridge. Another lightweight bridge structure was developed by Senatore et al. [116]. It spans a length of 6 m and its stiffness can be actively manipulated using electro-mechanical actuators. Neuhaeuser et al. [94] introduced a full-scale prototype of an adaptive shell structure where the bearing reaction can be controlled with hydraulic actuators. The CRC 1244 endeavors the construction of the first full-scale adaptive high-rise structure equipped with hydraulic actuators and adaptive facade elements on campus of the University of Stuttgart [138].

1.4.2 Decentralized observers for civil structures

As the complexity or the physical size of systems increases, at a certain point it becomes infeasible to estimate their state using a central processing unit. Think of power networks, automation of large process plants or ecosystems. Individual units operate on different time scales and can, for the most part, perform specific subtasks independently. On that account, decentralized methods for state estimation and control have been developed since the late 60s [107]. This led to the emergence of a large variety of methods and possible areas of application. A detailed presentation of all the contributions to date cannot be given here, which is why the focus is narrowed down to decentralized state estimation of large-scale civil structures. Nevertheless, a brief overview of some of the most important developments is given in the following with the intention of relating this specific field to the bigger picture.

One major line of developments stems from classical and robust control theory where decentralized control rather than state estimation is the main concern. Decentralized observers appear as the dual problem or as integral part of the control design in observer-based controllers. Bakule summarized important contributions in this field in a survey paper [7]. Distinct strategies were developed for systems that admit disjoint decompositions (i. e. subsystems do not share state variables) as opposed to systems with stronger physical coupling. Concerning the latter case, Ikeda et al. [62] pioneered decentralized control by overlapping decomposition. An in-depth treatise of both approaches is given in a textbook by Šiljak [117]. The increase of computer processing power enabled the emergence of optimal control techniques such as H_2- or H_∞-control [123] with many applications in decentralized control [7]. Networked estimation and control arose as a parallel development where subsystem interconnections are explicitly taken into account, considering non-idealities such as delays and communication faults [8, 59]. This gave rise to the notions of distributed estimation and control, event-based or event-driven strategies and multi-agent systems.

At this point, the approaches intermingle with another line of developments – decentralized data fusion – that is explicitly concerned with the state estimation problem. Prominent applications are the tracking of moving objects or the navigation problem in robotics using information from a multitude of (physically distributed) sensors. Introductory material is e. g. available by Durrant-Whyte and Henderson [39] and

Bar-Shalom and Li [11]. An extensive review of the field is given by Khalegi et al. [68]. Notable examples are the development of distributed and decentralized versions of the Kalman filter, as proposed e. g. by Mutambara [92], consensus filtering [99] and covariance intersection techniques [67] to name only a few. Many of these approaches are tailored to systems of low dimensionality [69], which renders them less suitable for the state estimation of large-scale civil structures with strong physical coupling.

Applications of decentralized data fusion methods in civil engineering are mostly confined to the problem of structural health monitoring using wireless sensor networks [15, 64, 82, 93, 95, 118]. Fewer research is committed to decentralized state estimation for active and adaptive structural control. This is attributed to the relative novelty of the field and the lack of actual practical implementations of such structures – as previously stated in Section 1.4.1.

Most available methods were developed for a variety of benchmark problems [98, 122] designed by the American society of civil engineers (ASCE) and the structural engineers association of California (SAC). Lei et al. [79] propose decentralized observers for a 20-story benchmark building by using disjoint substructure models and modified Kalman filters for the estimation of interconnection forces. Bakule et al. apply decentralized linear quadratic Gaussian (LQG) control to the same structure using disjoint system decomposition [9], overlapping decomposition [6] and a networked approach with switched observer-based controller systems [10]. The use of Luenberger observers for decentralized state estimation is studied by Amini et al. in [2]. A different benchmark structure is introduced by Loh et al. in [81]. They study decentralized wireless sensing and LQG control of a three-story structure equipped with magnetorheological (MR) dampers. Ghasemi et al. [50] propose to use collocated sensor-actuator pairs for decentralized structural control, which does not require any observer. Their test setup consists of a cantilever beam with piezoelectric actuators and strain gauge sensors.

1.4.3 Port-Hamiltonian systems

Port-Hamiltonian systems were first introduced by Maschke and van der Schaft in the early 90s [87] as a generalization of classical Hamiltonian systems. By drawing on ideas from port-based modeling as proposed by Paynter in the late 50s [101], several powerful concepts from electrical network modeling, geometric mechanics and system and control theory were interwoven into the approach. Recognizing energy and power as the natural means of exchange between systems from different physical domains, port-Hamiltonian systems are well suited for the modeling of multi-physics systems. Energy also plays an important role in nonlinear control, where it can be exploited to find robust and physically interpretable control laws [109]. The Hamiltonian, i. e. the energy of a port-Hamiltonian system, can be used to find suitable candidates for a Lyapunov function. Port-Hamiltonian systems theory provides tools for the shaping of both energy-storage and dissipation and also the incorporation of controller as virtual

system components [100]. It has been extended to the thermodynamical domain [40] and also to account for systems with memory [66].

Since its introduction, the port-Hamiltonian approach has been used for modeling a wide variety of systems. First application examples were LC-circuits [88] and switching power converters [42]. Systems from other domains, such as robotic manipulators [114], hydraulic actuators [73] or the continuous stirred-tank reactor [103], soon followed. Power-networks [46] and multi-carrier energy systems [125] as well as audio circuits [43] or even the vocal fold [41] are some of the more recent examples. This illustrates the increasing popularity of port-Hamiltonian theory for dealing with complex systems and that it constitutes a powerful tool for engineers working in a multi-disciplinary field.

The contributions listed so far are all examples of lumped parameter systems. Treating distributed parameter systems within the port-Hamiltonian framework requires an extension of the theory, which is why they can be considered a separate, but closely connected field of research. Since the majority of systems presented in this thesis are governed by infinite-dimensional equations, an overview of the developments regarding distributed parameter port-Hamiltonian systems is provided in the subsequent.

Distributed Parameter Port-Hamiltonian Systems

Van der Schaft and Maschke presented first extensions of their approach to distributed parameter systems in the early 2000s [108]. The field of infinite-dimensional systems has been growing ever since. For an introductory treatment see e. g. [109] or [37]. Zwart and Jacob give a detailed treatise of linear distributed parameter systems on one-dimensional spatial manifolds [142]. Boundary control methods were soon introduced for infinite-dimensional port-Hamiltonian (see e. g. [78]) and have received much attention lately.

Macchelli et al. presented boundary control of the Timoshenko beam [83] and the modeling of piezoelectric materials [85] as distributed parameter port-Hamiltonian systems. Control by energy shaping and interconnection was studied in [57] where boundary control is applied to the shallow water equations. Recently, an increase in more complex application examples can be observed. Wu et al. [140] presented the control of a nanotweezer. Falaize et al. [44] contributed with the nonlinear modeling of a Rhodes piano. A port-Hamiltonian model of plasma dynamics in fusion reactors (Tokamaks) was developed by Vu et al. [129] and later extended to plasma profile control [130]. Vincent et al. [128] studied the dual problem of plasma profile estimation. The problem of describing liquid sloshing in moving containers, which is relevant for aircraft control, was addressed by Cardoso-Ribeiro et al. [128]. Altmann et al. [1] introduced port-Hamiltonian models for the reactive flow in turbines. Recently, an open-source library for modeling heat transfer in open cell foams using a port-Hamiltonian approach was developed by Scheuermann et al. [110].

The list of examples could be further continued. In a recent survey, Rashad et al. [104] give a detailed overview of the developments in the field of distributed parameter port-Hamiltonian systems over the past twenty years. They conclude that the framework is very promising for future applications.

1.4.4 Summary

While currently still mostly in an experimental state, active control systems for ultra-lightweight construction constitute important tools for a future generation of buildings. From the list of examples given in Section 1.4.1, it becomes clear that adaptive structures are heterogeneous systems employing actuators from different physical domains. Thus, energy-based modeling of such systems is an adequate means to handle their complexity.

The range of different approaches for decentralized state estimation of large-scale civil structures is relatively limited to date. Local models are mostly derived by partitioning a global FE model into disjoint or overlapping substructures. Observers are either of Kalman or Luenberger type. With a shift of focus from control systems for preventing damage caused by storms or earthquakes to adaptive structures comes a need for advanced methods.

Port-Hamiltonian systems theory provides an elegant way for a modular and energy-based formulation of the dynamics of complex and heterogeneous systems. This includes nonlinear systems as well as distributed parameter systems from most engineering domains. At the same time, powerful concepts for robust and passivity-based control are available in the port-Hamiltonian framework that have received a lot of attention lately. Investing the extra effort that comes with the energy-based formulation is rewarded with a high sustainability potential and access to state-of-the-art methods.

1.5 Contributions

The contributions of this thesis are as follows:

- Distributed and lumped parameter port-Hamiltonian models for components of adaptive structures
- Structure preserving discretization with a port-based coupling procedure for system assembly and comparison to the finite element method
- Bottom-up and top-down approaches for the decentralized state estimation of large-scale structures

- Application-oriented approach with practical implementation and provisioning of supporting software tools[1]

1.6 Outline

Since it is assumed that the majority of readers is not familiar with port-based physical modeling and port-Hamiltonian systems, Chapter 2 covers the basic concepts. It starts with bond graph methodology and then proceeds to port-Hamiltonian systems, ending with a brief introduction to distributed parameter port-Hamiltonian systems.

Energy-based modeling of the mechanical structure of an adaptive structure is done in Chapter 3 by expressing the dynamical equations of various basic elements in port-Hamiltonian form. For the structures considered in this thesis, deformations are sufficiently small to assume linear elastic behavior. Elements required for truss structures and frames (e. g. beams and rods) as well as elements for planar structures (a disk and a plate element) are included.

Chapter 4 deals with the spatial discretization of the systems covered in Chapter 3. After a review on available structure preserving discretization methods, application of the one considered most suitable (the partitioned finite element method) is explained in detail. A comparison to established FEM methodology shows that the approaches are closely related. Numerical studies of the approximation error are carried out for each system and the chapter is concluded with a brief comment on time discretization.

The next part, Chapter 5, is concerned with the assembly of complex systems from simple elements or subsystems in an object-oriented way. Coupling constraints are generated in an automated way leading to a system of differential algebraic equations. For linear systems, an explicit representation can be easily obtained by elimination of constraints. It is also shown that the result can be transformed to the formulation of a port-Hamiltonian system from the mass and stiffness matrices computed via conventional FEM.

Due to their ability to exert large forces, hydraulic actuators are among the most important active elements of adaptive structures. In Chapter 6, port-Hamiltonian models for hydraulic cylinders are introduced and the response of an adaptive frame structure to actuation is simulated.

Two different ways to design decentralized observers for large-scale structures are introduced in Chapter 7. In the top-down approach, local dynamic models are obtained from a global system representation. The bottom-up variant focuses on modularity, assuming that a global system model is not known in advance. Coupling thus happens only at the interfaces with the help of algebraic constraints.

[1] An open source Matlab framework that was developed in the course of this thesis and comprises many of the methods introduced in it is available online at `https://github.com/awarsewa/ph_fem`

All experimental and numerical studies conducted to assess the performance of the models and approaches introduced in this thesis are presented in Chapter 8. A variety of experimental platforms and prototypes were developed in the CRC 1244, which serve as the application examples. Decentralized observers are tested on a dedicated laboratory scale test bench (a high-rise mockup) and on a simulation model of the high-rise demonstrator building being constructed on campus of the University of Stuttgart.

A short summary of this work with concluding remarks and suggestions for future developments is given in Chapter 9.

2 Energy-based modeling

In the following, a brief introduction to energy-based modeling is given. The basic principles are introduced and illustrated with the help of the *bond graph* formalism in Section 2.1. Generalized components of physical systems are introduced in Section 2.2. This makes it easier to introduce port-Hamiltonian systems in Section 2.3 and distributed parameter port-Hamiltonian systems in Section 2.4. Even though they constitute powerful tools, bond graphs are not further used in the remainder of this thesis, since this would go beyond its scope. Studying how bond graph models of adaptive structures can prove beneficial is considered a topic for further work.

2.1 Introduction to port-based physical modeling

In any dynamical physical system, energy is stored, transformed or dissipated – regardless of its physical domain. Coupling between systems takes place via an exchange of energy or a power flow. Domain-independent ways of modeling physical systems are based on these simple but profound observations.

In the bond graph formalism introduced by Paynter, the concept of a *power port* is used. Every element in the graph is represented by such a power port and its interaction with others is symbolized via power bonds [17]. For each physical domain, a pair of *power-conjugate variables* is introduced whose product equals power. These variables are labeled *efforts* e and *flows* f such that for each element

$$P = ef. \tag{2.1}$$

In the following, the active sign convention is adopted such that P denotes the power flow out of the element. Breedveld [19] proposed a decomposition of the 'conventional' physical domains (i. e. mechanical, electrical, hydraulic) into two separate domains, which gave rise to the notion of *generalized bond graphs* (GBGs). This formalism is adopted here[1]. Effort and flow variables for each domain are given in Tab. 2.1 along with commonly used symbols. Note that the state variables x are conveniently chosen as the *energy variables* (i. e. the flow variables integrated with respect to time). This way, they describe the energy accumulated in the system.

Power bonds are represented as edges between elements (nodes) in GBGs as depicted in Fig. 2.1a. In directed bond graphs, a half-arrow is added on one side of the edge stroke. It indicates the positive reference direction of the energy flow and is, by convention, located on the side of the flow variable [17]. A sample bond graph with elements A and B and their interconnections is shown in Fig. 2.1b.

When deriving a mathematical model from a bond graph, one needs to set up the constitutive equations of all the elements, which leads to a set of implicit equations.

[1] See e. g. [17] for a detailed discussion on how generalized bond graphs differ from their 'traditional' counterparts.

Table 2.1: Physical domains and their variables [37]

physical domain	flow $f \in \mathcal{F}$	effort $e \in \mathcal{E}$	state variable $x = -\int f \, \mathrm{d}t$
electric	current i	voltage u	charge q
magnetic	voltage u	current i	magnetic flux linkage λ
potential translation	velocity v	force F	displacement x
kinetic translation	force F	velocity v	momentum p
potential rotation	angular velocity ω	torque M	angular displacement θ
kinetic rotation	torque M	angular velocity ω	angular momentum L
elastic hydraulic	volume flow $\dot{V}$	pressure p	volume V
kinetic hydraulic	pressure p	volume flow $\dot{V}$	flow tube momentum Γ
thermal	temperature T	entropy flow $\dot{S}$	entropy S
chemical	molar flow $\dot{n}$	chemical potential μ	number of moles n

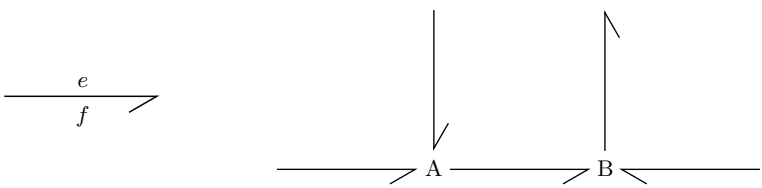

(a) Directed power bond (b) Interconnection of two systems in a sample bond graph

Figure 2.1: Power bonds in GBGs. The arrow indicates the positive reference direction of the energy flow

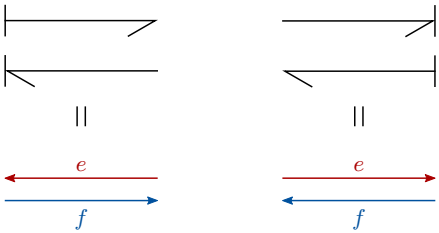

Figure 2.2: The causal stroke indicates at which end the effort acts as input as indicated by the signal arrows below

At this point it is not clear, which variables will be the inputs to an equation and which the outputs. Also, there is no unique solution to this problem. In the bond graph framework, making a choice is called an *assignment of computational causality*. This has many important implications, as detailed e. g. in [17]. Decisions on the computational causality can be made graphically – before setting up a model – by adding a so-called *causal stroke* at one end of a bond. At the port marked this way, the effort variable acts as an input to the constitutive equations of the element [37]. This is illustrated in Fig. 2.2. Note that the assignment of computational causality (i. e. the computational structure) is independent of the reference direction of the energy flows. Once the computational causality has been assigned at all bonds, a *causally completed* or simply *causal bond graph* results [17]. There are several rules for assigning computational causality, depending on the type of elements connected by a bond.

For the models presented in the remaining chapters, no bond graph representation is given. They are directly formulated as port-Hamiltonian systems. Systematic derivation of port-Hamiltonian system models from bond graphs is e. g. explained in [36]. Readers that are not familiar with the methodology are encouraged to study the referenced literature on bond graphs since the line of thought is intimately connected to port-Hamiltonian systems.

2.2 Basic components of physical systems

Basic elements of physical systems in the GBG formalism can be grouped into five different categories according to their physical behavior [37]:

- Energy storage
- Supply and demand
- Irreversible transformation

- Reversible transformation
- Energy distribution

The most important properties and the constitutive equations of elements in these categories are briefly summarized in the following. More advanced topics, such as multiports, entropy producing or modulated elements and signal ports, are not covered in this thesis.

Storage

Storage of energy is not power continuous (i. e. the net power flow into the node does not equal zero) and must be reversible. Commonly, a differentiation is made between storage elements of capacitor type (labeled 'C') and inertia type (labeled 'I') that are dual to each other. In the GBG framework, due to the decomposition of 'conventional' domains, I type storage is not used since it can also be represented with the help of C type storage. The constitutional equation of C type storage relates the energy variable to the effort variable as follows

$$x(t) = \Phi(e(t)) \quad \text{and in the linear case} \quad x(t) = Ce(t). \tag{2.2}$$

Reversibility dictates that the function $\Phi : \mathbb{R} \to \mathbb{R}$ must have a unique single-valued inverse Φ^{-1}. For a linear capacitor, the constant coefficient C would be its capacitance and for a mechanical spring its stiffness. From Tab. 2.1 follows the relation between flow and energy variable

$$\dot{x}(t) = -f(t). \tag{2.3}$$

Since the product of effort and flow equals power (cf. (2.1)), the energy stored in the element is obtained as

$$E(t) = -\int_0^t e(\tau) f(\tau)\,\mathrm{d}\tau = -\int_0^x \Phi^{-1}(\tilde{x})\,\mathrm{d}\tilde{x}, \tag{2.4}$$

assuming that no energy is stored at time $t = 0$. Although energy stores can be assigned both computational causalities, there is a preferred choice. If the effort of a C storage is the output of the constitutional equation (2.2), it can be calculated by integrating the flow variable with respect to time

$$e(t) = \Phi^{-1}(x(t)) = \Phi^{-1}\left(-\int_0^t f(\tau)\,\mathrm{d}\tau\right). \tag{2.5}$$

Otherwise, differentiation with respect to time is required to compute the flow variable

$$f(t) = -\frac{\mathrm{d}}{\mathrm{d}t}\Phi(e(t)) = -\frac{\mathrm{d}\Phi}{\mathrm{d}e}\dot{e}(t). \tag{2.6}$$

Equation (2.5) is thus referred to as *integral* causality and (2.6) as *derivative* causality [17]. Integral causality is preferred, since the time derivative of a discontinuous input to (2.6) would result in jumps of infinite height at the output. Also, if all storage elements have integral causality assigned, it is often possible to derive explicit differential equations for a given system. In case of mixed computational causality, a system of differential algebraic equations (DAEs) results in general, which is more difficult to handle from a computational point of view.

Supply and demand

Energy sources and sinks can be considered idealized storage elements with a capacity that is large with respect to the dynamics of the system. As such, they are not part of the system itself but boundary conditions that describe its interaction with the environment. Examples of sources and sinks include the gravitational force, the temperature of the environment or earth (ground) potential in electrical network modeling. Two types of sources are distinguished, depending on whether they impose a condition on the flow variable or the effort variable at a given node. Sources of effort are designated by the symbol 'Se' and 'Sf' is used for the dual type. Note that a source can also act as a sink and vice verse. Computational causality is decided on by the type of the source (since it determines which variable is the output).

Irreversible transformation

Energy cannot actually be lost according to the first law of thermodynamics. However, if the temperature of a system can be assumed homogeneous and constant over the time horizon of interest, conversion of other forms of energy into heat can be regarded as a dissipation of *free energy*. This defines free energy as the total system energy minus thermal energy – such that it can be lost. A dissipative element or a generalized resistor is obtained by establishing a static relation between effort and flow variable

$$e(t) = -\Phi_R(f(t)) \tag{2.7}$$

or alternatively

$$f(t) = -\Phi_G(e(t)), \tag{2.8}$$

where the former is referred to as impedance form and the latter as admittance form. Both Φ_R and Φ_G must have a unique, single-valued inverse [17]. In the linear case, one obtains

$$e(t) = -Rf(t), \quad R \geq 0, \tag{2.9}$$

which e. g. produces Ohm's law $u = -Ri$ for a linear resistor in the electrical domain. The minus sign is a consequence of adopting the active sign convention. Dissipative elements must satisfy the additional constraint

$$e(t)f(t) \leq 0, \quad t > 0, \tag{2.10}$$

(a) Transformer with modulus m (b) Gyrator with gyrator ratio r

Figure 2.3: Power conserving two-ports performing energy conversion

where the positive reference direction of the energy flow is away from the element. Otherwise, the elements would be able to generate power instead of dissipating it. There are no general rules for assigning the computational causality of resistors.

Reversible transformation

Reversible transformation of energy in GBGs is performed by *transformers* and *gyrators*. Both are power-continuous two-port (in general n-port) elements for which the power conservation reads

$$e_1 f_1 = e_2 f_2. \tag{2.11}$$

A transformer is represented by the symbol 'TF', as shown in Fig. 2.3a and has the following additional constitutive equation

$$e_1(t) = m \cdot e_2(t), \tag{2.12}$$

where the modulus m is a positive real constant. If the efforts e_1 and e_2 are the voltages across the element terminals, it describes an ideal electrical transformer – hence the name. For a mechanical gear pair, with the efforts being velocities, m is the gear ratio. The relationship between the flow variables results directly from the power conservation property (2.11)

$$f_2(t) = m \cdot f_1(t). \tag{2.13}$$

In contrast to a transformer, a gyrator establishes a relation between the effort variable of one terminal and the flow variable of the other. This results in the following constitutive relations [17]

$$e_1(t) = r \cdot f_2(t), \tag{2.14a}$$

$$e_2(t) = r \cdot f_1(t), \tag{2.14b}$$

in which the power conservation property is included. As depicted in Fig. 2.3b, the symbol 'GY' is used for gyrators with the gyrator ratio $r \in \mathbb{R}, r > 0$. Gyrators play an important role as interfaces between energy domains. For example, the conversion of electric into magnetic energy in an electrical coil can be represented by a gyrator.

Because transformers and gyrators have more than one port, there are rules for assigning their computational causality. Since one effort of a transformer acts as the input, the other must be the output. Gyrators enforce that both efforts are either inputs or outputs.

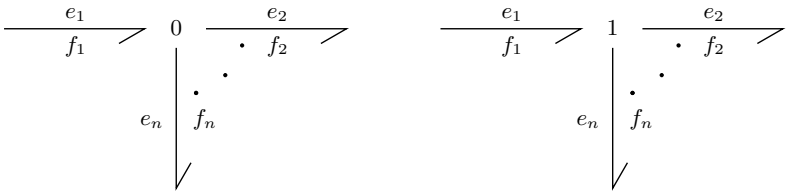

(a) Zero junction or flow junction

(b) One junction or effort junction

Figure 2.4: Power-conserving junctions in the GBG framework

Distribution

One of the most important concepts in the GBG framework is the generalization of the interconnection structure. Transformers, gyrators and ideal constraints are part of what is called the *generalized junction structure*. What is missing, are power conserving energy distribution nodes with more than two ports. These are called *0-junctions* and *1-junctions* and may be viewed as domain-independent versions of Kirchhoff's current and voltage law. See Figs. 2.4a and b for their graphical representation.

The 0-junction is also referred to as common effort junction because all the efforts at the node are set to be identical while all flows have to sum up to zero [17]

$$e_1 = e_2 = \cdots = e_n, \tag{2.15a}$$
$$f_1 - f_2 - \cdots - f_n = 0. \tag{2.15b}$$

Given the efforts are voltages, the second equation is Kirchhoff's current law. In the mechanical domain, with the flows being forces, d'Alembert's principle results. When the role of efforts and flows is interchanged, the constitutive equations for the 1-junction are obtained

$$f_1 = f_2 = \cdots = f_n, \tag{2.16a}$$
$$e_1 - e_2 - \cdots - e_n = 0. \tag{2.16b}$$

As previously mentioned, a 1-junction in the electrical domain yields Kirchhoffs's voltage law. If one effort of a 1-junction is defined as the output of the element, all others must be inputs. Consequently, the reverse is true in terms of computational causality for the 0-junction.

Example – DC motor

Let us study a simple example of a multi-domain system containing elements from each of the five physical categories introduced in this section. In Fig. 2.5, the circuit

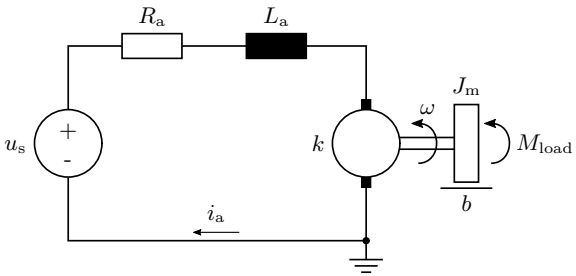

Figure 2.5: Circuit diagram of a DC motor driving a mechanical load [17]

diagram of a DC motor connected to a mechanical load is depicted. One possible bond graph representation of this system is given in Fig. 2.6. The example is also included in different text books, such as [17] and [109].

The shunt motor essentially converts the current i_a through its armature into a mechanical torque M_k. It also performs the reverse action – transforming the rotational velocity ω of the shaft into a voltage u_a. In the bond graph, this is represented by a gyrator

$$M_k = k \cdot i_\mathrm{a}, \qquad u_\mathrm{a} = -k \cdot \omega, \tag{2.17}$$

with torque constant k. Note that the gyrator connects the electrical domain (blue) to the mechanical domain (red) or rather converts energy between the two. The system contains two energy storage elements – the ideal inductance L_a of the armature coil and the rotor inertia J_m. In a 'conventional' bond graph, both would be represented by I type storage elements. Since those are not available in the GBG formalism, they are simply replaced by C storage elements connected to a gyrator with ratio $r = 1$ (a. k. a. *symplectic gyrator*). Taking the magnetic flux Φ and the angular momentum L as state variables, the constitutive equations of the stores can be stated as

$$\Phi = L_\mathrm{a} \cdot i_\mathrm{a}, \qquad L = J_\mathrm{m} \cdot \omega. \tag{2.18}$$

Energy dissipation is included by means of the electrical resistance R_a of the armature windings and mechanical friction of the rotor with friction coefficient b such that

$$u_R = -R_\mathrm{a} \cdot i_\mathrm{a}, \qquad M_b = -b \cdot \omega. \tag{2.19}$$

Two 1-junctions – one in each domain – connect the elements to each other. On the electrical side, the junction produces Kirchhoff's voltage law and on the mechanical side, d'Alembert's principle

$$u_\mathrm{s} + u_R + u_L + u_\mathrm{a} = 0, \quad \text{currents are equal,} \tag{2.20a}$$

$$M_\mathrm{load} + M_b + M_k + M_\mathrm{m} = 0, \quad \text{rotational velocities are equal.} \tag{2.20b}$$

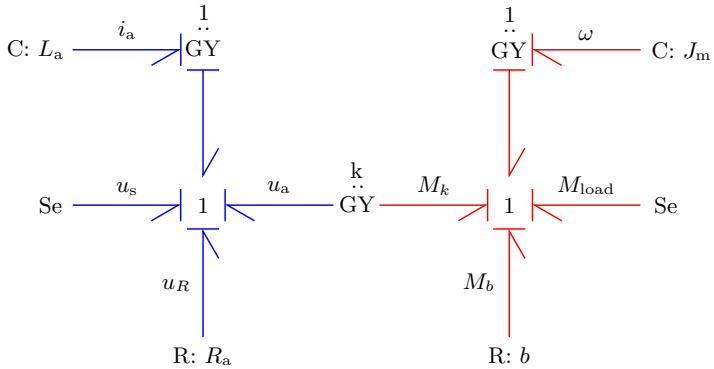

Figure 2.6: Causally complete bond graph corresponding to the DC motor in Fig. 2.5. The electrical domain is highlighted in blue and the mechanical one in red. Inter-domain coupling takes place via a gyrator

The voltage source u_s and the mechanical load M_load are considered inputs to the system. Hence, they are represented by sources in the bond graph. After assigning integral causality to the storage elements, the computational causality of the rest of the graph is determined by the rules stated above. In the next section, a dynamical model of this system in port-Hamiltonian form will be derived.

2.3 Port-Hamiltonian systems

Now that the basic terminology and concepts of energy-based modeling have been clarified, port-Hamiltonian systems can be introduced in more brevity. Port-Hamiltonian systems are dynamical physical systems associated with a *geometric structure*. As such, they can be obtained from bond graphs in a natural way, with the dynamics being defined by the storage and resistive elements and the geometric structure arising from the generalized junction structure.

Dirac structure

A fundamental concept of port-Hamiltonian system theory is the mathematical formulation of the interconnection structure as a *Dirac structure* [109]. Let $\mathcal{F}$ be the finite-dimensional linear space of flows with the elements $\boldsymbol{f} \in \mathcal{F}$. Then its dual is the space of efforts denoted $\mathcal{E} := \mathcal{F}^*$ with the elements $\boldsymbol{e} \in \mathcal{E}$. The combined space $\mathcal{F} \times \mathcal{E}$ is called the space of *port variables*. This enables the definition of a Dirac structure

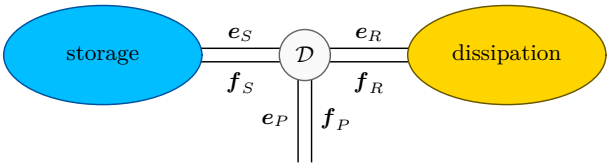

Figure 2.7: Port-Hamiltonian system as interconnection of energy storage and energy dissipation with external ports via a Dirac structure $\mathcal{D}$ [109]

on the space of port variables as a subspace $\mathcal{D} \subset \mathcal{F} \times \mathcal{F}^*$ with properties [37]

$$\langle \boldsymbol{e} | \boldsymbol{f} \rangle = 0, \text{ for all } (e, f) \in \mathcal{D}, \tag{2.21a}$$

$$\dim \mathcal{D} = \dim \mathcal{F}. \tag{2.21b}$$

The first equation is immediately recognized as the power conservation property, since $\langle \boldsymbol{e} | \boldsymbol{f} \rangle = \boldsymbol{e}^{\mathrm{T}} \boldsymbol{f} = P$, such that the total power entering or leaving a Dirac structure is zero. It can be proven that the maximal dimension of any subspace of $\mathcal{F} \times \mathcal{E}$ satisfying (2.21a) is $\dim \mathcal{F}$ (see e. g. [37] and [109]). An alternative definition of a Dirac structure, that can also be generalized to infinite-dimensional systems, is given with respect to the symmetric bilinear form $\ll \cdot, \cdot \gg$ on $\mathcal{E} \times \mathcal{F}$ defined as [109]

$$\ll (\boldsymbol{f}_1, \boldsymbol{e}_1), (\boldsymbol{f}_2, \boldsymbol{e}_2) \gg := \langle \boldsymbol{e}_1 | \boldsymbol{f}_2 \rangle + \langle \boldsymbol{e}_2 | \boldsymbol{f}_1 \rangle. \tag{2.22}$$

A Dirac structure $\mathcal{D} \subset \mathcal{E} \times \mathcal{F}$ is then equally defined by

$$\mathcal{D} = \mathcal{D}^{\perp}, \tag{2.23}$$

where $\perp$ denotes the orthogonal companion with respect to the bilinear form (2.22), such that the latter is zero restricted to this subspace.

All the power-conserving elements introduced in the previous section define a Dirac structure. It follows, that the composition of Dirac structures is again a Dirac structure. In Fig. 2.7, the composite Dirac structure $\mathcal{D}$ interconnects all energy storing elements of a system with the energy dissipating ones. Exchange of energy with the environment is enabled by external ports.

Storage port

The energy variables $\boldsymbol{x}$ of a system's energy storage are elements of the finite-dimensional state-space $\mathcal{X}$. Total energy contained in the system is expressed by its *Hamiltonian* function $H : \mathcal{X} \to \mathbb{R}$. Flows and efforts of the *storage port* of the Dirac

structure are denoted $\boldsymbol{f}_S$ and $\boldsymbol{e}_S$. They are connected to the energy storing elements by setting

$$\boldsymbol{f}_S = -\dot{\boldsymbol{x}}, \qquad \boldsymbol{e}_S = \frac{\partial H}{\partial \boldsymbol{x}}(\boldsymbol{x}). \tag{2.24}$$

For any current state $\boldsymbol{x}$, the flow vector $\dot{\boldsymbol{x}}$ lies on the tangent space $T_x\mathcal{X}$, while the effort vector $\frac{\partial H}{\partial \boldsymbol{x}}(\boldsymbol{x})$ is element of the dual space $T_x^*\mathcal{X}$, the cotangent space of $\mathcal{X}$ [109]. The energy balance of the storage port can now be stated as

$$\dot{H} = \left\langle \frac{\partial H}{\partial \boldsymbol{x}}(\boldsymbol{x}) \,\middle|\, \dot{\boldsymbol{x}} \right\rangle = -\boldsymbol{e}_S^{\mathrm{T}} \boldsymbol{f}_S, \tag{2.25}$$

where the minus sign indicates that $\boldsymbol{e}_S^{\mathrm{T}} \boldsymbol{f}_S$ is the power flowing from the energy storing elements into the Dirac structure [109].

Resistive port

Energy dissipation is ascribed to the *resistive port* of a system with the port variables $\boldsymbol{e}_R \in \mathcal{E}_R$ and $\boldsymbol{f}_R \in \mathcal{F}_R$. The resistive elements must satisfy a static relation $\mathcal{R} \subset \mathcal{E}_R \times \mathcal{F}_R$ of the form

$$R\left(\boldsymbol{f}_R, \boldsymbol{e}_R\right) = 0, \tag{2.26}$$

with all $(f_R, e_R) \in \mathcal{R}$ conforming to

$$\langle \boldsymbol{f}_R | \boldsymbol{e}_R \rangle \leq 0. \tag{2.27}$$

See Eqs. (2.9) and (2.10) for the case of a single linear resistive element.

External port

Energy exchange with entities considered external to a system takes place at the Dirac structure's *external port*, which has the port variables $\boldsymbol{e}_P \in \mathcal{E}_P$ and $\boldsymbol{f}_P \in \mathcal{F}_P$. It is often further distinguished between *controller* action ports, an *interaction port* for energy exchange with the physical environment and ports corresponding to sources [37]. Including the external port, the total power balance can be written as

$$\boldsymbol{e}_S^{\mathrm{T}} \boldsymbol{f}_S + \boldsymbol{e}_R^{\mathrm{T}} \boldsymbol{f}_R + \boldsymbol{e}_P^{\mathrm{T}} \boldsymbol{f}_P = 0. \tag{2.28}$$

Taking (2.25) and (2.27) into account, the energy flow becomes

$$\dot{H} = \boldsymbol{e}_R^{\mathrm{T}} \boldsymbol{f}_R + \boldsymbol{e}_P^{\mathrm{T}} \boldsymbol{f}_P \leq \boldsymbol{e}_P^{\mathrm{T}} \boldsymbol{f}_P, \tag{2.29}$$

which expresses the fact that the increase of system energy is always less than or equal to the externally supplied power.

Dynamics and common representations

Given the above, the dynamics of a port-Hamiltonian system on the state space $\mathcal{X}$ with Hamiltonian $H : \mathcal{X} \to \mathbb{R}$ are implicitly defined by

$$\left\{\dot{\boldsymbol{x}}, \frac{\partial H}{\partial \boldsymbol{x}}(\boldsymbol{x}), \boldsymbol{f}_R, \boldsymbol{e}_R, \boldsymbol{f}_P, \boldsymbol{e}_P\right\} \in \mathcal{D}, \quad (\boldsymbol{f}_R, \boldsymbol{e}_R) \in \mathcal{R}, \quad t > 0, \tag{2.30}$$

with the Dirac structure

$$\mathcal{D} \subset T_x\mathcal{X} \times T_x^*\mathcal{X} \times \mathcal{F}_R \times \mathcal{E}_R \times \mathcal{F}_P \times \mathcal{E}_P. \tag{2.31}$$

This coordinate-free definition of a port-Hamiltonian system is ineligible for e. g. simulation. However, different coordinate representations exist for different purposes. Perhaps the most convenient representation for control engineering purposes is the *input-state-output* form stated as [109]

$$\dot{\boldsymbol{x}} = [\boldsymbol{J}(\boldsymbol{x}) - \boldsymbol{R}(\boldsymbol{x})] \frac{\partial H}{\partial \boldsymbol{x}}(\boldsymbol{x}) + \boldsymbol{G}(\boldsymbol{x})\boldsymbol{u}, \tag{2.32a}$$

$$\boldsymbol{y} = \boldsymbol{G}^{\mathrm{T}}(\boldsymbol{x}) \frac{\partial H}{\partial \boldsymbol{x}}(\boldsymbol{x}), \tag{2.32b}$$

where $\boldsymbol{J}(\boldsymbol{x}) = -\boldsymbol{J}^{\mathrm{T}}(\boldsymbol{x})$ is a skew-symmetric map from $T_x^*\mathcal{X}$ to $T_x\mathcal{X}$ and $\boldsymbol{R}(\boldsymbol{x}) = \boldsymbol{R}^{\mathrm{T}}(\boldsymbol{x}) \geq 0$ is a symmetric, positive semi-definite matrix that specifies the resistive structure. The inputs and outputs $(\boldsymbol{u}, \boldsymbol{y})$ belong to the external port of the Dirac structure and $\boldsymbol{u}^{\mathrm{T}}\boldsymbol{y}$ equals the externally supplied power. Note that the input matrix $\boldsymbol{G}(\boldsymbol{x})$ is the transpose of the output matrix $\boldsymbol{G}^{\mathrm{T}}(\boldsymbol{x})$, which expresses the fact that inputs and outputs are collocated. In case of a linear system, the Hamiltonian is quadratic and

$$H(\boldsymbol{x}) = \frac{1}{2}\boldsymbol{x}^{\mathrm{T}}\boldsymbol{Q}\boldsymbol{x}, \tag{2.33}$$

for some symmetric, positive definite matrix $\boldsymbol{Q}$. Then, the effort variables of the energy storage are obtained as $\boldsymbol{e}_S = \frac{\partial H}{\partial \boldsymbol{x}}(\boldsymbol{x}) = \boldsymbol{Q}\boldsymbol{x}$.

In many cases, the equations (2.30) will constrain the set of admissible states $\boldsymbol{x}$. In fact, most power-conserving elements introduced in Section 2.2 impose constraints on a system. It can then be represented by a mixed set of differential and algebraic equations (DAEs)

$$\dot{\boldsymbol{x}} = [\boldsymbol{J}(\boldsymbol{x}) - \boldsymbol{R}(\boldsymbol{x})] \frac{\partial H}{\partial \boldsymbol{x}}(\boldsymbol{x}) + \boldsymbol{G}(\boldsymbol{x})\boldsymbol{u} + \boldsymbol{B}(\boldsymbol{x})\boldsymbol{\lambda} \tag{2.34a}$$

$$\boldsymbol{y} = \boldsymbol{G}^{\mathrm{T}}(\boldsymbol{x}) \frac{\partial H}{\partial \boldsymbol{x}}(\boldsymbol{x}), \tag{2.34b}$$

$$\boldsymbol{0} = \boldsymbol{B}^{\mathrm{T}}(\boldsymbol{x}) \frac{\partial H}{\partial \boldsymbol{x}}(\boldsymbol{x}), \tag{2.34c}$$

where $\boldsymbol{\lambda}$ are the Lagrange multipliers and $\boldsymbol{B}(\boldsymbol{x})\boldsymbol{\lambda}$ the constraint forces. In case the algebraic constraints are of index one, their elimination – if desired – is straightforward [109] and a system of the form (2.32) results.

Example

Let us now revisit the example of the DC motor in Fig. 2.5 from the previous section and formulate its dynamics as a port-Hamiltonian system in input-state-output form. Usually, the storage port is considered first. Since the Hamiltonian is defined as the total energy of the system, it is obtained from (2.18) using (2.4) as

$$H = \frac{1}{2}\frac{\Phi^2}{L_\mathrm{a}} + \frac{1}{2}\frac{L^2}{J_\mathrm{m}}. \tag{2.35}$$

Next, efforts and flows are defined as

$$\boldsymbol{f} := -\dot{\boldsymbol{x}} = \begin{bmatrix} -\dot{\Phi} \\ -\dot{L} \end{bmatrix} = \begin{bmatrix} u_L \\ M_\mathrm{m} \end{bmatrix}, \quad \boldsymbol{e} := \frac{\partial H}{\partial \boldsymbol{x}} = \begin{bmatrix} \Phi/L_\mathrm{a} \\ L/J_\mathrm{m} \end{bmatrix} = \begin{bmatrix} i_\mathrm{a} \\ \omega \end{bmatrix}. \tag{2.36}$$

The resistive port of the system is specified by (2.19) and its interconnection structure by (2.17) together with (2.20). Inputs and outputs are the efforts and flows of the sources

$$\boldsymbol{u}^\mathrm{T} = \begin{bmatrix} u_\mathrm{s} & M_\mathrm{load} \end{bmatrix}, \qquad \boldsymbol{y}^\mathrm{T} = \begin{bmatrix} i_\mathrm{a} & \omega \end{bmatrix}. \tag{2.37}$$

This completes the definition of the system's Dirac structure and its ports. The motor dynamics in input-state-output port-Hamiltonian form can now be stated as

$$\begin{bmatrix} \dot{\Phi} \\ \dot{L} \end{bmatrix} = \begin{bmatrix} -R_\mathrm{a} & -k \\ k & -b \end{bmatrix} \begin{bmatrix} i_\mathrm{a} \\ \omega \end{bmatrix} + \begin{bmatrix} 1 & 0 \\ 0 & 1 \end{bmatrix} \begin{bmatrix} u_\mathrm{s} \\ M_\mathrm{load} \end{bmatrix}, \tag{2.38a}$$

$$\boldsymbol{y} = \begin{bmatrix} 1 & 0 \\ 0 & 1 \end{bmatrix} \begin{bmatrix} i_\mathrm{a} \\ \omega \end{bmatrix}. \tag{2.38b}$$

It is easily verified that Eqs. (2.38a) are the interconnection laws (2.20) in which u_R, u_L, u_a and M_b, M_k, M_m have been substituted for using Eqs. (2.17)-(2.19). The energy flow into and out of the system is given by

$$\dot{H} = \dot{\Phi} i_\mathrm{a} + \dot{L}\omega = \boldsymbol{u}^\mathrm{T}\boldsymbol{y} - (R_\mathrm{a} i_\mathrm{a}^2 + b\omega^2) \leq \boldsymbol{u}^\mathrm{T}\boldsymbol{y}. \tag{2.39}$$

Even though the example is a simple one, it demonstrates that a port-Hamiltonian system can be systematically constructed from a bond graph following straightforward steps. This makes the two frameworks perfectly compatible. However, it is not always feasible, nor is it necessary, to start from a bond graph representation.

2.4 Distributed parameter port-Hamiltonian systems

Formal definitions of distributed parameter port-Hamiltonian systems make use of the language of differential forms, since it enables a coordinate-free formulation. Despite this being a powerful approach, differential geometry is avoided here to increase the

accessibility of the presented material. Therefore, this section starts with a simple example – the vibrating string – to introduce the basics. Descriptions of infinite-dimensional port-Hamiltonian systems are then generalized as much as necessary as the example proceeds.

The dynamics of the isotropic vibrating string are described by the one-dimensional wave equation defined on the compact spatial domain $Z = \begin{bmatrix} a & b \end{bmatrix}$ with coordinate $z \in Z$

$$\mu \frac{\partial^2}{\partial t^2} u = \tau \frac{\partial^2}{\partial z^2} u. \tag{2.40}$$

Here, $u(z,t)$ is the vertical displacement of the string in its plane of oscillation, μ the mass per unit length and τ the tension. Just as in the finite-dimensional case, the Hamiltonian H is the total energy of the system. For the vibrating string it is given as the integral over the *Hamiltonian density* $\mathcal{H}$ (energy per volume element)

$$H = \int_Z \mathcal{H} = \frac{1}{2} \int_a^b \mu \left(\frac{\partial u}{\partial t} \right)^2 + \tau \left(\frac{\partial u}{\partial z} \right)^2 \mathrm{d}z, \tag{2.41}$$

where $\mathcal{H}$ is the sum of the kinetic and the potential energy density. After defining the vector of energy variables as

$$\boldsymbol{x}^{\mathrm{T}} = \begin{bmatrix} x_p & x_q \end{bmatrix} = \begin{bmatrix} \mu \frac{\partial u}{\partial t} & \frac{\partial u}{\partial z} \end{bmatrix}, \tag{2.42}$$

the Hamiltonian can be written in terms of $\boldsymbol{x}$. Flows and efforts are then defined as

$$\boldsymbol{f} = -\frac{\partial \boldsymbol{x}}{\partial t}, \qquad \boldsymbol{e} = \frac{\delta H}{\delta \boldsymbol{x}}, \tag{2.43}$$

where the definition of the flows follows that of the lumped parameter case (2.24). The efforts, however, are now obtained by taking the *variational derivative* $\frac{\delta H}{\delta \boldsymbol{x}}$ of the Hamiltonian functional H with respect to $\boldsymbol{x}$. Let $\delta \boldsymbol{x}(\boldsymbol{z})$, $\boldsymbol{z} = (z_1, \ldots, z_d) \in Z$ be a smooth, real-valued function with $\delta \boldsymbol{x}(\boldsymbol{z})|_{\partial Z} = 0$, where ∂Z denotes the boundary of the domain $Z \in \mathbb{R}^d$. Then, the variational derivative satisfies for all $\delta \boldsymbol{x}(\boldsymbol{z})$ and all $\epsilon \in \mathbb{R}$ [37]

$$H(\boldsymbol{x} + \epsilon \delta \boldsymbol{x}) = H(\boldsymbol{x}) + \epsilon \int_Z \frac{\delta H}{\delta \boldsymbol{x}} \delta \boldsymbol{x} \, \mathrm{d}V + \mathcal{O}(\epsilon^2). \tag{2.44}$$

Often, the energy density $\mathcal{H}$ depends only on the function $\boldsymbol{x}$ and not on its derivatives. In this case, the variational derivative simplifies to

$$\frac{\delta H}{\delta \boldsymbol{x}} = \frac{\mathrm{d}\mathcal{H}}{\mathrm{d}\boldsymbol{x}}, \tag{2.45}$$

the derivation of the integrand. For the example of the vibrating string, this implies

$$\boldsymbol{e}^{\mathrm{T}} = \begin{bmatrix} e_p & e_q \end{bmatrix} = \begin{bmatrix} \frac{\partial \mathcal{H}}{\partial p} & \frac{\partial \mathcal{H}}{\partial q} \end{bmatrix} = \begin{bmatrix} \frac{\partial u}{\partial t} & \tau \frac{\partial u}{\partial z} \end{bmatrix}, \tag{2.46}$$

with e_p the distributed vertical velocity and e_q the vertical component of the string tension. With the definition of the power conjugate variables $\boldsymbol{e}$ and $\boldsymbol{f}$, the dynamics of the vibrating string can be written as a Hamiltonian system of two conservation laws

$$\dot{\boldsymbol{x}} = \begin{bmatrix} \dot{x}_p \\ \dot{x}_q \end{bmatrix} = \begin{bmatrix} 0 & \partial_z \\ \partial_z & 0 \end{bmatrix} \begin{bmatrix} e_p \\ e_q \end{bmatrix} = J\boldsymbol{e}. \tag{2.47}$$

Contrary to the finite-dimensional formulation, J is a skew-symmetric differential operator instead of a matrix as in (2.32). For a generalization to the class of systems considered in this thesis, the following definition of a constant matrix differential operator according to Macchelli et al. in [86] is employed.

Denote by $\mathcal{U}$ and $\mathcal{V}$ a pair of smooth functions from $\Omega \in \mathbb{R}^d$ to $\mathbb{R}^{n_u}$ and $\mathbb{R}^{n_v}$ respectively. A constant matrix differential operator of order N is a map L from $\mathcal{U}$ to $\mathcal{V}$, with $\boldsymbol{u} = (u_1, \ldots, u_{n_u}) \in \mathcal{U}$ and $\boldsymbol{v} = (v_1, \ldots, v_{n_v}) \in \mathcal{V}$, such that

$$\boldsymbol{v} = L\boldsymbol{u} \iff \boldsymbol{v} := \sum_{|\alpha|=0}^{N} \boldsymbol{P}_\alpha D^\alpha \boldsymbol{u}, \tag{2.48}$$

where $\alpha := (\alpha_1, \ldots, \alpha_d)$ is a multi-index of order $|\alpha| := \sum_{i=0}^{d} \alpha_i$, $\boldsymbol{P}_\alpha$ are a set of constant $n_v \times n_u$ matrices and $D^\alpha := \partial_{z_1}^{\alpha_1} \ldots \partial_{z_d}^{\alpha_d}$ a differential operator of order $|\alpha|$ resulting from a combination of spatial derivatives. The formal adjoint of the operator (2.48) is the map L^* from $\mathcal{V}$ to $\mathcal{U}$ that satisfies

$$\boldsymbol{u} = L^*\boldsymbol{v} \iff \boldsymbol{u} := \sum_{|\alpha|=0}^{N} (-1)^{|\alpha|} \boldsymbol{P}_\alpha^{\mathrm{T}} D^\alpha \boldsymbol{v}. \tag{2.49}$$

Let J denote a constant matrix differential operator. Then, J is skew-symmetric if and only if $J = -J^*$, which corresponds to the condition [20]

$$\boldsymbol{P}_\alpha = (-1)^{|\alpha|+1} \boldsymbol{P}_\alpha^{\mathrm{T}}, \quad \forall \alpha. \tag{2.50}$$

Note that the operator J in (2.47) belongs to this class of skew-symmetric differential operators with $N = 1$.

In the formulation (2.47), the vibrating string is not yet a port-Hamiltonian system, because it lacks ports for energy exchange. In order to extend the Hamiltonian formulation, let us analyze the energy flow

$$\begin{aligned} \dot{H}(\boldsymbol{x}) &= \int_a^b \left(\frac{\delta H}{\delta \boldsymbol{x}}\right)^{\mathrm{T}} \dot{\boldsymbol{x}} \,\mathrm{d}z = \int_a^b \boldsymbol{e}^{\mathrm{T}} J \boldsymbol{e} \,\mathrm{d}z \\ &= \int_a^b e_p \partial_z e_q + e_q \partial_z e_p \,\mathrm{d}z = \int_a^b e_p \partial_z e_q - \partial_z e_q e_p \,\mathrm{d}z + [e_p e_q]_a^b \\ &= e_p(b) e_q(b) - e_p(a) e_q(a). \end{aligned} \tag{2.51}$$

Integration by parts was applied, which – due to the formal skew-symmetry of the operator J – makes internal flows of energy cancel themselves out. It follows that an increase or decrease of system energy is solely determined by the energy flow over the boundary ∂Z. This motivates the definition of boundary port variables as

$$\begin{bmatrix} \boldsymbol{f}_\partial \\ \boldsymbol{e}_\partial \end{bmatrix} = \begin{bmatrix} \frac{\delta H}{\delta x_p} \\ \frac{\delta H}{\delta x_q} \end{bmatrix} \Bigg|_{\partial Z} = \begin{bmatrix} e_p(a) & e_p(b) & e_q(a) & e_q(b) \end{bmatrix}^{\mathrm{T}}. \tag{2.52}$$

Given this definition of the port variables, the linear subset $\mathcal{D} \subset \mathcal{E} \times \mathcal{F}$ defined by

$$\mathcal{D} = \left\{ (\boldsymbol{e}, \boldsymbol{f}, \boldsymbol{e}_\partial, \boldsymbol{f}_\partial) \in \mathcal{E} \times \mathcal{F} \mid \boldsymbol{f} = -J\boldsymbol{e}, \quad \begin{bmatrix} \boldsymbol{f}_\partial \\ \boldsymbol{e}_\partial \end{bmatrix} = \boldsymbol{e}(a,b) \right\} \tag{2.53}$$

is a *Stokes-Dirac* structure with respect to the bilinear form (2.22) when the pairing $\langle \cdot | \cdot \rangle$ is given by

$$\langle \boldsymbol{f} | \boldsymbol{e} \rangle = \int_a^b \boldsymbol{e}^{\mathrm{T}} \boldsymbol{f} \, \mathrm{d}z + [e_p e_q]_a^b. \tag{2.54}$$

For the proof, refer to Chapter 4.1 of [37]. The Stokes-Dirac strcuture can be viewed as a generalization of the Dirac structure to the infinite-dimensional case, which relies heavily on Stokes' theorem (hence its name). This becomes more evident when higher order spatial manifolds are considered. Note that the two conservation laws (2.47) together with the co-energy variables (2.46) and the port variables (2.52) define a port-Hamiltonian system with respect to the Stokes-Dirac structure (2.53). In the sequel of this section, the definition of the Stokes-Dirac structure and distributed parameter port-Hamiltonian systems will be extended to a bigger class of systems.

Consider a skew-symmetric matrix differential operator J and its formal adjoint J^* defined by (2.48) and (2.49) respectively together with (2.50). Then, for all functions $\boldsymbol{u} \in \mathcal{U}$ and $\boldsymbol{v} \in \mathcal{V}$, the following can be stated [86]

$$\int_\Omega \left[\boldsymbol{v}^{\mathrm{T}} J \boldsymbol{u} + \boldsymbol{u}^{\mathrm{T}} J \boldsymbol{v} \right] \mathrm{d}V = \int_{\partial\Omega} B_J(\boldsymbol{u}, \boldsymbol{v}) \cdot \mathrm{d}A, \tag{2.55}$$

where B_J is a symmetric constant differential operator induced on $\partial\Omega$ by J.

Now, denote again by $\mathcal{F}$ the space of flows. Assume that it is the space of smooth functions mapping from the compact set $\Omega \in \mathbb{R}^d$ to $\mathbb{R}^q$ and that $\mathcal{E} \equiv \mathcal{F}$. Let $\boldsymbol{f} = (f_1, \ldots, f_q) \in \mathcal{F}$ and $\boldsymbol{e} = (e_1, \ldots, e_q) \in \mathcal{E}$ and denote by $\boldsymbol{w} := B_Z(\boldsymbol{e})$ the boundary terms. The operator B_Z restricts the efforts e and their spatial derivatives up to the proper order to the boundary $\partial\Omega$. Then, it is possible to write [86]

$$\int_{\partial\Omega} B_J(\boldsymbol{e}_1, \boldsymbol{e}_2) \cdot dA = \int_{\partial\Omega} B_J(\boldsymbol{w}_1, \boldsymbol{w}_2) \cdot \mathrm{d}A, \tag{2.56}$$

with $\boldsymbol{w}_i = B_Z(\boldsymbol{e}_i),\ i = 1, 2$. This allows the introduction of the following set of boundary variables

$$\mathcal{W} := \{\boldsymbol{w} \mid \boldsymbol{w} = B_Z(\boldsymbol{e}), \quad \forall \boldsymbol{e} \in \mathcal{E}\}. \tag{2.57}$$

Then it can be shown that the following subset of $\mathcal{F} \times \mathcal{E} \times \mathcal{W}$

$$\mathcal{D} := \{(\boldsymbol{f}, \boldsymbol{e}, \boldsymbol{w}) \in \mathcal{F} \times \mathcal{E} \times \mathcal{W} \mid \boldsymbol{f} = -J\boldsymbol{e}, \boldsymbol{w} = B_\Omega(\boldsymbol{e})\} \tag{2.58}$$

is a Stokes-Dirac structure with respect to the pairing

$$\ll (\boldsymbol{f}_1, \boldsymbol{e}_1, \boldsymbol{w}_1), (\boldsymbol{f}_2, \boldsymbol{e}_2, \boldsymbol{w}_2) \gg := \int_\Omega \left[\boldsymbol{e}_1^{\mathrm{T}} \boldsymbol{f}_2 + \boldsymbol{e}_2^{\mathrm{T}} \boldsymbol{f}_1\right] \mathrm{d}V + \int_{\partial\Omega} B_J(\boldsymbol{w}_1, \boldsymbol{w}_2) \cdot \mathrm{d}A. \tag{2.59}$$

This definition can be extended to account for external ports and dissipation (see [86]) in the Stokes-Dirac structure.

For a more general definition of a distributed parameter port-Hamiltonian system, denote by $\mathcal{X}$ the space of smooth real valued functions on $[0, +\infty) \times U$ representing the space of energy *configuration*. Then, the total energy is provided by the functional $H : \mathcal{X} : \mathbb{R}$ defined by

$$H(\boldsymbol{x}) = \int_\Omega \mathcal{H}(\boldsymbol{z}, \boldsymbol{x}) \, \mathrm{d}V. \tag{2.60}$$

With the flows and efforts given as

$$\boldsymbol{f} = -\dot{\boldsymbol{x}}, \qquad \boldsymbol{e} = \frac{\delta H}{\delta \boldsymbol{x}}, \tag{2.61}$$

an infinite-dimensional port-Hamiltonian system with respect to a constant Stokes-Dirac structure specified by (2.58) is given by

$$\dot{\boldsymbol{x}} = J \frac{\delta H}{\delta \boldsymbol{x}}, \tag{2.62a}$$

$$\boldsymbol{w} = B_\Omega \left(\frac{\delta H}{\delta \boldsymbol{x}}\right). \tag{2.62b}$$

The general definitions presented in this section will become clearer (and probably more useful) after studying a few examples. The reader is referred to Chapter 3, where the port-Hamiltonian formulation is presented for a range of infinite-dimensional mechanical systems. A thorough treatise of distributed parameter port-Hamiltonian systems of one spatial dimension is given by Zwart and Jacob in [142].

3 Elastodynamics

In this chapter, port-Hamiltonian models for a variety of linear elastic systems are introduced. Beforehand, the necessary background on the mechanics of elastic bodies is briefly summarized. Stress-strain relationships, the principle of virtual work as well as the derivation of the equations of motion are covered. Readers with a solid background in mechanics can skip Section 3.1. One-dimensional elements, such as beams and rods are introduced in Section 3.2. In Section 3.3, port-Hamiltonian models of a disk element and the Mindlin-Reissner plate are provided for modeling plane load-bearing structures.

3.1 Fundamentals of the mechanics of elastic bodies

Intention of this section is to provide a quick introduction to, or a recapitulation of, the mechanics of elastic bodies. The basic definitions and principles required for the understanding of the material in the remainder of this chapter will be presented briefly. First, stress strain relations are recalled for linear elastic and isotropic materials. Then, the principle of virtual work and the Euler-Lagrange equations of motions are given. More detailed derivations can be found in Appendix A.

3.1.1 Stress-strain relationships

For a linear isotropic material, the stress-strain relations are obtained from Hooke's law as [53]

$$\begin{aligned} \varepsilon_x &= \frac{1}{E}\left[\sigma_x - \nu(\sigma_y + \sigma_z)\right], \quad \gamma_{xy} = \frac{1}{G}\tau_{xy}, \\ \varepsilon_y &= \frac{1}{E}\left[\sigma_y - \nu(\sigma_z + \sigma_x)\right], \quad \gamma_{yz} = \frac{1}{G}\tau_{yz}, \\ \varepsilon_z &= \frac{1}{E}\left[\sigma_z - \nu(\sigma_x + \sigma_y)\right], \quad \gamma_{zx} = \frac{1}{G}\tau_{zx}, \end{aligned} \tag{3.1}$$

where $\varepsilon_x, \varepsilon_y$ and ε_z are the axial strain components and γ_{xy}, γ_{yz} and γ_{zx} the shear strain components, with σ_x, σ_y and σ_z the corresponding stress terms and τ_{xy}, τ_{yz} and τ_{zx} the shear stress components. Here, ν denotes Poisson's ratio, E denotes Young's modulus and the shear modulus G can be expressed as

$$G = \frac{2(1+\nu)}{E}. \tag{3.2}$$

The material law (3.1) describes three-dimensional or volumetric strain. In the remainder of this chapter, only beams and plates are studied, such that the stress-strain relationship can be further simplified.

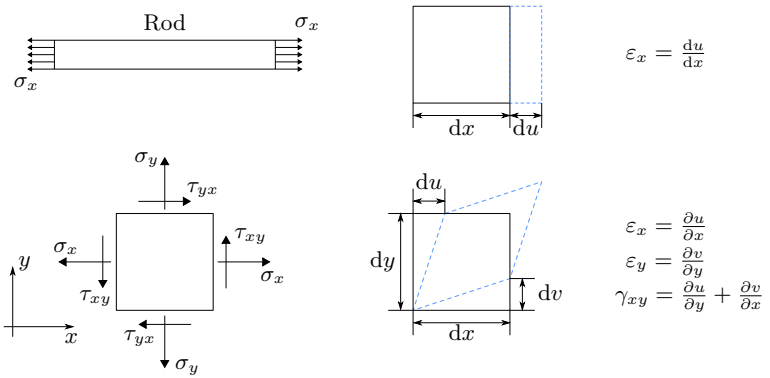

Figure 3.1: 1D and plane stress-strain and kinematic relations with the stress components σ_x, σ_y and the shear stress τ_{xy}. The displacements $\mathrm{d}u$ and $\mathrm{d}v$ are depicted for infinitesimal elements

For plane stress, it is assumed that $\sigma_z = \tau_{yz} = \tau_{xz} = 0$. Eliminating these terms in (3.1) and solving for the stress components, the material law can be expressed as

$$\begin{bmatrix} \sigma_x \\ \sigma_y \\ \tau_{xy} \end{bmatrix} = \frac{E}{1-\nu^2} \begin{bmatrix} 1 & \nu & 0 \\ \nu & 1 & 0 \\ 0 & 0 & \frac{1-\nu}{2} \end{bmatrix} \begin{bmatrix} \varepsilon_x \\ \varepsilon_y \\ \gamma_{xy} \end{bmatrix} = \boldsymbol{D}_{\mathrm{c}} \boldsymbol{\varepsilon}, \tag{3.3}$$

where $\boldsymbol{D}_{\mathrm{c}}$ is referred to as the *compliance matrix*. Note that σ_z is commonly neglected, since it is fully determined by ε_x and ε_y. Figure 3.1 can be consulted for an illustration of the deformations of an element under the state of plane stress. Denote by $u(x, y, t)$ the displacement of a point located at (x, y) on a planar element along the local x-axis and by $v(x, y, t)$ the displacement of the same point along the local y-axis. Then, the components of the strain vector $\boldsymbol{\varepsilon}$ for plane stress are given as

$$\boldsymbol{\varepsilon}^{\mathrm{T}} = \begin{bmatrix} \varepsilon_x & \varepsilon_y & \gamma_{xy} \end{bmatrix} = \begin{bmatrix} \frac{\partial u}{\partial x} & \frac{\partial v}{\partial y} & \frac{\partial u}{\partial y} + \frac{\partial v}{\partial x} \end{bmatrix}. \tag{3.4}$$

In the most simple case of a one-dimensional system, which is also depicted in Fig. 3.1, Hooke's law reduces to the well known form

$$\sigma = E\varepsilon. \tag{3.5}$$

Now that the static relationships between stress and strain have been introduced to sufficient detail, the next sections deal with the dynamics of elastic bodies.

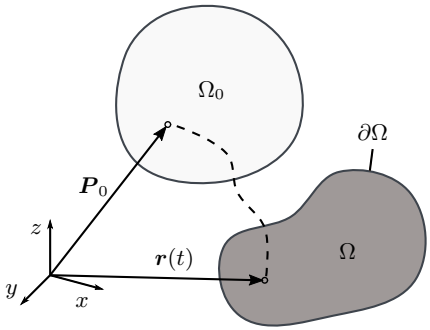

Figure 3.2: Elastic continuum Ω_0 in the reference configuration and its deformed state Ω at time t. Location of a point with initial position $\boldsymbol{P}_0$ over time is described by the vector $\boldsymbol{r}(t)$

3.1.2 Virtual work and the equations of motion

Consider an elastic continuum defined on the compact set Ω in $\mathbb{R}^3$, such as the one depicted in Fig. 3.2. In the reference configuration Ω_0, the position of a point P in this continuum is $\boldsymbol{P}_0$, whereas in the deformed state, its location is given by a vector $\boldsymbol{r}(P,t)$. Generally, the motion of each point is constrained, which implies that a reduced set of coordinates can be used to compute its location $\boldsymbol{r}$. If the number of variables in this set is minimal with respect to the constraints, they are referred to as *generalized coordinates*

$$\boldsymbol{q}^{\mathrm{T}} = \begin{bmatrix} q_1(x,y,z,t) & \dots & q_n(x,y,z,t) \end{bmatrix}, \tag{3.6}$$

where n is said smallest possible number of variables. In case each q_i describes a displacement u_i from the reference configuration, the term *generalized displacements* may be used interchangeably for $\boldsymbol{q}$. Now, the position $\boldsymbol{r}$ of each point can be uniquely expressed in terms of $\boldsymbol{q}$

$$\boldsymbol{r} = \boldsymbol{r}(\boldsymbol{q}, t). \tag{3.7}$$

The set of explicit constraints given by (3.7) is *scleronomic*, in case there is no explicit dependency on time and *rheonomic* otherwise. If constraints on the velocity are obtained by derivation of (3.7) with respect to time, they are called *holonomic* constraints. In case additional non-integrable constraints are present, the system is *nonholonmic* (i. e. its state depends on the path taken in order to achieve it). In the following, only systems subject to holonomic constraints are taken into account.

The principle of virtual work for an elastic continuum can be stated as [113]

$$\int_\Omega \boldsymbol{\delta r}^{\mathrm{T}}(\boldsymbol{k} - \rho\ddot{\boldsymbol{r}}) - \boldsymbol{\delta\varepsilon}^{\mathrm{T}}\boldsymbol{\sigma}\,\mathrm{d}V + \int_{\partial\Omega} \boldsymbol{\delta r}^{\mathrm{T}}\boldsymbol{p}\,\mathrm{d}A = 0, \tag{3.8}$$

with ρ the mass density, $\boldsymbol{k}$ the force density of the body forces (e. g. gravity) integrated over the volume V and $\boldsymbol{p}$ the force density of the surface forces integrated over the boundary surface A. The term $\boldsymbol{\delta r}$ denotes the *virtual displacements*, as introduced in more detail in Appendix A. With the help of (3.7), (3.8) can also be expressed in terms of the generalized coordinates $\boldsymbol{q}$.

The equations of motions can be derived from the principle of virtual work. Readers are again referred to Appendix A to see how this is done. Let U denote the potential energy of an elastic body and T its kinetic energy. Then, the Euler-Lagrange equations of motions for this body can be stated as

$$-\frac{\mathrm{d}}{\mathrm{d}t}\frac{\partial T}{\partial \dot{\boldsymbol{q}}}+\frac{\partial T}{\partial \boldsymbol{q}}-\frac{\partial U}{\partial \boldsymbol{q}}=\boldsymbol{0}, \tag{3.9}$$

which is already given in generalized coordinates $\boldsymbol{q}$.

3.2 Port-Hamiltonian dynamics of beams

This section is a modified version of the section on beam dynamics in [135]. The presentation here is slightly improved and adapted to the style of this thesis.

Models of complex civil engineering structures are usually built by interconnecting basic element types with different parameters. The number of elements forming a model is commonly higher than the number of basic types it is composed of. In this section, the dynamics of beams are formulated as distributed parameter port-Hamiltonian systems. The resulting systems can be used for the modeling of truss structures and frames. Beams, as systems of one spatial dimension, cannot be used for the modeling of plane load-bearing structures. Elements of plane load-bearing structures are introduced in Section 3.3.

Figure 3.3 depicts a beam of length L defined on the spatial domain $X := \begin{bmatrix}0 & L\end{bmatrix}$ with spatial coordinate x, which is subject to bending, torsional and axial stress. When subject to bending, the beam experiences a deflection $w(x)$ from the neutral axis and a rotation of the cross section by the angle $\varphi(x)$. For torsional loads, the cross section rotates by the angle $\omega(x)$ about the neutral axis. Axial strain is determined by the deflection under axial loads, $u(x)$. Since the load cases are considered linearly independent, their dynamics can be treated separately. A complete beam model thus consists of three basic components, which are presented in the following. In Section 3.2.1, the model for a rod element deforming due to axial loads is presented. Saint-Venant torsion is modeled in port-Hamiltonian form in Section 3.2.2. For bending, a port-Hamiltonian model is derived for both the Timoshenko beam in Section 3.2.3 and the Euler-Bernoulli beam equations in Section 3.2.4. The latter are used when the assumption that the cross section is always perpendicular to the neutral axis holds (i. e. for thin beams).

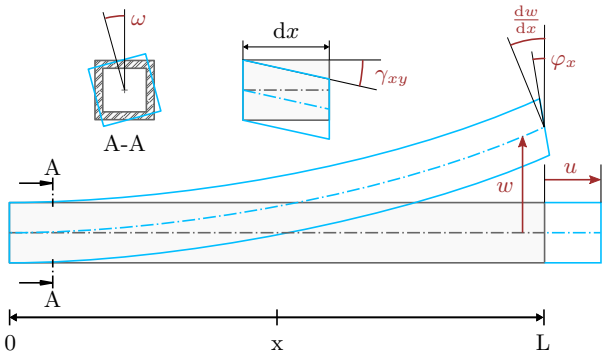

Figure 3.3: A beam element on the interval $X = \begin{bmatrix} 0 & L \end{bmatrix}$ and its deflections (blue) due to bending (w, φ_x), shear (γ_{xy}), torsional (ω) and axial loads (u) [135]

3.2.1 Rod element

The simplest component of beam dynamics is the rod element, or rather the beam's response to axial loads. Its constitutional law is given by (3.5), Hooke's law for a one-dimensional deformation. With the axial strain $\varepsilon_x = \partial u / \partial x$ and the elastic force $F_x = A\sigma_x$, the rod energy can be expressed as

$$U = \frac{1}{2}\int_0^L EA\left(\frac{\partial}{\partial x}u\right)^2 \mathrm{d}x, \quad T = \frac{1}{2}\int_0^L \mu\left(\frac{\partial}{\partial t}u\right)^2 \mathrm{d}x \quad \text{and} \quad H = T + U, \tag{3.10}$$

where μ is the mass per unit length, A the cross-sectional area and H the system Hamiltonian. With the generalized coordinate u, the equations of motion are obtained according to (3.9), as

$$\mu\frac{\partial^2 u}{\partial t^2} = \frac{\partial}{\partial x}\left(EA\frac{\partial u}{\partial x}\right). \tag{3.11}$$

Integration by parts was applied once to U to arrive at the above. Note that (3.11) corresponds to the vibrating string example in Section 2.4 when $\tau = EA$. The remaining steps for obtaining a port-Hamiltonian system thus are the same as for the vibrating string. Let the energy variables and the state vector be defined as

$$x_p := \mu\frac{\partial u}{\partial t}, \quad x_q := \varepsilon_x \quad \text{and} \quad \boldsymbol{x}^{\mathrm{T}} = \begin{bmatrix} x_p & x_q \end{bmatrix}. \tag{3.12}$$

Then, the effort variables are obtained by taking the variational derivative of H with respect to $\boldsymbol{x}$

$$e_p = \frac{\delta H}{\delta x_p} = \frac{\partial u}{\partial t}, \qquad e_q = \frac{\delta H}{\delta x_q} = EA\frac{\partial u}{\partial x}, \tag{3.13}$$

where e_p is the strain rate and e_q the axial force distributed over the interval X. By defining the flow variables as $\boldsymbol{f} := -\dot{\boldsymbol{x}}$, the rod element can be formulated as infinite-dimensional Hamiltonian system

$$-\boldsymbol{f} = \begin{bmatrix} \dot{x}_p \\ \dot{x}_q \end{bmatrix} = \begin{bmatrix} 0 & \partial_x \\ \partial_x & 0 \end{bmatrix} \begin{bmatrix} e_p \\ e_q \end{bmatrix}. \tag{3.14}$$

For a definition of the boundary ports, the energy flow needs to be taken into account

$$\begin{aligned} \dot{H} &= \int_0^L \left(\frac{\delta H}{\delta \boldsymbol{x}}\right)^{\mathrm{T}} \dot{\boldsymbol{x}} \,\mathrm{d}x \\ &= \int_0^L e_p \dot{p} + e_q \dot{q} \,\mathrm{d}x \\ &= \int_0^L e_p(\partial_x e_q) + e_q(\partial_x e_p) \,\mathrm{d}x \\ &= \int_0^L e_p(\partial_x e_q) - (\partial_x e_q) e_p \,\mathrm{d}x + \left[e_q e_p\right]_0^L. \end{aligned} \tag{3.15}$$

From the second line of (3.15), it follows that the energy flow depends only on the boundary values of the effort variables. This motivates the definition of boundary inputs $\boldsymbol{u}_\partial$ and outputs $\boldsymbol{y}_\partial$ such that the Hamiltonian rate of change can be expressed as $\dot{H} = \boldsymbol{u}_\partial^{\mathrm{T}} \boldsymbol{y}_\partial$. A possible choice of the boundary variables is given by

$$\boldsymbol{u}_\partial^{\mathrm{T}} = \begin{bmatrix} -e_q(0) & e_q(L) \end{bmatrix}, \quad \boldsymbol{y}_\partial^{\mathrm{T}} = \begin{bmatrix} e_p(0) & e_p(L) \end{bmatrix}. \tag{3.16}$$

As stated e. g. in [78], other definitions of the boundary variables are also valid. However, as will be shown later, (3.16) is a convenient choice as it has a normalizing property in the application of appropriate spatial discretization methods. The definition of $\boldsymbol{u}_\partial$ and $\boldsymbol{y}_\partial$ completes the formulation of (3.11) as distributed parameter port-Hamiltonian system with power exchange over the boundary.

3.2.2 Torque bar

Beam deformation due to torsion about the neutral axis is assumed to be warping-free such that only Saint-Venant torsion needs to be taken into account. Hence, the shear strain can be expressed as $\tau_x = G J_{\mathrm{t}} \gamma_x$, with J_t the torsion constant and $\gamma_x = \partial\omega/\partial x$. The system energy of the torque bar is given as

$$U = \frac{1}{2} \int_0^L G J_{\mathrm{t}} \left(\frac{\partial}{\partial x}\omega\right)^2 \mathrm{d}x, \quad T = \frac{1}{2} \int_0^L I_{\mathrm{p}} \left(\frac{\partial}{\partial t}\omega\right)^2 \mathrm{d}x, \tag{3.17}$$

from which the equation of motion is obtained according to (3.9)

$$I_\mathrm{p}\frac{\partial^2\omega}{\partial t^2} = \frac{\partial}{\partial x}\left(GJ_\mathrm{t}\frac{\partial\omega}{\partial x}\right), \tag{3.18}$$

where I_p is the polar moment of inertia. Note that (3.18) and (3.11) are, except for the choice of parameters, identical equations. Consequently, the port-Hamiltonian formulation will be identical to (3.14), with the boundary variables defined by (3.16), when choosing $x_p := I_\mathrm{p}\partial\omega/\partial t$ and $x_q := \gamma_x$ as the energy variables. Refer to the previous section or to [27] for the remaining steps.

3.2.3 Timoshenko beam

When shear deformations are taken into account, the total deflection of an infinitesimal beam element of length $\mathrm{d}x$ is given as

$$\mathrm{d}w = \varphi_x \mathrm{d}x + \gamma_{xz}\mathrm{d}x. \tag{3.19}$$

With the curvature $\kappa_x = \partial\varphi_x/\partial x$ and assuming the cross section is constant over the beam length, the bending moment M_x and the shear force Q_x are defined as

$$M_x = EI\kappa_x, \qquad \text{and} \qquad Q_x = A_\mathrm{s}\tau_{xz} = \kappa AG\gamma_{xz}. \tag{3.20}$$

Here, I is the second moment of area and $A_\mathrm{s} = \kappa A$ the shear area with the Timoshenko shear coefficient κ. The latter needs to be determined for each cross section. For rectangular cross sections, it amounts to $\kappa = 5/6$. The potential energy terms of bending and shear deformation are obtained as

$$U_\mathrm{b} = \frac{1}{2}\int_0^L M_x\kappa_x \,\mathrm{d}x = \frac{1}{2}\int_0^L EI\left(\frac{\partial}{\partial x}\varphi_x\right)^2 \mathrm{d}x, \tag{3.21}$$

$$U_\mathrm{s} = \frac{1}{2}\int_0^L Q_x\gamma_{xz} \,\mathrm{d}x = \frac{1}{2}\int_0^L \kappa AG\left(\frac{\partial w}{\partial x} - \varphi_x\right)^2 \mathrm{d}x. \tag{3.22}$$

With a definition of the system Hamiltonian and the kinetic energy

$$H = T + U_b + U_s \quad \text{and} \quad T = \frac{1}{2}\int_0^L \mu\left(\frac{\partial}{\partial t}w\right)^2 + \rho I\left(\frac{\partial}{\partial t}\gamma_{xz}\right)^2 \mathrm{d}x. \tag{3.23}$$

With the generalized coordinates w and γ_{xz}, the Euler-Lagrange equations of motion (3.9) for the Timoshenko beam are obtained

$$\begin{aligned} \mu\frac{\partial^2 w}{\partial t^2} &= \frac{\partial}{\partial x}\left[\kappa AG_\mathrm{s}\left(\frac{\partial w}{\partial x} - \varphi_x\right)\right] \\ \rho I\frac{\partial^2\varphi_x}{\partial t^2} &= \frac{\partial}{\partial x}\left(EI\frac{\partial}{\partial x}\varphi_x\right) + \kappa AG\left(\frac{\partial w}{\partial x} - \varphi_x\right). \end{aligned} \tag{3.24}$$

A port-Hamiltonian formulation of the equations above can be found e. g. in [83]. It is proceeded accordingly, by defining a set of energy variables

$$x_{p1} := \rho I \frac{\partial \varphi_x}{\partial t}, \quad x_{p2} := \mu \frac{\partial w}{\partial t}, \qquad x_{q1} := \kappa_x, \quad x_{q2} := \gamma_{xz}, \tag{3.25}$$

which are collected in the state vector $\boldsymbol{x}^{\mathrm{T}} := \begin{bmatrix} x_{p1} & x_{p2} & x_{q1} & x_{q2} \end{bmatrix}$. Parallel to the procedure in Section 3.2.1, the variational derivative of H with respect to $\boldsymbol{x}$ is taken to obtain the effort variables for the Timoshenko beam

$$e_{p1} := \frac{\partial \varphi_x}{\partial t}, \quad e_{p2} := \frac{\partial w}{\partial t}, \qquad e_{q1} := M_x, \quad e_{q2} := Q_x. \tag{3.26}$$

An infinite-dimensional Hamiltonian system is obtained by defining the flow variables as $\boldsymbol{f} := -\dot{\boldsymbol{x}}$ and establishing their relation to the effort variables as

$$-\boldsymbol{f} = \begin{bmatrix} \dot{x}_{p1} \\ \dot{x}_{p2} \\ \dot{x}_{q1} \\ \dot{x}_{q2} \end{bmatrix} = \begin{bmatrix} 0 & 0 & \partial_x & 1 \\ 0 & 0 & 0 & \partial_x \\ \partial_x & 0 & 0 & 0 \\ -1 & \partial_x & 0 & 0 \end{bmatrix} \begin{bmatrix} e_{p1} \\ e_{p2} \\ e_{q1} \\ e_{q2} \end{bmatrix}. \tag{3.27}$$

A convenient choice of the boundary variables for the Timoshenko beam is

$$\boldsymbol{u}_\partial = \begin{bmatrix} -e_{q1}(0) \\ e_{q1}(L) \\ -e_{q2}(0) \\ e_{q2}(L) \end{bmatrix}, \quad \boldsymbol{y}_\partial = \begin{bmatrix} e_{p1}(0) \\ e_{p1}(L) \\ e_{p2}(0) \\ e_{p2}(L) \end{bmatrix}. \tag{3.28}$$

It is easy to verify that the Hamiltonian rate of change can be expressed as $\dot{H} = \boldsymbol{u}_\partial^{\mathrm{T}} \boldsymbol{y}_\partial$ and the port-Hamiltonian system is completely defined by (3.27) and (3.28).

3.2.4 Euler-Bernoulli beam

For thin beams, the Bernoulli assumptions state that the cross section is always perpendicular to the neutral axis or rather that the shear angle γ_{xz} is equal to zero with $\kappa AG = \infty$. It follows from (3.19) that $\varphi_x = \partial w / \partial x$. Accordingly, the shear energy U_s and the kinetic energy term related to the shear angle disappear in (3.23). The equations of motion of the Euler-Bernoulli beam are thus obtained as

$$\mu \frac{\partial^2 w}{\partial t^2} = -\frac{\partial^2}{\partial x^2} \left(EI \frac{\partial^2}{\partial x^2} w \right). \tag{3.29}$$

A port-Hamiltonian formulation of the Euler-Bernoulli beam is e. g. given by Cardoso-Ribeiro et al. in [28], where it is used for describing the dynamics of a thin beam actuated by a piezoelectric patch. A similar formulation is given in the following. The

state variables, efforts and flows are those of the Timoshenko beam less the terms related to shear deformation

$$\boldsymbol{x}^{\mathrm{T}} = \left[\mu \frac{\partial w}{\partial t} \quad \kappa_x\right], \quad \boldsymbol{f} = -\dot{\boldsymbol{x}}, \quad \boldsymbol{e}^{\mathrm{T}} = \left[\frac{\partial w}{\partial t} \quad M_x\right] \tag{3.30}$$

and (3.29) can be written as a distributed parameter Hamiltonian system

$$\dot{\boldsymbol{x}} = \begin{bmatrix} 0 & -\partial_{x^2}^2 \\ \partial_{x^2}^2 & 0 \end{bmatrix} \boldsymbol{e}. \tag{3.31}$$

With the appearance of the second order spatial derivative in (3.31), the definition of the boundary variables becomes slightly more involved. The Hamiltonian rate of change of the Euler-Bernoulli beam is given as

$$\begin{aligned} \dot{H} &= \int_0^L e_p \dot{x}_p + e_q \dot{x}_q \,\mathrm{d}x = \int_0^L e_q \partial_{z^2}^2 e_p - e_p \partial_{z^2}^2 e_q \,\mathrm{d}x \\ &= \int_0^L \partial_z e_p \partial_z e_q - \partial_z e_q \partial_z e_p \,\mathrm{d}z + \Big[e_q \partial_z e_p - e_p \partial_z e_q\Big]_0^L. \end{aligned} \tag{3.32}$$

The power flow now additionally depends on the boundary values of the derivatives of the effort variables. Boundary inputs and outputs can be chosen as

$$\boldsymbol{u}_\partial = \begin{bmatrix} \partial_x e_q(0) \\ -\partial_x e_q(L) \\ -e_q(0) \\ e_q(L) \end{bmatrix}, \quad \boldsymbol{y}_\partial = \begin{bmatrix} e_p(0) \\ e_p(L) \\ \partial_x e_p(0) \\ \partial_x e_p(L) \end{bmatrix}, \tag{3.33}$$

such that $\dot{H} = \boldsymbol{u}_\partial^{\mathrm{T}} \boldsymbol{y}_\partial$. Note the reappearance of the shear force $Q_x = \partial_x e_q$ and the angular velocity $\dot{\varphi}_x = \partial_x e_p$ at the boundary.

3.3 Port-Hamiltonian dynamics of plates

The following presentation of the dynamic equations of plate elements will be restricted to Mindlin-Reissner theory for the bending of thick plates and a disk element for axial loading. While it is relatively straightforward to give a port-Hamiltonian formulation of the dynamics of thin plates in bending according to Kirchhoff-Love theory, finite elements for their physically correct numerical approximation have to be C^1-continuous. Brugnoli et al. show that spatial discretization is possible using conforming finite elements of Hermite, Bell or Argyris type in [21]. Those come with the disadvantage of introducing additional degrees of freedom (DOFs) that are not easily mapped to the standard six DOFs per node. An alternative conforming element that comes without additional DOFs is the Hsieh-Clough-Tocher (HCT) triangle [31]. Its implementation is, however, also rather cumbersome.

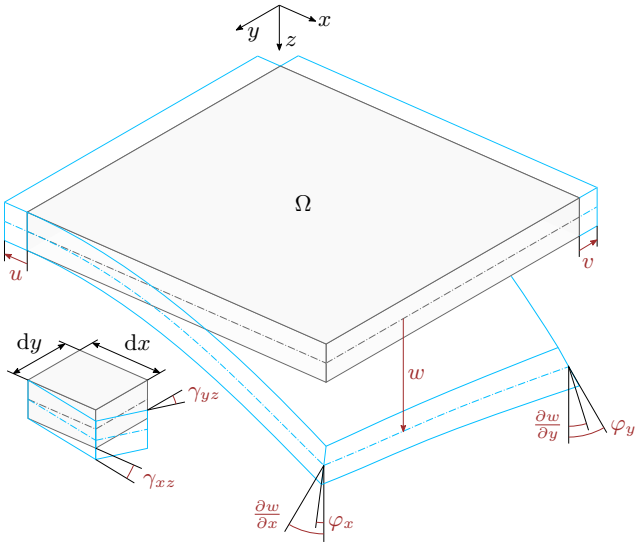

Figure 3.4: A plate element on the domain Ω and its deflections (blue) due to bending (w, φ_x, φ_y) and axial loads (u, v). Shear strain components γ_{xz} and γ_{yz} are depicted for an infinitesimal element of size $\mathrm{d}x \times \mathrm{d}y$

For the problems addressed in this thesis, thick plate bending is assumed sufficiently accurate. A distributed parameter port-Hamiltonian model of a disk element is given in Section 3.3.1 followed by a model for the Mindlin-Reissner plate in Section 3.3.2.

3.3.1 Disk

Existing literature on the port-Hamiltonian formulation of plate elements does not take axial deformations into account. Here, this gap is filled by a systematic derivation of the port-Hamiltonian dynamic equations of a linear isotropic disk subject to normal stress in both directions. The constitutive equations of a disk element are those of plane stress as given by (3.3) and illustrated in Fig. 3.1. A disk of constant thickness h has the elastic potential energy

$$U = \frac{1}{2}h \int_\Omega \boldsymbol{\varepsilon}^\mathrm{T} \boldsymbol{\sigma} \,\mathrm{d}\Omega = \frac{1}{2}h \int_\Omega \boldsymbol{\varepsilon}^\mathrm{T} \boldsymbol{D}_\mathrm{c} \boldsymbol{\varepsilon} \,\mathrm{d}\Omega, \tag{3.34}$$

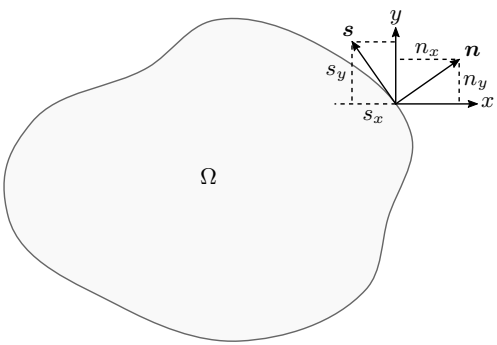

Figure 3.5: Normal ($\boldsymbol{n}$) and tangential ($\boldsymbol{s}$) directions on the boundary of a planar manifold Ω

where Ω is an open connected set on $\mathbb{R}^2$ and $\boldsymbol{D}_\mathrm{c}$ is the compliance matrix. With the generalized coordinates u and v, the system Hamiltonian is obtained as

$$H = T + U, \qquad T = \frac{1}{2} h \int_\Omega \rho \left(\frac{\partial}{\partial t} u\right)^2 + \left(\frac{\partial}{\partial t} v\right)^2 \mathrm{d}\Omega. \tag{3.35}$$

As in the previous section for one-dimensional elements, the equations of motion are obtained from the Lagrange formalism (3.9). The following two partial differential equations (PDEs) result

$$\begin{aligned} \rho h \frac{\partial^2 u}{\partial t^2} &= \frac{Eh}{1-\nu^2} \left(\frac{\partial^2 u}{\partial x^2} + \frac{1-\nu}{2} \frac{\partial^2 u}{\partial y^2} + \frac{1+\nu}{2} \frac{\partial^2 v}{\partial x \partial y} \right), \\ \rho h \frac{\partial^2 v}{\partial t^2} &= \frac{Eh}{1-\nu^2} \left(\frac{\partial^2 v}{\partial y^2} + \frac{1-\nu}{2} \frac{\partial^2 v}{\partial x^2} + \frac{1+\nu}{2} \frac{\partial^2 u}{\partial x \partial y} \right). \end{aligned} \tag{3.36}$$

The state vector and for the formulation as port-Hamiltonian system is chosen as

$$\boldsymbol{x}^\mathrm{T} = \begin{bmatrix} \rho h \frac{\partial u}{\partial t} & \rho h \frac{\partial v}{\partial t} & \varepsilon_x & \varepsilon_y & \gamma_{xy} \end{bmatrix}. \tag{3.37}$$

Power conjugate effort and flow variables are obtained according to the usual procedure as

$$\boldsymbol{e} = \frac{\delta H}{\delta \boldsymbol{x}} = \begin{bmatrix} \frac{\partial u}{\partial t} & \frac{\partial v}{\partial t} & F_x & F_y & Q_{xy} \end{bmatrix}^\mathrm{T}, \quad \boldsymbol{f} = -\dot{\boldsymbol{x}}, \tag{3.38}$$

which leads to the formulation of the disk element as infinite-dimensional Hamiltonian system

$$\dot{\boldsymbol{x}} = \begin{bmatrix} 0 & 0 & \partial_x & 0 & \partial_y \\ 0 & 0 & 0 & \partial_y & \partial_x \\ \partial_x & 0 & 0 & 0 & 0 \\ 0 & \partial_y & 0 & 0 & 0 \\ \partial_y & \partial_x & 0 & 0 & 0 \end{bmatrix} \begin{bmatrix} e_{p1} \\ e_{p2} \\ e_{q1} \\ e_{q2} \\ e_{q3} \end{bmatrix}. \tag{3.39}$$

As in the one-dimensional system in Section 3.2, the operator that relates $\boldsymbol{f}$ and $\boldsymbol{e}$ is formally skew-symmetric and power-conserving. An analysis of the Hamiltonian rate of change $\dot{H}$ yields a possible choice of the boundary variables

$$\begin{aligned} \dot{H} &= \int_\Omega e_{p1}\left(\partial_x e_{q1} + \partial_y e_{q3}\right) + e_{p2}\left(\partial_y e_{q2} + \partial_x e_{q3}\right) + \dots \\ &\quad + e_{q1}\partial_x e_{p1} + e_{q2}\partial_y e_{p2} + e_{q3}\left(\partial_y e_{p1} + \partial_x e_{p2}\right) \,\mathrm{d}\Omega \\ &= \int_\Omega \frac{\partial}{\partial x}\left(\dot{u}F_x + \dot{v}Q_{xy}\right) + \frac{\partial}{\partial y}\left(\dot{v}F_y + \dot{u}Q_{xy}\right) \,\mathrm{d}\Omega. \end{aligned} \tag{3.40}$$

Applying Green's theorem to (3.40) yields

$$\dot{H} = \oint_{\partial\Omega} \dot{q}_n F_n + \dot{q}_s Q_{ns} \,\mathrm{d}s, \tag{3.41}$$

where n denotes the normal and s the tangential direction along the boundary $\partial\Omega$ as illustrated in Fig. 3.5. The port variables are forces and velocities $\dot{q}$ that result from linear combinations of the effort variables evaluated on the boundary.

3.3.2 Mindlin-Reissner plate

Bending of thick plates is usually described using Mindlin-Reissner theory [90]. The Mindlin plate can also be viewed as an extension of the Timoshenko beam to the two-dimensional domain. Shear deformations as well as bending are taken into account in two spatial directions. Port-Hamiltonian formulations are e. g. given by Macchelli et al. in [84] and Brugnoli et al. in [20]. The former authors use a vectorial formulation while the latter authors derive a model in tensorial form which is independent of the choice of the coordinate frame. In the following a vectorial formulation of the Mindlin plate, similar to the one in [20], is derived. Defining the vector of curvatures

$$\boldsymbol{\kappa}^{\mathrm{T}} = \begin{bmatrix} \kappa_{xx} & \kappa_{yy} & \kappa_{xy} \end{bmatrix} = \begin{bmatrix} \frac{\partial \varphi_x}{\partial x} & \frac{\partial \varphi_y}{\partial y} & \left(\frac{\partial \varphi_y}{\partial x} + \frac{\partial \varphi_x}{\partial y}\right) \end{bmatrix}, \tag{3.42}$$

the element strain can be expressed as

$$\boldsymbol{\varepsilon} = -z\boldsymbol{\kappa}, \quad \boldsymbol{\gamma}_{\mathrm{s}}^{\mathrm{T}} = \begin{bmatrix} \gamma_{xz} & \gamma_{yz} \end{bmatrix} = \begin{bmatrix} \left(\frac{\partial w}{\partial x} - \varphi_x\right) & \left(\frac{\partial w}{\partial y} - \varphi_y\right) \end{bmatrix}. \tag{3.43}$$

All strain components are visualized in Fig. 3.4. The stress-strain relationship for the Mindlin plate is then given as

$$\boldsymbol{\sigma} = \frac{E}{1-\nu^2}\begin{bmatrix} 1 & \nu & 0 \\ \nu & 1 & 0 \\ 0 & 0 & \frac{1-\nu}{2} \end{bmatrix} \boldsymbol{\varepsilon}, \quad \boldsymbol{\tau}_\mathrm{s} = \kappa G \boldsymbol{\gamma}_\mathrm{s}, \tag{3.44}$$

with $\boldsymbol{\tau}_\mathrm{s}$ the shear stress and κ the Timoshenko shear coefficient as in (3.20). Separate terms for the elastic potential energy of bending and shear are obtained by multiplication of stress and strain

$$U_\mathrm{s} = \frac{1}{2} h \int_\Omega \boldsymbol{\gamma}_\mathrm{s}^\mathrm{T} \boldsymbol{\tau}_\mathrm{s} \,\mathrm{d}\Omega, \quad U_\mathrm{b} = \frac{1}{2} \int_\Omega \boldsymbol{\kappa}^\mathrm{T} \boldsymbol{D}_\mathrm{b} \boldsymbol{\kappa} \,\mathrm{d}\Omega, \quad \text{with} \quad \boldsymbol{D}_\mathrm{b} = \frac{h^3}{12} \boldsymbol{D}_\mathrm{c}, \tag{3.45}$$

where $\boldsymbol{D}_\mathrm{c}$ is the compliance matrix from (3.3). With the three generalized coordinates w, φ_x and φ_y, the kinetic energy of the plate is

$$T = \frac{1}{2} \int_\Omega \rho h \left(\frac{\partial}{\partial t} w\right)^2 + \frac{h^3}{12} \left(\frac{\partial}{\partial t} \varphi_x\right)^2 + \frac{h^3}{12} \left(\frac{\partial}{\partial t} \varphi_y\right)^2 \mathrm{d}\Omega \tag{3.46}$$

and the equations of motion result from the application of (3.9) as

$$\begin{aligned}
\rho h \frac{\partial^2 w}{\partial t^2} &= \kappa G_\mathrm{s} h \left(\frac{\partial^2 w}{\partial x^2} + \frac{\partial^2 w}{\partial y^2} - \frac{\partial \varphi_x}{\partial x} - \frac{\partial \varphi_y}{\partial y} \right), \\
\frac{\rho h^3}{12} \frac{\partial^2 \varphi_x}{\partial t^2} &= K \left[\frac{\partial^2 \varphi_x}{\partial x^2} + \frac{1-\nu}{2} \frac{\partial^2 \varphi_x}{\partial y^2} + \frac{1+\nu}{2} \frac{\partial^2 \varphi_y}{\partial x \partial y} + \frac{6\kappa(1-\nu)}{h^2} \left(\frac{\partial w}{\partial x} - \varphi_x \right) \right], \\
\frac{\rho h^3}{12} \frac{\partial^2 \varphi_y}{\partial t^2} &= K \left[\frac{\partial^2 \varphi_y}{\partial y^2} + \frac{1-\nu}{2} \frac{\partial^2 \varphi_y}{\partial x^2} + \frac{1+\nu}{2} \frac{\partial^2 \varphi_x}{\partial x \partial y} + \frac{6\kappa(1-\nu)}{h^2} \left(\frac{\partial w}{\partial y} - \varphi_y \right) \right],
\end{aligned} \tag{3.47}$$

with the flexural rigidity of the plate

$$K = \frac{E h^3}{12(1-\nu^2)}. \tag{3.48}$$

All impulse terms, the curvatures and the shear strain terms are collected in the state vector

$$\boldsymbol{x}^\mathrm{T} = \begin{bmatrix} \rho h \frac{\partial w}{\partial t} & \frac{\rho h^3}{12} \frac{\partial \varphi_x}{\partial t} & \frac{\rho h^3}{12} \frac{\partial \varphi_y}{\partial t} & \kappa_{xx} & \kappa_{yy} & \kappa_{xy} & \gamma_{xz} & \gamma_{yz} \end{bmatrix}. \tag{3.49}$$

Together with the system Hamiltonian $H = U_\mathrm{b} + U_\mathrm{s} + T$, the definition of the power conjugate variables follows

$$\boldsymbol{f} = -\dot{\boldsymbol{x}}, \quad \boldsymbol{e}^\mathrm{T} = \begin{bmatrix} \frac{\partial w}{\partial t} & \frac{\partial \varphi_x}{\partial t} & \frac{\partial \varphi_y}{\partial t} & \boldsymbol{e}_\mathrm{b}^\mathrm{T} & \boldsymbol{e}_\mathrm{s}^\mathrm{T} \end{bmatrix}, \tag{3.50}$$

with

$$\boldsymbol{e}_\mathrm{b} = \boldsymbol{D}_\mathrm{b}\boldsymbol{\kappa} = \begin{bmatrix} M_{xx} & M_{yy} & M_{xy} \end{bmatrix}^\mathrm{T}, \quad \boldsymbol{e}_\mathrm{s} = \kappa G h \boldsymbol{\gamma}_\mathrm{s} = \begin{bmatrix} Q_x & Q_y \end{bmatrix}^\mathrm{T}. \tag{3.51}$$

With the above definitions, a vectorial formulation of the Mindlin plate as Hamiltonian system is given by

$$\dot{\boldsymbol{x}} = \begin{bmatrix} 0 & 0 & 0 & 0 & 0 & 0 & \partial_x & \partial_y \\ 0 & 0 & 0 & \partial_x & 0 & \partial_y & 1 & 0 \\ 0 & 0 & 0 & 0 & \partial_y & \partial_x & 0 & 1 \\ 0 & \partial_x & 0 & 0 & 0 & 0 & 0 & 0 \\ 0 & 0 & \partial_y & 0 & 0 & 0 & 0 & 0 \\ 0 & \partial_y & \partial_x & 0 & 0 & 0 & 0 & 0 \\ \partial_x & -1 & 0 & 0 & 0 & 0 & 0 & 0 \\ \partial_y & 0 & -1 & 0 & 0 & 0 & 0 & 0 \end{bmatrix} \begin{bmatrix} e_{p1} \\ e_{p2} \\ e_{p3} \\ e_{q1} \\ e_{q2} \\ e_{q3} \\ e_{q4} \\ e_{q5} \end{bmatrix}. \tag{3.52}$$

For the definition of the boundary variables, the energy flow is analyzed

$$\begin{aligned} \dot{H} &= \int_\Omega \frac{\partial}{\partial x}\left(\dot{w}Q_x + \dot{\varphi}_x M_{xx} + \dot{\varphi}_y M_{xy}\right) + \frac{\partial}{\partial y}\left(\dot{w}Q_y + \dot{\varphi}_y M_{yy} + \dot{\varphi}_x M_{xy}\right) \mathrm{d}\Omega \\ &= \oint_{\partial\Omega} \dot{w}Q_n + \dot{\varphi}_n M_{nn} + \dot{\varphi}_s M_{ns} \,\mathrm{d}s. \end{aligned} \tag{3.53}$$

Here some of the intermediate steps shown in the calculation of $\dot{H}$ in (3.40) are skipped. The last expression results from the application of Green's theorem. As in case of the disk element, the normal and tangential directions in the integration along the boundary $\partial\Omega$ are illustrated in Fig. 3.5. The port variables of the Mindlin plate are moments and angular velocities as well as shear forces and velocities. Note the similarity to the Timoshenko beam, also considering (3.52). The similarity is even more striking when using a tensorial formulation as detailed in [20].

4 Discretization

When applying spatial discretization methods to the systems in Chapter 3 for their numerical simulation, care must be taken to preserve the port-Hamiltonian structure, which is why conventional approaches cannot be readily employed. A spatial discretization method is *structure preserving* if the resulting lumped parameter system remains symplectic and passive. It follows that the power balance equation (2.21a) or the bilinear form (2.22) need to be preserved in the approximation. An overview of structure preserving discretization methods is given in Sec 4.1. The partitioned finite element method (PFEM) is chosen from the available ones and is applied to beam equations on a system class level in Section 4.3.1. Plate equations are approximated with the same approach using quadrilateral elements in Section 4.3.2. The approximation error for each of the systems in Chapter 3 is studied in Section 4.5. In Section 4.4, PFEM is compared to FEM highlighting the differences between the structure preserving approach and the conventional one. Readers that want to review the FEM approach once again can consult the short summary in Section 4.2 and the references provided therein.

Like Section 3.2, Secs. 4.1, 4.3.1 and 4.5.1 were originally presented in [135]. All mentioned sections have been moderately improved compared to the original version and adapted to the layout and style of this thesis.

4.1 On spatial discretization of distributed parameter pH systems

A wide range of methods for the numerical approximation of PDEs is available [102]. The finite element method is a common technique in structural dynamics, however, it can not be applied in the usual way. Preserving the duality and passivity properties of an infinite-dimensional port-Hamiltonian system can be achieved by using mixed FEM approaches. First methods for the structure-preserving spatial discretization of port-Hamiltonian systems were presented by Golo and Tasalia et al. in [126] and [51]. They use differential forms for the numerical approximation of one- and two-dimensional systems, where different approximation spaces are used for flows and efforts. Their method was extended to allow for higher-order spatial derivatives by Bassi et. al [13] and for its application to a class of irreversible thermodynamic systems by Baaiu et al. [4]. For an accurate approximation, a relatively large number of finite elements is usually required with these approaches. Moulla et al. [91] adopted a collocation method to discretize 1D port-Hamiltonian systems. Using polynomial bases, this results in higher accuracy for lower-order approximations. In all of the approaches mentioned up to this point, the discretization happens in the strong form of the balance equations. This results in rather strict compatibility conditions. Also, an input feed-through term is present in the finite-dimensional approximation, which potentially complicates the application of control engineering methods.

Cardoso-Ribeiro et al. [28] relax the compatibility conditions by using the method of [91] in the weak formulation in order to apply it to model the dynamics of a beam

excited by a piezoelectric patch. Mixed finite element discretization in the weak form was introduced in a general way by Kotyczka et al. [74]. Their method can be applied to systems of any spatial dimension and resolves several issues that arise when approximating directly in the strong form. It requires an additional projection to ensure non-degeneracy of the power product, which introduces additional degrees of freedom that can be used to tune the discretized models. The boundary ports of resulting models are of alternating causality, which is not always desired. A particularly elegant and straightforward method, which circumvents the mentioned difficulties, is PFEM, as introduced by Cardoso-Ribeiro et al. [25]. It is closely related to the mixed Galerkin method used in [74]. Integration by parts is, however, only applied to one of the dual balance equations. This way, the port-Hamiltonian structure is obtained in a direct fashion and no further projection is required. Moreover, no feed-through term is produced in the discretization process. Causality of the boundary ports depends on which balance equation is selected for partial integration and does not alternate for individual elements. The method was also shown to be compatible with existing FEM software [20]. It is applicable to open systems of two conservation laws of principally any spatial dimension. Regarding plate dynamics, the application of PFEM to the Mindlin plate is shown in [20] and to the Kirchhoff-Love plate model in [21]. All in all, PFEM is considered the most suitable approach for the spatial approximation of the systems introduced in Chapter 3.

4.2 Recall on the finite element method

As PFEM is closely related to the FEM approach, the latter is briefly explained in the following. Intention of this section is to recall the basic method and some of its features in order to allow for a comparison to PFEM. Basic familiarity with FEM is assumed, since a complete introduction cannot be given here. For beginners, a thorough and comprehensive treatise of the approach can be found in e. g. [113] or [61].

In FEM, the system to be discretized is first divided into several smaller sections, called finite elements. If the size of the elements is sufficiently small, their behavior can be described using simpler functions that are nonzero only within the bounds of the respective element. The behavior of the global system can then be approximated by piecing the segments back together.

Let $\boldsymbol{q}_\mathrm{e}(x^\mathrm{e}, y^\mathrm{e}, z^\mathrm{e}, t)$ be the generalized coordinates (displacements and rotations) of an element in its local reference system $(x^\mathrm{e}, y^\mathrm{e}, z^\mathrm{e}) \in \mathbb{R}^3$, as illustrated in Fig. 4.1. Then, each q_e^i is approximated using a Ritz ansatz, such that

$$q_\mathrm{e}^i \approx (\boldsymbol{\phi}_\mathrm{e}^i)^\mathrm{T} \hat{\boldsymbol{q}}_\mathrm{e}^i, \qquad i = 1 \dots N_\mathrm{q}, \tag{4.1}$$

where N_q is the number of local generalized coordinates of the element, $\boldsymbol{\phi}_\mathrm{e}^i(x^\mathrm{e}, y^\mathrm{e}, z^\mathrm{e}) \in \mathbb{R}^{N_\mathrm{n}}$ are orthogonal basis functions and $\hat{\boldsymbol{q}}_\mathrm{e}^i(t) \in \mathbb{R}^{N_\mathrm{n}}$ is the evaluation of q_e^i at the

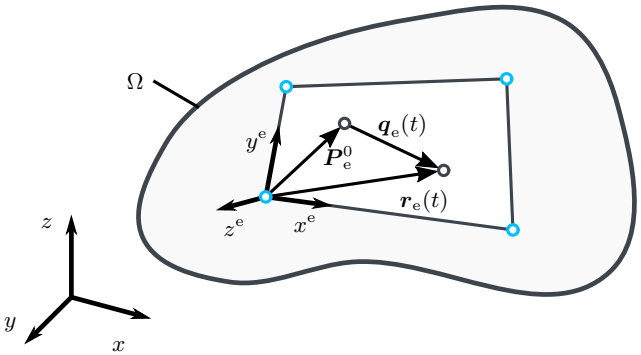

Figure 4.1: Finite element in an elastic continuum with local reference frame (x^e, y^e, z^e) and the displacement of a point $\boldsymbol{P}_0^e$ at time t

(boundary) nodes of the element. The number of nodes is given by N_n. Polynomials are often chosen for ϕ_e^i and the functions are required to satisfy the essential (kinematic) boundary conditions [113]. Merging the $\hat{\boldsymbol{q}}_e^i$ into the vector

$$\hat{\boldsymbol{q}}_e = \begin{bmatrix} \hat{\boldsymbol{q}}_e^1 \\ \vdots \\ \hat{\boldsymbol{q}}_e^{N_q} \end{bmatrix} \tag{4.2}$$

and combining the basis functions ϕ_e^i into a block diagonal matrix $\boldsymbol{\Phi}_e \in \mathbb{R}^{N_q \cdot N_n \times N_q}$, (4.1) may be rewritten as

$$\boldsymbol{q}_e \approx \boldsymbol{\Phi}_e^T \hat{\boldsymbol{q}}_e. \tag{4.3}$$

Now, recall the principle of virtual work (3.8) for an isotropic, linear elastic continuum. For the finite element considered above – assuming for the sake of simplicity that the system is conservative – it may be expressed in the local coordinates $\boldsymbol{q}_e$ as

$$\int_{V_e} \boldsymbol{\delta q}_e^T \rho \ddot{\boldsymbol{q}}_e + \boldsymbol{\delta \varepsilon}^T \boldsymbol{\sigma} \, \mathrm{d}\Omega = 0, \tag{4.4}$$

where V_e is the volume of the element. Substituting the approximations for the generalized coordinates into (4.4) results in

$$\boldsymbol{\delta \hat{q}}_e^T \int_{V_e} \boldsymbol{\Phi}_e \rho \boldsymbol{\Phi}_e^T \ddot{\boldsymbol{q}}_e \, \mathrm{d}\Omega + \int_{V_e} \boldsymbol{\delta \varepsilon}^T \boldsymbol{\sigma} \, \mathrm{d}\Omega = 0. \tag{4.5}$$

Since the strain $\boldsymbol{\varepsilon} \in \mathbb{R}^{N_q}$ can be expressed in terms of $\boldsymbol{q}_e$, it may be approximated as

$$\boldsymbol{\varepsilon}(x^e, y^e, z^e, t) \approx \boldsymbol{B}_e^T(x^e, y^e, z^e) \hat{\boldsymbol{q}}_e(t). \tag{4.6}$$

For a linear elastic material, the stress $\boldsymbol{\sigma} = \boldsymbol{D}_\mathrm{e}\boldsymbol{\varepsilon}$ is a linear function of the strain, where $\boldsymbol{D}_\mathrm{e} \in \mathbb{R}^{N_q \times N_q}$ is the element compliance matrix. Thus, the potential term in (4.4) can also be approximated using $\hat{\boldsymbol{q}}_\mathrm{e}$ and d'Alembert's principle becomes

$$\delta\hat{\boldsymbol{q}}_\mathrm{e}^\mathrm{T} \int_{V_\mathrm{e}} \boldsymbol{\Phi}_\mathrm{e}\rho\boldsymbol{\Phi}_\mathrm{e}^\mathrm{T}\ddot{\hat{\boldsymbol{q}}}_\mathrm{e} + \boldsymbol{B}_\mathrm{e}\boldsymbol{D}_\mathrm{e}\boldsymbol{B}_\mathrm{e}^\mathrm{T}\hat{\boldsymbol{q}}_\mathrm{e}\,\mathrm{d}\Omega = 0. \tag{4.7}$$

Since the virtual displacements $\delta\hat{\boldsymbol{q}}$ are arbitrary, the integral has to vanish. Integration with respect to the element volume can now be carried out, because $\boldsymbol{\Phi}_\mathrm{e}$ and $\boldsymbol{B}_\mathrm{e}$ do not depend on time. With the abbreviations

$$\boldsymbol{M}_\mathrm{e} = \int_{V_\mathrm{e}} \boldsymbol{\Phi}_\mathrm{e}\rho\boldsymbol{\Phi}_\mathrm{e}^\mathrm{T}\,\mathrm{d}\Omega, \qquad \boldsymbol{K}_\mathrm{e} = \int_{V_\mathrm{e}} \boldsymbol{B}_\mathrm{e}\boldsymbol{D}_\mathrm{e}\boldsymbol{B}_\mathrm{e}^\mathrm{T}\,\mathrm{d}\Omega, \tag{4.8}$$

the equations of motion of the unsupported element can be written in the compact form

$$\boldsymbol{M}_\mathrm{e}\ddot{\hat{\boldsymbol{q}}}_\mathrm{e} + \boldsymbol{K}_\mathrm{e}\hat{\boldsymbol{q}}_\mathrm{e} = \boldsymbol{0}, \tag{4.9}$$

where $\boldsymbol{M}_\mathrm{e} \in \mathbb{R}^{N_q \cdot N_\mathrm{n} \times N_q \cdot N_\mathrm{n}}$ is referred to as the element mass matrix and $\boldsymbol{K}_\mathrm{e} \in \mathbb{R}^{N_q \cdot N_\mathrm{n} \times N_q \cdot N_\mathrm{n}}$ as the element stiffness matrix.

Given that the DOFs of all the nodes of a structure approximated using finite elements are collected in the vector $\boldsymbol{q} \in \mathbb{R}^{n_\mathrm{DOF}}$, the local DOFs of each element are related to $\boldsymbol{q}$ as follows

$$\hat{\boldsymbol{q}}_\mathrm{e} = \boldsymbol{T}_\mathrm{e}\boldsymbol{q}, \tag{4.10}$$

with $\boldsymbol{T}_\mathrm{e}$ a coordinate transformation matrix and n_DOF the number of global DOFs. It can then be shown that the mass and stiffness matrices of the system as a whole are obtained as [113]

$$\boldsymbol{M} = \sum_{e=1}^{N_\mathrm{e}} \boldsymbol{T}_\mathrm{e}^\mathrm{T}\boldsymbol{M}_\mathrm{e}\boldsymbol{T}_\mathrm{e}, \qquad \boldsymbol{K} = \sum_{e=1}^{N_\mathrm{e}} \boldsymbol{T}_\mathrm{e}^\mathrm{T}\boldsymbol{K}_\mathrm{e}\boldsymbol{T}_\mathrm{e}, \tag{4.11}$$

where N_e is the number of finite elements. This implies that the contributions of an individual element to the mass and stiffness of each global DOF are simply added up. The dynamics of a general linear elastic system approximated using FEM can be written as a second order differential equation

$$\boldsymbol{M}\ddot{\boldsymbol{q}} + \boldsymbol{D}\dot{\boldsymbol{q}} + \boldsymbol{K}\boldsymbol{q} = \boldsymbol{f}_\mathrm{ext}, \tag{4.12}$$

where a damping term $\boldsymbol{D}\dot{\boldsymbol{q}}$ and external forces $\boldsymbol{f}_\mathrm{ext} \in \mathbb{R}^{n_\mathrm{DOF}}$ are included. The damping term is often approximated using a weighted sum of $\boldsymbol{M}$ and $\boldsymbol{K}$ (Rayleigh damping), while the external forces can be obtained by including external loads in (4.4) that are then discretized. They may also be added in discrete fashion directly, considering them as abstract forces and moments acting on the nodes of the approximated structure.

4.3 Applying the partitioned finite element method to elastic bodies

Spatial discretization of the elastic mechanical systems presented in Chapter 3 using PFEM can be treated on a general level, similar to the brief recapitulation of FEM given in the previous section. However, it is chosen to present discretization of one-dimensional systems separately from the two-dimensional ones in the following. This allows entering into specific details for both cases more easily, such that it becomes clearer how to apply the method, respectively.

4.3.1 Systems of one spatial dimension

For the simulation of the dynamic response of beam elements, numerical approximation of the infinite-dimensional port-Hamiltonian system equations derived in Section 3.2 is necessary. Here PFEM, as presented by Cardoso-Ribeiro et al. [26], is employed for this purpose, for reasons outlined in Section 4.1. In the following, the application of PFEM to systems of the form

$$\dot{\boldsymbol{x}} = \mathcal{J}\boldsymbol{e}, \quad \text{with } \mathcal{J} = \sum_{i=0}^{N} \begin{bmatrix} \boldsymbol{0} & \boldsymbol{A}_i \\ (-1)^{i+1}\boldsymbol{A}_i^{\mathrm{T}} & \boldsymbol{0} \end{bmatrix} \frac{\partial^i}{\partial x^i} \tag{4.13}$$

is presented. The entries of the matrices A_i are either zero or one, N is the maximum order of the spatial derivative and $\boldsymbol{x}, \boldsymbol{e} \in \mathbb{R}^n$. For the systems in Section 3.2, the matrices are quadratic, but this need not be the case in general. Taking for instance (3.27), the Timoshenko beam equations in Hamiltonian form with $N = 1$, the matrices A_i are

$$\boldsymbol{A}_0 = \begin{bmatrix} 0 & 1 \\ 0 & 0 \end{bmatrix}, \quad \boldsymbol{A}_1 = \begin{bmatrix} 1 & 0 \\ 0 & 1 \end{bmatrix}. \tag{4.14}$$

The system Hamiltonian can be expressed as

$$H(\boldsymbol{x}) = \frac{1}{2} \int_X \boldsymbol{x}^{\mathrm{T}} \mathcal{L} \boldsymbol{x} \, \mathrm{d}x, \tag{4.15}$$

where $\mathcal{L}$ can be a function of the state vector $\boldsymbol{x}$ on the interval $X = \begin{bmatrix} a & b \end{bmatrix}$. When observing the infinite-dimensional port-Hamiltonian systems in Section 3.2, note that they are all of this type with the order of the spatial derivative $N \leq 2$ and $\mathcal{L}$ independent of x for isotropic beams. Let the length of the system be denoted by L. Then, $\begin{bmatrix} a & b \end{bmatrix}$ is the interval $\begin{bmatrix} 0 & L \end{bmatrix}$. By treating the spatial discretization process on a system class level, explicit formulation of the process for every single load case of the beam is avoided. At the same time, it is more evident that the method's applicability is not limited to truss structures and frames.

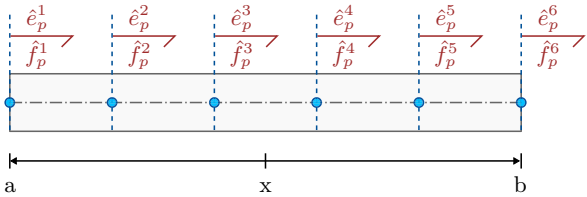

Figure 4.2: Division of a beam element into five intervals with $N_\mathrm{n} = 6$ nodes with corresponding flows and efforts for numerical approximation [135]

In a first step, the energy variables $\boldsymbol{x}$, flow variables $\boldsymbol{f}$ and effort variables $\boldsymbol{e}$ of a system of class (4.13) are approximated using polynomial approximation bases.

$$\begin{aligned} x_{pi}(x,t) &\approx \boldsymbol{\phi}^\mathrm{T}(x)\hat{\boldsymbol{x}}_{pi}(t), \quad & x_{qj}(x,t) &\approx \boldsymbol{\phi}^\mathrm{T}(x)\hat{\boldsymbol{x}}_{qj}(t), \\ f_{pi}(x,t) &\approx \boldsymbol{\phi}^\mathrm{T}(x)\hat{\boldsymbol{f}}_{pi}(t), \quad & f_{qj}(x,t) &\approx \boldsymbol{\phi}^\mathrm{T}(x)\hat{\boldsymbol{f}}_{qj}(t), \\ e_{pi}(x,t) &\approx \boldsymbol{\phi}^\mathrm{T}(x)\hat{\boldsymbol{e}}_{pi}(t), \quad & e_{qj}(x,t) &\approx \boldsymbol{\phi}^\mathrm{T}(x)\hat{\boldsymbol{e}}_{qj}(t), \end{aligned} \tag{4.16}$$

with $i = 1 \dots n_p$ and $j = 1 \dots n_q$, where n_p is the number of kinetic and n_q the number of potential energy related variables (e. g. for the Timoshenko beam $n_p = n_q = 2$). Here, the basis functions $\boldsymbol{\phi}(x)$ are chosen as the Lagrange polynomials of order $N_\mathrm{n} - 1$, where N_n is the number of nodes. It it possible to choose different orders of $\boldsymbol{\phi}(x)$ for kinetic and potential energy variables. However, since there is no obvious advantage in doing so considering the systems and methods presented in this thesis, equal orders are always chosen. The vectors $\hat{\boldsymbol{x}}_{pi}, \hat{\boldsymbol{f}}_{pi}, \hat{\boldsymbol{e}}_{pi} \in \mathbb{R}^{N_\mathrm{n}}$ and $\hat{\boldsymbol{x}}_{qj}, \hat{\boldsymbol{f}}_{qj}, \hat{\boldsymbol{e}}_{qj} \in \mathbb{R}^{N_\mathrm{n}}$ are the energy variables, flows and efforts evaluated at uniformly distributed points in $X = \begin{bmatrix} a & b \end{bmatrix}$. For values of $N_\mathrm{n} \geq 2$, the boundary is always included. This is illustrated for the kinetic variables of a beam element in Fig. 4.2 where $N_\mathrm{n} = 6$ nodes (i. e. a fifth order polynomial) are used. The approximations of kinetic efforts $\hat{e}_p^i$ and flows $\hat{f}_p^i$ are included in the figure with the half arrow pointing in the positive reference direction of the energy flow, respectively.

For the sake of a more compact notation, denote by $\boldsymbol{x}_p$ the concatenation of the x_{pi} and by $\hat{\boldsymbol{x}}_p$ the concatenation of nodal variables $\hat{\boldsymbol{x}}_{pi}$. The same applies to all the other variables appearing in (4.16). Accordingly, the Lagrange bases are grouped together in the matrices

$$\boldsymbol{\Phi}_p^\mathrm{T}(x) \in \mathbb{R}^{n_p \times n_p \cdot N_\mathrm{n}}, \qquad \boldsymbol{\Phi}_q^\mathrm{T}(x) \in \mathbb{R}^{n_q \times n_q \cdot N_\mathrm{n}}. \tag{4.17}$$

In line with the Galerkin method (see e. g. [61, 111]), PFEM proceeds via the weak form of (4.13)

$$\int_X \boldsymbol{\Phi}(x)\dot{\boldsymbol{x}}\,\mathrm{d}x = \int_X \boldsymbol{\Phi}(x)\mathcal{J}\boldsymbol{e}\,\mathrm{d}x, \quad \text{where } \boldsymbol{\Phi}(x) = \begin{bmatrix} \boldsymbol{\Phi}_p(x) & \mathbf{0} \\ \mathbf{0} & \boldsymbol{\Phi}_q(x) \end{bmatrix}, \tag{4.18}$$

using the matrix functions $\boldsymbol{\Phi}_p(x)$ and $\boldsymbol{\Phi}_q(x)$ as test functions. Substituting the approximations (4.16) for energy variables, flows and efforts into (4.18), yields

$$\begin{aligned}\left(\int_X \boldsymbol{\Phi}_p \boldsymbol{\Phi}_p^{\mathrm{T}} \,\mathrm{d}x\right) \dot{\hat{\boldsymbol{x}}}_p &= \left(\sum_{i=0}^{N} \int_X \boldsymbol{\Phi}_p \boldsymbol{A}_i \frac{\partial^i}{\partial x^i} \boldsymbol{\Phi}_q^{\mathrm{T}} \,\mathrm{d}x\right) \hat{\boldsymbol{e}}_q \\ \left(\int_X \boldsymbol{\Phi}_p \boldsymbol{\Phi}_q^{\mathrm{T}} \,\mathrm{d}x\right) \dot{\hat{\boldsymbol{x}}}_q &= \left(\sum_{i=0}^{N} (-1)^{i+1} \int_X \boldsymbol{\Phi}_q \boldsymbol{A}_i^{\mathrm{T}} \frac{\partial^i}{\partial x^i} \boldsymbol{\Phi}_p^{\mathrm{T}} \,\mathrm{d}x\right) \hat{\boldsymbol{e}}_p.\end{aligned} \tag{4.19}$$

For systems such as (4.13), structure-preserving mixed Galerkin approximation as presented in [74] can be used. However, with PFEM, the finite-dimensional port-Hamiltonian system can be obtained in a direct fashion without further projection. This is achieved by applying integration by parts to only one of the equations in (4.19). In principle, either equation can be integrated by parts. By choosing one or the other, a different causality of the boundary ports – i. e. which variables will be the boundary inputs and which the boundary outputs – results. When integrating the respective dual equation by parts instead, causality of the boundary ports is reversed. For the systems defined in Section 3.2, integrating the upper equation by parts results in forces and torques as boundary inputs and velocities and angular velocities as boundary outputs. Integrating the lower equation by parts instead, the role of boundary inputs and outputs is reversed. To be consistent with the FEM approach, where forces and torques generally act as inputs, integration by parts is applied N times to the equation containing the kinetic flows here. Intermediate steps of this calculation are shown in Appendix B. As a result, the following is obtained

$$\begin{aligned}\left(\int_X \boldsymbol{\Phi}_p \boldsymbol{\Phi}_p^{\mathrm{T}} \,\mathrm{d}x\right) \dot{\hat{\boldsymbol{x}}}_p = &\left(\sum_{i=0}^{N} (-1)^i \int_X \frac{\partial^i}{\partial x^i} \boldsymbol{\Phi}_p \boldsymbol{A}_i \boldsymbol{\Phi}_q^{\mathrm{T}} \,\mathrm{d}x\right) \hat{\boldsymbol{e}}_q \\ &+ \sum_{i=1}^{N} \sum_{j=1}^{i} (-1)^{j-1} \left[\frac{\partial^{j-1}}{\partial x^{j-1}} \boldsymbol{\Phi}_p \boldsymbol{A}_i \frac{\partial^{i-j}}{\partial x^{i-j}} \boldsymbol{\Phi}_q^{\mathrm{T}} \hat{\boldsymbol{e}}_q\right]_a^b.\end{aligned} \tag{4.20}$$

Observing the term in round brackets on the right hand side, note that it is the negative transpose of the term in front of $\hat{\boldsymbol{e}}_p$ in the lower equation in (4.19). Applying Gaussian quadrature to evaluate the integrals, a lunmped parameter approximation of the system dynamics is obtained

$$\underbrace{\begin{bmatrix}\boldsymbol{M}_p & \boldsymbol{0} \\ \boldsymbol{0} & \boldsymbol{M}_q\end{bmatrix}}_{\boldsymbol{M}_{pq}} \dot{\hat{\boldsymbol{x}}} = \underbrace{\begin{bmatrix}\boldsymbol{0} & \boldsymbol{P} \\ -\boldsymbol{P}^{\mathrm{T}} & \boldsymbol{0}\end{bmatrix}}_{\boldsymbol{J}} \hat{\boldsymbol{e}} + \underbrace{\begin{bmatrix}\boldsymbol{G}_p \\ \boldsymbol{0}\end{bmatrix}}_{\boldsymbol{G}} \boldsymbol{u}_\partial, \tag{4.21}$$

with the symmetric positive definite matrices $\boldsymbol{M}_p \in \mathbb{R}^{n_p \cdot N_\mathrm{n} \times n_p \cdot N_\mathrm{n}}$ and $\boldsymbol{M}_q \in \mathbb{R}^{n_q \cdot N_\mathrm{n} \times n_q \cdot N_\mathrm{n}}$, the skew-symmetric interconnection matrix $\boldsymbol{J}$ with $\boldsymbol{P} \in \mathbb{R}^{n_p \cdot N_\mathrm{n} \times n_q \cdot N_\mathrm{n}}$,

the input matrix $\boldsymbol{G}$ and the boundary input variables $\boldsymbol{u}_\partial$. The latter are the efforts $\boldsymbol{\Phi}_q^{\mathrm{T}}\hat{\boldsymbol{e}}_q$ and their spatial derivatives, appearing in the second term on the right hand side in (4.20), evaluated at the boundary. According to the effort definitions in Section 3.2 in case of the beam dynamics, the inputs are forces and bending moments. For one-dimensional systems such as beam elements, the number of boundary inputs amounts to $n_q \cdot 2N$ with $\boldsymbol{u}_\partial \in \mathbb{R}^{n_q \cdot 2N}$ and $\boldsymbol{G}_p \in \mathbb{R}^{n_p \cdot N_\mathrm{n} \times n_q \cdot 2N}$. With the boundary inputs stated for the individual systems in Section 3.2, it can be easily verified that $\boldsymbol{G}_p$ is directly obtained by evaluation of $\boldsymbol{\phi}(x)$ (and $\partial_x \boldsymbol{\phi}(x)$ in case of the Euler-Bernoulli beam) at the boundary. This is why they are regarded as "natural" choices for the application of PFEM. For the systems (3.14) and (3.27), $\boldsymbol{G}_p = \boldsymbol{I}$ follows when $n_p \cdot N_\mathrm{n} = n_q \cdot 2N$, since $\boldsymbol{\phi}|_{\partial X} = 1$.

It is convenient to also have forces and moments acting on intermediate nodes when $n_p \cdot N_\mathrm{n} > n_q \cdot 2N$. Therefore, additional inputs are introduced, such that, independent of N_n, the rank of $\boldsymbol{G}_p$ is $n_p \cdot N_\mathrm{n}$. For systems with differential order $N = 1$ and $n_p = n_q$, this means that n_p additional inputs are added at each intermediate node. In case $N = 2$ and $n_q = n_p$, $N_\mathrm{n} \geq 4$ has to be restricted to even numbers and n_p additional inputs are added – but at intermediate nodes when dividing X into $N_\mathrm{n} - 4$ equally sized segments. For $N_\mathrm{n} = 6$, as depicted in Fig, 4.2, n_p additional inputs would be added at a node in the middle of the beam.

Equation (4.21) is already a valid finite-dimensional approximation of the port-Hamiltonian system, but it is not yet in the desired input-state-output form (2.32). To bring it to this form, recall that $f := \dot{x}$ and the energy variables are transformed as follows

$$\tilde{\boldsymbol{x}} := \boldsymbol{M}_{pq}\hat{\boldsymbol{x}}. \tag{4.22}$$

For a lumped parameter port-Hamiltonian system, the effort variables are obtained by taking the gradient of the system Hamiltonian with respect to the energy variables. Thus, it remains to show that

$$\hat{\boldsymbol{e}} = \nabla_{\tilde{\boldsymbol{x}}} H(\tilde{\boldsymbol{x}}). \tag{4.23}$$

First, the system Hamiltonian needs to be written in terms of $\tilde{\boldsymbol{x}}$, which is achieved by substitution of the approximations (4.16) into (4.15) and application of the transformation (4.22)

$$H(\tilde{\boldsymbol{x}}) = \frac{1}{2}\tilde{\boldsymbol{x}}^{\mathrm{T}}\boldsymbol{M}_{pq}^{-1}\left(\int_X \boldsymbol{\Phi}\mathcal{L}\boldsymbol{\Phi}^{\mathrm{T}}\mathrm{d}x\right)\boldsymbol{M}_{pq}^{-1}\tilde{\boldsymbol{x}}. \tag{4.24}$$

Recall that $\boldsymbol{e} = \partial H/\partial \boldsymbol{x}$. After substitution of the approximations (4.16) and transformation to the weak form, this expression becomes

$$\left(\int_X \boldsymbol{\Phi}\boldsymbol{\Phi}^{\mathrm{T}}\mathrm{d}x\right)\hat{\boldsymbol{e}} = \left(\int_X \boldsymbol{\Phi}\mathcal{L}\boldsymbol{\Phi}^{\mathrm{T}}\mathrm{d}x\right)\hat{\boldsymbol{x}}. \tag{4.25}$$

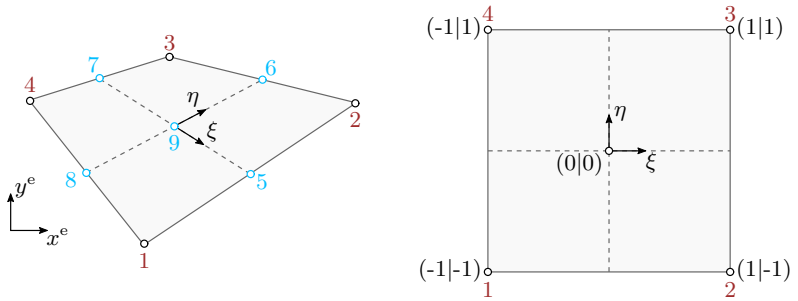

Figure 4.3: Discrete quadrilateral element with mapping to the natural coordinates ξ and η on the unit square. Four nodes (red) are required for an approximation polynomial of order one, whereas nine are necessary in case of a second order approximation

Since the integral on the left hand side is $\boldsymbol{M}_{pq}$, it is easily seen that (4.23) is true. By defining

$$\boldsymbol{Q} := \boldsymbol{M}_{pq}^{-1} \left(\int_X \boldsymbol{\Phi} \mathcal{L} \boldsymbol{\Phi}^{\mathrm{T}} \mathrm{d}x \right) \boldsymbol{M}_{pq}^{-1}, \tag{4.26}$$

the system (4.21) can be written as

$$\begin{aligned} \dot{\tilde{\boldsymbol{x}}} &= \boldsymbol{J}\boldsymbol{Q}\tilde{\boldsymbol{x}} + \boldsymbol{G}\boldsymbol{u}_\partial, \\ \boldsymbol{y}_\partial &= \boldsymbol{G}^{\mathrm{T}}\boldsymbol{Q}\tilde{\boldsymbol{x}}, \end{aligned} \tag{4.27}$$

with the boundary output variables $\boldsymbol{y}_\partial$ being the input-collocated velocities and angular velocities for all systems considered in Section 3.2.

4.3.2 Elements for two-dimensional systems

While finite elements for one-dimensional systems are always line segments, taking a second spatial dimension into account allows for many different primitive elements. The surface of a two-dimensional continuum may in principle be approximated using any polygon with at least three corner nodes. Elements with curved boundaries are also possible. For both the disk and the plate equations from Section 3.3, quadrilateral elements with straight edges are used in the following. A sample quadrilateral is depicted on the left hand side of Fig. 4.3. It is considered both a versatile and simple to employ element.

Both the location of nodes and the orientation can be different for each element. This complicates e. g. integration along the coordinates x^{e} and y^{e} of the local reference

frame. Therefore, the geometry of each quadrilateral is mapped to the unit square shown on the right hand side of Fig. 4.3. Operations on the element can then be carried out with respect to the natural coordinates ξ and η without having to mind its individual geometry explicitly. The local coordinates can be approximately expressed in terms of the natural coordinates as follows [61]

$$\begin{bmatrix} x^{\mathrm{e}}(\xi,\eta) \\ y^{\mathrm{e}}(\xi,\eta) \end{bmatrix} \approx \begin{bmatrix} \phi_{\mathrm{g}}^1 & 0 & \phi_{\mathrm{g}}^2 & 0 & \phi_{\mathrm{g}}^3 & 0 & \phi_{\mathrm{g}}^4 & 0 \\ 0 & \phi_{\mathrm{g}}^1 & 0 & \phi_{\mathrm{g}}^2 & 0 & \phi_{\mathrm{g}}^3 & 0 & \phi_{\mathrm{g}}^4 \end{bmatrix} \begin{bmatrix} x_1^{\mathrm{e}} \\ y_1^{\mathrm{e}} \\ x_2^{\mathrm{e}} \\ y_2^{\mathrm{e}} \\ x_3^{\mathrm{e}} \\ y_3^{\mathrm{e}} \\ x_4^{\mathrm{e}} \\ y_4^{\mathrm{e}} \end{bmatrix}, \tag{4.28}$$

where x_i^{e} and y_i^{e} are the local coordinates and ϕ_{g}^i the two-dimensional Lagrange polynomials of order one for each corner node i. Note that the approximation is more accurate the more the shape of the quadrilateral resembles that of the unit square. The basis functions for the geometry approximation are explicitly given as [61]

$$\begin{aligned} \phi_{\mathrm{g}}^1(\xi,\eta) &= \frac{1}{4}(1-\xi)(1-\eta), & \phi_{\mathrm{g}}^2(\xi,\eta) &= \frac{1}{4}(1+\xi)(1-\eta), \\ \phi_{\mathrm{g}}^3(\xi,\eta) &= \frac{1}{4}(1+\xi)(1+\eta), & \phi_{\mathrm{g}}^4(\xi,\eta) &= \frac{1}{4}(1-\xi)(1+\eta). \end{aligned} \tag{4.29}$$

Observe, that each ϕ_{g}^i evaluates to one at the i-th corner and to zero at each other node $j \neq i$. While other variables on the quadrilateral may be approximated using higher order basis functions with more nodes, only four nodes are required for a quadrilateral with straight edges. If the order of the approximation bases equals four for both the geometry and the DOFs of the element, it is referred to as *isoparametric*. Otherwise, when higher order approximations are used for the DOFs, the element is called *subparametric*. In Fig. 4.3 on the left, the five additional nodes required for e. g. the second order Lagrange polynomials are depicted in blue.

For a change of variables from $(x^{\mathrm{e}}, y^{\mathrm{e}})$ to (ξ, η) in equations evaluated on the quadrilateral, it is convenient to define the following mapping

$$\boldsymbol{J}_{\mathrm{g}}^{\mathrm{e}} = \begin{bmatrix} \frac{\partial x^{\mathrm{e}}}{\partial \xi} & \frac{\partial y^{\mathrm{e}}}{\partial \xi} \\ \frac{\partial x^{\mathrm{e}}}{\partial \eta} & \frac{\partial y^{\mathrm{e}}}{\partial \eta} \end{bmatrix}, \tag{4.30}$$

which is the Jacobian of (4.28). With $\boldsymbol{J}_{\mathrm{g}}^{\mathrm{e}}$, the derivative of a function of ξ and η with

respect to x^e or y^e becomes

$$\begin{bmatrix} \frac{\partial()}{\partial x^\mathrm{e}} \\ \frac{\partial()}{\partial y^\mathrm{e}} \end{bmatrix} = (\boldsymbol{J}_\mathrm{g}^\mathrm{e})^{-1} \begin{bmatrix} \frac{\partial()}{\partial \xi} \\ \frac{\partial()}{\partial \eta} \end{bmatrix}. \tag{4.31}$$

Similarly, integration with respect to the element volume may be carried out along ξ and η in the following way [61]

$$\int_{V_\mathrm{e}} \dots \,\mathrm{d}\Omega = \int_{-1}^{1} \int_{-1}^{1} \dots h |\boldsymbol{J}_\mathrm{g}^\mathrm{e}| \,\mathrm{d}\xi \,\mathrm{d}\eta, \tag{4.32}$$

where h is the thickness of the element, as previously introduced in Section 3.3. Both the determinant $|\boldsymbol{J}_\mathrm{g}^\mathrm{e}|$ and the inverse of $\boldsymbol{J}_\mathrm{g}^\mathrm{e}$ are constant if the quadrilateral is a parallelogram. In that case, applying Gaussian quadrature to compute the integral yields the exact solution. This closes the preliminary for the application of PFEM to the port-Hamiltonian representations of the disk and plate elements.

Parallel to the procedure in the previous section, let us proceed by introducing a class of systems that encompasses the ones presented in Section 3.3. Recalling the definition of the multi-index that is employed e. g. in (2.48), Eqs. (3.39) and (3.52) for a finite element may be written as

$$\dot{\boldsymbol{x}} = \mathcal{J}\boldsymbol{e}, \quad \text{with } \mathcal{J} = \sum_{|\alpha|=0}^{1} \begin{bmatrix} \boldsymbol{0} & \boldsymbol{A}_\alpha \\ (-1)^{|\alpha|+1} \boldsymbol{A}_\alpha^\mathrm{T} & \boldsymbol{0} \end{bmatrix} D^\alpha, \tag{4.33}$$

with the differential operator $D^\alpha = \partial_{x^\mathrm{e}}^{\alpha_1} \partial_{y^\mathrm{e}}^{\alpha_2}$ and the Boolean or logical matrices $\boldsymbol{A}_\alpha$. The element system Hamiltonian can be expressed as

$$H(\boldsymbol{x}) = \frac{1}{2} h \int_{A_\mathrm{e}} \boldsymbol{x}^\mathrm{T} \mathcal{L} \boldsymbol{x} \,\mathrm{d}\Omega, \tag{4.34}$$

with $\mathcal{L}$, as before, independent of the local coordinates x^e and y^e.

Instead of directly plugging approximations for the system variables into (4.33), a few steps of PFEM are carried out on the infinite-dimensional system first. This is just as valid and allows for some additional manipulation before discretization. Begin by putting the system dynamics into weak form using arbitrary test functions $\boldsymbol{c}_p(x^\mathrm{e}, y^\mathrm{e})$ and $\boldsymbol{c}_q(x^\mathrm{e}, y^\mathrm{e})$

$$\begin{aligned} \int_{A_\mathrm{e}} \boldsymbol{c}_p \dot{\boldsymbol{x}}_p \,\mathrm{d}\Omega &= \sum_{|\alpha|=0}^{1} \int_{A_\mathrm{e}} \boldsymbol{c}_q \boldsymbol{A}_\alpha D^\alpha \boldsymbol{e}_q \,\mathrm{d}\Omega \\ \int_{A_\mathrm{e}} \boldsymbol{c}_q \dot{\boldsymbol{x}}_q \,\mathrm{d}\Omega &= \sum_{|\alpha|=0}^{1} (-1)^{|\alpha|+1} \int_{A_\mathrm{e}} \boldsymbol{c}_q \boldsymbol{A}_\alpha^\mathrm{T} D^\alpha \boldsymbol{e}_p \,\mathrm{d}\Omega. \end{aligned} \tag{4.35}$$

Next, one of the above systems of equations is integrated by parts, which reveals the boundary input. Again, it is chosen to integrate the equations for the kinetic flows $\boldsymbol{f}_p$ such that the boundary inputs are forces and moments

$$\int_{A_\mathrm{e}} \boldsymbol{c}_p \dot{\boldsymbol{x}}_p \,\mathrm{d}\Omega = \sum_{|\alpha|=0}^{1} (-1)^{|\alpha|} \int_{A_\mathrm{e}} D^\alpha \boldsymbol{c}_p \boldsymbol{A}_\alpha \boldsymbol{e}_q \,\mathrm{d}\Omega + \sum_{|\alpha|=1}^{1} \oint_{\partial\Omega_\mathrm{e}} \boldsymbol{c}_p n_\alpha \boldsymbol{A}_\alpha \boldsymbol{e}_q \,\mathrm{d}s. \tag{4.36}$$

Here, $\partial\Omega_\mathrm{e}$ denotes the element boundary and $n_\alpha(s)$ is the component of the vector normal to the boundary selected by α (for $\alpha = (1,0)$, n_α becomes n_x). For an illustration of the vector normal and its components along the boundary curve, see Fig. 3.5.

As to the question why integration by parts is performed on the distributed parameter system, note that the term

$$\boldsymbol{u}_\partial(s,t) = \sum_{|\alpha|=1}^{1} n_\alpha(s) \boldsymbol{A}_\alpha \boldsymbol{e}_q(s,t) \tag{4.37}$$

under the line integral is the boundary input. It is now possible to choose a different approximation for $\boldsymbol{u}_\partial$ than for $\boldsymbol{e}_q$, which was the point of working with the infinite-dimensional equations. Let each $u^i_\partial(s,t)$ be approximated by

$$u^i_\partial(s,t) \approx \boldsymbol{\psi}(s)^\mathrm{T} \hat{\boldsymbol{u}}^i_\partial(t), \qquad i = 1 \ldots n_q, \tag{4.38}$$

where $\boldsymbol{\psi}(s)$ is a vector of orthogonal basis functions. It may be chosen depending on the desired form of the input.

In the FEM approach, the inputs are usually the nodal forces and moments. In order to be consistent with that, $\boldsymbol{\psi}$ is chosen as

$$\boldsymbol{\psi}(s)^\mathrm{T} = \left[\delta(x^\mathrm{e}(s) - x^\mathrm{e}_1, y^\mathrm{e}(s) - y^\mathrm{e}_1) \quad \ldots \quad \delta(x^\mathrm{e}(s) - x^\mathrm{e}_{N_\mathrm{n}}, y^\mathrm{e}(s) - y^\mathrm{e}_{N_\mathrm{n}})\right], \tag{4.39}$$

where $\delta(x^\mathrm{e}, y^\mathrm{e})$ denotes the Dirac delta function, $(x^\mathrm{e}_i, y^\mathrm{e}_i)$ are the coordinates of the i-th node and N_n is the number of nodes. Note that N_n is not the number of nodes used for the approximation of the quadrilateral's geometry in (4.28) (four nodes). It is the number of nodes used for the approximation of the energy and power variables. Thus, when $N_\mathrm{n} > 4$, the element is subparametric, as explained above. The system variables are approximated as

$$\begin{aligned}
\boldsymbol{x}_p(x^\mathrm{e}, y^\mathrm{e}, t) &\approx \boldsymbol{\Phi}_p^\mathrm{T}(\xi,\eta)\hat{\boldsymbol{x}}_p(t), \quad & \boldsymbol{x}_q(x^\mathrm{e}, y^\mathrm{e}, t) &\approx \boldsymbol{\Phi}_q^\mathrm{T}(\xi,\eta)\hat{\boldsymbol{x}}_q(t),\\
\boldsymbol{f}_p(x^\mathrm{e}, y^\mathrm{e}, t) &\approx \boldsymbol{\Phi}_p^\mathrm{T}(\xi,\eta)\hat{\boldsymbol{f}}_p(t), \quad & \boldsymbol{f}_q(x^\mathrm{e}, y^\mathrm{e}, t) &\approx \boldsymbol{\Phi}_q^\mathrm{T}(\xi,\eta)\hat{\boldsymbol{f}}_q(t),\\
\boldsymbol{e}_p(x^\mathrm{e}, y^\mathrm{e}, t) &\approx \boldsymbol{\Phi}_p^\mathrm{T}(\xi,\eta)\hat{\boldsymbol{e}}_p(t), \quad & \boldsymbol{e}_q(x^\mathrm{e}, y^\mathrm{e}, t) &\approx \boldsymbol{\Phi}_q^\mathrm{T}(\xi,\eta)\hat{\boldsymbol{e}}_q(t).
\end{aligned} \tag{4.40}$$

The notation follows that of Section 4.3.1. Except that the Lagrange polynomials $\boldsymbol{\Phi}_p \in \mathbb{R}^{n_p \times n_p \cdot N_\mathrm{n}}$ and $\boldsymbol{\Phi}_q \in \mathbb{R}^{n_q \times n_q \cdot N_\mathrm{n}}$ are two-dimensional here and the approximation

is carried out on the unit square with coordinates (ξ, η). With N_n nodes, the order of the polynomial bases is $\sqrt{N_\mathrm{n}} - 1$. It follows that N_n must be obtained from the square of a natural number greater than two in case of a full-order Lagrange polynomial. The nine nodes of the second order Lagrange polynomials are depicted on the left hand side of Fig. 4.3. Just as in the one-dimensional case, the N_n orthogonal basis functions that form $\boldsymbol{\phi}(\xi, \eta)$ evaluate to one only at the node they correspond to and to zero at all other nodes.

After inserting the approximations (4.40) and (4.38) into (4.19) and (4.36), all that remains to arrive at a discrete representation, is to specify the test functions $\boldsymbol{c}_p$ and $\boldsymbol{c}_q$. A choice that is particularly convenient, is given by $\boldsymbol{c}_p = \boldsymbol{\Phi}_p$ and $\boldsymbol{c}_q = \boldsymbol{\Phi}_q$. Then, the integrals over the element surface and its boundary can be carried out by employing Gaussian quadrature and (4.21) results. It may help to bring to mind, that the derivatives of Φ_p and Φ_q with respect to x^e and y^e can be written in terms of ∂_ξ and ∂_η according to (4.31). Also, note that the Dirac delta function has the convenient property of being premultiplied by the inverse of the Jacobian determinant $|\boldsymbol{J}_\mathrm{g}^\mathrm{e}|$ on change of coordinates from $(x^\mathrm{e}, y^\mathrm{e})$ to (ξ, η).

The discrete boundary input corresponding to Q_{ns} of the disk element is set to zero since – for the above choice of elements and approximation bases – it can be expressed as a linear combination of F_x and F_y at each node. For the same reason, the input corresponding to M_{ns} of the Mindlin-Reissner plate is eliminated. Then, it follows that $\boldsymbol{G}_p$ in (4.21) becomes the identity matrix of size $n_p \cdot N_\mathrm{n}$ when $N_\mathrm{n} = 4$ (i. e. the quadrilateral is isoparametric). For higher order elements, extra inputs are added at interior nodes to ensure that $\boldsymbol{G}_p = \boldsymbol{I}$ and that all nodes can be externally manipulated. Recall, that this was also done for the one-dimensional elements in Section 4.3.1.

For the remaining steps to obtain a system in input-state-output form (2.32), the reader is referred to the previous section. Since they are identical, it is refrained from repeating them here.

4.4 Comparison between FEM and PFEM

In the interdisciplinary context that this work stems from, the finite element method is a well established and well understood approach. Presenting the application of PFEM to beam and plate equations on different occasions gave rise to some misunderstandings. This section is dedicated to showing that the methods are actually closely related. Important differences and their implications are also discussed.

For the following analysis, it is assumed that $\boldsymbol{\Phi}_p = \boldsymbol{\Phi}_q = \boldsymbol{\Phi}_\mathrm{e}$, where $\boldsymbol{\Phi}_\mathrm{e}$ is the matrix from (4.3). Strictly speaking, this excludes the two-dimensional systems. However, the observations made in this section apply to the disk and plate systems just as well. Showing this requires more extensive notation, but otherwise readily follows from the subsequent.

Given the mass matrix $\boldsymbol{M}_\mathrm{e}$ and the stiffness matrix $\boldsymbol{K}_\mathrm{e}$ obtained from applying FEM, the element dynamics (4.9) can be expressed in port-Hamiltonian form by choosing the state vector as $\boldsymbol{x}_\mathrm{e}^\mathrm{T} = \begin{bmatrix}(\boldsymbol{M}_\mathrm{e}\dot{\hat{\boldsymbol{q}}}_\mathrm{e})^\mathrm{T} & \hat{\boldsymbol{q}}_\mathrm{e}^\mathrm{T}\end{bmatrix} \in \mathbb{R}^{2N_q \cdot N_\mathrm{n}}$. Denote by $\boldsymbol{f}_\mathrm{ext}^\mathrm{e} \in \mathbb{R}^{N_q \cdot N_\mathrm{n}}$ the external forces and moments acting on the element nodes. Then, a port-Hamiltonian system in input-state-output form results as

$$\begin{aligned}\dot{\boldsymbol{x}}_\mathrm{e} &= \begin{bmatrix}\boldsymbol{0} & -\boldsymbol{I}\\ \boldsymbol{I} & \boldsymbol{0}\end{bmatrix}\begin{bmatrix}\boldsymbol{M}_\mathrm{e}^{-1} & \boldsymbol{0}\\ \boldsymbol{0} & \boldsymbol{K}_\mathrm{e}\end{bmatrix}\boldsymbol{x}_\mathrm{e} + \begin{bmatrix}\boldsymbol{I}\\ \boldsymbol{0}\end{bmatrix}\boldsymbol{f}_\mathrm{ext}^\mathrm{e},\\ \boldsymbol{y}_\mathrm{e} &= \begin{bmatrix}\boldsymbol{I} & \boldsymbol{0}\end{bmatrix}\begin{bmatrix}\boldsymbol{M}_\mathrm{e}^{-1} & \boldsymbol{0}\\ \boldsymbol{0} & \boldsymbol{K}_\mathrm{e}\end{bmatrix}\boldsymbol{x}_\mathrm{e},\end{aligned} \tag{4.41}$$

where $\boldsymbol{y}_\mathrm{e}$ are the velocities of the element nodes. This representation is convenient for comparison with (4.27). So far, it is not apparent how the two systems are related to each other and whether there are any commonalities. In order to show the similarities, first observe that for the systems presented in Chapter 3, $\mathcal{L}$ and $\boldsymbol{Q}$ are block diagonal matrices

$$\mathcal{L} = \begin{bmatrix}\mathcal{L}_p & \boldsymbol{0}\\ \boldsymbol{0} & \mathcal{L}_q\end{bmatrix}, \qquad \boldsymbol{Q} = \begin{bmatrix}\boldsymbol{Q}_p & \boldsymbol{0}\\ \boldsymbol{0} & \boldsymbol{Q}_q\end{bmatrix}. \tag{4.42}$$

Since $\mathcal{L}_p$ is a diagonal matrix, and recalling that $\boldsymbol{\Phi}$ in (4.26) is also block diagonal, observe that

$$\boldsymbol{Q}_p = \boldsymbol{M}_p^{-1}\mathcal{L}_p\left(\int_{V_\mathrm{e}} \boldsymbol{\Phi}_p\boldsymbol{\Phi}_p^\mathrm{T}\,\mathrm{d}\Omega\right)\boldsymbol{M}_p^{-1} = \boldsymbol{M}_\mathrm{e}^{-1}. \tag{4.43}$$

To check that the above is true, note that $\mathcal{L}_p = 1/\rho \cdot \boldsymbol{I}$ (for the planar systems $\mathcal{L}_p = 1/(\rho h) \cdot \boldsymbol{I}$) and recall that $\boldsymbol{\Phi}_\mathrm{e} = \boldsymbol{\Phi}_p$ was assumed. The matrix $\mathcal{L}_q$ is not always diagonal. However, the block diagonal property of $\boldsymbol{\Phi}_q$ still allows for a reformulation of $\boldsymbol{Q}_q$. Let $\mathcal{L}_q = \boldsymbol{D}_\mathrm{e}$, with $\boldsymbol{D}_\mathrm{e}$ from (4.7). Then it can be stated that

$$\boldsymbol{Q}_q = \boldsymbol{M}_q^{-1}\left(\int_{V_\mathrm{e}} \boldsymbol{\Phi}_q\boldsymbol{D}_\mathrm{e}\boldsymbol{\Phi}_q^\mathrm{T}\,\mathrm{d}\Omega\right)\boldsymbol{M}_q^{-1} = \hat{\boldsymbol{D}}_\mathrm{e}\boldsymbol{M}_q^{-1}, \tag{4.44}$$

where $\hat{\boldsymbol{D}}_\mathrm{e}$ is simply $\boldsymbol{D}_\mathrm{e}$ with each entry expanded to N_n nodes such that $\hat{\boldsymbol{\sigma}}_\mathrm{e} = \hat{\boldsymbol{D}}_\mathrm{e}\hat{\boldsymbol{\varepsilon}}_\mathrm{e}$ and $\hat{\boldsymbol{\varepsilon}}_\mathrm{e}, \hat{\boldsymbol{\sigma}}_\mathrm{e} \in \mathbb{R}^{n_q \cdot N_\mathrm{n}}$. This result can be generalized to the two-dimensional case by including shear terms in $\boldsymbol{D}_\mathrm{e}$. Now, and realizing that $\boldsymbol{u}_\partial = \boldsymbol{f}_\mathrm{ext}^\mathrm{e}$, the upper equations of (4.27) may be rewritten as

$$\dot{\tilde{\boldsymbol{x}}} = \begin{bmatrix}\boldsymbol{0} & \boldsymbol{P}\\ -\boldsymbol{P}^\mathrm{T} & 0\end{bmatrix}\begin{bmatrix}\boldsymbol{M}_e^{-1} & \boldsymbol{0}\\ \boldsymbol{0} & \hat{\boldsymbol{D}}_\mathrm{e}\boldsymbol{M}_q^{-1}\end{bmatrix}\tilde{\boldsymbol{x}} + \begin{bmatrix}\boldsymbol{I}\\ \boldsymbol{0}\end{bmatrix}\boldsymbol{f}_\mathrm{ext}^\mathrm{e}. \tag{4.45}$$

Examining again (4.22) and the definitions of the energy variables for the systems in Chapter 3, it follows that $\tilde{\boldsymbol{x}}^\mathrm{T} = \begin{bmatrix}(\boldsymbol{M}_\mathrm{e}\dot{\hat{\boldsymbol{q}}}_\mathrm{e})^\mathrm{T} & (\boldsymbol{M}_q\hat{\boldsymbol{\varepsilon}}_\mathrm{e})^\mathrm{T}\end{bmatrix}$. In this representation, it is easy to spot the common points and the differences.

With regard to the differences, it all comes down to the the fact that, in FEM, the displacements $\boldsymbol{q}_\mathrm{e}$ instead of the strains $\boldsymbol{\varepsilon}_\mathrm{e}$ are used as state variables. To come to this insight, it is not actually necessary to analyze the respective discrete representations. Still, it is considered important to understand how this affects the latter. In (4.45), the matrix $\boldsymbol{P}$ can be considered a discrete differential operator that is not present in (4.41). One consequence of the different choice of state variables in the port-Hamiltonian formulation is that the full system may not, in general, be assembled by summing up the transformed element matrices. This is due to the fact that the strains of individual elements are usually not equivalent at the nodes. Especially when different types of elements are interconnected at a node.

For a purely mechanical system, it may thus be advantageous to simply rewrite the second order equations (4.12) of the assembled system obtained via FEM as a port-Hamiltonian system. As already shown above, this is achieved by choosing the state vector as $\boldsymbol{x}^\mathrm{T} = \begin{bmatrix}(\boldsymbol{M}\dot{\boldsymbol{q}})^\mathrm{T} & \boldsymbol{q}^\mathrm{T}\end{bmatrix} \in \mathbb{R}^{2n_\mathrm{DOF}}$

$$\begin{aligned}\dot{\boldsymbol{x}} &= \left(\underbrace{\begin{bmatrix}\boldsymbol{0} & -\boldsymbol{I}\\ \boldsymbol{I} & \boldsymbol{0}\end{bmatrix}}_{\boldsymbol{J}} - \underbrace{\begin{bmatrix}\boldsymbol{D} & \boldsymbol{0}\\ \boldsymbol{0} & \boldsymbol{0}\end{bmatrix}}_{\boldsymbol{R}}\right)\underbrace{\begin{bmatrix}\boldsymbol{M}^{-1} & \boldsymbol{0}\\ \boldsymbol{0} & \boldsymbol{K}\end{bmatrix}}_{\boldsymbol{Q}}\boldsymbol{x} + \underbrace{\begin{bmatrix}\boldsymbol{I}\\ \boldsymbol{0}\end{bmatrix}}_{\boldsymbol{G}}\boldsymbol{f}_\mathrm{ext},\\ \boldsymbol{y} &= \boldsymbol{G}^\mathrm{T}\boldsymbol{Q}\boldsymbol{x},\end{aligned} \tag{4.46}$$

where the output $\boldsymbol{y} \in \mathbb{R}^{n_\mathrm{DOF}}$ contains the nodal velocities or angular velocities for each DOF. Note that the symmetric positive semi-definite matrix $\boldsymbol{R}$ yields the damping term $\boldsymbol{D}\dot{\boldsymbol{q}}$ introduced in (4.12) above when multiplied by $\boldsymbol{Q}\boldsymbol{x}$. Damping on the distributed parameter level is not discussed in this thesis.

In an energy-based formulation, the interesting part is, however, the interconnection of mechanical systems with elements from non-mechanical or hybrid domains. Suppose, that such elements are described by PDEs or include nonlinear relations. In those cases, it is not clear how to obtain a port-Hamiltonian formulation of the coupled system, given only the mechanical part (4.12). This is why a port-Hamiltonian way of assembling linear elastic structures is presented in this thesis.

In Chapter 5, a port-based method, or rather an algorithm, for the automatic assembly of systems composed of mechanical and non-mechanical components is introduced. It is more in line with the energy-based philosophy (than adding up the element matrices) and allows for another perspective on the assembly process. Together with the discretization methods presented in this chapter, this allows for a complete and consistent port-Hamiltonian formulation of the finite element approach. In each step – from the infinite-dimensional equations via spatial discretization to the interconnected lumped parameter system – the port-Hamiltonian structure is preserved. It is also shown that, for the purely mechanical case, the resulting system representation is identical and can be transformed to (4.46) when the same approximation bases are used. To the best of our knowledge, such a connection has not been established before.

With a thorough understanding of the port-Hamiltonian way of modeling linear elastic mechanical systems and its relation to more established FE methods, extensions are achieved more easily and mutual understanding across disciplines is promoted.

4.5 Approximation error analysis

In this section, the accuracy of the numerical discretization methods presented in Section 4.3 is investigated. A common way to do this, is to compute the eigenfrequencies of the discretized system and to check whether they converge to a reference solution. When steadily increasing the number of elements or the order of the approximation bases, it is likewise important how quickly the error reduces. Analytical solutions are available for some specific boundary conditions and element geometries. If this is not the case, reverting to accurate numerical approximations from literature is another possibility.

Approximation error analysis is done for beam elements in Section 4.5.1 and for the disk and plate elements in Section 4.5.2. Only the most common test scenarios are considered here. In further work, elements with irregular shapes might be addressed in the error analysis of the two-dimensional systems (e. g. in a patch test).

4.5.1 Beam elements

For each of the systems presented in Section 3.2, a numerical analysis of the approximation error is performed for the case of a single beam with a quadratic cross section and $L/h = 50$, where h is the cross sectional height. Different boundary conditions are chosen for bending and axial loads. In case of the Timoshenko and Euler-Bernoulli equations, the beam is simply supported and otherwise it is clamped at one end and free at the other. A Poisson ratio of $\nu = 0.1$ is chosen and the Timoshenko shear coefficient is set to $\kappa = 5/6$. The beam is then approximated using an increasing number of elements and the error in the first eigenfrequency is computed. Analytical solutions for the eigenfrequencies of each of the considered load cases can e. g. obtained from [111]. The results are depicted in Fig. 4.4 for all of the beam equations with the number of elements ranging from $N_\mathrm{e} = 1 \ldots 100$.

In Fig. 4.4 a), $N_\mathrm{n} = 2$ nodes were chosen in case of the rod and the Saint-Venant element and $N_\mathrm{n} = 4$ for both Euler-Bernoulli and Timoshenko beam. For all systems, the error starts at a value of $\approx 10\,\%$ and decreases monotonically until $N_\mathrm{e} \approx 40$ where it starts to oscillate around a more or less stationary value for the bending elements. The results for the rod and Saint-Venant element are not discernible from each other. This was to be expected as the systems only differ in terms of parameters but are otherwise identical. A saturation of the error is not visible for the axial loads. The oscillating behavior about an error of $\approx 1 \times 10^{-6}\,\%$ for the Euler-Bernoulli beam and

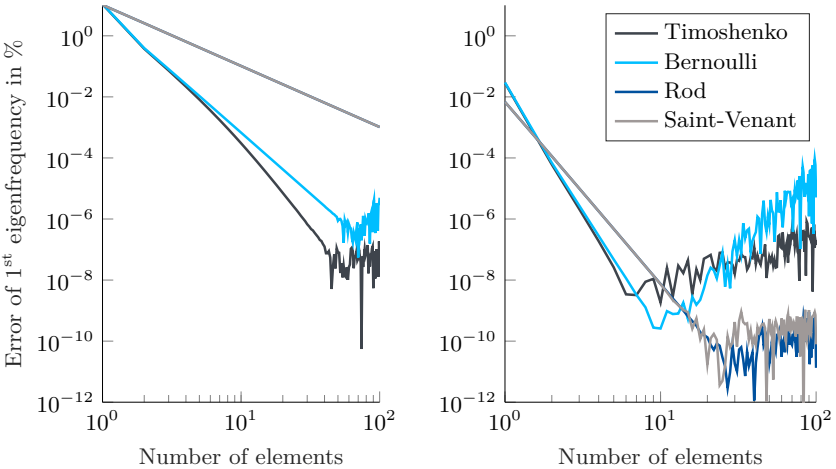

(a) $N_\mathrm{n} = 2$ for axial loads and $N_\mathrm{n} = 4$ for bending

(b) $N_\mathrm{n} = 4$ for axial loads and $N_\mathrm{n} = 6$ for bending

Figure 4.4: Analysis of the approximation error of PFEM for the beam models with a different number of elements and supporting points

Table 4.1: Eigenvalue analysis for a free rectangular disk ($b/a = 0.5$)

Mode	N=10($\mathbb{P}_1$)	N=20($\mathbb{P}_1$)	N=5($\mathbb{P}_2$)	N=10($\mathbb{P}_2$)	Ref.
$\hat{\omega}_1$	0.9961	0.9817	0.9782	0.9769	0.9830
$\hat{\omega}_2$	1.4873	1.4821	1.4806	1.4804	1.4806
$\hat{\omega}_3$	1.6733	1.6437	1.6384	1.6339	1.6340
$\hat{\omega}_4$	2.4469	2.3843	2.3794	2.3644	1.8588

$\approx 5 \times 10^{-8}$ % for the Timoshenko beam is explained by the fact that the composite system becomes numerically ill-conditioned for a high number of elements. The smaller individual elements become, the more stiff their behavior. This effect can be reduced by stabilizing the numerical methods involved in the system assembly (see Chapter 5) and eigenfrequency calculation.

As the approximation error does not only depend on the number of elements, but also on the order of the approximation polynomials, an additional analysis was conducted with a higher order of the approximation bases. This time, $N_\mathrm{n} = 4$ nodes were chosen for the axial loads and $N_\mathrm{n} = 6$ for bending. The results are shown in Fig. 4.4 b). With only a single element, the error is now about three orders of magnitudes lower than before for all systems. It also decreases more rapidly and is already below the minimum value visible in Fig. 4.4 a) for $N_\mathrm{e} = 5$ elements (with the exception of the Timoshenko beam, for which a lower value results at $N_\mathrm{e} = 74$). However, for $N_e > 10$ the systems start to become numerically ill-conditioned, which results in a saturation of the approximation error for the rod and Saint-Venant elements. Instead of a saturation, an increasing trend is visible for the error of the simply supported Timoshenko and Euler-Bernoulli beams.

The numerical analysis of the approximation error is limited by the accuracy of the employed numerical methods and the numerical conditioning of the systems, for which the error is calculated. A mathematical analysis of the convergence properties of PFEM for the systems considered here would alleviate those issues, but is beyond the scope of this work. With the results shown in Fig. 4.4, it is concluded that reasonable accuracy can be achieved for a low number of approximating elements, especially when using more than the minimum number of nodes required per element. However, numerical ill-conditioning becomes a problem for a high number of elements which, depending on the application, needs to properly addressed. Optimizing the algorithms for system assembly that are presented in Chapter 5 on this account is to be considered in further work.

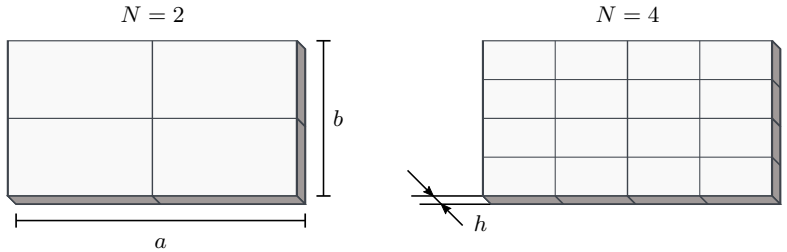

Figure 4.5: Discretization meshes with different refinement N for a rectangular disk/plate element with side lengths a and b and thickness h

4.5.2 Disk and plate elements

Approximate solutions for the primary eigenfrequencies of the free vibrations of a disk element are e. g. available in [137]. Those are compared to the eigenfrequencies of the discrete disk equations obtained according to the procedure presented in Section 4.3.2. The solutions in [137] are reported for a rectangular disk with side lengths $a = 2b$ and all sides unsupported (free). For the approximation, a mesh with N^2 elements of identical size was used, which is illustrated in Fig. 4.5. Different numbers of elements as well as a different number of nodes per element were tested. To allow comparison to the values given in [137], the computed eigenfrequencies ω_k are converted to the non-dimensional quantities [124]

$$\hat{\omega}_k^2 = \omega_k^2 \frac{4E}{\rho a^2 (1-\nu)^2}. \tag{4.47}$$

Results are listed up to the fourth eigenmode in Tab. 4.1, where $\mathbb{P}_1$ and $\mathbb{P}_2$ indicate that Lagrange polynomials of first ($N_\mathrm{n} = 4$) and second order ($N_\mathrm{n} = 9$) were used, respectively. The Poisson ratio was set to $\nu = 0.3$. Reference solutions from [137] are given in the rightmost column. For the the first three modes, the deviation is already below three percent for $N = 10$ using first order Lagrange polynomials. In the other cases, it reduces to values below one percent. However, in all cases, the frequency of the fourth mode does not match with the reference value. Since the values given in [137] are also approximations, this does not necessarily indicate an error. Further investigations are necessary to find out, where exactly the difference originates from and which solution is more accurate.

The following analysis of the approximation error for the Mindlin-Reissner plate is guided by the one performed by Brugnoli et al. in [20]. Reference solutions for the free vibrations of a quadratic plate ($a = b = L$) are taken from [38]. Eigenfrequencies are reported for four different boundary conditions, namely

Table 4.2: Eigenvalue analysis for a thick plate ($h/L = 0.1$)

B. C.	Mode	N=10($\mathbb{P}_1$)	N=20($\mathbb{P}_1$)	N=5($\mathbb{P}_2$)	N=10($\mathbb{P}_2$)	Ref.
CCCC	$\hat{\omega}_{11}$	1.7811	1.6401	1.6132	1.5927	1.594
CCCC	$\hat{\omega}_{21}$	3.4756	3.1499	3.1254	3.0454	3.046
CCCC	$\hat{\omega}_{12}$	3.4756	3.1499	3.1254	3.0454	3.046
CCCC	$\hat{\omega}_{22}$	4.7897	4.3955	4.3752	4.2712	4.285
SSSS	$\hat{\omega}_{11}$	1.0027	0.9487	0.9319	0.9304	0.930
SSSS	$\hat{\omega}_{21}$	2.4916	2.2877	2.2411	2.2209	2.219
SSSS	$\hat{\omega}_{12}$	2.4916	2.2877	2.2411	2.2209	2.219
SSSS	$\hat{\omega}_{22}$	3.7418	3.4895	3.4339	3.4077	3.406
SCSC	$\hat{\omega}_{11}$	1.4366	1.3352	1.3136	1.3011	1.302
SCSC	$\hat{\omega}_{21}$	2.6832	2.4670	2.4222	2.3961	2.398
SCSC	$\hat{\omega}_{12}$	3.2889	2.9870	2.9645	2.8903	2.888
SCSC	$\hat{\omega}_{22}$	4.2627	3.9455	3.9109	3.8446	3.852
CCCF	$\hat{\omega}_{11}$	1.2322	1.1201	1.0975	1.0818	1.089
CCCF	$\hat{\omega}_{21}$	1.9229	1.7898	1.7664	1.7452	1.758
CCCF	$\hat{\omega}_{12}$	3.1181	2.7746	2.7502	2.6627	2.673
CCCF	$\hat{\omega}_{22}$	3.6440	3.3097	3.2727	3.2015	3.216

- fully clamped (CCCC), i. e. $\dot{w} = 0$, $\dot{\varphi}_n = 0$ and $\dot{\varphi}_s = 0$;
- hard simply supported (SSSS), i. e. $\dot{w} = 0$, $\dot{\varphi}_s = 0$ and $M_{nn} = 0$;
- half clamped half simply supported (SCSC);
- all sides clamped except one (CCCF).

Additionally, two different thickness to length ratios are considered - a thick plate with $h/L = 0.1$ and a thin plate with $h/L = 0.01$. Again, for comparison with the results given in [38], the frequencies are converted to a dimensionless form

$$\hat{\omega}^h_{mn} = \omega^h_{mn} L \sqrt{\frac{2(1+\nu)\rho}{E}}, \tag{4.48}$$

where m and n indicate the number of half waves in the mode shapes in the x- and y-direction, respectively. Just as in [38], the Poisson ratio is set to $\nu = 0.3$ in all scenarios. The Timoshenko shear coefficient is set to $\kappa = 0.8601$ for CCCC and CCCF, $\kappa = 0.8333$ for SSSS and 0.822 for SCSC. Aside from the thickness to length ratio, these are the only parameters that influence the results. Results for $h/L = 0.1$ are given in Tab. 4.2 and Tab. 4.3 list those obtained for a thin plate with $h/L = 0.01$. The same combinations of N and $\mathbb{P}$ as previously for the disk elements were used.

Table 4.3: Eigenvalue analysis for a thin plate ($h/L = 0.01$)

B. C.	Mode	N=10($\mathbb{P}_1$)	N=20($\mathbb{P}_1$)	N=5($\mathbb{P}_2$)	N=10($\mathbb{P}_2$)	Ref.
CCCC	$\hat{\omega}_{11}$	0.8727	0.4593	0.1906	0.1785	0.1754
CCCC	$\hat{\omega}_{21}$	1.8500	0.9550	0.4253	0.3699	0.3576
CCCC	$\hat{\omega}_{12}$	1.8500	0.9550	0.4253	0.3700	0.3576
CCCC	$\hat{\omega}_{22}$	2.4757	1.2903	0.6333	0.5458	0.5274
SSSS	$\hat{\omega}_{11}$	0.3832	0.2079	0.0971	0.0965	0.0963
SSSS	$\hat{\omega}_{21}$	1.1327	0.5917	0.2511	0.2428	0.2406
SSSS	$\hat{\omega}_{12}$	1.1327	0.5917	0.2512	0.2428	0.2406
SSSS	$\hat{\omega}_{22}$	1.5686	0.8358	0.3984	0.3875	0.3848
SCSC	$\hat{\omega}_{11}$	0.6611	0.3504	0.1504	0.1430	0.1411
SCSC	$\hat{\omega}_{21}$	1.2494	0.6551	0.2839	0.2704	0.2668
SCSC	$\hat{\omega}_{12}$	1.7267	0.8909	0.4017	0.3492	0.3377
SCSC	$\hat{\omega}_{22}$	2.0369	1.0707	0.5250	0.4720	0.4608
CCCF	$\hat{\omega}_{11}$	0.6232	0.3258	0.1265	0.1187	0.1171
CCCF	$\hat{\omega}_{21}$	0.8713	0.4649	0.2089	0.1979	0.1951
CCCF	$\hat{\omega}_{12}$	1.7425	0.8902	0.3742	0.3204	0.3093
CCCF	$\hat{\omega}_{22}$	1.8545	0.9621	0.4206	0.3831	0.3740

Satisfactory results are achieved for the thick plate with errors below one percent for all boundary conditions when using $N^2 = 100$ elements and second order polynomials. Errors not higher than three percent are obtained for $N = 5$. Approximation quality with first order polynomials is slightly worse (errors below four percent) in case $N = 20$. Using $N^2 = 100$ elements in the $\mathbb{P}_1$ case yields errors around 10–15 % in most test scenarios.

Examining the results for the thin plate in Tab. 4.2, it is apparent that the Mindlin-Reissner equations are intended for thick plates. When using first order polynomials ($\mathbb{P}_1$), the element behavior is way too stiff even for $N = 20$. As already pointed out in [20], this is most likely related to the shear locking phenomenon. Increasing the order of the polynomials to two leads to a significant decrease in error. While errors between 5–20 % are still obtained for $N = 5$ elements per side, the deviation from the reference reduces to values below four percent for $N = 10$.

Brugnoli et al. use triangular elements for the discretization of the Mindlin-Reissner plate in [20] and achieve lower deviation from the reference values – especially for the thin plate. Therefore, one might conclude that triangular elements are superior to quadrilaterals. However, bear in mind that this also depends on the accuracy of the numerical algorithms employed for both discretization and system assembly from individual elements. A professional FE software package (FEniCS) was used in [20],

while a self-written Matlab framework performs all the steps leading to the results presented in this section. Note that the port-based coupling procedure introduced in Chapter 5 that is implemented in said framework involves a series of numerical operations that potentially accumulate inaccuracies. Unless the elements are compared using the same software package, it cannot be judged whether one of them actually outperforms the other.

4.6 A note on time discretization

Not much will be said about time discretization in this section. First and foremost, it is important to remark that numerical methods for time discretization of port-Hamiltonian systems need to be structure preserving as well. This implies that not just any solver can be used to integrate the dynamic equations of a port-Hamiltonian system with respect to time. Only the use of *symplectic numerical integration* schemes guarantees that the energy balance is preserved during the simulation [71]. A thorough discussion of suitable integration methods is given in [71]. Among the methods presented therein, s-stage Gauss-Legendre schemes are shown to be the only ones that preserve the energy balance exactly.

The simplest possible choice of a structure preserving integration scheme is the symplectic Euler method, as used e. g. in [72]. It has the advantage of being a semi-explicit method, which can be easily implemented. However, it is not very suitable for stiff systems, such as the ones considered in this thesis. Generally, employing a Gauss-Legendre solver of order $s = 1$ led to satisfactory results when simulating the systems presented here. For extremely stiff systems, consider reducing the time step or increasing the order of the integration scheme.

5 Assembly of complex systems

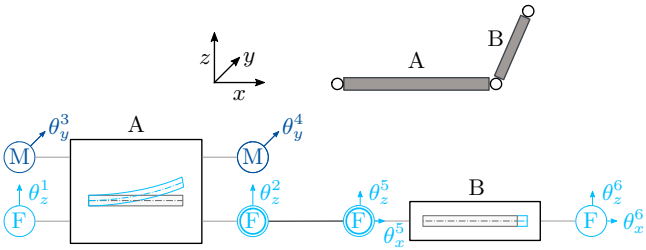

Figure 5.1: Interconnection of two linear elastic elements with boundary mechanical ports of torque type 'M' or force type 'F'. The orientation of the power ports in the global reference frame is specified by the components of the vector $\boldsymbol{\theta}^i \in \mathbb{R}^3$, respectively [135]

As a preface to this chapter, note that it is mostly taken from [135] with minor modifications.

With the systems defined in Chapter 3 and the numerical approximation method described in Chapter 4, the dynamics of one- or two-dimensional structural primitives can be obtained as the set of ordinary differential equations (ODEs) (4.27). To model more complex structures, the interconnection and coupling of multiple basic elements needs to be taken into account. In the following, a port-based method for the automatic assembly of arbitrary 3D structures composed of the elements introduced in Chapter 3 is derived. Some of the methods presented in this chapter are only applicable to linear systems. Coupling with the nonlinear systems presented in Chapter 6 or systems from other non-mechanical domains, is briefly covered in Section 5.6.

Throughout this chapter, Fig. 5.1 is drawn on to illustrate the concepts. It depicts the interconnection of an Euler-Bernoulli beam and a rod element, respectively labeled system "A" and "B". No two-dimensional elements are included in the example for reasons of simplicity. However, the presented methods are applicable to systems including plate and disk elements in exactly the same fashion. The system equations of the Euler-Bernoulli beam are

$$\begin{aligned} \dot{\tilde{\boldsymbol{x}}}^{\mathrm{A}} &= \boldsymbol{J}^{\mathrm{A}} \hat{\boldsymbol{e}}^{\mathrm{A}} + \boldsymbol{G}^{\mathrm{A}} \boldsymbol{u}_{\partial}^{\mathrm{A}}, \\ \boldsymbol{y}_{\partial}^{\mathrm{A}} &= (\boldsymbol{G}^{\mathrm{A}})^{\mathrm{T}} \hat{\boldsymbol{e}}^{\mathrm{A}}, \end{aligned} \tag{5.1}$$

with $\boldsymbol{u}_{\partial}^{\mathrm{A}} \in \mathbb{R}^4$ the shear forces and bending moments at the boundary and $\boldsymbol{y}_{\partial}^{\mathrm{A}}$ the corresponding collocated velocities and angular velocities. The dimension of $\tilde{\boldsymbol{x}}^{\mathrm{A}}$ and $\hat{\boldsymbol{e}}^{\mathrm{A}}$ depends on the order of the approximation polynomials $\boldsymbol{\phi}$ in (4.16). Let n_{A} denote the number of nodes used for approximating each x_i^{A} and e_i^{A}. It follows that

$\tilde{\boldsymbol{x}}^{\mathrm{A}}, \hat{\boldsymbol{e}}^{\mathrm{A}} \in \mathbb{R}^{2n_{\mathrm{A}}}$. For the rod element, the approximated dynamics are

$$\begin{aligned} \dot{\tilde{\boldsymbol{x}}}^{\mathrm{B}} &= \boldsymbol{J}^{\mathrm{B}} \hat{\boldsymbol{e}}^{\mathrm{B}} + \boldsymbol{G}^{\mathrm{B}} \boldsymbol{u}_{\partial}^{\mathrm{B}}, \\ \boldsymbol{y}_{\partial}^{\mathrm{B}} &= (\boldsymbol{G}^{\mathrm{B}})^{\mathrm{T}} \hat{\boldsymbol{e}}^{\mathrm{B}}, \end{aligned} \tag{5.2}$$

where $\boldsymbol{u}_{\partial}^{\mathrm{B}} \in \mathbb{R}^2$ are the axial forces at the boundary and $\boldsymbol{y}_{\partial}^{\mathrm{B}}$ the collocated velocities. As for system A above, $\tilde{\boldsymbol{x}}^{\mathrm{B}}, \hat{\boldsymbol{e}}^{\mathrm{B}} \in \mathbb{R}^{2n_{\mathrm{B}}}$, where n_{B} is the number of nodes used for approximating each x_i^{B} and e_i^{B}.

In the bottom part of Fig. 5.1 the interconnection of A and B is depicted in a mechanical network diagram. Specific to this block diagram representation is the appearance of a normalized orientation vector $\boldsymbol{\theta}^i \in \mathbb{R}^3$ at each boundary port, where i denotes the port number. A port labeled 'M' indicates a torque/angular velocity pair at the boundary and 'F' marks ports with a force/velocity pair. Ports of the same type with a non-zero scalar product of the orientation vectors can be coupled. Given the information in Fig. 5.1, it is possible to write an algorithm for the automatic assembly of the coupled system.

In the remainder of this chapter, the necessary steps such an algorithm needs to perform are explained in detail. First, in Section 5.1, a way to concatenate the system matrices of individual elements is shown, followed by the generation of coupling constraints in Section 5.2. Elimination of those constraints, as presented in Section 5.3, leads to systems that do not have full rank due to linear dependencies between states. A way to remove redundant equations is shown in Section 5.4. The resulting system on the constraint manifold needs to be normalized in order to obtain a description of the dynamics in global DOFs or generalized coordinates $\boldsymbol{q}$. This is achieved in two steps, as presented in Section 5.5.

5.1 System concatenation

Without considering the coupling of the dynamic equations yet, there are several ways to concatenate the system matrices of systems A and B. When performing integration by parts on the equations involving the kinetic flows, the boundary inputs always act on $\boldsymbol{f}_p$ and never on $\boldsymbol{f}_q$. Thus, it is proposed to maintain the separation of kinetic and potential energy on concatenation. This also facilitates notation in further steps. For both (5.1) and (5.2), the interconnection matrix and input matrix have the following structure

$$\boldsymbol{J} = \begin{bmatrix} \boldsymbol{0} & \boldsymbol{J}_p \\ \boldsymbol{J}_q & \boldsymbol{0} \end{bmatrix}, \quad \boldsymbol{G} = \begin{bmatrix} \boldsymbol{G}_p \\ \boldsymbol{0} \end{bmatrix}. \tag{5.3}$$

When defining the concatenated energy variables as

$$\tilde{\boldsymbol{x}}^{\mathrm{AB}} := \begin{bmatrix} \tilde{\boldsymbol{x}}_p^{\mathrm{B}} \\ \tilde{\boldsymbol{x}}_p^{\mathrm{A}} \\ \tilde{\boldsymbol{x}}_q^{\mathrm{A}} \\ \tilde{\boldsymbol{x}}_q^{\mathrm{B}} \end{bmatrix}, \quad \tilde{\boldsymbol{x}}^{\mathrm{AB}} \in \mathbb{R}^{2n_{\mathrm{A}}+2n_{\mathrm{B}}} \tag{5.4}$$

and the joint boundary input as

$$\boldsymbol{u}_\partial^{\mathrm{AB}} := \begin{bmatrix} \boldsymbol{u}_\partial^{\mathrm{A}} \\ \boldsymbol{u}_\partial^{\mathrm{B}} \end{bmatrix}, \quad \boldsymbol{u}_\partial^{\mathrm{AB}} \in \mathbb{R}^6, \tag{5.5}$$

the resulting joint system matrices become

$$\boldsymbol{J}^{\mathrm{AB}} = \begin{bmatrix} \boldsymbol{0} & \boldsymbol{0} & \boldsymbol{0} & \boldsymbol{J}_p^{\mathrm{B}} \\ \boldsymbol{0} & \boldsymbol{0} & \boldsymbol{J}_p^{\mathrm{A}} & \boldsymbol{0} \\ \boldsymbol{0} & \boldsymbol{J}_q^{\mathrm{A}} & \boldsymbol{0} & \boldsymbol{0} \\ \boldsymbol{J}_q^{\mathrm{B}} & \boldsymbol{0} & \boldsymbol{0} & \boldsymbol{0} \end{bmatrix}, \quad \boldsymbol{G}^{\mathrm{AB}} = \begin{bmatrix} \boldsymbol{0} & \boldsymbol{G}_p^{\mathrm{B}} \\ \boldsymbol{G}_p^{\mathrm{A}} & \boldsymbol{0} \\ \boldsymbol{0} & \boldsymbol{0} \\ \boldsymbol{0} & \boldsymbol{0} \end{bmatrix}. \tag{5.6}$$

This way, the structural separation of energy domains is maintained.

5.2 Formulation of constraint equations

According to Newton's second law of motion, forces and torques at each nodal point of a structure have to sum up to zero for each degree of freedom considered. At the same time, velocities and angular velocities with the same orientation have to be identical. Looking again at the example in Fig. 5.1, this implies

$$v_b^{\mathrm{A}} = v_z^2, \quad v_a^{\mathrm{B}} = \theta_z^5 v_z^2, \tag{5.7}$$

where v_b^{A} is the right boundary velocity in z-direction of system A, v_a^{B} the left boundary velocity in z-direction of the rod and v_z^2 the velocity in z-direction of the second node. The components of the orientation vector of the fifth port $\boldsymbol{\theta}^5$ are depicted in Fig. 5.1. Since the Euler-Bernoulli beam cannot take loads in the x-direction, θ_x^5 does not appear in the formulation of constraints. For the boundary forces F_b^{A} and F_a^{B} it follows

$$F_b^{\mathrm{A}} + \theta_z^5 F_a^{\mathrm{B}} + F_z^2 = 0, \tag{5.8}$$

with the additional contribution of an external force F_z^2 in z-direction.

Since the boundary outputs of the concatenated system include all boundary velocities and angular velocities, (5.7) can be written in a more general fashion. For an arbitrary structure, let $\dot{\boldsymbol{q}} \in \mathbb{R}^{n_{\mathrm{DOF}}}$ denote its vector of global nodal velocities with n_{DOF} the total number of DOFs. It contains a velocity or angular velocity variable for each

DOF. This way, each boundary output can be expressed as a linear combination of entries of $\dot{\boldsymbol{q}}$

$$y_\partial^i = (\boldsymbol{c}_v^i)^{\mathrm{T}} \dot{\boldsymbol{q}}, \quad i = 1 \dots n_u, \tag{5.9}$$

where n_u is the total number of boundary inputs or outputs and $\boldsymbol{c}_v^i \in \mathbb{R}^{n_{\mathrm{DOF}}}$ maps $\boldsymbol{\theta}^i$ to the corresponding nodal velocity or angular velocity. From the relation between $\dot{\boldsymbol{q}}$ and $\boldsymbol{y}_\partial$, algebraic constraints on the state variables $\tilde{\boldsymbol{x}} \in \mathbb{R}^n$, are obtained by eliminating $\dot{\boldsymbol{q}}$. Here, $n = n_p \cdot N_{\mathrm{n}} + n_q \cdot N_{\mathrm{n}}$ is the system order of the concatenated, but uncoupled system. From Section 4.3, recall that n_p denotes the number of potential, n_q the number of kinetic energy variables and N_{n} is the number of approximation nodes. Rewriting (5.9) in matrix form, the following is obtained

$$\boldsymbol{y}_\partial = \boldsymbol{C}_v \dot{\boldsymbol{q}} \quad \Rightarrow \quad \boldsymbol{C}_v^\perp \boldsymbol{y}_\partial = \boldsymbol{0}, \tag{5.10}$$

where $\boldsymbol{C}_v^\perp$ denotes the left annihilator of $\boldsymbol{C}_v \in \mathbb{R}^{n_u \times n_{\mathrm{DOF}}}$. Substituting the output equation of (4.27) into the above, yields algebraic constraints of the form

$$\boldsymbol{0} = \boldsymbol{B}^{\mathrm{T}} \boldsymbol{Q} \tilde{\boldsymbol{x}}. \tag{5.11}$$

For statically determinate structures, the row rank of $\boldsymbol{C}_v^\perp$ is n_{DOF} and it follows that $\boldsymbol{B} \in \mathbb{R}^{n \times n_{\mathrm{c}}}$ with $n_{\mathrm{c}} = n_u - n_{\mathrm{DOF}}$.

In a similar fashion, a generalized expression for (5.8) can be obtained, which is used to reformulate the boundary input $\boldsymbol{u}_\partial \in \mathbb{R}^{n_u}$. For each global DOF, an external force or torque is introduced and they are collected in the vector of external forces and torques $\boldsymbol{f}_{\mathrm{ext}} \in \mathbb{R}^{n_{\mathrm{DOF}}}$. Consequently, each external force or torque can be equated with a linear combination of boundary inputs

$$\begin{aligned} (\boldsymbol{c}_u^j)^{\mathrm{T}} \boldsymbol{u}_\partial &= f_{\mathrm{ext}}^j, \quad j = 1 \dots n_{\mathrm{DOF}} \\ \boldsymbol{C}_u \boldsymbol{u}_\partial &= \boldsymbol{f}_{\mathrm{ext}}. \end{aligned} \tag{5.12}$$

Usually, the number of DOFs is lower than the number of boundary inputs. With n_{DOF} input constraints, this means that free boundary inputs $\boldsymbol{u}_{\mathrm{f}} \in \mathbb{R}^{n_{\mathrm{c}}}$ can be chosen. This enables a reformulation of the input term $\boldsymbol{G}\boldsymbol{u}_\partial$ as

$$\boldsymbol{G}\boldsymbol{u}_\partial = \boldsymbol{G}_{\mathrm{f}} \boldsymbol{u}_{\mathrm{f}} + \boldsymbol{G}_{\mathrm{ext}} \boldsymbol{f}_{\mathrm{ext}}, \tag{5.13}$$

where $\boldsymbol{G}_{\mathrm{f}} \in \mathbb{R}^{n \times n_{\mathrm{c}}}$ is the resulting input matrix of the free inputs $\boldsymbol{u}_{\mathrm{f}}$ and $\boldsymbol{G}_{\mathrm{ext}} \in \mathbb{R}^{n \times n_{\mathrm{DOF}}}$ that of the external forces $\boldsymbol{f}_{\mathrm{ext}}$. Assuming $\boldsymbol{G}_{\mathrm{f}}$ has full row rank, its right inverse $\boldsymbol{G}_{\mathrm{f}}^+ = \boldsymbol{G}_{\mathrm{f}}^{\mathrm{T}} (\boldsymbol{G}_{\mathrm{f}} \boldsymbol{G}_{\mathrm{f}}^{\mathrm{T}})^{-1}$ can be constructed and $\boldsymbol{u}_{\mathrm{f}}$ can be rewritten as

$$\boldsymbol{u}_{\mathrm{f}} = \boldsymbol{G}_{\mathrm{f}}^+ \boldsymbol{B} \boldsymbol{\lambda}, \tag{5.14}$$

where $\boldsymbol{\lambda} \in \mathbb{R}^{n_{\mathrm{c}}}$ are the Lagrange multipliers corresponding to the algebraic constraints (5.11). Given (5.11), (5.13) and (5.14), the coupled structure can be written as a DAE

system

$$\begin{aligned}\dot{\tilde{\boldsymbol{x}}} &= \boldsymbol{J}\boldsymbol{Q}\tilde{\boldsymbol{x}} + \boldsymbol{G}_{\mathrm{ext}}\boldsymbol{f}_{\mathrm{ext}} + \boldsymbol{B}\boldsymbol{\lambda},\\ \dot{\boldsymbol{q}} &= \boldsymbol{G}_{\mathrm{ext}}^{\mathrm{T}}\boldsymbol{Q}\tilde{\boldsymbol{x}},\\ \boldsymbol{0} &= \boldsymbol{B}^{\mathrm{T}}\boldsymbol{Q}\tilde{\boldsymbol{x}},\end{aligned} \tag{5.15}$$

where the collocated outputs to the external force inputs are the global nodal velocities $\dot{\boldsymbol{q}}$. It can be shown that the DAE system (5.15) is of index one, in case the matrix $\boldsymbol{B}^{\mathrm{T}}\boldsymbol{Q}\boldsymbol{B}$ has full rank [109], which is always the case for the systems considered here. Refer to Section 5.6 for more details. In the next section, elimination of the algebraic constraints in order to obtain an ODE formulation of the structural dynamics is shown.

5.3 Algebraic constraint elimination

Systems of the form (5.15) can be reduced to the constrained state space $\mathcal{X}_{\mathrm{c}}$ with uniquely defined dynamics. As a consequence, the algebraic constraints are eliminated. A procedure for doing so is described in detail in e. g. [29] and [140]. The necessary steps are repeated here, to give a complete description of the methodology used to obtain the dynamic equations for arbitrary structure models in ODE form.

In a first step, the transformation

$$\boldsymbol{V} = \begin{bmatrix}\boldsymbol{B}^{\perp}\\ \boldsymbol{B}^{+}\end{bmatrix} \tag{5.16}$$

is introduced. It is composed of both the left annihilator $\boldsymbol{B}^{\perp} \in \mathbb{R}^{n-n_{\mathrm{c}}\times n}$ and the left inverse $\boldsymbol{B}^{+} \in \mathbb{R}^{n_{\mathrm{c}}\times n}$ of $\boldsymbol{B}$. Left-multiplying the uppermost equation in (5.15) with $\boldsymbol{V}$ and defining a new state vector $\boldsymbol{z} := \boldsymbol{V}\tilde{\boldsymbol{x}}, \boldsymbol{z} \in \mathbb{R}^{n}$, yields

$$\dot{\boldsymbol{z}} = \boldsymbol{V}\boldsymbol{J}\boldsymbol{Q}\tilde{\boldsymbol{x}} + \boldsymbol{V}\boldsymbol{G}_{\mathrm{ext}}\boldsymbol{f}_{\mathrm{ext}} + \begin{bmatrix}\boldsymbol{0}\\ \boldsymbol{I}\end{bmatrix}\boldsymbol{\lambda}. \tag{5.17}$$

To retain the port-Hamiltonian form, the term $\boldsymbol{Q}\tilde{\boldsymbol{x}}$ needs to be replaced with the gradient of the Hamiltonian H with respect to $\boldsymbol{z}$

$$\begin{aligned}\nabla_{\boldsymbol{z}}H &= \left(\frac{\partial\tilde{\boldsymbol{x}}}{\partial\boldsymbol{z}}\right)^{\mathrm{T}}\nabla_{\tilde{\boldsymbol{x}}}H,\\ &= \boldsymbol{V}^{-\mathrm{T}}\boldsymbol{Q}\boldsymbol{V}^{-1}\boldsymbol{z},\\ &= \tilde{\boldsymbol{Q}}\boldsymbol{z}.\end{aligned} \tag{5.18}$$

Defining $\tilde{\boldsymbol{J}} := \boldsymbol{V}\boldsymbol{J}\boldsymbol{V}^{\mathrm{T}}$ and $\tilde{\boldsymbol{G}}_{\mathrm{ext}} := \boldsymbol{V}\boldsymbol{G}_{\mathrm{ext}}$ and dividing $\boldsymbol{z}$ into $\boldsymbol{z}_1 \in \mathbb{R}^{n-n_c}$ and $\boldsymbol{z}_2 \in \mathbb{R}^{n_c}$, the system can be reformulated as follows

$$\begin{aligned}
\begin{bmatrix}\dot{\boldsymbol{z}}_1\\ \dot{\boldsymbol{z}}_2\end{bmatrix} &= \begin{bmatrix}\tilde{\boldsymbol{J}}_{11} & \tilde{\boldsymbol{J}}_{12}\\ \tilde{\boldsymbol{J}}_{21} & \tilde{\boldsymbol{J}}_{22}\end{bmatrix}\begin{bmatrix}\tilde{\boldsymbol{Q}}_{11} & \tilde{\boldsymbol{Q}}_{12}\\ \tilde{\boldsymbol{Q}}_{21} & \tilde{\boldsymbol{Q}}_{22}\end{bmatrix}\begin{bmatrix}\boldsymbol{z}_1\\ \boldsymbol{z}_2\end{bmatrix} + \begin{bmatrix}\tilde{\boldsymbol{G}}_{\mathrm{ext},1}\\ \tilde{\boldsymbol{G}}_{\mathrm{ext},2}\end{bmatrix}\boldsymbol{f}_{\mathrm{ext}} + \begin{bmatrix}\boldsymbol{0}\\ \boldsymbol{I}\end{bmatrix}\boldsymbol{\lambda},\\
\dot{\boldsymbol{q}} &= \begin{bmatrix}\tilde{\boldsymbol{G}}_{\mathrm{ext},1}^{\mathrm{T}} & \tilde{\boldsymbol{G}}_{\mathrm{ext},2}^{\mathrm{T}}\end{bmatrix}\begin{bmatrix}\tilde{\boldsymbol{Q}}_{11} & \tilde{\boldsymbol{Q}}_{12}\\ \tilde{\boldsymbol{Q}}_{21} & \tilde{\boldsymbol{Q}}_{22}\end{bmatrix}\begin{bmatrix}\boldsymbol{z}_1\\ \boldsymbol{z}_2\end{bmatrix},\\
\boldsymbol{0} &= \begin{bmatrix}\boldsymbol{0} & \boldsymbol{I}\end{bmatrix}\begin{bmatrix}\tilde{\boldsymbol{Q}}_{11} & \tilde{\boldsymbol{Q}}_{12}\\ \tilde{\boldsymbol{Q}}_{21} & \tilde{\boldsymbol{Q}}_{22}\end{bmatrix}\begin{bmatrix}\boldsymbol{z}_1\\ \boldsymbol{z}_2\end{bmatrix}.
\end{aligned} \tag{5.19}$$

The third equation implies $\nabla_{\boldsymbol{z}_2} H = 0$ and that $\boldsymbol{z}_2$ can be expressed as

$$\boldsymbol{z}_2 = -\tilde{\boldsymbol{Q}}_{22}^{-1}\tilde{\boldsymbol{Q}}_{21}\boldsymbol{z}_1. \tag{5.20}$$

Therefore, the system dynamics on the constrained state space $\mathcal{X}_{\mathrm{c}}$ are given as

$$\begin{aligned}
\dot{\boldsymbol{z}}_1 &= \tilde{\boldsymbol{J}}_{11}(\tilde{\boldsymbol{Q}}_{11} - \tilde{\boldsymbol{Q}}_{12}\tilde{\boldsymbol{Q}}_{22}^{-1}\tilde{\boldsymbol{Q}}_{21})\boldsymbol{z}_1 + \tilde{\boldsymbol{G}}_{\mathrm{ext},1}\boldsymbol{f}_{\mathrm{ext}},\\
\dot{\boldsymbol{q}} &= \tilde{\boldsymbol{G}}_{\mathrm{ext},1}^{\mathrm{T}}(\tilde{\boldsymbol{Q}}_{11} - \tilde{\boldsymbol{Q}}_{12}\tilde{\boldsymbol{Q}}_{22}^{-1}\tilde{\boldsymbol{Q}}_{21})\boldsymbol{z}_1.
\end{aligned} \tag{5.21}$$

Due to the separation of energy and co-energy related terms according to (5.6), the interconnection matrix $\tilde{\boldsymbol{J}}_{11}$ of the ODE system now has the following structure

$$\tilde{\boldsymbol{J}}_{11} = \begin{bmatrix}\boldsymbol{0} & \tilde{\boldsymbol{J}}_p\\ -\tilde{\boldsymbol{J}}_p^{\mathrm{T}} & \boldsymbol{0}\end{bmatrix}, \tag{5.22}$$

with $\tilde{\boldsymbol{J}}_p \in \mathbb{R}^{(n_p\cdot N_{\mathrm{n}}-n_c)\times(n-n_c)}$ and $(n_p - n_c) = n_{\mathrm{DOF}}$. Since the external forces $\boldsymbol{f}_{\mathrm{ext}}$ and the constraint forces $\boldsymbol{\lambda}$ in (5.15) act on $\tilde{\boldsymbol{x}}_p$ only, the transformation (5.16) retains $\tilde{\boldsymbol{x}}_q \in \mathbb{R}^{n_q\cdot N_{\mathrm{n}}}$ in the new state $\boldsymbol{z}_1$.

5.4 Elimination of linearly dependent states

With $\tilde{\boldsymbol{x}}_q$ retained in the state vector $\boldsymbol{z}_1$, the system dynamics of the reduced order ODE system can be formulated as follows, using $\boldsymbol{z}_1^{\mathrm{T}} = \begin{bmatrix}\boldsymbol{z}_p^{\mathrm{T}} & \tilde{\boldsymbol{x}}_q^{\mathrm{T}}\end{bmatrix}$

$$\begin{aligned}
\begin{bmatrix}\dot{\boldsymbol{z}}_p\\ \dot{\tilde{\boldsymbol{x}}}_q\end{bmatrix} &= \begin{bmatrix}\boldsymbol{0} & \tilde{\boldsymbol{J}}_p\\ -\tilde{\boldsymbol{J}}_p^{\mathrm{T}} & \boldsymbol{0}\end{bmatrix}\begin{bmatrix}\tilde{\boldsymbol{Q}}_p & \boldsymbol{0}\\ \boldsymbol{0} & \boldsymbol{Q}_q\end{bmatrix}\begin{bmatrix}\boldsymbol{z}_p\\ \tilde{\boldsymbol{x}}_q\end{bmatrix} + \begin{bmatrix}\tilde{\boldsymbol{G}}_{\mathrm{ext},p}\\ \boldsymbol{0}\end{bmatrix}\boldsymbol{f}_{\mathrm{ext}},\\
\dot{\boldsymbol{q}} &= \begin{bmatrix}\tilde{\boldsymbol{G}}_{\mathrm{ext},p}^{\mathrm{T}} & \boldsymbol{0}\end{bmatrix}\begin{bmatrix}\tilde{\boldsymbol{Q}}_p & \boldsymbol{0}\\ \boldsymbol{0} & \boldsymbol{Q}_q\end{bmatrix}\begin{bmatrix}\boldsymbol{z}_p\\ \tilde{\boldsymbol{x}}_q\end{bmatrix}.
\end{aligned} \tag{5.23}$$

In this representation, it is evident that the $n_q \cdot N_{\mathrm{n}}$ state derivatives $\dot{\tilde{\boldsymbol{x}}}_q$ are linearly dependent since they are computed using a reduced number of potential energy

variables $\boldsymbol{z}_p \in \mathbb{R}^{n_{\mathrm{DOF}}}$. For ease of notation, let $n_p = n_q$ in the following, without loss of generality, as long as $n_q \cdot N_{\mathrm{n}} > n_p \cdot N_{\mathrm{n}} - n_c$. Constructing an orthonormal basis $\boldsymbol{T}_q$ of $-\tilde{\boldsymbol{J}}_p^{\mathrm{T}}$, such that

$$\tilde{\boldsymbol{x}}_q = \boldsymbol{T}_q \boldsymbol{z}_q, \tag{5.24}$$

no redundant states are retained in $\boldsymbol{z}_q \in \mathbb{R}^{n_{\mathrm{DOF}}}$. The effort variables $\tilde{\boldsymbol{e}}_q \in \mathbb{R}^{n_q \cdot N_{\mathrm{n}}}$ are then related to $\boldsymbol{z}_q$ as follows

$$\tilde{\boldsymbol{e}}_q = \nabla_{\tilde{\boldsymbol{x}}_q} H(\boldsymbol{z}_1) = \boldsymbol{Q}_q \tilde{\boldsymbol{x}}_q = \boldsymbol{Q}_q \boldsymbol{T}_q \boldsymbol{z}_q. \tag{5.25}$$

This allows a formulation of algebraic constraints on $\tilde{\boldsymbol{e}}_q$ using $\boldsymbol{B}^* = \ker\left[(\boldsymbol{Q}_q \boldsymbol{T}_q)^{\mathrm{T}}\right]$ such that

$$(\boldsymbol{B}^*)^{\mathrm{T}} \boldsymbol{Q}_q \tilde{\boldsymbol{x}}_q = \boldsymbol{0}. \tag{5.26}$$

The constraints defined by (5.26) are of the the same form as the constraints (5.11). Therefore, the procedure described in the previous section can be followed once again in order to project (5.23) to a new constrained manifold. This results in the elimination of linearly dependent efforts or rather state variables. Afterward, the system (5.23) is expressed in the new coordinates $\bar{\boldsymbol{z}}^{\mathrm{T}} = \begin{bmatrix} \boldsymbol{z}_p^{\mathrm{T}} & \boldsymbol{z}_q^{\mathrm{T}} \end{bmatrix}$ as

$$\begin{aligned} \dot{\bar{\boldsymbol{z}}} &= \bar{\boldsymbol{J}} \bar{\boldsymbol{Q}} \bar{\boldsymbol{z}} + \bar{\boldsymbol{G}}_{\mathrm{ext}} \boldsymbol{f}_{\mathrm{ext}}, \\ \dot{\boldsymbol{q}} &= \bar{\boldsymbol{G}}_{\mathrm{ext}}^{\mathrm{T}} \bar{\boldsymbol{Q}} \bar{\boldsymbol{z}}, \end{aligned} \tag{5.27}$$

with $\bar{\boldsymbol{z}} \in \mathbb{R}^{2n_{\mathrm{DOF}}}$. Note that the reduced order system (5.27) is of the same order as the second order mechanical system in ISO port-Hamiltonian form (4.46), given the global DOFs $\boldsymbol{q}$ are identical. Since the potential energy variables $\boldsymbol{z}_q$ are not uniquely defined, the coordinates $\boldsymbol{z}_p$ and $\boldsymbol{z}_q$ span the same space, but their physical meaning cannot be necessarily grasped. In the next section, it is shown how to transform (5.27) to obtain the dynamics in global coordinates.

5.5 Transformation to global coordinates

In the following, assume that (4.46) – without the damping term – and (5.27) describe the same system. In this case, (4.46) with $\boldsymbol{R} = \boldsymbol{0}$ can be obtained from (5.27) by means of two consecutive transformations. With the first transformation

$$\boldsymbol{T}_u = \begin{bmatrix} \bar{\boldsymbol{G}}_{\mathrm{ext}}^{+} \\ \bar{\boldsymbol{G}}_{\mathrm{ext}}^{\perp} \end{bmatrix}, \tag{5.28}$$

where $\bar{\boldsymbol{G}}_{\mathrm{ext}}^{+}, \bar{\boldsymbol{G}}_{\mathrm{ext}}^{\perp} \in \mathbb{R}^{n_{\mathrm{DOF}} \times n_{\mathrm{DOF}}}$, a normalization of (5.27) with respect to the input $\boldsymbol{f}_{\mathrm{ext}}$ is achieved. It is applied as follows

$$\boldsymbol{T}_u \dot{\bar{\boldsymbol{z}}} = \boldsymbol{T}_u \bar{\boldsymbol{J}} \boldsymbol{T}_u^{\mathrm{T}} \boldsymbol{T}_u^{-\mathrm{T}} \bar{\boldsymbol{Q}} \boldsymbol{T}_u^{-1} \boldsymbol{T}_u \bar{\boldsymbol{z}} + \boldsymbol{T}_u \bar{\boldsymbol{G}}_{\mathrm{ext}} \boldsymbol{f}_{\mathrm{ext}}. \tag{5.29}$$

Since $\boldsymbol{T}_u\bar{\boldsymbol{G}}_{\text{ext}} = \begin{bmatrix}\boldsymbol{I} & \boldsymbol{0}\end{bmatrix}^{\mathrm{T}}$, it follows that $\boldsymbol{T}_u\dot{\tilde{\boldsymbol{z}}} = \begin{bmatrix}(\boldsymbol{M}\ddot{\boldsymbol{q}})^{\mathrm{T}} & \dot{\tilde{\boldsymbol{z}}}_q^{\mathrm{T}}\end{bmatrix}^{\mathrm{T}}$, which results in

$$\begin{aligned}\begin{bmatrix}\boldsymbol{M}\ddot{\boldsymbol{q}}\\ \dot{\tilde{\boldsymbol{z}}}_q\end{bmatrix} &= \underbrace{\begin{bmatrix}\boldsymbol{0} & \bar{\boldsymbol{P}}\\ -\bar{\boldsymbol{P}}^{\mathrm{T}} & \boldsymbol{0}\end{bmatrix}}_{\boldsymbol{T}_u\bar{\boldsymbol{J}}\boldsymbol{T}_u^{\mathrm{T}}}\underbrace{\begin{bmatrix}\boldsymbol{M}^{-1} & \boldsymbol{0}\\ \boldsymbol{0} & \bar{\boldsymbol{S}}\end{bmatrix}}_{\boldsymbol{T}_u^{-\mathrm{T}}\bar{\boldsymbol{Q}}\boldsymbol{T}_u^{-1}}\begin{bmatrix}\boldsymbol{M}\dot{\boldsymbol{q}}\\ \tilde{\boldsymbol{z}}_q\end{bmatrix} + \begin{bmatrix}\boldsymbol{I}\\ \boldsymbol{0}\end{bmatrix}\boldsymbol{f}_{\text{ext}},\\ \dot{\boldsymbol{q}} &= \begin{bmatrix}\boldsymbol{I} & \boldsymbol{0}\end{bmatrix}\begin{bmatrix}\boldsymbol{M}^{-1} & \boldsymbol{0}\\ \boldsymbol{0} & \bar{\boldsymbol{S}}\end{bmatrix}\begin{bmatrix}\boldsymbol{M}\dot{\boldsymbol{q}}\\ \tilde{\boldsymbol{z}}_q\end{bmatrix},\end{aligned} \tag{5.30}$$

with $\boldsymbol{I}, \boldsymbol{M}, \bar{\boldsymbol{P}}, \bar{\boldsymbol{S}} \in \mathbb{R}^{n_{\text{DOF}}\times n_{\text{DOF}}}$. The final step to obtain (4.46) is the construction of a second transformation

$$\boldsymbol{T}_p = \begin{bmatrix}\boldsymbol{I} & \boldsymbol{0}\\ \boldsymbol{0} & (-\bar{\boldsymbol{P}}^{\mathrm{T}})^{+}\end{bmatrix}, \quad \text{with } \boldsymbol{T}_p\boldsymbol{T}_u\bar{\boldsymbol{J}}\boldsymbol{T}_u^{\mathrm{T}}\boldsymbol{T}_p^{\mathrm{T}} = \begin{bmatrix}\boldsymbol{0} & -\boldsymbol{I}\\ \boldsymbol{I} & \boldsymbol{0}\end{bmatrix}. \tag{5.31}$$

When $\boldsymbol{T}_p$ is applied to (5.30) in the same fashion as $\boldsymbol{T}_u$ in (5.29), it follows that the transformed system must be identical to (4.46) with $\boldsymbol{R} = \boldsymbol{0}$. Note that the second transformation (5.31) can only be applied as long as the stiffness matrix $\boldsymbol{K}$ in (4.46) is nonsingular. In case $\boldsymbol{K}$ is singular, so is $\boldsymbol{T}_p$ and it is advisable to skip the second step in the transformation to global coordinates.

If $\boldsymbol{D}$ in (4.12) is a Rayleigh or Caughey type damping term, $\boldsymbol{R}$ can now be easily constructed from $\boldsymbol{M}$ and $\boldsymbol{K}$. It is also possible to add Rayleigh damping before the system assembly process or in any stage of the process as long as the structural separation of kinetic and potential terms is maintained. This done by converting the system to a second-order form as e. g. explained in [23]. Other types of damping might involve adding dissipation terms on the PDE level, but this is not considered here.

5.6 Coupling with other domains

Even though the methods in this section are intended for the assembly of mechanical systems, most of them can be applied to systems from other domains as well. Maintaining the separation of energy domains on concatenation of system matrices can also be advantageous for non-mechanical systems. When the spatial orientation of the ports is irrelevant, the generation of constraints simplifies, but can otherwise be carried out in the same fashion. In that case, transformation to a set of global coordinates is not necessary.

Constraint elimination and the elimination of linear dependent states are domain-independent procedures but require the systems to be linear. For nonlinear systems, such as the hydraulic actuators presented in Chapter 6, constraints for the mechanical ports can still be generated according to approach described in Section 5.2. However, an automated procedure for their elimination cannot be formulated in the general

case. It is still possible to obtain an explicit system of equations by solving for the Lagrange multipliers (see e. g. [37] and [109]). Consider a nonlinear system in input-state-output-form (2.34). Taking the derivative of (2.34c) with respect to time, results in

$$\mathbf{0} = \boldsymbol{B}^{\mathrm{T}}(\boldsymbol{x}) \frac{\partial^2 H}{\partial \boldsymbol{x}^2}(\boldsymbol{x}) \dot{\boldsymbol{x}} \tag{5.32}$$

$$= \boldsymbol{B}^{\mathrm{T}}(\boldsymbol{x}) \frac{\partial^2 H}{\partial \boldsymbol{x}^2}(\boldsymbol{x}) \left([\boldsymbol{J}(\boldsymbol{x}) - \boldsymbol{R}(\boldsymbol{x})] \frac{\partial H}{\partial \boldsymbol{x}}(\boldsymbol{x}) + \boldsymbol{G}(\boldsymbol{x})\boldsymbol{u} + \boldsymbol{B}(\boldsymbol{x})\boldsymbol{\lambda} \right). \tag{5.33}$$

As long as the matrix $\boldsymbol{B}^{\mathrm{T}}(\boldsymbol{x}) \frac{\partial^2 H}{\partial \boldsymbol{x}^2}(\boldsymbol{x}) \boldsymbol{B}(\boldsymbol{x})$ has full rank for all $\boldsymbol{x} \in \mathcal{X}_c$, where $\mathcal{X}_c$ denotes the constrained state space, the above can be solved for the Lagrange multipliers

$$\boldsymbol{\lambda} = - \left(\boldsymbol{B}^{\mathrm{T}}(\boldsymbol{x}) \frac{\partial^2 H}{\partial \boldsymbol{x}^2}(\boldsymbol{x}) \boldsymbol{B}(\boldsymbol{x}) \right)^{-1} \boldsymbol{B}(\boldsymbol{x}) \frac{\partial^2 H}{\partial \boldsymbol{x}^2}(\boldsymbol{x}) \left(\boldsymbol{J}(\boldsymbol{x}) \frac{\partial H}{\partial \boldsymbol{x}}(\boldsymbol{x}) + \boldsymbol{G}(\boldsymbol{x})\boldsymbol{u} \right). \tag{5.34}$$

For linear systems, $\frac{\partial^2 H}{\partial \boldsymbol{x}^2}(\boldsymbol{x}) = \boldsymbol{Q}$. Numerical simulation of (2.34) is possible using explicit integration methods when the coupling forces $\boldsymbol{\lambda}$ can be computed according to (5.34).

6 Hydraulic actuators

Integration of actuators and sensors into the load-carrying structure renders it adaptive. Not just any type of actuator can be used for this purpose since the active manipulation of a structure requires considerable forces or certain maximum strokes. As discussed in [138], linear direct drives and hydraulic actuators meet the requirements. Hydraulic actuators, however, are considered more efficient. In the CRC 1244, hydraulic cylinders therefore are the active devices of choice.

A port-Hamiltonian model of a generic hydraulic piston actuator is introduced in the following. Some basic thermodynamics are recalled first in Section 6.1. With the definition of the internal energy and the dynamic equations of a fluid compartment at hand, the actuator model is derived in Section 6.2. The chapter closes with Section 6.3, where a simulation of an adaptive frame structure equipped with hydraulic actuators is presented.

6.1 Fundamentals of hydraulic systems

A few thermodynamic basics have to be recalled in order to arrive at port-Hamiltonian representations of hydraulic systems. The writing of this section was mostly influenced by [65] and [75]. See especially the first reference for a more detailed introduction to hydraulic servo-systems in general.

The first law of thermodynamics, which can be stated as

$$dU = \delta Q - \delta W, \tag{6.1}$$

states that the internal energy U of a closed system can be changed by a transfer of heat Q to the system and by the system performing work W on its surroundings. Here, δQ denotes the *inexact* differential (i. e. a differential 1-form) of Q. As opposed to the exact differential $\mathrm{d}U$, it is path-dependent. Let us also recall the second law

$$\vartheta \mathrm{d}S \geq \delta Q, \tag{6.2}$$

with S the entropy of the system and ϑ its temperature. For a reversible process, the above becomes $\delta Q = \vartheta \mathrm{d}S$. If it is further assumed that the system performs only work of expansion, then $\delta W = p\mathrm{d}V$, where p is the pressure and V the volume of the system. In this case, the first law of thermodynamics (6.1) simplifies to

$$\mathrm{d}U = \vartheta \mathrm{d}S - p\mathrm{d}V. \tag{6.3}$$

In the following, only *adiabatic* systems, i. e. systems that do not exchange heat with the environment such that $\delta Q = 0$, will be considered. Adiabatic processes are also always *isentropic* with the entropy S being constant. Introducing the specific internal energy $u = U/m$ and the specific volume $v = V/m$, where m is the mass of the substance in the system, (6.3) becomes

$$\mathrm{d}u = -p\mathrm{d}v = -p\mathrm{d}(\rho^{-1}) = \frac{p}{\rho^2}\mathrm{d}\rho, \tag{6.4}$$

for an isentropic and adiabatic system. The density of the substance is denoted by $\rho = 1/v$. Now, the internal energy can be calculated by integration of the above

$$U = mu = \int_{\rho} \frac{p(\tilde{\rho})}{\tilde{\rho}^2} \mathrm{d}\tilde{\rho}. \tag{6.5}$$

To obtain a closed-form expression for u, an explicit relationship between ρ and p needs to be established. In classical hydraulics, this is done by linearizing the bulk modulus β of the hydraulic fluid such that, at a constant temperature T,

$$\rho \left(\frac{\partial p}{\partial \rho} \right) \Big|_T = \beta. \tag{6.6}$$

Integrating the above along an isentrope, p is obtained in terms of ρ as

$$p(\rho) = p_0 + \beta \ln \left(\frac{\rho}{\rho_0} \right), \quad \text{with } p_0 = p(\rho_0). \tag{6.7}$$

Solving this expression for ρ yields the reverse relation

$$\rho(p) = \rho_0 \exp \left(\frac{p - p_0}{\beta} \right), \quad \text{with } \rho_0 = \rho(p_0). \tag{6.8}$$

Subsequently, it is assumed that $p_0 = 0$ such that ρ_0 becomes the density at zero pressure. Then, carrying out the integration in (6.5) using (6.7) results in a specific internal energy of

$$u(p) = -\frac{p + \beta}{\rho_0} \exp \left(\frac{-p}{\beta} \right). \tag{6.9}$$

Consequently, the internal energy U can be expressed as

$$U(p) = V \rho(p) u(p) = V \left(\beta \left(\exp \left(\frac{p}{\beta} \right) - 1 \right) - p \right). \tag{6.10}$$

For the dynamics of a hydraulic system, consider the mass conservation equation [65]

$$\sum \dot{m}_{\text{in}} - \sum \dot{m}_{\text{out}} = \frac{\mathrm{d}(\rho V)}{\mathrm{d}t} = \rho \dot{V} + V \dot{\rho}, \tag{6.11}$$

where $\dot{m}_{\text{in}}$ denotes the flow of mass into the system and $\dot{m}_{\text{out}}$ the reverse. Using the time derivative of (6.8) and dividing the expression by ρ, results in the pressure dynamics

$$\dot{p} = \frac{\beta}{V} \left(\sum \dot{q}_{\text{in}} - \sum \dot{q}_{\text{out}} - \dot{V} \right), \tag{6.12}$$

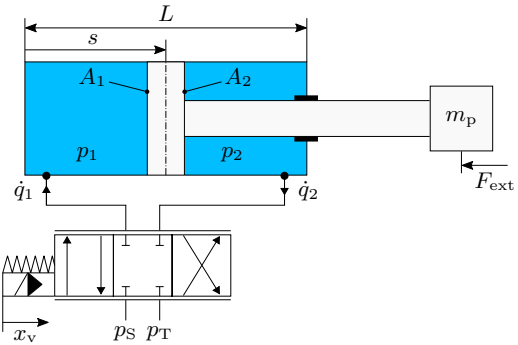

Figure 6.1: Double-acting hydraulic piston actuator of length L connected to a three-land four-way valve. An external force F_{ext} acts on the piston with mass m_{p} and position s. The pressures p_1 and p_2 in the two chambers are also influenced by the volumetric flows $\dot{q}_1$ and $\dot{q}_2$ between actuator and hydraulic power supply.

where $\dot{q}$ denotes a volume flow. If the fluidic compartment whose dynamics are described by (6.12) is connected to a spool valve, the flow through the valve orifices can be described by the following equation

$$\dot{q}_{\text{v}} = k_{\text{v}} x_{\text{v}} \sqrt{|\Delta p|}\, \text{sign}(\Delta p). \tag{6.13}$$

Here, k_{v} is the valve coefficient, x_{v} with $-1 \leq x_{\text{v}} \leq 1$ the normalized spool position and Δp the pressure difference between the valve ports. Depending on the type of the valve and what its outlets are connected to, more specific expressions for q_{v} can be stated.

6.2 Double-acting piston actuator

The writing of this section is again guided by the work of Kugi and Kemmetmüller presented in [75, 76]. Consider the double-acting valve-controlled hydraulic piston actuator depicted in Fig. 6.1. Its cylinder chambers are connected to a three-way four-land valve, which in turn is connected to a hydraulic power supply that provides the supply pressure p_{S} and a reservoir with the tank pressure p_{T}. Considering (6.13),

the volumetric flows into an out of the cylinder chambers can be expressed as

$$\dot{q}_1 = \Gamma_1 x_\mathrm{v} = \begin{cases} k_\mathrm{v}\sqrt{p_\mathrm{S} - p_1}x_\mathrm{v} & \text{for } x_\mathrm{v} \geq 0 \\ k_\mathrm{v}\sqrt{p_1 - p_\mathrm{T}}x_\mathrm{v} & \text{for } x_\mathrm{v} < 0 \end{cases}, \tag{6.14}$$

$$\dot{q}_2 = \Gamma_2 x_\mathrm{v} = \begin{cases} k_\mathrm{v}\sqrt{p_2 - p_\mathrm{T}}x_\mathrm{v} & \text{for } x_\mathrm{v} \geq 0 \\ k_\mathrm{v}\sqrt{p_\mathrm{S} - p_2}x_\mathrm{v} & \text{for } x_\mathrm{v} < 0 \end{cases}, \tag{6.15}$$

where p_1 and p_2 are the respective chamber pressures. For the pressure dynamics in the two cylinder chambers, (6.12) may be used, which results in

$$\dot{p}_1 = \frac{\beta}{A_1 s}(-\frac{A_1}{m_\mathrm{p}}p_\mathrm{p} + \Gamma_1 x_\mathrm{v}), \tag{6.16a}$$

$$\dot{p}_2 = \frac{\beta}{A_2(L-s)}(\frac{A_2}{m_\mathrm{p}}p_\mathrm{p} - \Gamma_2 x_\mathrm{v}). \tag{6.16b}$$

Here L denotes the cylinder length and A_1 and A_2 the cross-sectional area of the chambers, respectively. The piston position is denoted by s and $p_\mathrm{p} = m_\mathrm{p}\dot{s}$ the corresponding momentum, where m_p is the piston mass. Recall that in the port-Hamiltonian context, the impulse is commonly chosen over the velocity as a state variable. The piston dynamics are obtained by considering the force balance for the piston, which yields

$$\dot{s} = \frac{1}{m_\mathrm{p}}p_\mathrm{p}, \quad \dot{p}_\mathrm{p} = p_1 A_1 - p_2 A_2 - F_\mathrm{ext}, \tag{6.17}$$

where F_ext is an external force acting on the piston, as illustrated in Fig. 6.1.

To formulate (6.16) and (6.17) in port-Hamiltonian form, the system energy needs to be taken into account. With the internal energy of each chamber given by (6.10), respectively, the system Hamiltonian is obtained as

$$H = U_1 + U_2 + \frac{1}{2m_\mathrm{p}}p_\mathrm{p}^2. \tag{6.18}$$

The kinetic energy of the fluid is assumed negligible. Everything necessary for the formulation of the actuator dynamics as a nonlinear port-Hamiltonian system has now been defined. Choosing the state vector as $\boldsymbol{x}^\mathrm{T} = \begin{bmatrix} s & p_\mathrm{p} & p_1 & p_2 \end{bmatrix}$ and the input as $\boldsymbol{u}^\mathrm{T} = \begin{bmatrix} x_\mathrm{v} & F_\mathrm{ext} \end{bmatrix}$, Eqs. (6.16) and (6.17) can be rewritten as

$$\begin{aligned} \dot{\boldsymbol{x}} &= \boldsymbol{J}(\boldsymbol{x})\frac{\partial H}{\partial \boldsymbol{x}}(\boldsymbol{x}) + \boldsymbol{g}(\boldsymbol{x})\boldsymbol{u}, \\ \boldsymbol{y} &= \boldsymbol{g}^\mathrm{T}(\boldsymbol{x})\frac{\partial H}{\partial \boldsymbol{x}}(\boldsymbol{x}), \end{aligned} \tag{6.19}$$

where

$$\boldsymbol{J}(\boldsymbol{x}) = \begin{bmatrix} 0 & 1 & 0 & 0 \\ -1 & 0 & \frac{\beta}{s} & -\frac{\beta}{L-s} \\ 0 & -\frac{\beta}{s} & 0 & 0 \\ 0 & \frac{\beta}{L-s} & 0 & 0 \end{bmatrix}, \quad \boldsymbol{g}(\boldsymbol{x}) = \begin{bmatrix} 0 & 0 \\ 0 & -1 \\ \frac{\beta}{A_1 s}\Gamma_1 & 0 \\ -\frac{\beta}{A_2(L-s)}\Gamma_2 & 0 \end{bmatrix}. \tag{6.20}$$

When taking the gradient of H with respect to $\boldsymbol{x}$, the effort variables are obtained as

$$\frac{\partial H}{\partial \boldsymbol{x}} = \boldsymbol{e}(\boldsymbol{x}) = \begin{bmatrix} F_\mathrm{h}(p_1, p_2) & \dot{s} & \Delta V_1(s, p_1) & \Delta V_2(s, p_2) \end{bmatrix}^\mathrm{T}, \tag{6.21}$$

where F_h denotes the hydraulic force resulting from a change in pressure only and $\Delta V_1, \Delta V_2$ the change in chamber volume, respectively. The system output y_1 corresponding to $u_1 = x_\mathrm{v}$ is a quantity related to the differential pressure between the chambers, while $y_2 = \dot{s}$. As remarked in [76], the presented model can be used for both single- and double-ended, as well as single- and double-acting cylinders.

6.3 Simulation of an adaptive frame structure

A prototype frame was built to validate the actuation concepts developed in the CRC 1244 before beginning with the construction of the high-rise demonstrator. The prototype is depicted in Fig. 6.2 in both a picture and a schematic drawing. In the latter, the integration of the hydraulic actuators is visible with one of them installed in the left support and the other in a diagonal bracing. Since the bracing yields to compressive forces, its actuator can only perform a pulling action. In the following, a simulation of the frame using the model introduced in Section 6.2 is presented.

Not only was the structure in Fig. 6.2 a successful means to evaluate the active elements of the high-rise demonstrator before their full-scale implementation – it is also available as an experimentation platform. In a joint publication [54] with colleagues from the Institute of Applied Optics (ITO), their precise camera-based deformation measurement system was tested under real-world conditions on the prototype. It tracks the position of the emitters depicted in Fig. 6.2 a). A simplified model, in which the hydraulic actuators are represented by force inputs, was used for estimating the displacements of the frame using strain gauge measurements. The camera-based measurements were in good agreement with both the model-based estimates and a laser Doppler vibrometer (LDV) reference. The interested reader is referred to [54] for details.

Aim of this section is to show that the model introduced in Section 6.2 can be used in case the dynamics of the hydraulic actuators installed in the prototype frame are not neglected. This section is basically a reproduction of the simulation presented in [135] supplemented with additional details on the prototype frame. A slightly simplified

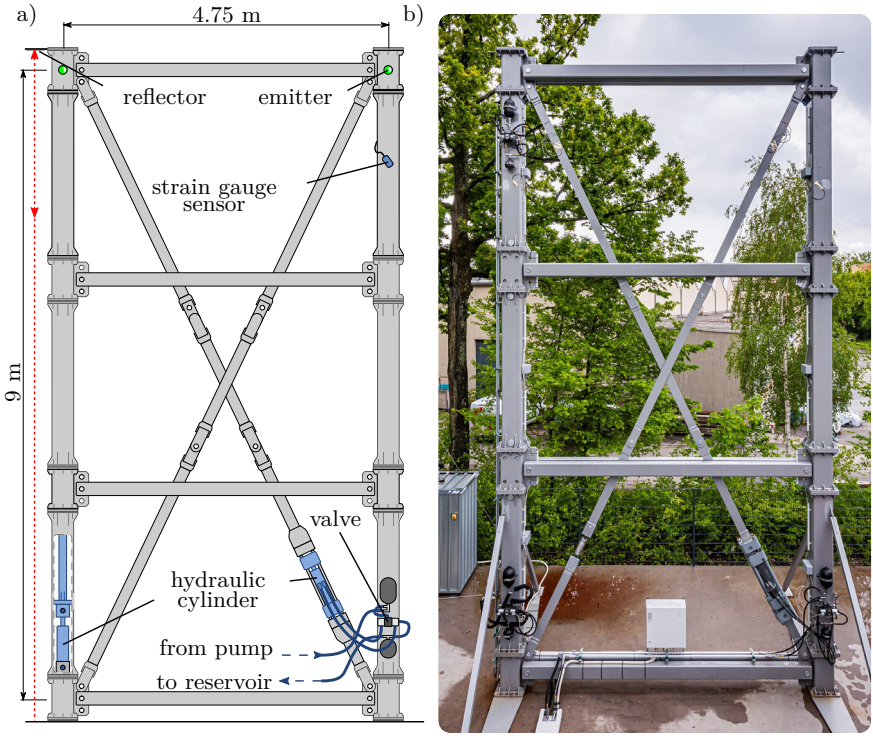

Figure 6.2: Adaptive structures prototype frame in a) a schematic drawing and b) a picture of the realization on campus [54]

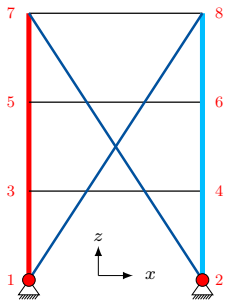

Figure 6.3: Prototype frame (see Fig. 6.2) with parallel hydraulic cylinder (red) [135]

model of the structure is considered in the following. The nonlinear behavior of the diagonal bracings on compression is neglected. Furthermore, the actuator attached to the diagonal that is visible in Fig. 6.2 is also not included.

With these simplifications, the mechanical part of the prototype frame can be modeled using beam elements and rods only. A schematic illustration of the frame model is depicted in Fig. 6.3. Vertical columns (three on each side) are modeled as beams, all other mechanical elements as rods. A double-acting hydraulic piston actuator according to Section 6.2 is connected in parallel to the left supports acting across all three stories. Its parameters are listed in Tab. 6.1. Since the prototype frame represents a part of the high-rise demonstrator, the parameters of the mechanical structure are the same as those assumed in simulations of the full-scale building. Refer to Section 8.2 and Tab. 8.2, where details on materials and geometry are specified.

Coupling of the frame and the cylinder is done as described in Section 5.6, which produces system of the form (5.15). It can be converted to an explicit representation by solving for the Lagrange multipliers $\boldsymbol{\lambda}$. A simulation of the coupled multi-domain system is shown in Fig. 6.4, where the valve displacement x_v follows a sinusoidal excitation.

In Fig. 6.4 a), the x- and z-displacements of the topmost nodes of the frame are shown, whereas Fig. 6.4 b) depicts the chamber pressures and the piston displacement Δs. The coupling between piston displacement and the motion of the frame is immediately visible. Comparing the z-displacement of node 7 in Fig. 6.3 a) with Δs in Fig. 6.3 b), especially at the peaks at $t = 0.5\,\mathrm{s}$ and $t = 1.0\,\mathrm{s}$, shows that they are identical. If the frame dynamics are modeled with a regular FEM approach and the hydraulic cylinder separately in the hydraulic domain, physical coupling of the two systems is not as straightforward. In the port-Hamiltonian modeling approach, coupling via the port variables is a standard procedure and can be handled without difficulties. The example demonstrates the feasibility and elegance of the approach when applied to

Table 6.1: Hydraulic actuator parameters of the prototype frame model

Symbol	Value	Unit	Description
L	35	cm	hydraulic cylinder length
A_1	133	cm^2	cross sectional area 1^{st} chamber
A_2	94.2	cm^2	cross sectional area 2^{nd} chamber
m_p	10	kg	piston mass
β	1.3	GPa	fluid bulk modulus
p_T	0	bar	tank pressure
p_S	200	bar	supply pressure
k_v	2.0	l/min	valve coefficient

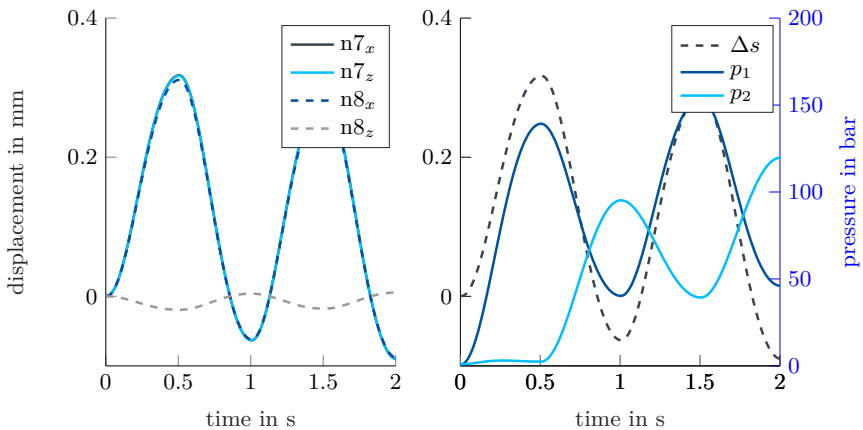

(a) Displacements of the topmost nodes

(b) Hydraulic cylinder dynamics

Figure 6.4: Structural response of the system shown in Fig. 6.3 to sinusoidal excitation of the hydraulic cylinder

the modeling of multi-domain systems and also that it is not limited to linear systems.

7 Decentralized state estimation

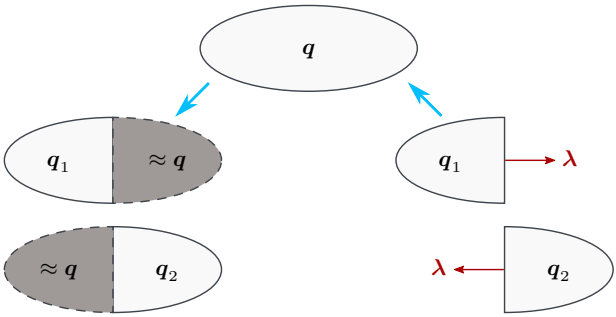

Figure 7.1: Two ways to decentralize a dynamic system model. Local models can be derived from a global model by dynamic condensation, where an approximation of the global DOFs $\boldsymbol{q}$ is retained in each subsystem. Another approach is to represent the global dynamics by interconnection of separate modules via coupling forces $\boldsymbol{\lambda}$

Decentralization is a means to break down the complexity of large systems that are difficult to grasp in their entirety into smaller and therefore manageable parts. Furthermore, it is perfectly in line with the modular and object-oriented energy-based modeling principles. In this chapter, two different ways to construct model-based decentralized observers for linear port-Hamiltonian systems are suggested. The presented approaches focus on the decentralization of the system model. Local observers are then designed for each subsystem. Principally, more methods for decentralized observer design than the ones considered here are thinkable. Aim of this chapter is to provide a basis and conceptual ideas from which more elaborate concepts may be derived.

Generally, it makes a difference whether a model of the system to be observed in a decentralized manner is available or unknown in advance. In the first case, information about the global system behavior may be included in local subsystems. Otherwise, local units are considered independent modules that may or may not share information with other units they are connected to. In this latter case, a global system model or a global observer can results from the interconnection of the subsystems. However, it is also possible to partially retain the independence of each module for decentralized operation. This is especially advantageous, if certain details of individual modules are not to be shared between project partners due to intellectual property issues. In that case, the exchange of information can be restricted to the interfaces. Both scenarios are illustrated in Fig. 7.1, where some specifics of the approaches presented in the following are already included.

Given a global system model of a mechanical structure with DOFs $\boldsymbol{q}$ is available, a method for its decentralization using dynamic condensation is presented in Section 7.2. Subsystem observers operate only on local DOFs ($\boldsymbol{q}_1$ and $\boldsymbol{q}_2$ in Fig. 7.1), but retain an approximation of the global dynamic behavior. This idea was previously presented in [132] and further elaborated on in [136] and [133] without using any energy-based methods and system representations. In the following, both the models and the observers are expressed as port-Hamiltonian systems.

In contrast to this approach, decentralized observers for a modular conception of the problem are presented in Section 7.3. Two local modules that are connected to each other need to share information to arrive at a joint estimation of the global system dynamics. It is assumed that both subsystems share the DOFs of the nodes, at which their interconnection takes place. In this case, constraint equations are formulated for $\boldsymbol{q}_1$ and $\boldsymbol{q}_2$ to ensure that shared states are identical. The coupling forces $\boldsymbol{\lambda}$ resulting from these constraints may then be communicated between the local units. This is illustrated on the right hand side of Fig. 7.1.

For both approaches, the same type of observer may be used for local state estimation, since they primarily focus on the partitioning of the model. Probably, the simplest possible choice is the *Luenberger* observer, for which a passive formulation can be found. Before elaborating on decentralized state estimation, Luenberger observers in port-Hamiltonian form are introduced in Section 7.1. The basic and well-established formulation is extended to account for non-collocated outputs and for position-based measurements. The methods presented in this chapter are applied to estimate the state of adaptive structures in Chapter 8.

7.1 Damping injection observers

Consider a linear port-Hamiltonian system in input-state-output form (2.32), reprinted here for convenience as

$$\dot{\boldsymbol{x}} = (\boldsymbol{J} - \boldsymbol{R})\,\boldsymbol{Q}\boldsymbol{x} + \boldsymbol{G}\boldsymbol{u}, \tag{7.1a}$$

$$\boldsymbol{y} = \boldsymbol{G}^{\mathrm{T}}\boldsymbol{Q}\boldsymbol{x}, \tag{7.1b}$$

with $\boldsymbol{x} \in \mathbb{R}^n$ and $\boldsymbol{u}, \boldsymbol{y} \in \mathbb{R}^{n_u}$. If $\boldsymbol{y}$ is the measurement output of the system, a Luenberger observer for the above is given by

$$\begin{aligned} \dot{\hat{\boldsymbol{x}}} &= \left(\boldsymbol{J} - \boldsymbol{R} - \boldsymbol{L}\boldsymbol{G}^{\mathrm{T}}\right)\boldsymbol{Q}\hat{\boldsymbol{x}} + \boldsymbol{G}\boldsymbol{u} + \boldsymbol{L}\boldsymbol{y}, \\ \hat{\boldsymbol{y}} &= \boldsymbol{G}^{\mathrm{T}}\boldsymbol{Q}\hat{\boldsymbol{x}}, \end{aligned} \tag{7.2}$$

where $\hat{\boldsymbol{x}}$ denotes the state estimate and $\boldsymbol{L} \in \mathbb{R}^{n \times n_u}$ the observer gain, which in turn is chosen as

$$\boldsymbol{L} = \boldsymbol{G}\boldsymbol{R}_{\mathrm{f}}^{-1}. \tag{7.3}$$

For any positive semi-definite symmetric matrix $\boldsymbol{R}_\mathrm{f} = \boldsymbol{R}_\mathrm{f}^\mathrm{T}, \boldsymbol{R}_\mathrm{f} \geq 0$, the observer system (7.2) is positive real. Moreover, it follows that $\boldsymbol{L}\boldsymbol{G}^\mathrm{T}$ has the same properties as the matrix $\boldsymbol{R}$ in (7.1) and can therefore be considered a damping term. This gave rise to the notion of a *damping injection observer*, as employed e. g. in [72].

In a general setting, the measurement output is often not collocated to the input $\boldsymbol{u}$. Let $\boldsymbol{y}_\mathrm{f} \in \mathbb{R}^{n_\mathrm{f}}$ denote the output related to n_f non-collocated sensor signals with

$$\boldsymbol{y}_\mathrm{f} = \boldsymbol{G}_\mathrm{f}^\mathrm{T} \boldsymbol{Q} \boldsymbol{x}. \tag{7.4}$$

If this output is used instead of $\boldsymbol{y}$, the resulting observer is not passive anymore and, strictly speaking, also no port-Hamiltonian system. To formally retain the passivity property, let us make use of a simple trick described e. g. by Cardoso-Ribeiro et al. [24]. Denote by $\boldsymbol{u}_\mathrm{f}$ the virtual input collocated to $\boldsymbol{y}_\mathrm{f}$, which will not be utilized (i. e. $\boldsymbol{u}_\mathrm{f} = 0$). Then, a port-Hamiltonian system that includes this input is given by

$$\dot{\boldsymbol{x}} = (\boldsymbol{J} - \boldsymbol{R})\, \boldsymbol{Q}\boldsymbol{x} + \boldsymbol{G}\boldsymbol{u} + \boldsymbol{G}_\mathrm{f}\boldsymbol{u}_\mathrm{f}, \tag{7.5a}$$

$$\boldsymbol{y} = \boldsymbol{G}^\mathrm{T}\boldsymbol{Q}\boldsymbol{x}, \tag{7.5b}$$

$$\boldsymbol{y}_\mathrm{f} = \boldsymbol{G}_\mathrm{f}^\mathrm{T}\boldsymbol{Q}\boldsymbol{x}, \tag{7.5c}$$

which is seen to be passive again. For a mechanical system, the output $\boldsymbol{y}$ or $\boldsymbol{y}_\mathrm{f}$ can include forces and velocities or torques and angular velocities since it is composed of the efforts $\boldsymbol{e} = \boldsymbol{Q}\boldsymbol{x}$ of the system. However, it is more realistic that positions or displacements of certain points of a structure are tracked instead in a practical application. Corresponding velocities may be obtained by taking the time-derivative of those location-based measurements. If the derivative has to be numerically approximated, which is often the case, noise is amplified in the process. Oversampling can potentially reduce this effect, but is not generally applicable in practice. On that account, specifying the output by (7.4) is still somewhat restrictive. A more general measurement output is given by

$$\boldsymbol{y}_\mathrm{f} = \boldsymbol{C}\boldsymbol{x}. \tag{7.6}$$

Now, $\boldsymbol{L}$ needs to be modified accordingly such that it still produces a damping term in a Luenberger observer with this output. This is achieved by choosing

$$\boldsymbol{L}_\mathrm{f} = \boldsymbol{Q}^{-1}\boldsymbol{C}^\mathrm{T}\boldsymbol{R}_\mathrm{f}^{-1}. \tag{7.7}$$

Consequently, the observer equations (7.2) become

$$\begin{aligned}
\dot{\hat{\boldsymbol{x}}} &= (\boldsymbol{J} - \boldsymbol{R} - \boldsymbol{L}_\mathrm{f}\boldsymbol{C}\boldsymbol{Q}^{-1})\boldsymbol{Q}\hat{\boldsymbol{x}} + \boldsymbol{G}\boldsymbol{u} + \boldsymbol{Q}^{-1}\boldsymbol{C}^\mathrm{T}\boldsymbol{u}_\mathrm{f} + \boldsymbol{L}_\mathrm{f}\boldsymbol{y}_\mathrm{f}, \\
\hat{\boldsymbol{y}} &= \boldsymbol{G}^\mathrm{T}\boldsymbol{Q}\hat{\boldsymbol{x}}, \\
\hat{\boldsymbol{y}}_\mathrm{f} &= \boldsymbol{C}\hat{\boldsymbol{x}},
\end{aligned} \tag{7.8}$$

where $\boldsymbol{L}_\mathrm{f}\boldsymbol{C}\boldsymbol{Q}^{-1}$ is again positive semi-definite and symmetric. Port-Hamiltonian observers of this type are used for the decentralized systems in the next two sections.

7.2 Local models from a global system model

In this section, a dynamic condensation approach is applied to a general dynamical model of a mechanical system in port-Hamiltonian form

$$\begin{bmatrix} \boldsymbol{M}\ddot{\boldsymbol{q}} \\ \dot{\boldsymbol{q}} \end{bmatrix} = \left(\underbrace{\begin{bmatrix} \boldsymbol{0} & -\boldsymbol{I} \\ \boldsymbol{I} & \boldsymbol{0} \end{bmatrix}}_{\boldsymbol{J}} - \underbrace{\begin{bmatrix} \boldsymbol{D} & \boldsymbol{0} \\ \boldsymbol{0} & \boldsymbol{0} \end{bmatrix}}_{\boldsymbol{R}} \right) \underbrace{\begin{bmatrix} \boldsymbol{M}^{-1} & \boldsymbol{0} \\ \boldsymbol{0} & \boldsymbol{K} \end{bmatrix}}_{\boldsymbol{Q}} \underbrace{\begin{bmatrix} \boldsymbol{M}\dot{\boldsymbol{q}} \\ \boldsymbol{q} \end{bmatrix}}_{\boldsymbol{x}} + \boldsymbol{G}\boldsymbol{u}, \tag{7.9a}$$

$$\boldsymbol{y} = \boldsymbol{G}^{\mathrm{T}}\boldsymbol{Q}\boldsymbol{x}, \tag{7.9b}$$

where $\boldsymbol{q} \in \mathbb{R}^n$ are the global DOFs of the structure. Compare with (4.46).

As in [132], local models are derived using a combination of two different model order reduction techniques - the system equivalent reduction expansion process (SEREP) and Guyan condensation. Consider this an example of a reduction method that serves the purpose of deriving functional subsystems from the models considered in this thesis. Many other ways of projecting from the global DOFs to local ones using some kind of coordinate transformation are possible (see e. g. [60]). The one presented in the following proved to be well applicable, but is not necessarily optimal. A thorough study of suitable reduction methods and their comparison is, however, beyond the focus of this work.

Guyan condensation is an established static condensation method. For its application, the model's DOFs are divided into a set of active coordinates $\boldsymbol{q}_{\mathrm{a}}(t) \in \mathbb{R}^{n_{\mathrm{a}}}$ and a set of dependent ones $\boldsymbol{q}_{\mathrm{d}}(t) \in \mathbb{R}^{n_{\mathrm{d}}}$ with $\boldsymbol{q}_{\mathrm{f}}^{\mathrm{T}}(t) = \begin{bmatrix} \boldsymbol{q}_{\mathrm{a}}^{\mathrm{T}}(t) & \boldsymbol{q}_{\mathrm{d}}^{\mathrm{T}}(t) \end{bmatrix}$. Mass and stiffness matrix are rearranged accordingly

$$\boldsymbol{M}_{\mathrm{f}} = \begin{bmatrix} \boldsymbol{M}_{\mathrm{aa}} & \boldsymbol{M}_{\mathrm{ad}} \\ \boldsymbol{M}_{\mathrm{da}} & \boldsymbol{M}_{\mathrm{dd}} \end{bmatrix}, \qquad \boldsymbol{K}_{\mathrm{f}} = \begin{bmatrix} \boldsymbol{K}_{\mathrm{aa}} & \boldsymbol{K}_{\mathrm{ad}} \\ \boldsymbol{K}_{\mathrm{da}} & \boldsymbol{K}_{\mathrm{dd}} \end{bmatrix}. \tag{7.10}$$

For each subsystem, its respective DOFs are retained in $\boldsymbol{q}_{\mathrm{a}}$, while all other DOFs become dependent. The full global state vector $\boldsymbol{q}_{\mathrm{f}}$ of the whole structure can then be calculated using the Guyan transformation as stated in [56]

$$\boldsymbol{q}_{\mathrm{f}} = \begin{bmatrix} \boldsymbol{I} \\ -\boldsymbol{K}_{\mathrm{dd}}^{-1}\boldsymbol{K}_{\mathrm{da}} \end{bmatrix} \boldsymbol{q}_{\mathrm{a}} = \boldsymbol{T}_{\mathrm{G}}\boldsymbol{q}_{\mathrm{a}}. \tag{7.11}$$

As a static technique, Guyan condensation on its own does not allow accurate reproduction of the structural dynamics, because inertia terms are neglected in the transformation (7.11). In the application of the SEREP method, the dynamics are expressed by a reduced set of system eigenmodes, as obtained from modal analysis.

To carry out a modal analysis for the second order system (4.12), note that its solution without damping and input terms amounts to

$$\boldsymbol{q}(t) = \varphi_i e^{j\omega_i t} \tag{7.12}$$

with the eigenvalues ω_i and the corresponding eigenvectors φ_i. Taking the second derivative of the above with respect to time, the dynamic equations without damping and external excitation can be reformulated as

$$(\boldsymbol{K} - \omega_i^2 \boldsymbol{M})\varphi_i = 0, \quad i = 1, 2, \dots n. \tag{7.13}$$

This equation can be solved for ω_i and the eigenvectors φ_i. Since the latter are not uniquely determined, they are normalized such that

$$\boldsymbol{\Phi}^{\mathrm{T}} \boldsymbol{M} \boldsymbol{\Phi} = \boldsymbol{I}, \quad \text{with } \boldsymbol{\Phi}^{\mathrm{T}} = \begin{bmatrix} \varphi_1 & \varphi_2 & \dots & \varphi_n \end{bmatrix}. \tag{7.14}$$

A reduced order model in modal coordinates is then obtained by approximating the vector of DOFs $\boldsymbol{q}$ by a reduced number of primary eigenmodes

$$\boldsymbol{q}(t) \approx \boldsymbol{\Phi}_{\mathrm{r}} \boldsymbol{\eta}_{\mathrm{r}}. \tag{7.15}$$

Here, the eigenmodes $\boldsymbol{\eta}_{\mathrm{r}} \in \mathbb{R}^{n_{\mathrm{r}}}$ with the lowest magnitude eigenvalue and therefore lowest frequency are chosen. For the application of SEREP, the eigenvectors $\boldsymbol{\Phi}_{\mathrm{r}}$ belonging to this reduced set of eigenmodes are again partitioned into an active and a dependent part

$$\boldsymbol{q}_{\mathrm{f}}(t) = \begin{bmatrix} \boldsymbol{q}_{\mathrm{a}} \\ \boldsymbol{q}_{\mathrm{d}} \end{bmatrix} \approx \underbrace{\begin{bmatrix} \boldsymbol{\Phi}_{\mathrm{a}} \\ \boldsymbol{\Phi}_{\mathrm{d}} \end{bmatrix}}_{\boldsymbol{\Phi}_{\mathrm{fr}}} \boldsymbol{\eta}_{\mathrm{r}}. \tag{7.16}$$

A reduced order model in active DOFs $\boldsymbol{q}_{\mathrm{a}}$ is then obtained using a generalized inverse of $\boldsymbol{\Phi}_{\mathrm{a}}$

$$\boldsymbol{q}_{\mathrm{f}} \approx \boldsymbol{\Phi}_{\mathrm{fr}} \left[\boldsymbol{\Phi}_{\mathrm{a}}^{\mathrm{T}} \boldsymbol{\Phi}_{\mathrm{a}} \right]^{-1} \boldsymbol{\Phi}_{\mathrm{a}}^{\mathrm{T}} \boldsymbol{q}_{\mathrm{a}} = \boldsymbol{T}_{\mathrm{U}} \boldsymbol{q}_{\mathrm{a}} \tag{7.17}$$

according to [97], where $\boldsymbol{\Phi}_{\mathrm{a}} \in \mathbb{R}^{n_{\mathrm{a}} \times n_{\mathrm{r}}}$ contains the parts of the eigenvectors mapping to the n_{a} active DOFs. The transformations $\boldsymbol{T}_{\mathrm{G}}$ and $\boldsymbol{T}_{\mathrm{U}}$ can be combined to a single one, as proposed in [3]

$$\boldsymbol{T}_{\mathrm{H}} = \boldsymbol{T}_{\mathrm{G}} + (\boldsymbol{T}_{\mathrm{G}} - \boldsymbol{T}_{\mathrm{U}}) \left[\boldsymbol{\Phi}_{\mathrm{a}} \boldsymbol{\Phi}_{\mathrm{a}}^{\mathrm{T}} \boldsymbol{T}_{\mathrm{U}}^{\mathrm{T}} \boldsymbol{M}_{\mathrm{f}} \boldsymbol{T}_{\mathrm{U}} \right] \tag{7.18}$$

which is known as the SEREP-Guyan transformation. For each subsystem, a transformation $\boldsymbol{T}_{\mathrm{H}} \in \mathbb{R}^{n \times n_{\mathrm{a}}}$ is obtained that projects from the local coordinates $\boldsymbol{q}_a$ to the global state. Applying it to the mass and stiffness matrix of system yields

$$\boldsymbol{M}_{\mathrm{a}} = \boldsymbol{T}_{\mathrm{H}}^{\mathrm{T}} \boldsymbol{M} \boldsymbol{T}_{\mathrm{H}}, \qquad \boldsymbol{K}_{\mathrm{a}} = \boldsymbol{T}_{H}^{\mathrm{T}} \boldsymbol{K} \boldsymbol{T}_{\mathrm{H}}. \tag{7.19}$$

It is expedient to truncate high frequency eigenmodes of the system defined by $\boldsymbol{M}_{\mathrm{a}}$ and $\boldsymbol{K}_{\mathrm{a}}$, which leads to an increase in stability. Applying modal analysis again with $\boldsymbol{M}_{\mathrm{a}}$ and $\boldsymbol{K}_{\mathrm{a}}$, the local DOFs $\boldsymbol{q}_{\mathrm{a}}$ can be approximated using a reduced number of primary eigenmodes

$$\boldsymbol{q}_{\mathrm{a}} \approx \boldsymbol{\Phi}_m \boldsymbol{\eta}_m, \qquad \boldsymbol{\eta}_m \in \mathbb{R}^{n_m}, \tag{7.20}$$

with n_m the number of local module eigenmodes and $\boldsymbol{\Phi}_m \in \mathbb{R}^{n_\mathrm{a} \times n_m}$ the corresponding matrix of eigenvectors.

In order to transform (7.9), two transformations are constructed from $\boldsymbol{T}_\mathrm{H}$ and $\boldsymbol{\Phi}_m$ of a subsystem

$$\boldsymbol{T}_m = \begin{bmatrix} \boldsymbol{M}\boldsymbol{T}_\mathrm{H}\boldsymbol{\Phi}_m & \boldsymbol{0} \\ \boldsymbol{0} & \boldsymbol{T}_\mathrm{H}\boldsymbol{\Phi}_m \end{bmatrix}, \qquad \boldsymbol{U}_m = \begin{bmatrix} \boldsymbol{T}_\mathrm{H}\boldsymbol{\Phi}_m & \boldsymbol{0} \\ \boldsymbol{0} & \boldsymbol{M}\boldsymbol{T}_\mathrm{H}\boldsymbol{\Phi}_m \end{bmatrix}. \tag{7.21}$$

Local system matrices can now be obtained by utilizing $\boldsymbol{T}_m$ and $\boldsymbol{U}_m$

$$\boldsymbol{J}_m = \boldsymbol{T}_m^+ \boldsymbol{J} \boldsymbol{U}_m, \quad \boldsymbol{R}_m = \boldsymbol{T}_m^+ \boldsymbol{R} \boldsymbol{U}_m, \quad \boldsymbol{Q}_m = \boldsymbol{U}_m^+ \boldsymbol{Q} \boldsymbol{T}_m, \quad \boldsymbol{G}_m = \boldsymbol{T}_m^+ \boldsymbol{G}, \tag{7.22}$$

where $\boldsymbol{T}_m^+$ and $\boldsymbol{U}_m^+$ denote the generalized inverse of $\boldsymbol{T}_m$ and $\boldsymbol{U}_m$, respectively. Finally, a reduced order local dynamic model of the subsystem is given by

$$\dot{\boldsymbol{x}}_m = (\boldsymbol{J}_m - \boldsymbol{R}_m)\, \boldsymbol{Q}_m + \boldsymbol{G}_m \boldsymbol{u}, \tag{7.23a}$$

$$\boldsymbol{y} = \boldsymbol{G}_m^\mathrm{T} \boldsymbol{Q}_m \boldsymbol{x}_m. \tag{7.23b}$$

A local observer can be designed for $\boldsymbol{x}_m \in \mathbb{R}^{2n_m}$ according to Section 7.1. Note that it is possible to include sensor signals and actuator inputs from other subsystems since each subsystem can project its local state $\boldsymbol{x}_m$ to the global one and vice verse using $\boldsymbol{T}_m$ and $\boldsymbol{U}_m$. This is also a convenient property when communication between the local observers is to be established.

7.3 Modular approach with coupling at the interfaces

Instead of deriving local models from a global one, as explained in the previous section, the inverse approach of composing a structure from separate subsystems is considered in this section. This has the advantage that the global model need not be known in advance and that simple modules can be flexibly interconnected to form variants of complex systems. For simplicity, the process is demonstrated for two modules with DOFs $\boldsymbol{q}_1 \in \mathbb{R}^{n_1}$ and $\boldsymbol{q}_2 \in \mathbb{R}^{n_2}$ first and then generalized to N_s interconnected subsystems.

Let $\boldsymbol{M}_1$, $\boldsymbol{K}_1$ and $\boldsymbol{D}_1$ denote the mass, stiffness and damping matrix of the first module, respectively. Its dynamics may be expressed in port-Hamiltonian form, similar to (4.46), as

$$\begin{bmatrix} \boldsymbol{M}_1 \ddot{\boldsymbol{q}}_1 \\ \dot{\boldsymbol{q}}_1 \end{bmatrix} = \Bigg(\underbrace{\begin{bmatrix} \boldsymbol{0} & -\boldsymbol{I} \\ \boldsymbol{I} & \boldsymbol{0} \end{bmatrix}}_{\boldsymbol{J}_1} - \underbrace{\begin{bmatrix} \boldsymbol{D}_1 & \boldsymbol{0} \\ \boldsymbol{0} & \boldsymbol{0} \end{bmatrix}}_{\boldsymbol{R}_1} \Bigg) \underbrace{\begin{bmatrix} \boldsymbol{M}_1^{-1} & \boldsymbol{0} \\ \boldsymbol{0} & \boldsymbol{K}_1 \end{bmatrix}}_{\boldsymbol{Q}_1} \underbrace{\begin{bmatrix} \boldsymbol{M}_1 \dot{\boldsymbol{q}}_1 \\ \boldsymbol{q}_1 \end{bmatrix}}_{\boldsymbol{x}_1} + \boldsymbol{G}_1 \boldsymbol{u}_1, \tag{7.24a}$$

$$\boldsymbol{y}_1 = \boldsymbol{G}_1^\mathrm{T} \boldsymbol{Q}_1 \boldsymbol{x}_1, \tag{7.24b}$$

where $\boldsymbol{G}_1$ is the input matrix corresponding to the input $\boldsymbol{u}_1 \in \mathbb{R}^{n_{u1}}$ to actuators available in the first module. Accordingly, for the second module, the local dynamic equations can be stated as

$$\begin{bmatrix} \boldsymbol{M}_2\ddot{\boldsymbol{q}}_2 \\ \dot{\boldsymbol{q}}_2 \end{bmatrix} = \left(\underbrace{\begin{bmatrix} \boldsymbol{0} & -\boldsymbol{I} \\ \boldsymbol{I} & \boldsymbol{0} \end{bmatrix}}_{\boldsymbol{J}_2} - \underbrace{\begin{bmatrix} \boldsymbol{D}_2 & \boldsymbol{0} \\ \boldsymbol{0} & \boldsymbol{0} \end{bmatrix}}_{\boldsymbol{R}_2} \right) \underbrace{\begin{bmatrix} \boldsymbol{M}_2^{-1} & \boldsymbol{0} \\ \boldsymbol{0} & \boldsymbol{K}_2 \end{bmatrix}}_{\boldsymbol{Q}_2} \underbrace{\begin{bmatrix} \boldsymbol{M}_2\dot{\boldsymbol{q}}_2 \\ \boldsymbol{q}_2 \end{bmatrix}}_{\boldsymbol{x}_2} + \boldsymbol{G}_2\boldsymbol{u}_2, \tag{7.25a}$$

$$\boldsymbol{y}_2 = \boldsymbol{G}_2^{\mathrm{T}}\boldsymbol{Q}_2\boldsymbol{x}_2, \tag{7.25b}$$

where $\boldsymbol{u}_2, \boldsymbol{y}_2 \in \mathbb{R}^{n_{u2}}$. To proceed, a composite system is formed by concatenation of the system matrices as suggested in Section 5.1. The composite state vector is thus chosen as

$$\boldsymbol{x}_{\mathrm{c}}^{\mathrm{T}} = \begin{bmatrix} (\boldsymbol{M}_2\dot{\boldsymbol{q}}_2)^{\mathrm{T}} & (\boldsymbol{M}_1\dot{\boldsymbol{q}}_1)^{\mathrm{T}} & \boldsymbol{q}_1^{\mathrm{T}} & \boldsymbol{q}_2^{\mathrm{T}} \end{bmatrix}, \quad \boldsymbol{x}_c \in \mathbb{R}^{2n_1+2n_2} \tag{7.26}$$

which results in the combined, but still uncoupled system

$$\dot{\boldsymbol{x}}_{\mathrm{c}} = (\boldsymbol{J}_{\mathrm{c}} - \boldsymbol{R}_{\mathrm{c}})\boldsymbol{Q}_{\mathrm{c}}\boldsymbol{x}_{\mathrm{c}} + \boldsymbol{G}_{\mathrm{c}}\boldsymbol{u}_{\mathrm{c}}, \tag{7.27a}$$

$$\boldsymbol{y}_{\mathrm{c}} = \boldsymbol{G}_{\mathrm{c}}^{\mathrm{T}}\boldsymbol{Q}_{\mathrm{c}}\boldsymbol{x}_{\mathrm{c}}, \tag{7.27b}$$

where $\boldsymbol{u}_{\mathrm{c}}^{\mathrm{T}} = \begin{bmatrix} \boldsymbol{u}_1^{\mathrm{T}} & \boldsymbol{u}_2^{\mathrm{T}} \end{bmatrix}$. At the nodes, at which the systems are interconnected, they share a set of DOFs. Hence, $\boldsymbol{q}_1$ and $\boldsymbol{q}_2$ can be partitioned as follows

$$\boldsymbol{q}_1^{\mathrm{T}} = \begin{bmatrix} \boldsymbol{q}_{11}^{\mathrm{T}} & \boldsymbol{q}_{12}^{\mathrm{T}} \end{bmatrix}, \qquad \boldsymbol{q}_2^{\mathrm{T}} = \begin{bmatrix} \boldsymbol{q}_{21}^{\mathrm{T}} & \boldsymbol{q}_{22}^{\mathrm{T}} \end{bmatrix}, \tag{7.28}$$

where $\boldsymbol{q}_{11} \in \mathbb{R}^{n_1-n_{\mathrm{s}}}$ and $\boldsymbol{q}_{22} \in \mathbb{R}^{n_2-n_{\mathrm{s}}}$ denote the DOFs belonging exclusively to the first and second module, respectively. The vectors $\boldsymbol{q}_{12} \in \mathbb{R}^{n_{\mathrm{s}}}$ and $\boldsymbol{q}_{21} \in \mathbb{R}^{n_{\mathrm{s}}}$, on the other hand, denote the n_{s} shared DOFs. Coupling of the modules can be realized by establishing constraints on the velocity level, that require the shared velocities to be equal

$$\boldsymbol{B}_{\mathrm{c}}^{\mathrm{T}}\boldsymbol{Q}_{\mathrm{c}}\boldsymbol{x}_{\mathrm{c}} = \dot{\boldsymbol{q}}_{12} - \dot{\boldsymbol{q}}_{21} = \boldsymbol{0}. \tag{7.29}$$

Recalling Section 5.6, the Lagrange multipliers belonging to these constraints are forces and can be solved for by taking the derivative of the above with respect to time

$$\begin{aligned} 0 &= \boldsymbol{B}_{\mathrm{c}}^{\mathrm{T}}\boldsymbol{Q}_{\mathrm{c}}\dot{\boldsymbol{x}}_c \\ &= \boldsymbol{B}_{\mathrm{c}}^{\mathrm{T}}\boldsymbol{Q}_{\mathrm{c}}\left[(\boldsymbol{J}_{\mathrm{c}} - \boldsymbol{R}_{\mathrm{c}})\boldsymbol{Q}_{\mathrm{c}}\boldsymbol{x}_{\mathrm{c}} + \boldsymbol{G}_{\mathrm{c}}\boldsymbol{u}_{\mathrm{c}} + \boldsymbol{B}_{\mathrm{c}}\boldsymbol{\lambda}\right] \\ \boldsymbol{\lambda} &= (\boldsymbol{B}_{\mathrm{c}}^{\mathrm{T}}\boldsymbol{Q}_{\mathrm{c}}\boldsymbol{B}_{\mathrm{c}})^{-1}\boldsymbol{B}_{\mathrm{c}}^{\mathrm{T}}\boldsymbol{Q}_{\mathrm{c}}\left[(\boldsymbol{J}_{\mathrm{c}} - \boldsymbol{R}_{\mathrm{c}})\boldsymbol{Q}_{\mathrm{c}}\boldsymbol{x}_{\mathrm{c}} + \boldsymbol{G}_{\mathrm{c}}\boldsymbol{u}_{\mathrm{c}}\right]. \end{aligned} \tag{7.30}$$

To obtain a coupled system, the constraints could be eliminated along with $\boldsymbol{\lambda} \in \mathbb{R}^{n_{\mathrm{s}}}$ according to the procedure described in Section 5.3. However, if a modular configuration with communicating, but otherwise independent modules is desired, another system representation is required. Partitioning the composite system back

into the original modules while retaining the coupling between them is possible by observing that

$$\boldsymbol{\lambda} = \boldsymbol{\lambda}_1 + \boldsymbol{\lambda}_2 = \boldsymbol{A}_1 \dot{\boldsymbol{x}}_1 + \boldsymbol{A}_2 \dot{\boldsymbol{x}}_2, \tag{7.31}$$

i. e. the Lagrange multipliers may be computed by adding up the respective contribution from each module. The matrices $\boldsymbol{A}_1 \in \mathbb{R}^{n_\mathrm{s} \times 2n_1}$ and $\boldsymbol{A}_2 \in \mathbb{R}^{n_\mathrm{s} \times 2n_2}$ are the columns of $(\boldsymbol{B}^\mathrm{T} \boldsymbol{Q}_\mathrm{c} \boldsymbol{B})^{-1} \boldsymbol{B}^\mathrm{T} \boldsymbol{Q}_\mathrm{c}$ corresponding to the first and second module, respectively. In the coupled configuration, the dynamics of each module can thus be expressed as

$$\dot{\boldsymbol{x}}_i = (\boldsymbol{J}_i - \boldsymbol{R}_i)\, \boldsymbol{Q}_i \boldsymbol{x}_i + \boldsymbol{G}_i \boldsymbol{u}_i + \boldsymbol{B}_i \boldsymbol{\lambda}, \tag{7.32a}$$

$$\boldsymbol{y}_i = \boldsymbol{G}_i^\mathrm{T} \boldsymbol{Q}_i \boldsymbol{x}_i, \tag{7.32b}$$

with $i \in \{1, 2\}$ and $\boldsymbol{B}_i \in \mathbb{R}^{2n_i \times n_\mathrm{s}}$ the input matrix of the coupling forces in subsystem i. Separate simulation of each module now requires communicating either the state vector $\boldsymbol{x}_i$ or the contribution to the coupling forces $\boldsymbol{\lambda}_i$ between interconnected systems. The latter is considered advantageous, because $\boldsymbol{\lambda}_i$ is usually of smaller dimension than $\boldsymbol{x}_i$.

In case a module $i = 1 \dots N_\mathrm{s}$ is coupled with $N_\mathrm{c}^i > 1$ others, the constraints can be formulated for the concatenated system in the same way. The Lagrange multipliers are also obtained by summing up all N_c^i contributions

$$\boldsymbol{\lambda}^i = \sum_{j=1}^{N_\mathrm{c}^i} \boldsymbol{\lambda}_j^i = \sum_{j=1}^{N_\mathrm{c}^i} \boldsymbol{A}_j^i \dot{\boldsymbol{x}}_j. \tag{7.33}$$

The dynamics of module i may still be expressed using (7.32) when replacing $\boldsymbol{\lambda}$ with $\boldsymbol{\lambda}^i$. However, a different number of coupling forces $\boldsymbol{\lambda}^i$ is now required in each module as long as the modules are not fully connected. Individual modules can still share their contributions to the coupling forces of the others.

The observers introduced in Section 7.1 can be used for estimating the state of each module. Note that there are several issues to consider when implementing such modular observers in practice using numerical simulation methods and finite measurement sample times. These are discussed in Section 7.4.

7.4 Notes regarding the numerical implementation

The observers presented in this chapter are continuous time systems. However, measurements are available at discrete instants in time, usually with a constant sample time in between. In the following, it is assumed that the measurement sample time T_s matches with the macro time step of the observer. When a new measurement arrives, the observer system is simulated from the previous time step t_{k-1} to the current one t_k using a single-stage Gauss-Legendre collocation method, with $T_\mathrm{s} = t_k - t_{k-1}$.

First-order hold sampling is used for the measurements such that (7.2) between t_{k-1} and t_k becomes

$$\dot{\hat{\boldsymbol{x}}} = \left(\boldsymbol{J} - \boldsymbol{R} - \boldsymbol{L}\boldsymbol{G}^{\mathrm{T}}\right)\boldsymbol{Q}\hat{\boldsymbol{x}} + \boldsymbol{G}\boldsymbol{u} + \boldsymbol{L}\left[\boldsymbol{y}_k \frac{t - t_{k-1}}{T_{\mathrm{s}}} + \boldsymbol{y}_{k-1}\left(1 - \frac{t - t_{k-1}}{T_{\mathrm{s}}}\right)\right], \tag{7.34a}$$

$$\hat{\boldsymbol{y}} = \boldsymbol{G}^{\mathrm{T}}\boldsymbol{Q}\hat{\boldsymbol{x}}, \tag{7.34b}$$

where $\boldsymbol{y}_k$ and $\boldsymbol{y}_{k-1}$ are the measurements received at the current and previous macro time step, respectively, and $\hat{\boldsymbol{x}}(t_{k-1}) = \hat{\boldsymbol{x}}_{k-1}$. For observers with non-collocated outputs or displacement-based measurements, modify the above according to Section 7.1.

Concerning the modular approach described in Section 7.3, the question of how to simulate the systems independently arises. Several methods were developed on this account that are commonly referred to as *co-simulation* techniques or *solver coupling* approaches. See e. g. the recent survey by Gomes et al. [52] for an overview of the field. With regard to the coupling of solvers, it is discriminated between approaches where the dynamics of each module are integrated in parallel (Jacobi type) and sequential methods (Gauss-Seidel type). Since the former has a higher parallelization potential, it is preferred over the latter in the context of this work. Schweizer et al. [112] introduced several methods for co-simulation using Jacobi type integration schemes. Either kinematic variables or forces can be exchanged at the interfaces, which allows for a number of different variants. A multibody version of a force–force coupling approach as presented by Wang et al. [131] is used in this thesis. For simplicity, the co-simulation of two modules coupled by the constraints (7.29) is considered in the following.

Without direct coupling of the integrators used for the forward simulation of each local model, one has to resort to estimates of $\boldsymbol{\lambda} \in \mathbb{R}^{n_{\mathrm{s}}}$ between macro time steps. A simple solution is to use the Lagrange multipliers calculated at time t_{k-1} with the contribution $\boldsymbol{\lambda}_{j,k-1}$ received from the other module. In the interval $t \in \left[t_{k-1}, \quad t_k\right]$, the equations for each module thus become

$$\dot{\boldsymbol{x}}_i = \left(\boldsymbol{J}_i - \boldsymbol{R}_i\right)\boldsymbol{Q}_i\boldsymbol{x}_i + \boldsymbol{G}_i\boldsymbol{u}_i + \boldsymbol{B}_i\boldsymbol{\lambda}_k^{\mathrm{p}}, \tag{7.35a}$$

$$\boldsymbol{y}_i = \boldsymbol{G}_i^{\mathrm{T}}\boldsymbol{Q}_i\boldsymbol{x}_i, \tag{7.35b}$$

where $\boldsymbol{\lambda}_k^{\mathrm{p}} \in \mathbb{R}^{n_{\mathrm{s}}}$ are the predicted coupling forces calculated according to (7.30). Higher order polynomial approximations may be used for increased accuracy [112]. Integrating the above between t_{k-1} and t_k with the state at t_{k-1} as the initial condition yields the predicted states $\boldsymbol{x}_{i,k}^{\mathrm{p}}$. However, the constraints (7.29) are generally not satisfied for $\boldsymbol{x}_{i,k}^{\mathrm{p}}$. To prevent a violation of the constraints, the Lagrange multipliers need to be corrected. This can be achieved by noting that $\boldsymbol{x}_{i,k}$ is a function of $\boldsymbol{\lambda}$ and linearizing (7.29) about $\boldsymbol{\lambda}_k^{\mathrm{p}}$

$$\boldsymbol{0} \approx \boldsymbol{B}_{\mathrm{c}}^{\mathrm{T}}\boldsymbol{Q}_{\mathrm{c}}\boldsymbol{x}_{\mathrm{c},k}^{\mathrm{p}} + \boldsymbol{B}_{\mathrm{c}}^{\mathrm{T}}\boldsymbol{Q}_{\mathrm{c}}\left.\frac{\partial \boldsymbol{x}_{\mathrm{c},k}}{\partial \boldsymbol{\lambda}_k}\right|_{\boldsymbol{\lambda}_k^{\mathrm{p}}}\left(\boldsymbol{\lambda}_k - \boldsymbol{\lambda}_k^{\mathrm{p}}\right). \tag{7.36}$$

The corrected coupling forces are then obtained as

$$\boldsymbol{\lambda}_k = \boldsymbol{\lambda}_k^{\mathrm{p}} - \left(\boldsymbol{B}_{\mathrm{c}}^{\mathrm{T}} \boldsymbol{Q}_{\mathrm{c}} \frac{\partial \boldsymbol{x}_{\mathrm{c},k}}{\partial \boldsymbol{\lambda}_k} \Big|_{\boldsymbol{\lambda}_k^{\mathrm{p}}} \right)^{-1} \boldsymbol{B}_{\mathrm{c}}^{\mathrm{T}} \boldsymbol{Q}_{\mathrm{c}} \boldsymbol{x}_{\mathrm{c},k}^{\mathrm{p}}. \tag{7.37}$$

The derivative of $\boldsymbol{x}_{\mathrm{c},k}$ with respect to to $\boldsymbol{\lambda}_k$ can be approximated with finite differences. For each $\lambda_{j,k}$, the system (7.36) needs to be simulated again, but with a small perturbation $\Delta\lambda_{j,k}$ added to $\lambda_{j,k}^{\mathrm{p}}$. Since n_{s} is the number of constraints, $j = 1 \dots n_{\mathrm{s}}$ and

$$\frac{\partial \boldsymbol{x}_{\mathrm{c},k}}{\partial \lambda_{j,k}} \approx \frac{\boldsymbol{x}_{\mathrm{c},k}(\boldsymbol{\lambda}_k^{\mathrm{p}} + \boldsymbol{\Delta}\lambda_{j,k}) - \boldsymbol{x}_{\mathrm{c},k}^{\mathrm{p}}}{\Delta\lambda_{j,k}}. \tag{7.38}$$

Depending on the number of constraints n_{s} and the system dimension, repeating the forward simulation n_{s} times for each module can be a rather costly operation. To save computation time, parallel processing on suitable hardware is suggested. With the corrected Lagrange multipliers, each module is simulated one more time to obtain the corrected states $\boldsymbol{x}_{i,k}$. For nonlinear systems, the corrected Lagrange multipliers may be computed using a Newton-Raphson algorithm, as described in [131].

7.5 Filters to increase agreement between local estimates

In case there is no communication between observers for local systems derived by the method described in Section 7.2, the estimates of shared DOFs are generally not identical. The same problem arises for the modular approach (see Section 7.3), where position drifts can occur, because the coupling forces are computed from velocity constraints. One way to deal with this issue, is to introduce additional filters of Luenberger type charged with the task to minimize the difference between estimates of shared DOFs. This requires communication of the estimates of shared states between local observers, where the data transfer can be one-way only or both ways. If all modules that share a certain set of states are equipped with the same filter, this results in a consensus-type operation. Otherwise, a module uses the shared state communicated from another local subsystem as an additional weighted measurement input, which may be regarded as a tracking operation.

Let the estimated shared displacements or, in general, state variables of module i be given by the relation $\hat{\boldsymbol{x}}_{\mathrm{s}i} = \boldsymbol{C}_{\mathrm{s}i}\hat{\boldsymbol{x}}_i$. In that case, a filter gain that decreases the difference between $\hat{\boldsymbol{x}}_{\mathrm{s}i} \in \mathbb{R}^{n_{\mathrm{s}}^{ij}}$ and the corresponding states $\hat{\boldsymbol{x}}_{\mathrm{s}j}$ of module j is given by

$$\boldsymbol{F}_i = \boldsymbol{Q}_i^{-1} \boldsymbol{C}_{\mathrm{s}i}^{\mathrm{T}} \boldsymbol{R}_{\mathrm{s}i}^{-1}, \tag{7.39}$$

where $\boldsymbol{R}_{\mathrm{s}i} \in \mathbb{R}^{n_{\mathrm{s}}^{ij} \times n_{\mathrm{s}}^{ij}}$ is a positive semi-definite symmetric matrix. Together with

(7.2), the local observer for module i becomes

$$\begin{aligned}\dot{\hat{\boldsymbol{x}}}_i &= (\boldsymbol{J}_i - \boldsymbol{R}_i - \boldsymbol{L}_i\boldsymbol{G}^{\mathrm{T}} - \boldsymbol{F}_i\boldsymbol{C}_{\mathrm{s}i}\boldsymbol{Q}_i^{-1})\boldsymbol{Q}_i\hat{\boldsymbol{x}}_i + \boldsymbol{G}_i\boldsymbol{u}_i + \boldsymbol{Q}_i^{-1}\boldsymbol{C}_{\mathrm{s}i}^{\mathrm{T}}\boldsymbol{u}_{\mathrm{s}i} + \boldsymbol{L}_i\boldsymbol{y}_i + \boldsymbol{F}_i\hat{\boldsymbol{x}}_{\mathrm{s}j},\\ \hat{\boldsymbol{y}}_i &= \boldsymbol{G}_i^{\mathrm{T}}\boldsymbol{Q}_i\hat{\boldsymbol{x}}_i,\\ \hat{\boldsymbol{x}}_{\mathrm{s}i} &= \boldsymbol{C}_{\mathrm{s}i}\hat{\boldsymbol{x}}_i,\end{aligned} \tag{7.40}$$

with $\boldsymbol{u}_{\mathrm{s}i} = 0$ the virtual input that is required for the system to be formally passive. For modular decentralized formulation, the coupling forces $\boldsymbol{\lambda}$ need to be included in the above. In some of the scenarios studied in the next chapter, the filters described in this section are employed to stabilize the observers and to increase estimation accuracy.

8 Application to adaptive structures

Figure 8.1: Rendering of the adaptive high-rise demonstrator under construction at the University of Stuttgart (image by courtesy of ILEK[1])

As stated in the introduction, this thesis one of the results of the interdisciplinary work within the CRC 1244 – "Adaptive skins and structures for the built environment of tomorrow". The unique experimental environment produced and provided by the research center is briefly introduced in the following.

Combined research efforts over the past four years are converging in the construction of the world's first adaptive high-rise structure. At the time this thesis is written, this demonstrator building is under construction on campus of the University of Stuttgart. A rendering of the architects is depicted in Fig. 8.1, showing a vision of the operational structure equipped with various adaptive facades. Loads acting on the structure (e. g.

[1]Institute for Lightweight Structures and Conceptual Design at the University of Stuttgart, Germany

Figure 8.2: Vertical supports of the adaptive high-rise demonstrator after installation of hydraulic actuators (image by courtesy of IKTD[2])

storms) can be actively compensated with the help of hydraulic actuators installed in selected supports and diagonal bracings of the building. In Fig. 8.2, such adaptive supports with mounted hydraulic actuators are shown. Actuators are connected in parallel to the steel columns and can exert forces in the order of several hundred kilonewton. On closer inspection of the topmost section of the building in Fig. 8.1, diagonal bracings are visible that span three floors, respectively. Hydraulic actuators will also be connected in series to selected bracings for a better control of e. g. torsional deformation.

While it will be very interesting to follow the further development of the adaptive high-rise and its impact on the field of adaptive structures, the methods presented in this thesis cannot yet be applied to it. Smaller scale prototypes were, however, available for conducting experiments and for comparative simulation studies. A scaled mockup of the building was designed that can be used for testing control engineering approaches as well as for demonstration purposes. This laboratory size test bench is presented in detail in Section 8.1, where some of the observer concepts introduced in

[2] Institute for Engineering Design and Industrial Design (German: Institut für Konstruktionstechnik und Technisches Design, IKTD) at the University of Stuttgart

Chapter 7 are assessed using actual experimental data. Both centralized sensor fusion as well as decentralized observers with local models derived from a global system representation (see Section 7.2) are implemented on the experimental platform.

The alternative approach that leads to decentralized observers by coupling of separate subsystem or modules (see Section 7.3) is investigated in Section 8.2. In a simulation study conducted with a dynamical model of the high-rise demonstrator, its performance is compared to both a centralized observer and local observers according to Section 7.2. Application of the methods to the actual high-rise demonstrator is highly anticipated.

8.1 State estimation on an adaptive structures test bench

As mentioned above, a laboratory scale test bench for adaptive structures was designed as a mockup of the adaptive high-rise constructed in scope of the CRC 1244. It represents a scale 1:18 version of this demonstrator building and is used to validate control engineering methods before they are applied to the actual high-rise. The mockup was designed to have eigenfrequencies similar to the ones expected for the demonstrator. Thus, only the dimensions were adopted to scale, while material stiffness and truss diameters were not. Note that the scaled version represents the design of the high-rise at an earlier stage of planning. In the final version, the demonstrator consists of four modules instead of five but the overall height and the footprint dimensions were conserved.

In the following, sensor fusion for the scale model using camera-based position measurements and strain gauges is performed. Both the approach and the presentation of results are closely related to the ones published in a previous contribution [134]. However, there are some major differences to the version presented in this thesis. First of all, the system model and the observers are represented as port-Hamiltonian systems in the following. Secondly, the decentralized observer approach introduced in Chapter 7 is tested on the high-rise mockup. As a matter of focus and simplicity, sensor placement and the compensation of image processing delays are omitted.

Subsequently, in Section 8.1.1, the experimental setup is explained in detail. This includes a description of the hardware and software components that make up the test bench as well as a brief section on the working principle of the camera-based position tracking system. In Section 8.1.2, a port-Hamiltonian model for the high-rise mockup is introduced. This is followed by the presentation of the centralized and decentralized filters used for state estimation in Section 8.1.3. A parameter tuning algorithm that makes use of the accurate camera measurements is employed for parameter identification of both system model and filters. It is described in Section 8.1.4. Results are presented and discussed in Section 8.1.5.

8.1.1 Experimental setup

A full view of the scale model is shown in Fig. 8.3 a). Composed of five modules of identical size with a footprint of 26×26 cm and a height of 40 cm each, it extends to a total height of 2 m, which corresponds to 36 m in reality[1]. Each module represents two stories of the demonstrator building. Intermediate floor plates were not installed to make room for the control hardware. A module comprises 4 vertical columns, 8 diagonal bracings and a ceiling plate. Columns are connected to plates via universal joints with two rotational DOFs about the local x- and y-axes. Rotation about the local z-axis is blocked. Bracings are attached to the structure via a rotational joint with one DOF at each end. The lowermost module is mounted to a controllable table (7) that can move in a plane parallel to the ground. Using the table, excitation of the structure as well as the simulation of earthquake primary waves is possible. Selected columns and bracings of the scale model are actuated, where the number of active elements differs in each module. The top module is entirely passive.

A closeup view of the 3rd module in Fig. 8.3 b) reveals how columns and bracings are actuated. When one of the panels of a column is removed (3), two identical springs are visible inside, which are connected in parallel. For actuated columns, the connecting point of the two springs can be moved by a motor via a threaded bar. This generates a force, as illustrated by the schematic drawing on the left of Fig. 8.3 c). The stiffness of a diagonal bracing is determined by a spring which, in case of a passive bracing (5), is tautened between corner nodes using a steel cable and a screw system. One cable end of an active bracing (6) is attached to a guide roller, which can be rotated using a DC-motor in combination with a worm gear. Accordingly, the spring of an active bracing can be directly extended or relaxed. In order to minimize slackening, all diagonal bracing springs are pretensioned. Each motor is driven by a motor controller (4), which in turn is controlled by custom signal processing hardware (2). Details on the test bench's computational hardware, sensors, actuators and data processing are given in the following.

Signal Processing and Control of Actuated Components

Fig. 8.4 depicts the interconnection of sensors, actuators and computational hardware. A rapid prototyping device (dSpace MicroLabBox DS1202) acts as central processing unit. It is interfaced with the host PC via Ethernet and programmed using a Matlab/Simulink real-time interface in combination with dSpace ControlDesk.

For measuring forces, each column and bracing is equipped with two half bridge strain gauges (Vishay EA-06-062TZ-350) mounted on opposing sides and connected

[1] The high-rise demonstrator shown in Fig. 8.1 consist of only four modules. The mockup represents the building as envisioned at an earlier stage of the planning process.

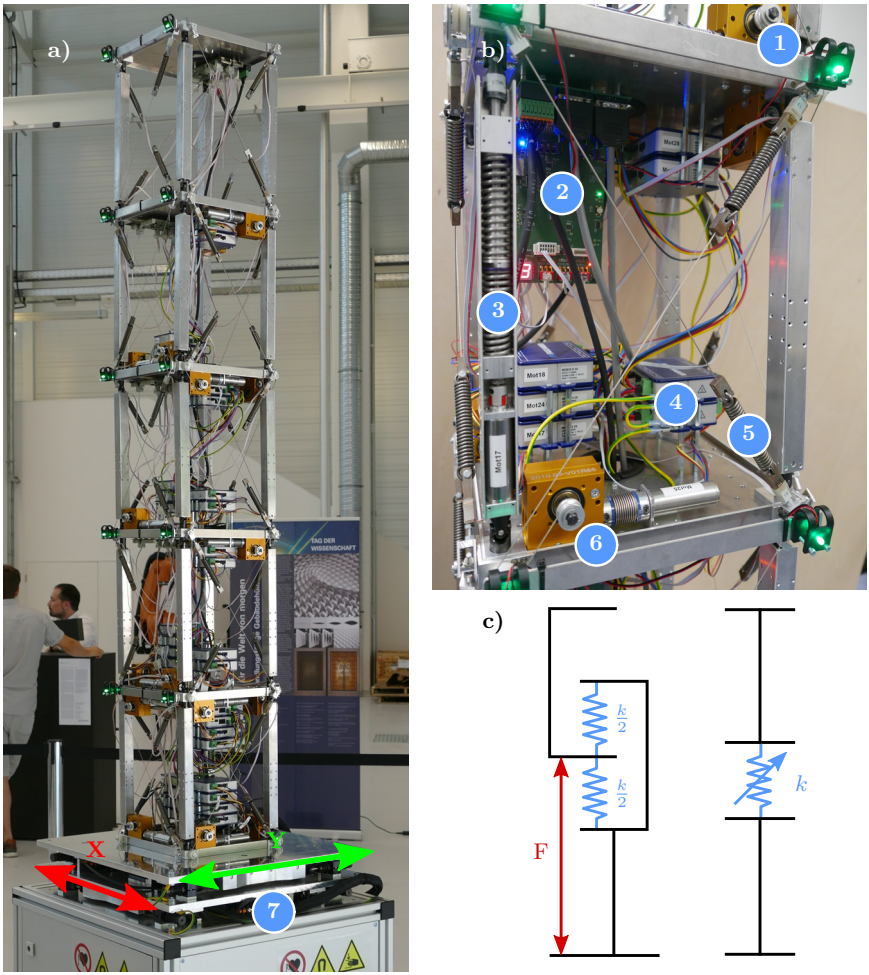

Figure 8.3: Adaptive structures test bench. a) View of all 5 modules including the controllable table (7) used for exciting the structure. b) Closer view of the 3rd module showing LED emitters (1), custom signal processing hardware (2), an actuated column with dismantled cover (3), motor controllers (4) for active elements, passive diagonal bracings (5) and actuated bracings (6). c) Parallel force actuation of columns (left) and change of pretension/elongation for bracings (right) [134]

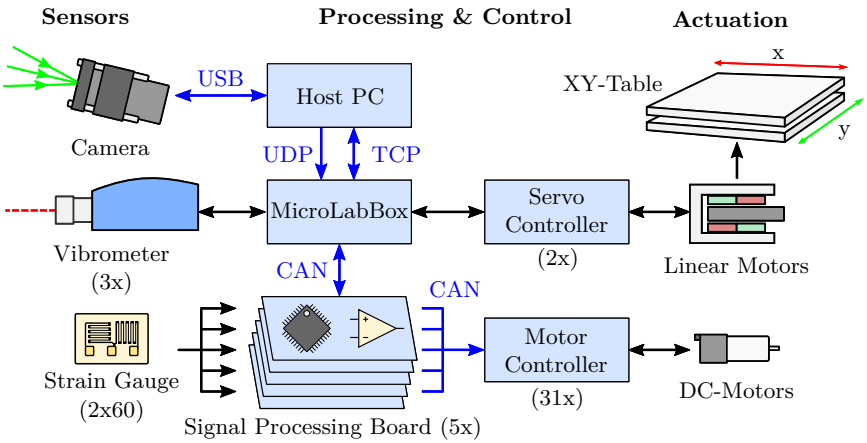

Figure 8.4: Interconnection of sensors, processing units and actuators for the adaptive structures test bench. Sensor signals from camera, vibrometer and strain gauges are processed on the host PC, a rapid prototyping device (MicroLabBox) and custom PCBs respectively. The MicroLabBox acts as CPU and controls table motion via intermediary servo controllers. The DC-motors of active truss elements are accessed by the signal processing boards story-wise [134]

to form a full bridge circuit. The sensors are attached to steel components with high flexural rigidity such that forces due to bending can be neglected. Strain gauge signals are amplified and processed on custom-built printed circuit boards (PCBs) that communicate with the MicroLabBox via CAN bus. Each storey is equipped with one PCB stack that is entrusted with the task of reading out local sensors and controlling the actuated elements in the respective module. The microcontrollers on the PCBs can also be used for decentralized preprocessing and control. Motor controllers (Faulhaber MC5010) are accessed via local CAN buses and brushless DC-motors (Faulhaber 2264W024BP4 3692) are used for active truss elements. The x/y-motion of the table is controlled by servo amplifiers (Metronix ARS 2105) connected to analog I/O-ports of the MicroLabBox. Iron-free linear motors (Tecnotion UX 9N) in combination with optical encoders (Heidenhain LC485) facilitate the table motion.

A digital camera (Ximea MC023MG-SY) attached to a tripod is located at a distance of approximately 2 m from the test bench. It tracks the position of a total of 10 light emitting diodes (LEDs), positioned, as shown in Fig. 8.3 a) and Fig. 8.3 b) (1), in line with the nodal points of one face of the structure. Standard green LEDs with a diameter of 5 mm are used. They are clipped to aluminum slats parallel to the plate edges with custom made 3D printed plastic brackets. The bracket angle can be adjusted such that the emitters point towards the camera. An optical bandwidth filter (ThorLabs FL05532-10) is mounted in front of the camera. Given the exposure time is sufficiently short, it passes only the green LED light. Image data is read in via USB and processed on the host PC. More details on how the emitter positions are determined are provided in the following section.

Besides the strain gauges, three LDVs are connected to the MicroLabBox and provide accurate displacement information in one axis. They are used as a reference to validate the estimation results in Section 8.1.5.

Nodal Position Tracking

Light from the LEDs attached to the scale model is registered by charge-coupled devices (CCDs) in the camera and is mapped to nodal positions from pixel coordinates. Calibration of the camera and correction of lens distortion is done with the help of a printed checkerboard pattern of known size and location. The algorithms used for this purpose are part of the Open Source Computer Vision Library (openCV) [18].

Precise locations are usually obtained for high integration times which, however, result in low sampling frequencies. Mounting a filter that matches with the emitter wavelength in front of the camera lens significantly increases the signal-to-noise ratio (SNR) and allows for shorter sampling periods. Image positions obtained for the emitters are preprocessed on the host PC, as shown in Fig. 8.4. A simple model comprising the expected number of points as well as their approximate location is

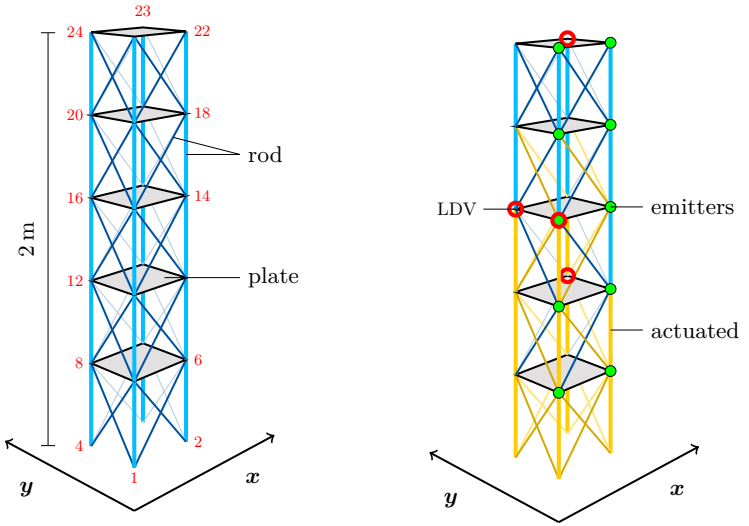

(a) Columns and bracings are modeled as rods, floors as plates. Node numbers are shown in red

(b) Actuated elements (yellow), camera-tracked nodes (green) and LDV-tracked nodes (red)

Figure 8.5: Adaptive truss structure scale model [134]

used to test for measurement errors and to ensure that the information is always sent to the MicroLabBox in a predetermined order.

In the following sections, the model used for state estimation and the corresponding sensor fusion algorithms for the integration of camera system measurements and strain gauge data are presented.

8.1.2 System dynamics

The dynamics of the scale model are described by a linear port-Hamiltonian system model of the form (4.46)

$$\begin{bmatrix} M\ddot{q} \\ \dot{q} \end{bmatrix} = \left(\underbrace{\begin{bmatrix} 0 & -I \\ I & 0 \end{bmatrix}}_{J} - \underbrace{\begin{bmatrix} D & 0 \\ 0 & 0 \end{bmatrix}}_{R} \right) \underbrace{\begin{bmatrix} M^{-1} & 0 \\ 0 & K \end{bmatrix}}_{Q} \underbrace{\begin{bmatrix} M\dot{q} \\ q \end{bmatrix}}_{x} + \underbrace{\begin{bmatrix} F_{\mathrm{a}} \\ 0 \end{bmatrix}}_{G} u, \tag{8.1a}$$

$$y = G^{\mathrm{T}} Q x, \tag{8.1b}$$

with $\boldsymbol{q} \in \mathbb{R}^{n_{\mathrm{DOF}}}$, $\boldsymbol{x} \in \mathbb{R}^{2n_{\mathrm{DOF}}}$ and $\boldsymbol{u} \in \mathbb{R}^{n_a}$, where n_a denotes the number of actuators. Mass and stiffness matrix of the structure are assembled according to the procedure described in Chapter 5 with element types as indicated in Fig. 8.5 a). Columns and diagonal bracings are modeled as rods ($N_{\mathrm{n}} = 2$ nodes), module floors and ceilings as Mindlin plates combined with a disk element for axial loads ($N_{\mathrm{n}} = 9$ each). Translational DOFs for nodes one to four are eliminated. After system assembly, the resulting structure model has $n_{\mathrm{DOF}} = 225$ DOFs. Different stiffness values are assumed for active and passive columns due to constructional differences. In Fig. 8.5 b) the $n_u = 31$ actuated elements are highlighted in yellow. The actuator dynamics are assumed negligible such that the actuators can be included in the dynamic equations as force inputs with the input matrix $\boldsymbol{F}_{\mathrm{a}}$. Accurate determination of the matrix $\boldsymbol{D}$ is demanding, due to the complex interplay of different damping effects. A common approximation is the assumption of Rayleigh damping with

$$\boldsymbol{D} = \alpha_0 \boldsymbol{M} + \alpha_1 \boldsymbol{K}. \tag{8.2}$$

The coefficients α_0 and α_1 can be determined through an experiment or by parameter identification as in [80]. Rayleigh damping is not physically motivated, but it has several convenient properties. For instance, it ensures that the mode shapes remain the same as for the undamped system. This is desirable when performing a modal analysis of (8.1).

As described in Section 8.1.1, strain gauges and a camera are used as sensors. Signals from the strain gauges are converted to force measurements. The force F_{e}^i acting on each element i is related to the state as follows

$$F_{\mathrm{e}}^i(\boldsymbol{x}) = k_i \left(\left\| \boldsymbol{d}^i \boldsymbol{x} + \boldsymbol{e}_0^i \right\|_2 - L_0^i \right), \quad i = 1 \dots n_{\mathrm{sg}} \tag{8.3}$$

with k_i the spring constant and n_{sg} the number of strain gauges. In case of zero stress, L_0^i denotes the element length and $\boldsymbol{e}_0^i$ the i-th element vector. Multiplying $\boldsymbol{d}^i$ by $\boldsymbol{x}$ yields the displacement vector of the respective element. For the output mapping, (8.3) is linearized with respect to the initial state $\boldsymbol{x}_0 = 0$ such that

$$\boldsymbol{y}_{\mathrm{sg}} = \boldsymbol{C}_{\mathrm{sg}} \boldsymbol{x} = \left. \frac{\partial \boldsymbol{F}_e}{\partial \boldsymbol{x}} \right|_{\boldsymbol{x}_0} \boldsymbol{x}. \tag{8.4}$$

As the strain gauges were not calibrated for measuring absolute element forces, the predicted forces $\boldsymbol{F}_{\mathrm{e}}$ cannot be directly related to the measured signals. To circumvent this difficulty, both the measured forces $\boldsymbol{y}_{\mathrm{sg}}$ and the predicted forces are filtered with a first-order Butterworth high-pass filter with a cutoff frequency of $f_{\mathrm{c}} = 0.1\,\mathrm{Hz}$. This removes the constant offset between modeled and measured element forces. It comes, however, at the cost of having to rely on the model for estimating the stationary element forces. Previous calibration of each individual strain gauge sensor is recommended in order to avoid this issue.

The camera measures the x- and z- displacements of the nodes highlighted in green in Fig. 8.5 b). A corresponding output mapping is easily obtained by selecting the respective DOFs from $\boldsymbol{q}$ such that the total measurement output is given by

$$\boldsymbol{y}_\mathrm{f} = \begin{bmatrix} \boldsymbol{y}_\mathrm{sg} \\ \boldsymbol{y}_\mathrm{cam} \end{bmatrix} = \begin{bmatrix} \boldsymbol{C}_\mathrm{sg} \\ \boldsymbol{C}_\mathrm{cam} \end{bmatrix} \boldsymbol{x} = \boldsymbol{C}\boldsymbol{x}. \tag{8.5}$$

With 10 emitters and two spatial directions, the number of camera measurements $\boldsymbol{y}_\mathrm{cam} \in \mathbb{R}^{n_\mathrm{cam}}$ amounts to $n_\mathrm{cam} = 20$. Both strain gauge signals and camera measurements are obtained at a sampling frequency of $T_\mathrm{s} = 100\,\mathrm{Hz}$. In the following, the dynamic model (8.1) is used together with the output mapping (8.5) to design both centralized and decentralized observers.

8.1.3 Centralized and decentralized sensor fusion

Decentralized observers with local models obtained by dynamic condensation are tested on the scale model. Centralized estimation is performed for comparison. Since the scaled high-rise consists of five structurally identical modules, these naturally offer themselves as local subsystems for decentralized sensor fusion. A local observer is designed according to the approach presented in Section 7.2 by selecting the local DOFs $\boldsymbol{q}_\mathrm{a}$ of each module accordingly. Each observer is assigned the full camera measurement output, assuming that it is communicated to all subsystems via a bus. Only the locally available strain gauges (12 in each module) are accessed. Accordingly, the local measurement output becomes

$$\boldsymbol{y}_{\mathrm{f},m} = \begin{bmatrix} \boldsymbol{C}_{\mathrm{sg},m} \\ \boldsymbol{C}_\mathrm{cam} \end{bmatrix} \boldsymbol{x}_m = \boldsymbol{C}_m \boldsymbol{x}_m, \tag{8.6}$$

where $m = 1 \ldots 5$. With the local subsystems according to (7.23), the decentralized observers are given as

$$\dot{\hat{\boldsymbol{x}}}_m = (\boldsymbol{J}_m - \boldsymbol{R}_m - \boldsymbol{L}_m \boldsymbol{C}_m \boldsymbol{Q}_m^{-1}) \boldsymbol{Q}_m \hat{\boldsymbol{x}}_m + \boldsymbol{G}_m \boldsymbol{u} + \boldsymbol{Q}_m^{-1} \boldsymbol{C}_m^\mathrm{T} \boldsymbol{u}_{\mathrm{f},m} + \boldsymbol{L}_m \boldsymbol{y}_{\mathrm{f},m}, \tag{8.7a}$$

$$\hat{\boldsymbol{y}} = \boldsymbol{G}_m^\mathrm{T} \boldsymbol{Q}_m \hat{\boldsymbol{x}}_m, \tag{8.7b}$$

$$\hat{\boldsymbol{y}}_{\mathrm{f},m} = \boldsymbol{C}_m \hat{\boldsymbol{x}}_m, \tag{8.7c}$$

with $\boldsymbol{u}_{\mathrm{f},m} = 0$ the virtual input that is collocated to $\boldsymbol{y}_{\mathrm{f},m}$. The gain $\boldsymbol{L}_m$ of each local Luenberger observer is given by (7.7) as

$$\boldsymbol{L}_m = \boldsymbol{Q}_m^{-1} \boldsymbol{C}_m^\mathrm{T} \boldsymbol{R}_{\mathrm{f},m}^{-1}. \tag{8.8}$$

A diagonal matrix is chosen for $\boldsymbol{R}_{\mathrm{f},m}$ with different weights for the camera and the strain gauge sensor signals. Regarding the strain gauge weights, it is further differentiated between bracings and columns such that

$$\boldsymbol{R}_{\mathrm{f},m} = \mathrm{diag}\left(r_\mathrm{b} \cdot \boldsymbol{b}_m + r_\mathrm{c} \cdot \boldsymbol{c}_m, \quad r_\mathrm{cam} \cdot \boldsymbol{I} \right), \tag{8.9}$$

where r_b, r_c and r_cam are the weights on strain gauges mounted on bracings, columns and the camera measurements, respectively. The vector $\boldsymbol{b}_m$ selects the module's bracings from the set of available strain gauge measurements, whereas $\boldsymbol{c}_m$ selects its columns. All local observers use the same weight factors.

For the centralized observer, the output equation (8.5) is used, while measurement weights remain identical to the ones in the decentralized setting. Centralized sensor fusion cannot be performed in real-time on the hardware described in Section 8.1.1 when using the full-order model (8.1). Thus, modal analysis, as described in Section 7.2, is employed to truncate high-frequency eigenmodes. Selecting a reduced number of primary eigenmodes $\boldsymbol{\eta}_\mathrm{r} \in \mathbb{R}^{n_\mathrm{r}}$, the centralized observer can be expressed as

$$\dot{\hat{\boldsymbol{x}}}_\mathrm{c} = (\boldsymbol{J}_\mathrm{c} - \boldsymbol{R}_\mathrm{c} - \boldsymbol{L}_\mathrm{c}\boldsymbol{C}_\mathrm{c}\boldsymbol{Q}_\mathrm{c}^{-1})\boldsymbol{Q}_\mathrm{c}\hat{\boldsymbol{x}}_\mathrm{c} + \boldsymbol{G}_\mathrm{c}\boldsymbol{u} + \boldsymbol{Q}_\mathrm{c}^{-1}\boldsymbol{C}_\mathrm{c}^\mathrm{T}\boldsymbol{u}_\mathrm{f} + \boldsymbol{L}_\mathrm{c}\boldsymbol{y}_\mathrm{f}, \tag{8.10a}$$

$$\hat{\boldsymbol{y}} = \boldsymbol{G}_\mathrm{c}^\mathrm{T}\boldsymbol{Q}_\mathrm{c}\hat{\boldsymbol{x}}_\mathrm{c}, \tag{8.10b}$$

$$\hat{\boldsymbol{y}}_\mathrm{f} = \boldsymbol{C}_\mathrm{c}\hat{\boldsymbol{x}}_\mathrm{c}, \tag{8.10c}$$

where $\boldsymbol{J}_\mathrm{c}$, $\boldsymbol{R}_\mathrm{c}$, $\boldsymbol{Q}_\mathrm{c}$ and $\boldsymbol{G}_\mathrm{c}$ are computed according to (7.22) with $\boldsymbol{T}_\mathrm{H} = \boldsymbol{I}$ and $\boldsymbol{\Phi}_m = \boldsymbol{\Phi}_\mathrm{r}$ from (7.15). The state vector of the centralized observer becomes $\boldsymbol{x}_\mathrm{c}^\mathrm{T} = \begin{bmatrix}\dot{\boldsymbol{\eta}}_\mathrm{r}^\mathrm{T} & \boldsymbol{\eta}_\mathrm{r}^\mathrm{T}\end{bmatrix}$ and the gain of the Luenberger observer is given by

$$\boldsymbol{L}_\mathrm{c} = \boldsymbol{Q}_\mathrm{c}^{-1}\boldsymbol{C}_\mathrm{c}^\mathrm{T}\,\mathrm{diag}\left(r_\mathrm{b}\cdot\boldsymbol{b} + r_\mathrm{c}\cdot\boldsymbol{c},\quad r_\mathrm{cam}\cdot\boldsymbol{I}\right)^{-1}, \tag{8.11}$$

where $\boldsymbol{C}_\mathrm{c}$ is the transformed output matrix and $\boldsymbol{b}, \boldsymbol{c} \in \mathbb{R}^{n_\mathrm{sg}}$ are the binary bracing and column selection vectors for the full set of strain gauges.

8.1.4 Self-tuning algorithm

With the stiffness and damping parameters initially assumed in the modeling process, state estimation results are not satisfactory. As it is usually the case, assumed model parameters do not reproduce the behavior of the real structure exactly. Neglecting friction and additional mass due to motor controllers are possible reasons for the occurrence of such mismatches. Also, table excitation is not modeled as a disturbance.

In the following, an optimization-based method for simultaneous tuning of both model and observer parameters is presented. The algorithm employs the centralized observer, but resulting parameter values are adopted for the local observers as well. While the parameters are varied, estimated displacements are compared to reference measurements aiming to minimize the estimation error. In order for the algorithm to be self-tuning, selected camera measurements serve as reference measurements and are consequently not used for state estimation. Although the method presented here cannot be used for real-time adaptation of parameters, it can be applied for periodic model updating, given that a number of accurate measurements are available during excitation. Considering that structural parameters are not expected to change

significantly over longer periods of time, this is a reasonable option. Online joint state-parameter estimation, on the other hand, leads to a considerable increase in complexity.

In the optimization process, stiffness and damping parameters are adjusted along with the observer weights in order to minimize the estimation error. To avoid reassembly of the model for each parameter set, only the spring constants in (8.3) are adapted. The vector of element spring constants is defined as follows

$$\boldsymbol{\kappa} = \boldsymbol{b} \cdot k_\mathrm{b} + \boldsymbol{c}_\mathrm{a} \cdot k_\mathrm{ca} + \boldsymbol{c}_\mathrm{p} \cdot k_\mathrm{cp}, \tag{8.12}$$

where k_b is the spring constant corresponding to diagonal bracings. The centralized column selection vector $\boldsymbol{c}$ is split into active columns $\boldsymbol{c}_\mathrm{a}$ and passive columns $\boldsymbol{c}_\mathrm{p}$, since the spring constant of active columns $\boldsymbol{k}_\mathrm{ca}$ differs from $\boldsymbol{k}_\mathrm{cp}$ of the passive ones. Including the Rayleigh damping coefficients and the observer weights, the tunable parameters are summarized in the vector

$$\boldsymbol{p}^\mathrm{T} = \begin{bmatrix} \alpha_0 & \alpha_1 & k_\mathrm{b} & k_\mathrm{ca} & k_\mathrm{cp} & r_\mathrm{b} & r_\mathrm{c} \end{bmatrix}.$$

Note that the camera weight $\boldsymbol{r}_\mathrm{cam}$ is not included in the set of tunable parameters. Else, the optimization algorithm tends to put excessive weight on the camera measurements.

For self-tuning, the table is excited with a chirp signal in x-direction. A disturbance input is used for identification on purpose since active excitation of the structure is not desired in a real scenario. Considering an actual building, recorded measurements during a storm can be used. The tuning algorithm is formulated as an optimization problem

$$\begin{aligned} \min_{\boldsymbol{p}} \quad & \frac{1}{n_\mathrm{c} \cdot N} \sum_{k=k_0}^{N} \left| \bar{\boldsymbol{y}}_k^\mathrm{cam} - \overline{\boldsymbol{C}} \hat{\boldsymbol{x}}_k \right| \\ \text{subject to} \quad & \boldsymbol{p}^\mathrm{l} \leq \boldsymbol{p} \leq \boldsymbol{p}^\mathrm{u}, \end{aligned} \tag{8.13}$$

where $\boldsymbol{p}^l$ and $\boldsymbol{p}^u$ define the upper and lower bounds for the parameter values. The matrix $\overline{\boldsymbol{C}}$ maps the state estimate $\hat{\boldsymbol{x}}_k^+$ at time t_k to the n_c camera measurements used as references and N is the number of processed samples. To reduce errors due to deviations of emitter locations from actual nodal positions, both $\bar{\boldsymbol{y}}^\mathrm{cam}$ and the estimated displacements are high-pass-filtered to obtain relative displacements for comparison. All parameters, including bounds, are normalized to the values initially assumed. The resulting stiffness parameters are adopted and the system matrices are recalculated.

8.1.5 Results and discussion

In this section, results obtained for both the parameter tuning algorithm and for centralized and decentralized state estimation are presented (in this order).

Table 8.1: Parameter tuning results

Name	Initial guess	p^{l}	p^{u}	p
α_1	0.5×10^{-1}	0.01	100	1.17
α_2	0.5×10^{-2}	0.01	100	1.80
k_{b}	18200 N/m	0.5	2	1.81
k_{ca}	19500 N/m	0.5	2	1.05
k_{cp}	22100 N/m	0.5	2	1.20
r_{b}	1.0×10^{3}	0.01	100	0.07
r_{c}	1.0×10^{3}	0.01	100	2.41

Parameter tuning

Parameter tuning is performed with the centralized observer (8.10). The dynamic model of the observer is composed of the 12 primary eigenmodes $\boldsymbol{\eta}_{\mathrm{r}}$ with lowest magnitude eigenvalues. Recorded signals for a table excitation in x-direction with a chirp signal ranging from $0.1 - 6$ Hz over a period of 10 s with an amplitude of 2 mm are used for parameter identification. The camera measurement weight is set to $r_{\mathrm{cam}} = 5 \times 10^{-6}$ in all experiments, for which results are reported in the following. Camera measurements for the x-displacements of nodes 6, 13 and 22 and the z-displacements of nodes 5, 14 and 21 are used as references. As depicted in Fig. 8.5 a), node numbers are assigned counter-clockwise and from bottom to top. Fig. 8.5 b) shows which nodes are tracked by either camera, LDVs or both measurement systems. When applying the method described in Section 8.1.4, the results shown in Tab. 8.1 are obtained. Note that p^{l}, p^{u} and p are normalized to the respective initial guess. Values from the spring manufacturer's data sheets were used as initial guesses for the spring constants k_{b}, k_{ca} and k_{cp}. They are identical to the values used for assembling the dynamic system model before tuning.

After optimization, damping coefficients are within reasonable ranges from their respective initial guesses. For the spring constant of passive columns k_{cp}, about 20 % deviation from the datasheet value is observed. The increase in stiffness can be explained by friction effects that were neglected in the modeling process. There is no straightforward explanation for the 81 % increase in diagonal bracing stiffness. Slackening of diagonal cables represents a strong nonlinearity that is entirely neglected. Pretension and the associated geometric stiffness, which is different in magnitude for each individual diagonal bracing, also partially explains this result. This also explains, why considerably more weight is put on bracing measurements as opposed to column strain gauge signals. A more accurate nonlinear model that includes the slackening effect of diagonal bracings is a potential remedy. However, this would lead to a significant increase in complexity and most likely to a loss of real-time performance. The effect is also not expected to be dominant in case of a full-scale building.

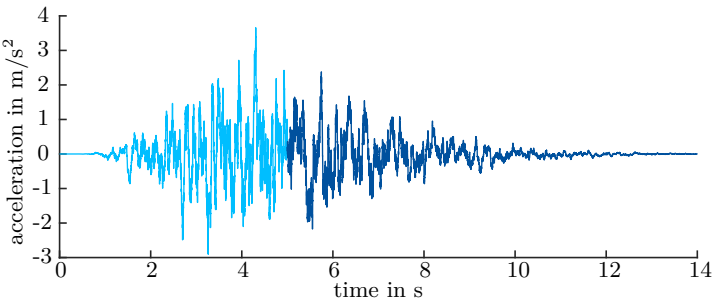

Figure 8.6: Sample generated ground acceleration record used for XY-table excitation. The displayed earthquake is of strong intensity with a peak ground acceleration of about 0.37 g and a dominant frequency of 4 Hz. Results in Section 8.1.5 are shown for the first 5 s (highlighted) [134]

Centralized observer

Using the model and filter parameters in Tab. 8.1, performance of the observers is evaluated for earthquake-like excitations of the XY-table. For high-rise buildings, strong wind loads occur more frequently than earthquakes, but are not easily transferable to the test bench. Therefore, it is chosen to evaluate the observer performance using earthquake excitations.

The ground acceleration data of different earthquakes was generated using Matlab code from [30]. Based on the work of [105] and [55], a non-stationary Kanai-Taijimi Model is used to create artificial earthquake records. Among other parameters, the duration, dominant frequency as well as the standard deviation in the power spectrum can be adapted. Experiments were conducted on the test bench with various earthquakes that were downscaled in amplitude to be consistent with the scale of the model. Scaling of a ground motion record is also done in e. g. [34], where the earthquake is applied to a similar structure model with a height of 1.8 m. The ground acceleration record that is used in the following to investigate the performance of observers, is shown in Fig. 8.6. Although several different earthquakes were applied to the structure, the conclusions that can be drawn from the results are similar, which is why only one representative ground motion is presented in detail here. The earthquake in Fig. 8.6 is of strong intensity with a dominant frequency of 4 Hz and a standard deviation of 4 Hz. Excitation of the test bench with the scaled earthquake was conducted in both directions separately.

Measurement results results in both x- and y-direction for a table excitation with the earthquake depicted in Fig. 8.6 are presented in Fig. 8.7. To enhance readability, only the onset and the first couple of seconds of the earthquake are shown. Similar results

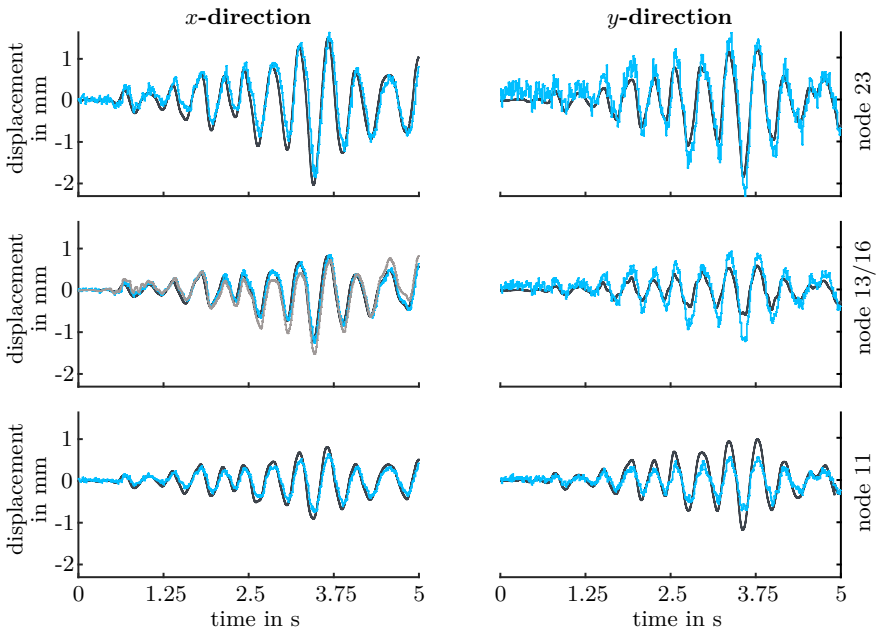

Figure 8.7: Estimated relative displacements of the centralized observer (light blue) compared to LDV measurements (dark gray) for nodes 11, 13 (x) or 16 (y) and 23. The table is excited in both x- and y-direction with the earthquake (to scale) shown in Fig. 8.6. The camera signal (light gray) is shown for node 13

are obtained for the remaining duration of the motion. A comparison between LDV measurements and state estimation results for the displacement of nodes 11, 13 (16 for the y-direction) and 23 is shown. Refer to Fig. 8.5 a) for the node numbering scheme.

Among the nodes tracked by LDVs, only node 13 is simultaneously tracked by the camera system, which is why the camera measurement is also visible for this node. Displacements are shown relative to the deformation before excitation and the table motion is subtracted from the LDV measurement. A maximum displacement of about 2 mm is observed for the topmost measured node.

Phase and amplitude of the estimated displacements in the x-direction are generally in good agreement with the LDV measurements. When comparing the camera measurement for node 13 with the motion recorded by the LDV, sub-mm deviations as well as a variable delay are visible. Owing to the strain gauge measurements, the estimated displacement is, however, more in phase with the reference and also tracks the amplitude more accurately. In the y-direction, the estimation accuracy is lower with respect to the oscillation amplitude. Overshoots are observed for nodes 16 and 23 while the amplitude is underestimated for node 11. There is no visible difference in phase tracking accuracy between the x- and y-direction. When going from the lowest measured node to the highest, the signal-to-noise ratio (SNR) decreases noticeably.

The difference between LDV and camera measurement can be attributed to two different factors. First, distortion is not completely eliminated by the projections involved in the image processing algorithm. Also, even though the LEDs were carefully positioned, their locations do not exactly match with the nodal points. Care must be taken in a real application to determine the position of LEDs as exactly as possible, as well as to ensure accurate camera calibration. With the current test bench setup, the varying camera delay cannot be determined reliably. More accurate phase tracking is expected when this information is available and employed by the observers.

A straightforward explanation for the lower estimation accuracy in the y-direction is that the observers lack camera measurements in this direction. Parameter identification in Section 8.1.4 was done for a motion in the x-direction, which is another reason for the observed differences. Supplying another camera for the y-direction (or using a stereo vision setup) potentially eliminates the differences.

Since the camera sensor is observed to be rather precise, it is concluded that the noise on the displacement estimations results almost entirely from the strain gauge sensors, which have a much lower SNR. The fact that the SNR decreases for higher stories is attributed to relative impacts of nodal displacements on each other. When a node in the first module moves, this causes relatively large displacements in the topmost story while a deformation of the top has little effect on the first floor in terms of displacements. Thus, noise of the strain gauges in the lower stories is amplified when computing the displacements of higher nodes. This has to be kept in mind when using strain gauges to estimate the building state, especially when sub-mm accuracy is to be achieved, which is desirable for a real building.

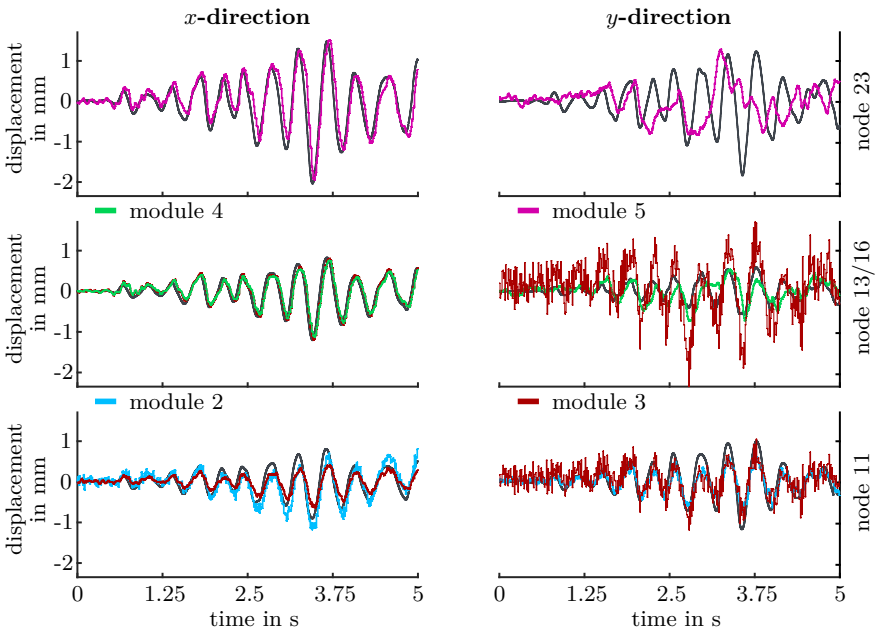

Figure 8.8: Estimated relative displacements from local observers compared to LDV measurements (dark gray) for nodes 11, 13 (x) or 16 (y) and 23. The table is excited in both x- and y-direction with the earthquake (to scale) shown in Fig. 8.6

Decentralized observers

Local models for the decentralized observers were derived from (8.1) by dynamic condensation (see Section 7.2) with $n_\mathrm{r} = n_m = 6$ primary eigenmodes for the lowermost module and $n_\mathrm{r} = n_m = 12$ primary eigenmodes for all others. The set of active DOFs $\boldsymbol{q}_\mathrm{a}$ of each subsystem includes all local DOFs (it is also possible to select only specific ones). Observers do not exchange state information and operate independently.

To enable comparison with the centralized observer, results are presented for the same earthquake record (see Fig. 8.6). In Fig. 8.8, the estimated displacements are depicted in the same style as in Fig. 8.7. Both an excitation in the x-direction and in the y-direction are considered. For each node tracked by an LDV, the available estimates of modules containing the respective DOF are shown. Since no LDV measurement is available in the first module, results are not shown for its observer. Because the

module DOFs overlap at nodes 11, 13 and 16, two estimates are visible, respectively. The DOFs of node 23 are only included in the model of module five.

When comparing the results for an excitation in x-direction with the centralized observer estimates, a similar estimation accuracy is observed. At node 13, the estimates calculated in the third module match well with those obtained in the fourth. However, in module four, the estimated amplitude is slightly lower while the phase delay is somewhat higher. The same can be observed for node 11 and modules two and three, where the difference in amplitude is more pronounced.

In the y-direction, the estimation results are worse than those obtained with the centralized observer in a variety of ways. First of all, high-frequency oscillations are visible for the estimates of module three. While the estimated displacement is still closely oriented at the LDV reference, the noise is considerably higher than in any of the other estimates. The estimated y-displacement of node 23 in module 5 shows similar oscillation frequencies and amplitudes, but is otherwise completely off the LDV measurement. However, there is less noise on the estimate than in the centralized case. The local observer of module four manages to track the reference approximately but sometimes fails to follow oscillation peaks and produces a varying phase delay. For node 11, the second module achieves an acceptable estimation accuracy that is also comparable to that of the centralized observer.

The observation that the estimation accuracy is lower for higher modules compared to lower ones can be explained by the fact that the SNR of the strain gauges is lower, the higher a strain gauge is located in the high-rise mockup. Measured forces are always highest in the lowermost module. When camera measurements are lacking (in y-direction) and the observers have to rely on the strain gauge measurements only, the estimation quality deteriorates. This explains the bad estimation quality for nodes 16 and 23 in the y-direction and stresses the importance of absolute position measurements in this sensor configuration. Since the local observers in higher modules do not access the strain gauges of the first, the noise-amplification effect discussed earlier does not occur in the decentralized case.

The excessive noise on the estimates of module three is due to an ill-conditioning caused by the highest-frequency mode included in the local dynamic model. In order to improve the estimation quality in the y-direction, two modifications are made to the decentralized observers. Firstly, the ill-conditioned mode is removed from the local model of the third module. To improve the tracking accuracy of the fifth module, a filter of the type presented in Section 7.5 is added. Since all modules can project their local estimates to the global state, information exchange between modules is easily achieved. A connection between module four and five is established by the the following filter gain

$$\boldsymbol{F}_5 = \boldsymbol{Q}_5^{-1}(\boldsymbol{T}_4^{+}\boldsymbol{U}_5)^{\mathrm{T}}\boldsymbol{R}_{\mathrm{s}5}^{-1}, \tag{8.14}$$

where $\boldsymbol{R}_{\mathrm{s}5}$ is chosen as a diagonal matrix with all diagonal entries set to 1×10^{-5} and $\boldsymbol{T}_4$ and $\boldsymbol{U}_5$ are the transformations from (7.21). Module five receives the full state

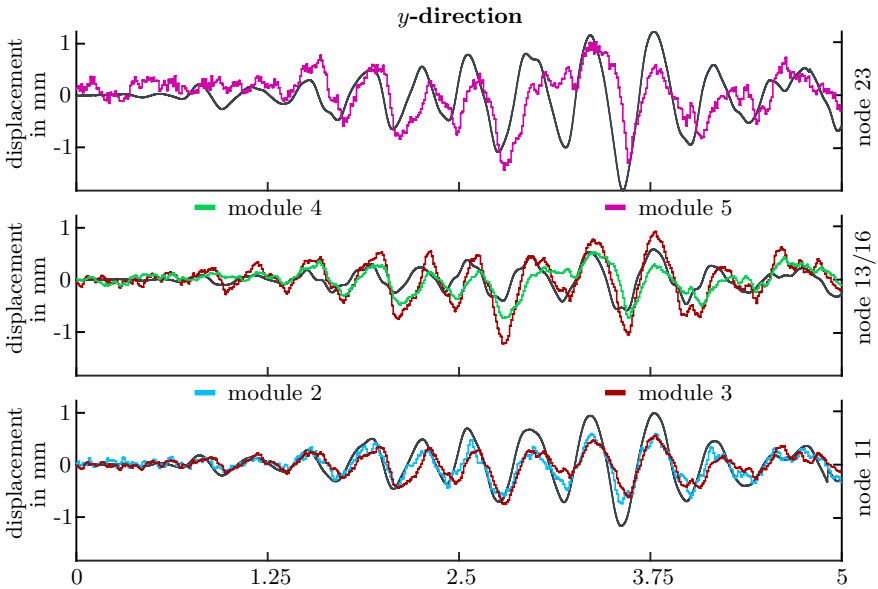

Figure 8.9: Estimated displacements for an earthquake in the y-direction with modified local observers

estimate $\hat{\boldsymbol{x}}_4$ in each time step and treats it as an additional measurement. It is also possible to transmit only the shared states to reduce bus or network load.

As visible in Fig. 8.9, the above modifications have the desired effects. The high-frequency noise on the local estimates of module three vanishes entirely. Estimation accuracy of the fifth module is also significantly higher. However, whenever module four fails to follow the reference signal, module five now mirrors this behavior. Interconnecting more modules with each other or giving each module access to more sensors would further increase both the estimation accuracy as well as the agreement between estimates of different modules.

It was shown that the approach presented in Section 7.2 together with the filters of Section 7.5 constitute flexible tools for designing decentralized observers for complex structures. For stiff systems, such as the ones considered here, numerical instability and ill-conditioned system matrices can become problematic issues. It is also important to supply each observer with an appropriate number of good quality measurements – either directly or by interconnection with other modules. In that case, the performance of the decentralized observers can be almost on a par with a centralized realization.

8.2 Decentralized observers for the high-rise demonstrator

In this application example, the adaptive high-rise demonstrator of the CRC 1244 is studied in numerical simulations using a simplified dynamical model. Both of the decentralized observer concepts introduced in Chapter 7 are implemented and compared to each other as well as to a centralized observer in terms of performance. As in the previous study of the scale model on the test bench in Section 8.1, strain gauges and cameras are used as sensors.

The same structure was studied in [132], [133] and [136], where the model was, however, not a port-Hamiltonian system. In the latter two contributions, control of the structure is also considered, which will not be done in the following. The model used for state estimation is briefly presented in Section 8.2.1, followed by the introduction of the different observer variants in Section 8.2.2. Estimation results obtained with each observer are compared and discussed in Section 8.2.3.

8.2.1 System dynamics

An illustration of the high-rise demonstrator model is shown in Fig. 8.10, together with its decomposition into the two substructures used for decentralized state estimation. The building is composed of four structurally identical three-story modules with a height of 9 m each. Its dynamics can be described in port-Hamiltonian form as

$$\begin{bmatrix} \boldsymbol{M}\ddot{\boldsymbol{q}} \\ \dot{\boldsymbol{q}} \end{bmatrix} = \left(\underbrace{\begin{bmatrix} \boldsymbol{0} & -\boldsymbol{I} \\ \boldsymbol{I} & \boldsymbol{0} \end{bmatrix}}_{\boldsymbol{J}} - \underbrace{\begin{bmatrix} \boldsymbol{D} & \boldsymbol{0} \\ \boldsymbol{0} & \boldsymbol{0} \end{bmatrix}}_{\boldsymbol{R}} \right) \underbrace{\begin{bmatrix} \boldsymbol{M}^{-1} & \boldsymbol{0} \\ \boldsymbol{0} & \boldsymbol{K} \end{bmatrix}}_{\boldsymbol{Q}} \underbrace{\begin{bmatrix} \boldsymbol{M}\dot{\boldsymbol{q}} \\ \boldsymbol{q} \end{bmatrix}}_{\boldsymbol{x}}, \tag{8.15}$$

where $\boldsymbol{q} \in \mathbb{R}^{n_{\mathrm{DOF}}}$ and $\boldsymbol{x} \in \mathbb{R}^{2n_{\mathrm{DOF}}}$. Since control of the structure is not considered in the following, no actuator input is included in the model.

The system matrices $\boldsymbol{M}$ and $\boldsymbol{K}$ are obtained by assembly of simple elements according to the procedure introduced in Chapter 5. Vertical columns are modeled as Euler-Bernoulli beams ($N_{\mathrm{n}} = 4$) with an additional rod and torsion bar for torsional and axial loads ($N_{\mathrm{n}} = 2$ each). The rest of the elements depicted in Fig. 8.10 are modeled as rods ($N_{\mathrm{n}} = 2$). Horizontal bars at the edges combined with two intersecting diagonal rods are used to represent floors plates. For the remaining geometry and material parameters of the structure, see Tab. 8.2. All translational DOFs as well as the rotation about the z-axis are locked for the lowermost four nodes. After the port-based assembly process, the global number of DOFs amounts to $n_{\mathrm{DOF}} = 296$. Rayleigh damping is assumed, such that

$$\boldsymbol{D} = \alpha_0 \boldsymbol{M} + \alpha_1 \boldsymbol{K}. \tag{8.16}$$

Table 8.2: Geometry and material parameters of the structure in Fig. 8.10

Description	**Formula sign**	**Value**	**Unit**
Density	ρ	7850	$\mathrm{kg/m^3}$
Young's modulus	E	210×10^9	$\mathrm{N/m^2}$
Poisson's ratio	ν	0.3	
Vertical columns, square hollow profiles			
Length	L_v	3	m
Width	w_v	0.3	m
Wall thickness	t_v	0.01	m
Horizontal rods, rectangular hollow profiles			
Length	L_h	4.75	m
Width	w_h	0.504	m
Height	h_h	0.12	m
Wall thickness	t_h	0.008	m
Horizontal diagonal rods			
Length	L_hd	6.72	m
Width	w_hd	0.01	m
Height	h_hd	0.06	m
Diagonal rods			
Length	L_vd	10.18	m
Width	w_vd	0.15	m
Height	h_vd	0.012	m

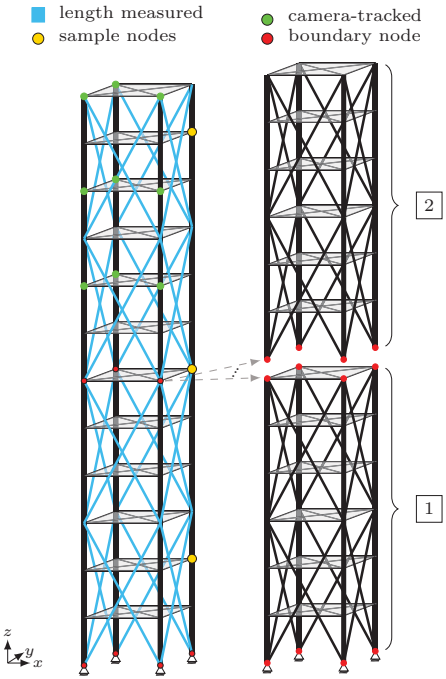

Figure 8.10: Schematic drawing of an adaptive high-rise building and its decomposition into two modules with elements equipped with strain gauges (blue), camera-tracked nodes (green), boundary nodes (red) and the nodes for which the x-displacement is plotted in the results section (yellow)

It is further assumed that all diagonal bracings are equipped with a strain gauge sensor measuring the element strain. The elements are colored in blue in Fig. 8.10. Nodes, for which the in-plane displacements are tracked by a camera-based system, are highlighted in green. In contrast to the test bench setup presented in Section 8.1, it is assumed that an additional camera (or a stereo-vision system) is at hand to measure motion in the y-z-plane. Then, the system output available to the observers can be expressed as

$$\boldsymbol{y}_{\mathrm{f}} = \begin{bmatrix} \boldsymbol{C}_{\mathrm{sg}} \\ \boldsymbol{C}_{\mathrm{cam}} \end{bmatrix} \boldsymbol{x} = \boldsymbol{C}\boldsymbol{x}, \tag{8.17}$$

where $\boldsymbol{C}_{\mathrm{sg}} \in \mathbb{R}^{32\times 2n_{\mathrm{DOF}}}$ maps the state vector to the strain of the diagonal bracings and $\boldsymbol{C}_{\mathrm{cam}} \in \mathbb{R}^{24\times 2n_{\mathrm{DOF}}}$ maps $\boldsymbol{x}$ to the respective displacements tracked by the cameras.

8.2.2 Observers

Main objective of this section is the comparison of the observer methods presented in Chapter 7. For this purpose, three observers are introduced for (8.15) – a centralized observer, decentralized observers with local models obtained by dynamic condensation and decentralized observers using a modular formulation.

In case of the scale model in Section 8.1, modal analysis is used to obtain a reduced order model for the centralized observer. The same is done for the high-rise demonstrator model here, which results in the centralized observer

$$\dot{\hat{\boldsymbol{x}}}_\mathrm{c} = (\boldsymbol{J}_\mathrm{c} - \boldsymbol{R}_\mathrm{c} - \boldsymbol{L}_\mathrm{c}\boldsymbol{C}_\mathrm{c}\boldsymbol{Q}_\mathrm{c}^{-1})\boldsymbol{Q}_\mathrm{c}\hat{\boldsymbol{x}}_\mathrm{c} + \boldsymbol{Q}_\mathrm{c}^{-1}\boldsymbol{C}_\mathrm{c}^\mathrm{T}\boldsymbol{u}_\mathrm{f} + \boldsymbol{L}_\mathrm{c}\boldsymbol{y}_\mathrm{f}, \tag{8.18a}$$

$$\hat{\boldsymbol{y}}_\mathrm{f} = \boldsymbol{C}_\mathrm{c}\hat{\boldsymbol{x}}_\mathrm{c}, \tag{8.18b}$$

where the state vector $\boldsymbol{x}_\mathrm{c}^\mathrm{T} = \begin{bmatrix}\dot{\boldsymbol{\eta}}_\mathrm{r}^\mathrm{T} & \boldsymbol{\eta}_\mathrm{r}^\mathrm{T}\end{bmatrix}$ is composed of a reduced number n_r of primary eigenmodes and their time derivatives. Compare with (8.10). The Luenberger observer gain $\boldsymbol{L}_\mathrm{c}$ is determined by

$$\boldsymbol{L}_\mathrm{c} = \boldsymbol{Q}_\mathrm{c}^{-1}\boldsymbol{C}_\mathrm{c}^\mathrm{T}\,\mathrm{diag}\left(r_\mathrm{sg}\cdot\boldsymbol{I}, \quad r_\mathrm{cam}\cdot\boldsymbol{I}\right)^{-1}, \tag{8.19}$$

with the strain gauge weights r_sg and the camera weights r_cam.

Decentralized observers with local models obtained from (8.15) are constructed just as in Section 8.1.3. Here, the number of modules amounts to two, with the local subsystems comprising half of the building, respectively (see Fig. 8.10). Only locally available strain gauges are used in each module, whereas the camera measurements are made available to both. Application of the method in Section 7.2 yields local observers of the form (7.23) as

$$\dot{\hat{\boldsymbol{x}}}_m = (\boldsymbol{J}_m - \boldsymbol{R}_m - \boldsymbol{L}_m\boldsymbol{C}_m\boldsymbol{Q}_m^{-1})\boldsymbol{Q}_m\hat{\boldsymbol{x}}_m + \boldsymbol{Q}_m^{-1}\boldsymbol{C}_m^\mathrm{T}\boldsymbol{u}_{\mathrm{f},m} + \boldsymbol{L}_m\boldsymbol{y}_{\mathrm{f},m}, \tag{8.20a}$$

$$\hat{\boldsymbol{y}}_{\mathrm{f},m} = \boldsymbol{C}_m\hat{\boldsymbol{x}}_m, \tag{8.20b}$$

where $\boldsymbol{C}_m$ is the local output map such that only the measurements of strain gauges in module m are included in $y_{\mathrm{f},m}$ and $m \in \{1, 2\}$. The local observer gain is given by

$$\boldsymbol{L}_m = \boldsymbol{Q}_m^{-1}\boldsymbol{C}_m^\mathrm{T}\,\mathrm{diag}\left(r_\mathrm{sg}\cdot\boldsymbol{I}, \quad r_\mathrm{cam}\cdot\boldsymbol{I}\right)^{-1}, \tag{8.21}$$

with a lower dimension of the identity matrix in case of the strain gauges than above. As in case of the decentralized observer for the scale model, all local DOFs are included in $\boldsymbol{x}_m$.

So far, the conceptually reverse approach to construct decentralized observers has not been investigated. Suppose that a model of the global system is not available in advance or not desired in the first place because certain details are not to be communicated. Further assume that dynamical models for the two subsystems depicted in Fig. 8.10 are available, respectively. In this case, decentralized observers may be designed according

to the approach explained in Section 7.3. For the implementation here, the system matrices of the two modules are assembled independently with the element types as described in the previous section.

Since the lowermost nodes of the second module are completely unsupported, the transformation to global coordinates (5.31) is singular. To cope with this issue, elastic bearings with a small stiffness are introduced for the translational DOFs and the rotation about the z-axis at each of the bottom nodes. The stiffness k_h of these "helper" bearings is set to a value that is negligible in comparison to that of the elements of the structure. This allows to carry out the transformation to global coordinates completely, without altering the dynamics to any significant extent.

Constraints between the two local systems are formulated according to (7.29). A local Luenberger observer is introduced for both modules with the gain

$$\boldsymbol{L}_i = \boldsymbol{Q}_i^{-1}\boldsymbol{C}_i^\mathrm{T}\,\mathrm{diag}\left(r_\mathrm{sg}\cdot\boldsymbol{I},\quad r_\mathrm{cam}\cdot\boldsymbol{I}\right)^{-1}, \tag{8.22}$$

where $i \in \{1,2\}$. With the dynamics of the coupled systems according to (7.32), the observer for the first module becomes

$$\begin{aligned}\dot{\hat{\boldsymbol{x}}}_1 &= (\boldsymbol{J}_1 - \boldsymbol{R}_1 - \boldsymbol{L}_1\boldsymbol{C}_1\boldsymbol{Q}_1^{-1})\boldsymbol{Q}_1\hat{\boldsymbol{x}}_1 + \boldsymbol{L}_1\boldsymbol{y}_{\mathrm{f},1} + \boldsymbol{B}_1\boldsymbol{\lambda},\\ \hat{\boldsymbol{y}}_{\mathrm{f},1} &= \boldsymbol{C}_1\hat{\boldsymbol{x}}_1,\\ \hat{\boldsymbol{x}}_{\mathrm{s}1} &= \boldsymbol{C}_{\mathrm{s}1}\hat{\boldsymbol{x}}_1,\end{aligned} \tag{8.23}$$

with $\boldsymbol{x}_1 \in \mathbb{R}^{304}$, $\boldsymbol{x}_{\mathrm{s}1} \in \mathbb{R}^{24}$ the interface DOFs shared with the upper module and $\boldsymbol{\lambda} \in \mathbb{R}^{24}$ the coupling forces. Note that the virtual input collocated to $\boldsymbol{y}_{\mathrm{f},1}$ has been omitted in the above for the sake of a more compact notation.

The coupling forces "punish", or rather, prevent differences in (angular) velocity at the interface, but not in absolute displacement and rotation angle. This is especially problematic for the second module, which is only minimally supported with the "helper" bearings. The filters introduced in Section 7.5 are designed to resolve this issue. Thus, an additional Luenberger-type filter is added to the observer of the second module with the gain

$$\boldsymbol{F}_2 = \boldsymbol{Q}_2^{-1}\boldsymbol{C}_{\mathrm{s}2}^\mathrm{T}\boldsymbol{R}_{\mathrm{s}2}^{-1}, \tag{8.24}$$

where $\boldsymbol{C}_{\mathrm{s}2}$ maps the state vector $\boldsymbol{x}_2 \in \mathbb{R}^{336}$ of the second module to the shared interface DOFs and $\boldsymbol{R}_{\mathrm{s}2} = r_\mathrm{s}\cdot\boldsymbol{I}$. Effectively, this filter will make the local observer of the second module track the positions (angles) of the first. Accordingly, the observer of the upper subsystem is given as

$$\begin{aligned}\dot{\hat{\boldsymbol{x}}}_2 &= [\boldsymbol{J}_2 - \boldsymbol{R}_2 - (\boldsymbol{L}_2\boldsymbol{C}_2 + \boldsymbol{F}_2\boldsymbol{C}_{\mathrm{s}2})\boldsymbol{Q}_2^{-1}]\boldsymbol{Q}_2\hat{\boldsymbol{x}}_2 + \boldsymbol{L}_2\boldsymbol{y}_{\mathrm{f},2} + \boldsymbol{F}_2\hat{\boldsymbol{x}}_{\mathrm{s}1} + \boldsymbol{B}_2\boldsymbol{\lambda},\\ \hat{\boldsymbol{y}}_{\mathrm{f},2} &= \boldsymbol{C}_2\hat{\boldsymbol{x}}_2,\\ \hat{\boldsymbol{x}}_{\mathrm{s}2} &= \boldsymbol{C}_{\mathrm{s}2}\hat{\boldsymbol{x}}_2,\end{aligned} \tag{8.25}$$

where the virtual inputs collocated to $\boldsymbol{x}_{\mathrm{s}2}$ and $\boldsymbol{y}_{\mathrm{f}2}$ were again left out. For details on the numerical implementation of the observers, refer to Section 7.4.

8.2.3 Results and discussion

As test scenario for the different observers, an initial displacement of the structure in the x-direction caused by a strong stationary wind load is considered. Gaussian noise is superimposed on the system output (8.17) to get the virtual measurements. The variance is set to $\sigma_{\mathrm{sg}} = 5.0 \times 10^{-9}\,\mathrm{m}^2$ for the strain gauges and to $\sigma_{\mathrm{cam}} = 3.0 \times 10^{-7}\,\mathrm{m}^2$ for the camera. A sample time of $T_{\mathrm{s}} = 0.01\,\mathrm{s}$ is used, which is also taken to be the time step of the observers. Damping coefficients of the structure are set to $\alpha_0 = 0.03$ and $\alpha_1 = 0.003$.

In the centralized observer's dynamic model, $n_{\mathrm{r}} = 12$ primary eigenmodes with the lowest magnitude eigenvalues are retained. The measurement weights are set to $r_{\mathrm{sg}} = 1.0 \times 10^{-10}$ and $r_{\mathrm{cam}} = 1.0 \times 10^{-7}$ for all observers. When deriving local observers from (8.15), $n_{\mathrm{r}} = 12$ primary eigenmodes are used for SEREP and again $n_{\mathrm{m}} = 12$ eigenmodes with lowest magnitude eigenvalues for modal truncation. For the additional filter $\boldsymbol{F}_2$ of the second substructure's modular observer, $r_{\mathrm{s}} = 1.0 \times 10^{-5}$ is chosen.

In Fig. 8.11, the estimates of the centralized observer (blue) are shown in comparison to the reference values (dark gray) for the first two seconds of the motion induced by the initial displacement. In this figure and in the ones that follow, the x-displacement q_x is shown on the left hand side and the velocity in x-direction, v_x, on the right hand side. Results are shown for the nodes highlighted in yellow in Fig. 8.10 from top to bottom. With zero initial displacement, the centralized observer requires a few time steps until it is in agreement with the reference. The onset takes almost 0.5 s for the velocity estimates and slight overshoots are visible. Afterward, no noticeable deviation from the reference values is visible.

In the same test scenario and with the parameters specified above, the decentralized observers with local models obtained from (8.15) produce the results shown in Fig. 8.12. Here, estimates that belong to the upper module ($m = 2$) are displayed in red, while estimates of the lower module ($m = 1$) are displayed in blue. Since the middle node belongs to the interface, estimates of both observers are available for it. Compared to the centralized observer, the decentralized observers have more noise on their estimates – especially considering v_x of the lowermost node. However, the decentralized observers has a significantly lower settling time. At the interface, good agreement between the estimated displacement is maintained, although minor differences can be spotted. Slightly higher deviations are visible from time to time in case of the velocities at the interface. Note that slight disagreement emerges between the reference and the estimate for v_x of the uppermost node around $t = 1.5\,\mathrm{s}$.

Virtually all of the unfavorable effects observed for the decentralized observers can be ascribed to numerical ill-conditioning of the local dynamic systems. In the previous study with the scale model conducted in Section 8.1, an ill-conditioned eigenmode had significant impact on the estimation quality. While the effects are less pronounced

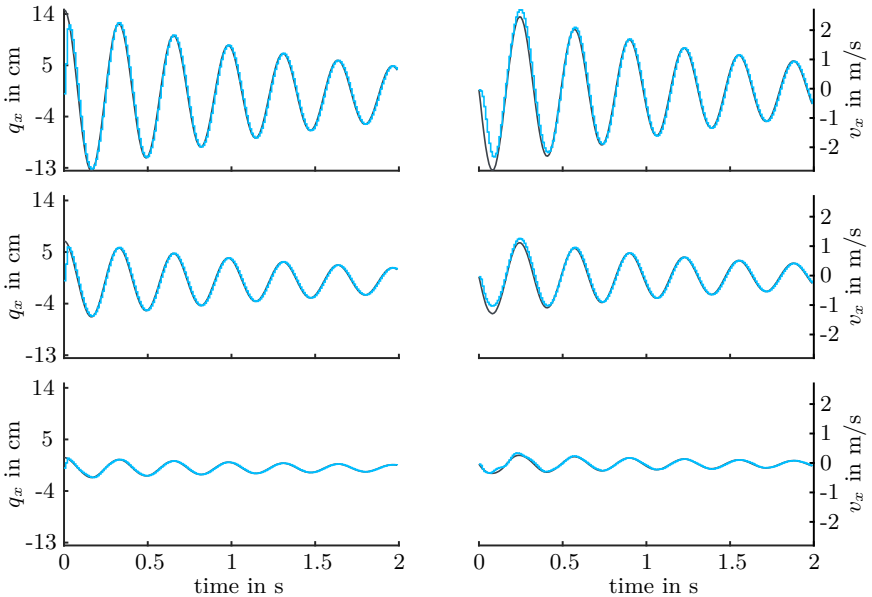

Figure 8.11: Estimated displacements q_x and velocities v_x of the centralized observer for an initial displacement shown for the nodes highlighted in yellow in Fig. 8.10 from top to bottom

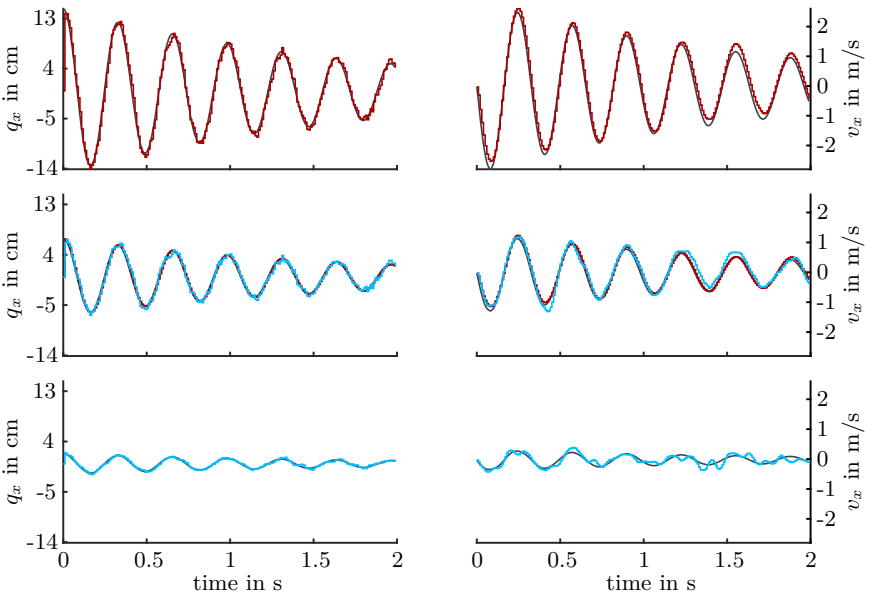

Figure 8.12: Estimated displacements q_x and velocities v_x of decentralized observers derived from (8.15) according to the method in Section 7.2

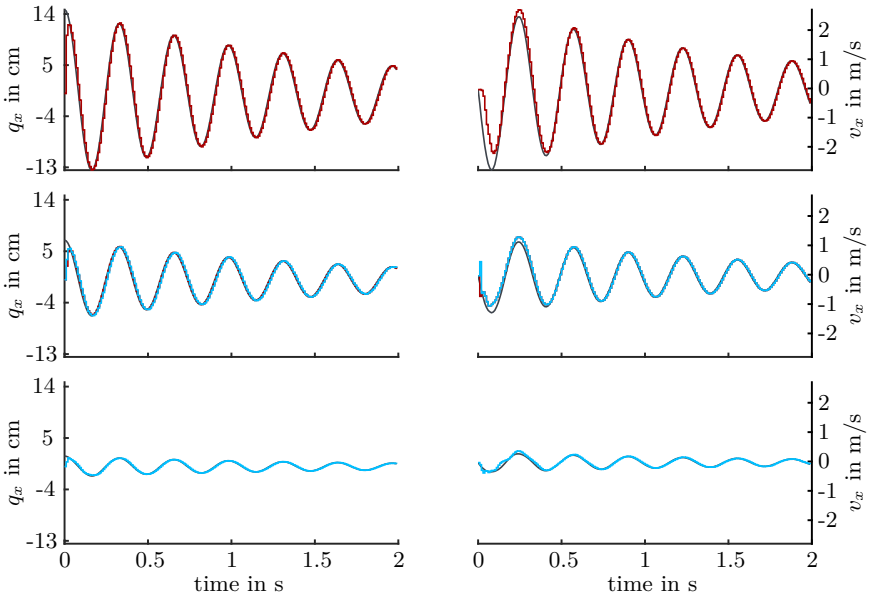

Figure 8.13: Estimated displacements q_x and velocities v_x of modular observers constructed according to the method in Section 7.3

here, it still shows that the dynamic condensation method combined with modal truncation has to be employed with caution. It is prone to reduce the prediction quality of the local models and potentially also destabilizes them. SEREP-Guyan reduction is, however, just one out of many possible ways to arrive at local models from a global one. While it is easily applicable and mostly produces acceptable results, other reduction approaches such as e. g. Krylov subspace methods need to be studied for finding even more suitable projection candidates for this purpose.

The results obtained with the modular observers are depicted in Fig. 8.13. On first sight, not much of a difference in performance is visible with respect to the centralized observer. Settling time and tracking capability are almost identical. A closer look on the onset of the simulation reveals that there is a slight difference between the estimates of q_x and v_x at the interface. In case of the velocities, this deviation is effectively reduced to zero after not more than two time steps. The displacements do not match perfectly over the whole two second interval, although this is hardly visible in Fig. 8.13.

For a less qualitative comparison between the observers, the root mean square (RMS)

Table 8.3: RMS errors of the observer estimates ($t = 0 \ldots 5\,\mathrm{s}$)

Obs.	Mod.	E_q in mm	E_φ in mrad	E_v in mm/s	E_ω in mrad/s
CO	1	1.28	0.120	18.8	2.39
CO	2	3.61	0.158	52.3	4.38
DO	1	1.39	0.296	60.0	19.1
DO	2	3.90	0.223	76.4	17.1
MO	1	1.34	0.135	24.5	5.47
MO	2	3.29	0.157	65.5	6.56

error is calculated for the displacements $\boldsymbol{q}$, the rotation angles $\boldsymbol{\varphi}$, the velocities $\boldsymbol{v}$ and the angular velocities $\boldsymbol{\omega}$ in the interval $t = 0 \ldots 5\,\mathrm{s}$. The RMS errors E_q, E_φ, E_v and E_ω are listed per module in Tab. 8.3. Note that "CO" stands for "centralized observer", "DO" for "decentralized observer" and "MO" for "modular observers".

The error analysis shows that the modular observers perform slightly worse than the centralized observer in all categories. This was to be expected, since the local observers do not have access to all the measurements. The performance of the decentralized observers is comparatively poor, but still acceptable. This is filed as the trade-off that comes with the easy implementation and flexibility of the approach. In case an even more suitable reduction method is found, the negative side effects can be reduced.

The attentive reader might have noticed that the high-rise depicted in Fig. 8.10 perfectly offers itself for a decomposition into four, instead of two substructures. The reason why the two-module case is studied here, is – beside simplicity – that implementing the modular approach with four local modules led to an unstable system. The higher stiffness and the additional difficulty of having to couple virtually unsupported modules with each other cannot be handled for this high-rise building in a straightforward manner. Especially the latter issue is of unpleasant nature and requires further investigation. This problem does not arise for e. g. bridges with a wide span, where individual modules are always supported on the ground if they are of adequate size. The approaches presented in this thesis provide a good starting point for the development of more involved methods adapted to specific applications.

9 Conclusion

Adaptive structures constitute a viable means to reduce the negative ecological impact of the construction sector, which is of utmost importance for a more sustainable society. Technological development in this field enables ultra-lightweight construction with a significantly lower embodied energy. At the same time, taller, wider and more slender structures can be realized due to the ability of an adaptive structure to manipulate its configuration or the internal stress distribution when faced with changing loads. Research on and practical implementation of adaptive structures is currently very limited. Yet, technological challenges that need to be solved for a broader acceptance of the concepts are numerous. This thesis has been concerned with two of them – suitable modeling of these complex and heterogeneous systems, as well as state estimation for active structural control.

Energy-based approaches, in particular port-Hamiltonian systems, are considered especially fitting for describing the dynamics of adaptive structures. Natural incorporation of systems from other physical domains with mechanical structures and the preservation of convenient properties on manipulation and interconnection are among the most notable advantages. The port-based modeling approach is intrinsically tied to a modular system conception, which makes it suitable for decentralizing methods for state estimation and control. With the complexity and size of adaptive structures in mind, methods for decentralized state estimation have been proposed in this work. This leads to locally reduced complexity and enhances redundancy, reusability and exchangeability.

Port-Hamiltonian models to capture the dynamic behavior of adaptive structures have been introduced. This includes linear elastic components, such as rods, beams and also elements for plane load-bearing structures. The dynamics of elastic elements are described by PDEs that need to be spatially discretized to perform numerical simulations. This has to be done in a way that the symplectic structure of the systems is preserved. Amongst the available structure-preserving methods, PFEM has been considered a suitable choice and its application to the class of systems presented in this thesis has been demonstrated. Analysis of the method's approximation error has been conducted in a variety of test scenarios for each system of equations. In a comparison to FEM, the common points and the differences of the approaches have been highlighted to make the energy-based approach more accessible for readers associated with the "classical" disciplines.

Coupling individual elements to form complex systems the way it is e. g. done for FE models is not in line with the port-based philosophy of the energy-based approach. On this account, a straightforward and automatic way to couple subsystem at their ports using algebraic constraints has been proposed. Also, it has been demonstrated that the resulting systems can be transformed until it is revealed that they match with a port-Hamiltonian reformulation of the second-order equations of motion obtained via FEM. This yields valuable insights and promotes the understanding of the energy-based concepts across disciplines. Hydraulic actuators have served as an example

of non-mechanical subsystems that can be seamlessly coupled with the mechanical structure within the port-Hamiltonian framework. Even though the proposed coupling procedure can only be fully carried out for linear systems, it can still be used to generate coupling constraints for the nonlinear hydraulic components. These can then be solved for to obtain an explicit system representation.

With the models assembled according to the procedure that has been introduced in this thesis, state observers for adaptive structures can be constructed. It is possible to design Luenberger-type observers in a way that they constitute port-Hamiltonian systems themselves. Decentralization of these observers can be carried out on the level of the system model. Two different approaches have been proposed to obtain local dynamic models. Either, one projects from the state space of a global system model to local DOFs, or a decentralized setup is obtained by interconnection of individual modules – without prior knowledge of the global model. In the former case, the SEREP-Guyan transformation has been suggested for deriving local subsystems. In the latter, coupling constraints are formulated at the interface of interconnected modules. Separate simulation of the modules then requires the use of co-simulation techniques to prevent violation of the constraints between discrete simulation steps.

Various simulation models of adaptive structures from the CRC 1244 have served for evaluating the performance of the methods presented in this work. Actual experiments have been conducted on a laboratory scale mockup of the demonstrator, for which decentralized sensor fusion has been carried out using strain gauge signals and camera-based displacement measurements. It has been observed that the mockup exhibits nonlinear behavior due to the slackening of diagonal bracings and friction, which impairs the accuracy of the linear system model. However, performance of both centralized and decentralized observers has been satisfactory, as long as measurements of the absolute node positions are available in the directions of interest. In the test bench study, as well as in simulations with the full scale demonstrator model, it has been noticed that local models obtained via the SEREP-Guyan method suffer from numerical ill-conditioning. This motivates the investigation of alternative approaches for projecting from global to local DOFs and a thorough study with a greater variety of test scenarios. While being more involved regarding its implementation, modular observers interconnected using algebraic constraints have shown superior performance.

Work on the topics addressed in this thesis is far from being complete. Consider this an attempt to make energy-based methods accessible for the application to adaptive structures, which turned out a solid foundation for further research. Developing methods for decentralized control is perceived a logical continuation. Studying different types of adaptive structures, e. g. plane load-bearing ones but also larger and more complex ones, another. Investigating different actuation principles also suggests itself. The author hopes that readers, with the help of this document, are encouraged to give the port-Hamiltonian approach a try – not only in the context of adaptive structures.

A From virtual work to the equations of motion

A.1 The principle of virtual work

Suppose that the location $\boldsymbol{r}$ of a point P varies along a trajectory that complies with the laws of mechanics at all times. Let t_1 and t_2 be two instants in time with $t_2 > t_1$. Between t_1 and t_2, consider an arbitrary alternate trajectory $\boldsymbol{r}^*(t)$ that does not necessarily comply with the laws of mechanics. Then, the *virtual displacement* and the *virtual velocity* are defined as

$$\boldsymbol{\delta r} = \boldsymbol{r}^* - \boldsymbol{r} \quad \text{and} \quad \boldsymbol{\delta \dot{r}} = \dot{\boldsymbol{r}}^* - \dot{\boldsymbol{r}}. \tag{A.1}$$

This is illustrated in Fig. A.1. Note that both trajectories overlap at t_1 and t_2, such that

$$\boldsymbol{\delta r}(t_1) = \boldsymbol{\delta r}(t_2) = \boldsymbol{0}. \tag{A.2}$$

A virtual displacement $\boldsymbol{\delta r}$ takes place immediately in time $\delta t = 0$ and is compatible with the system constraints [113]. Note that the varied trajectory $r^*(t)$ is only compatible with the constraints in case they are holonomic.

Given the force balance for a point with mass m is multiplied by the virtual displacement $\boldsymbol{\delta r}$, the principle of d'Alembert for this point results as

$$(m\ddot{\boldsymbol{r}} - \boldsymbol{F})\boldsymbol{\delta r} = \boldsymbol{0}, \tag{A.3}$$

where $\boldsymbol{F}$ are the applied forces. It states that the virtual work performed by the forces acting on the mass particle for a virtual displacement $\boldsymbol{\delta r}$ is equal to zero [49]. This

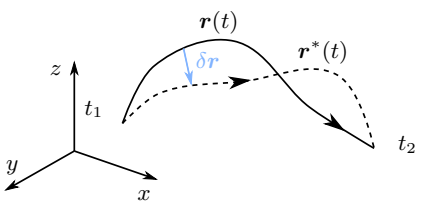

Figure A.1: Motion of a point along separate trajectories $\boldsymbol{r}(t)$ and $\boldsymbol{r}^*(t)$ with the virtual displacement $\delta\boldsymbol{r}(t)$

can be generalized to the case of continuous systems. Consider again the isotropic elastic continuum in Fig. 3.2 with boundary $\partial\Omega$. Then, the principle of d'Alembert for this body is obtained by integrating over all points in the body [113]

$$\int_\Omega \boldsymbol{\delta r}^{\mathrm{T}}(\boldsymbol{k} - \rho\ddot{\boldsymbol{r}}) - \boldsymbol{\delta\varepsilon}^{\mathrm{T}}\boldsymbol{\sigma}\,\mathrm{d}V + \int_{\partial\Omega} \boldsymbol{\delta r}^{\mathrm{T}}\boldsymbol{p}\,\mathrm{d}A = 0, \tag{A.4}$$

which is the same as (3.8). This can be written in compact form as

$$\delta W_{\mathrm{i}} + \delta W = 0, \tag{A.5}$$

where W_i denotes the virtual work performed by inertial forces given by

$$\delta W_{\mathrm{i}} = \int_\Omega \boldsymbol{\delta r}^{\mathrm{T}}\ddot{\boldsymbol{r}}\rho\,\mathrm{d}V. \tag{A.6}$$

The virtual work W_{int} produced by the internal forces and the virtual work W_{ext} associated with the external forces are summarized in $\delta W = \delta W_{\mathrm{int}} + \delta W_{\mathrm{ext}}$, with

$$\delta W_{\mathrm{int}} = -\delta U = -\int_\Omega \boldsymbol{\delta\varepsilon}^{\mathrm{T}}\boldsymbol{\sigma}\,\mathrm{d}V, \tag{A.7}$$

where U denotes a potential from which the forces are derived. The work performed by external forces is obtained as

$$\delta W_{\mathrm{ext}} = \int_\Omega \boldsymbol{\delta r}^{\mathrm{T}}\boldsymbol{k}\,\mathrm{d}V + \int_{\partial\Omega} \boldsymbol{\delta r}^{\mathrm{T}}\boldsymbol{p}\,\mathrm{d}A. \tag{A.8}$$

Subsequently, using the definitions of this section, the equations of motion for an elastic body are derived from Hamilton's principle.

A.2 Equations of motion

For the derivation of the equations of motion from the principle of virtual work, the following definition of the variation of a functional is required. Consider a functional $\Phi(\boldsymbol{q}, \dot{\boldsymbol{q}}, t)$ evaluated e. g. on the trajectory $\boldsymbol{r}(t)$. The difference between the values of Φ on $\boldsymbol{r}^*(t)$ and the real trajectory can be expressed as

$$\Phi(\boldsymbol{q} + \boldsymbol{\delta q}, \dot{\boldsymbol{q}} + \boldsymbol{\delta}\dot{\boldsymbol{q}}, t) - \Phi(\boldsymbol{q}, \dot{\boldsymbol{q}}, t). \tag{A.9}$$

When the first term in the above equation is expanded into its first order Taylor approximation, the resulting linear approximation

$$\delta\Phi = \sum_{i=1}^{n} \frac{\partial\Phi}{\partial q_i}\delta q_i + \frac{\partial\Phi}{\partial\dot{q}_i}\delta\dot{q}_i \tag{A.10}$$

is referred to as the variation of the functional Φ [113].

The kinetic energy of a system is defined as

$$T = \frac{1}{2} \int_{\Omega} \dot{\boldsymbol{r}}^{\mathrm{T}} \dot{\boldsymbol{r}} \rho \, \mathrm{d}V. \tag{A.11}$$

After a series of transformations (see e. g. [113] or [49]), it can be shown that the term δW_{i} belonging to the inertial forces in (A.5) can be replaced with the variation of T. Integrating the result with respect to time between t_1 and t_2 yields a generalized version of Hamilton's principle

$$\int_{t_1}^{t_2} \delta T + \delta W = 0. \tag{A.12}$$

For conservative systems, external forces are required to result from a potential, such that (A.12) can be rewritten as [113]

$$\delta \int_{t_1}^{t_2} T(\boldsymbol{q}, \dot{\boldsymbol{q}}, t) - U(\boldsymbol{q}, t) \, \mathrm{d}t = 0, \tag{A.13}$$

where (3.7) was used and the variation was pulled out of the integral. With (A.10), the variations of T and U are obtained as

$$\delta T = \frac{\partial T}{\partial \boldsymbol{q}} \boldsymbol{\delta q} + \frac{\partial T}{\partial \dot{\boldsymbol{q}}} \boldsymbol{\delta} \dot{\boldsymbol{q}}, \quad \text{and} \quad \delta U = \frac{\partial U}{\partial \boldsymbol{q}} \boldsymbol{\delta q}. \tag{A.14}$$

After partial integration of the second term of δT in (A.13) with respect to time and taking into account that the virtual work is zero at the integration bounds, the following form results

$$\int_{t_1}^{t_2} \left[-\frac{\mathrm{d}}{\mathrm{d}t} \frac{\partial T}{\partial \dot{\boldsymbol{q}}} + \frac{\partial T}{\partial \boldsymbol{q}} - \frac{\partial U}{\partial \boldsymbol{q}} \right] \boldsymbol{\delta q} \, \mathrm{d}t = 0. \tag{A.15}$$

Now, since the virtual displacements $\boldsymbol{\delta q}$ are arbitrary, the term in brackets has to vanish over the entire time interval. This finally yields

$$-\frac{\mathrm{d}}{\mathrm{d}t} \frac{\partial T}{\partial \dot{\boldsymbol{q}}} + \frac{\partial T}{\partial \boldsymbol{q}} - \frac{\partial U}{\partial \boldsymbol{q}} = \boldsymbol{0}, \tag{A.16}$$

which are referred to as the Euler-Lagrange equations of motion.

B Intermediate steps in discretization

Since it is not immediately clear how to obtain (4.20) from (4.19) using integration by parts, some intermediate steps are shown here to enhance comprehensibility. Let us begin with the term including the first order spatial derivative

$$\int_X \boldsymbol{\Phi}_p \boldsymbol{A}_1 \frac{\partial}{\partial x} \boldsymbol{\Phi}_q^{\mathrm{T}} \hat{\boldsymbol{e}}_q \,\mathrm{d}x = -\int_X \frac{\partial}{\partial x} \boldsymbol{\Phi}_p \boldsymbol{A}_1 \boldsymbol{\Phi}_q^{\mathrm{T}} \hat{\boldsymbol{e}}_q \,\mathrm{d}x + \left[\boldsymbol{\Phi}_p \boldsymbol{A}_1 \boldsymbol{\Phi}_q^{\mathrm{T}} \hat{\boldsymbol{e}}_q\right]_a^b. \tag{B.1}$$

No further steps are required in case the system has no higher-order spatial derivatives. For the second order spatial derivative, integration by parts needs to be applied twice. The term

$$\int_X \boldsymbol{\Phi}_p \boldsymbol{A}_2 \frac{\partial^2}{\partial x^2} \boldsymbol{\Phi}_q^{\mathrm{T}} \hat{\boldsymbol{e}}_q \,\mathrm{d}x \tag{B.2}$$

is omitted on the left hand side in the following due to limited space and it is proceeded with

$$\begin{aligned} \ldots &= -\int_X \frac{\partial}{\partial x} \boldsymbol{\Phi}_p \boldsymbol{A}_2 \frac{\partial}{\partial x} \boldsymbol{\Phi}_q^{\mathrm{T}} \hat{\boldsymbol{e}}_q \,\mathrm{d}x + \left[\boldsymbol{\Phi}_p \boldsymbol{A}_2 \frac{\partial}{\partial x} \boldsymbol{\Phi}_q^{\mathrm{T}} \hat{\boldsymbol{e}}_q\right]_a^b \\ &= \int_X \frac{\partial^2}{\partial x^2} \boldsymbol{\Phi}_p \boldsymbol{A}_2 \boldsymbol{\Phi}_q^{\mathrm{T}} \hat{\boldsymbol{e}}_q \,\mathrm{d}x + \left[\boldsymbol{\Phi}_p A_2 \frac{\partial}{\partial x} \boldsymbol{\Phi}_q^{\mathrm{T}} \hat{\boldsymbol{e}}_q\right]_a^b - \left[\frac{\partial}{\partial x} \boldsymbol{\Phi}_p \boldsymbol{A}_2 \boldsymbol{\Phi}_q^{\mathrm{T}} \hat{\boldsymbol{e}}_q\right]_a^b. \end{aligned} \tag{B.3}$$

Accordingly, integration by parts needs to be applied N times to

$$\int_X \boldsymbol{\Phi}_p \boldsymbol{A}_N \frac{\partial^N}{\partial x^N} \boldsymbol{\Phi}_q^{\mathrm{T}} \hat{\boldsymbol{e}}_q \,\mathrm{d}x, \tag{B.4}$$

which yields

$$\begin{aligned} \cdots &= -\int_Z \frac{\partial}{\partial x} \boldsymbol{\Phi}_p A_N \frac{\partial^{N-1}}{\partial x^{N-1}} \boldsymbol{\Phi}_q^{\mathrm{T}} \hat{\boldsymbol{e}}_q \,\mathrm{d}x + \left[\boldsymbol{\Phi}_p A_N \frac{\partial^{N-1}}{\partial x^{N-1}} \boldsymbol{\Phi}_q^{\mathrm{T}} \hat{\boldsymbol{e}}_q\right]_a^b \\ &= \ldots \\ &= (-1)^N \int_Z \frac{\partial^N}{\partial x^N} \boldsymbol{\Phi}_p A_N \boldsymbol{\Phi}_q^{\mathrm{T}} \hat{\boldsymbol{e}}_q \,\mathrm{d}x + \left[\boldsymbol{\Phi}_p A_N \frac{\partial^{N-1}}{\partial x^{N-1}} \boldsymbol{\Phi}_q^{\mathrm{T}} \hat{\boldsymbol{e}}_q\right]_a^b - \ldots \\ &\quad + (-1)^{N-1} \left[\frac{\partial^{N-1}}{\partial x^{N-1}} \boldsymbol{\Phi}_p A_N \boldsymbol{\Phi}_q^{\mathrm{T}} \hat{\boldsymbol{e}}_q\right]_a^b. \end{aligned} \tag{B.5}$$

Merging (B.1), (B.3) and (B.5) and combining the bracketed integrals in sums respectively, it can be seen that the result of applying integration by parts N times is indeed given by (4.20).

List of Figures

List of Tables

List of Symbols

Symbol	description
A	surface area / cross sectional area
A_e	element surface area
$\boldsymbol{A}_i, \boldsymbol{A}_\alpha$	square Boolean matrices
a, b	bounds of a spatial domain
$\boldsymbol{B}$	Lagrange multiplier mapping
$\boldsymbol{C}$	measurement output mapping
$\boldsymbol{c}_p, \boldsymbol{c}_q$	test functions for kinetic and potential variables
D^α	differential operator
$\boldsymbol{D}$	damping matrix
$\boldsymbol{D}_\mathrm{c}$	compliance matrix
E	Young's modulus
$e, \boldsymbol{e}$	effort variables
$\boldsymbol{e}_P$, $\boldsymbol{e}_R$, $\boldsymbol{e}_S$	efforts of external, storage and resistive port
$\boldsymbol{e}_p, \boldsymbol{e}_q$	efforts related to kinetic and potential energy
$\boldsymbol{e}_\partial$	boundary efforts
$\hat{\boldsymbol{e}}$	efforts evaluated at discrete points (nodes)
$F, \boldsymbol{F}$	forces
$\boldsymbol{F}_i$	tracking or consensus filter gain
$f, \boldsymbol{f}$	flow variables
$\boldsymbol{f}_\mathrm{ext}$	external forces
$\boldsymbol{f}_P$, $\boldsymbol{f}_R$, $\boldsymbol{f}_S$	flows of external, storage and resistive port
$\boldsymbol{f}_p, \boldsymbol{f}_q$	flows related to kinetic and potential energy
$\boldsymbol{f}_\partial$	boundary flows
$\hat{\boldsymbol{f}}$	flows evaluated discrete points (nodes)
G	shear modulus
$\boldsymbol{G}$	input mapping
$\boldsymbol{G}_p$	force/torque input mapping
H	system Hamiltonian
h	disk or plate thickness
I	second moment of area
$\boldsymbol{I}$	identity matrix
I_p	polar moment of inertia
J_t	torsion constant

Symbol	description
$\boldsymbol{J}$	skew symmetric structure matrix
$\boldsymbol{J}_{\mathrm{g}}^{\mathrm{e}}$	local Jacobian of the geometry approximation
K	flexural rigidity
$\boldsymbol{K}$	stiffness matrix
$\boldsymbol{K}_{\mathrm{e}}$	element stiffness matrix
k_{v}	valve coefficient
L	length
$\boldsymbol{L}$	Luenberger observer gain
M	bending moment or torque
$\boldsymbol{M}$	mass matrix
$\boldsymbol{M}_{\mathrm{e}}$	element mass matrix
$\boldsymbol{M}_p, \boldsymbol{M}_q$	discrete mass matrix of kinetic and potential variables
$\boldsymbol{M}_{pq}$	concatenation of $\boldsymbol{M}_p$ and $\boldsymbol{M}_q$
m	mass
N	differential order
N_{n}	number of nodes
n_{a}	number of actice DOFs
nm	number of local module eigenmodes
n_q, n_p	number of kinetic and potential variables
n_{r}	number of retained eigenmodes
$\boldsymbol{n}$	normal vector
P	power
$\boldsymbol{P}$	discrete differential operator
p	impulse or pressure
$p_{\mathrm{S}}, p_{\mathrm{T}}$	supply and tank pressure
Q	shear force
$\boldsymbol{Q}$	positive definite symmetric mapping between efforts and states
$q, \boldsymbol{q}$	generalized coordinates or global DOFs
$q_{\mathrm{e}}, \boldsymbol{q}_{\mathrm{e}}$	local generalized coordinates
$\dot{q}$	generalized velocity or volumetric flow (thermodynamics)
$\hat{\boldsymbol{q}}, \hat{\boldsymbol{q}}_{\mathrm{e}}$	evaluation of q and q_{e} at the element nodes
R	resistance or resistive relation
$\boldsymbol{r}$	position of a point in an elastic body
$\boldsymbol{R}$	positive semi-definite symmetric matrix specifying the resistive structure
s	boundary curve coordinate or chamber diameter
$\boldsymbol{s}$	tangent vector
T	kinetic energy
$\boldsymbol{T}$	coordinate transformation
t	time
U	potential energy or internal energy (thermodynamics)

Symbol	description
$U_\mathrm{b}, U_\mathrm{s}$	potential energy of bending and shear
u, v, w	displacements
$\boldsymbol{u}$	system input
$\boldsymbol{u}_\partial$	boundary input
V	volume
V_e	element volume
X	spatial interval
x	state/energy variable or spatial coordinate
x, y, z	spatial coordinates
$x^\mathrm{e}, y^\mathrm{e}, z^\mathrm{e}$	local coordinates of an element
$\boldsymbol{x}$	system state
$\boldsymbol{x}_p, \boldsymbol{x}_q$	kinetic and potential energy variables
x_v	normalized spool position (valve)
$\hat{\boldsymbol{x}}$	state variables at discrete points or state estimate (observer)
$\tilde{\boldsymbol{x}}$	state vector after multiplication by $\boldsymbol{M}_{pq}$
$\boldsymbol{y}$	system output
$\boldsymbol{y}_\partial$	boundary output
$\hat{\boldsymbol{y}}$	estimated measurement output
α	multi-index
β	fluid bulk modulus
Γ	valve flow function
$\gamma, \boldsymbol{\gamma}$	shear strain
δ	variation, inexact differential or Dirac delta function
δW	virtual work performed by internal and external forces
δW_i	virtual work performed by inertia forces
$\boldsymbol{\delta r}$	virtual displacement
$\varepsilon, \boldsymbol{\varepsilon}$	strain
η, ξ	natural coordinates (of the unit square)
$\boldsymbol{\eta}$	eigenmodes
ϑ	temperature
κ	Timoshenko shear coefficient
$\boldsymbol{\kappa}$	vector of curvatures
$\boldsymbol{\lambda}$	Lagrange multipliers
μ	mass per unit length
ν	Poisson's ratio
Π_{ab}	rectangular function
ρ	density
$\sigma, \boldsymbol{\sigma}$	stress
$\tau, \boldsymbol{\tau}$	shear stress
φ	rotation angle

Symbol	description
φ_i	eigenvalues
$\boldsymbol{\Phi}$	approximation bases or eigenvectors (modal analysis)
$\boldsymbol{\Phi}_\mathrm{e}$	local orthonormal basis functions (FEM)
$\boldsymbol{\Phi}_p, \boldsymbol{\Phi}_q$	approximation bases of kinetic and potential variables
ϕ	polynomial approximation basis
ϕ_e	local approximation basis
ϕ_g	Lagrange polynomials for geometry approximation
$\boldsymbol{\psi}$	approximation bases for the boundary input
Ω	spatial domain
ω	angular velocity
ω_i	eigenvalues
$\mathcal{D}$	Dirac structure
$\mathcal{E}$	space of efforts
$\mathcal{F}$	space of flows
$\mathcal{H}$	Hamiltonian density
$\mathcal{L}$	parameter matrix or function of energy variables
$\mathcal{X}$	state space

Bibliography

[1] R. Altmann and P. Schulze. "A port-Hamiltonian formulation of the Navier–Stokes equations for reactive flows". *Systems & Control Letters* 100 (2017), pp. 51–55.

[2] F. Amini, S. Aghajanian, and B. Moaveni. "Decentralized control of uncertain structures using Luenberger observer". *Structural Engineering International* 27 (2017), pp. 127–133.

[3] P. Avitabile. "Model reduction and model expansion and their applications–part 1 theory". *Proceedings of the Twenty-Third International Modal Analysis Conference, Orlando, FL, USA*. 2005.

[4] A. Baaiu, F. Couenne, L. Lefevre, Y. Le Gorrec, and M. Tayakout. "Structure-preserving infinite dimensional model reduction: Application to adsorption processes". *Journal of Process Control* 19 (2009), pp. 394–404.

[5] E. Baker, A. Mensah, J. Rice, J. Grellier, A. A. Alkhatlan, et al. "Oceans and coasts-Global Environment Outlook (GEO-6): Healthy planet, healthy people chapter 7". *Global Environment Outlook (GEO-6): Healthy Planet, Healthy People* (2019).

[6] L. Bakule, M. Papík, and B. Rehák. "Decentralized overlapping control for civil structures". *Proceedings of the 7th ECCOMAS Thematic Conference on Smart Structures and Materials*. IDMEC, Azores, Portugal. 2015, pp. 1–15.

[7] L. Bakule. "Decentralized control: An overview". *Annual reviews in control* 32 (2008), pp. 87–98.

[8] L. Bakule. "Decentralized control: Status and outlook". *Annual Reviews in Control* 38 (2014), pp. 71–80.

[9] L. Bakule, M. Papík, and B. Rehák. "Decentralized stabilization of large-scale civil structures". *IFAC Proceedings Volumes* 47 (2014), pp. 10427–10432.

[10] L. Bakule, B. Rehák, and M. Papík. "Decentralized networked control of building structures". *Computer-Aided Civil and Infrastructure Engineering* 31 (2016), pp. 871–886.

[11] Y. Bar-Shalom and X.-R. Li. *Multitarget-multisensor tracking: principles and techniques*. Vol. 19. YBs Storrs, CT, 1995.

[12] F. Barbosa, J. Woetzel, and J. Mischke. *Reinventing construction: A route of higher productivity*. Tech. rep. McKinsey Global Institute, 2017.

[13] L. Bassi, A. Macchelli, and C. Melchiorri. "An algorithm to discretize one-dimensional distributed port-Hamiltonian systems". In: *Lagrangian and Hamiltonian methods for nonlinear control 2006*. Springer, 2007, pp. 61–73.

[14] B. Basu, O. S. Bursi, F. Casciati, S. Casciati, A. E. Del Grosso, M. Domaneschi, L. Faravelli, J. Holnicki-Szulc, H. Irschik, M. Krommer, et al. "A European association for the control of structures joint perspective. Recent studies in civil structural control across Europe". *Structural Control and Health Monitoring* 21 (2014), pp. 1414–1436.

[15] M. Z. A. Bhuiyan, G. Wang, J. Cao, and J. Wu. "Deploying wireless sensor networks with fault-tolerance for structural health monitoring". *IEEE Transactions on Computers* 64 (2013), pp. 382–395.

[16] A. Bleicher, M. Schlaich, Y. Fujino, and T. Schauer. "Model-based design and experimental validation of active vibration control for a stress ribbon bridge using pneumatic muscle actuators". *Engineering structures* 33 (2011), pp. 2237–2247.

[17] W. Borutzky. *Bond graph methodology: development and analysis of multidisciplinary dynamic system models*. Springer Science & Business Media, 2009.

[18] G. Bradski and A. Kaehler. "OpenCV". *Dr. Dobb's journal of software tools* 3 (2000).

[19] P. C. Breedveld. "Thermodynamic bond graphs and the problem of thermal inertance". *Journal of the Franklin Institute* 314 (1982), pp. 15–40.

[20] A. Brugnoli, D. Alazard, V. Pommier-Budinger, and D. Matignon. "Port-Hamiltonian formulation and symplectic discretization of plate models Part I: Mindlin model for thick plates". *Applied Mathematical Modelling* 75 (2019), pp. 940–960.

[21] A. Brugnoli, D. Alazard, V. Pommier-Budinger, and D. Matignon. "Port-Hamiltonian formulation and symplectic discretization of plate models Part II: Kirchhoff model for thin plates". *Applied Mathematical Modelling* 75 (2019), pp. 961–981.

[22] L. F. Cabeza, C. Barreneche, L. Miro, M. Martínez, A. I. Fernández, and D. Urge-Vorsatz. "Affordable construction towards sustainable buildings: review on embodied energy in building materials". *Current Opinion in Environmental Sustainability* 5 (2013), pp. 229–236.

[23] F. L. Cardoso-Ribeiro. “Port-Hamiltonian modeling and control of a fluidstructure system”. PhD thesis. PhD thesis, Université de Toulouse, 2016.

[24] F. L. Cardoso-Ribeiro, D. Matignon, and V. Pommier-Budinger. “Modeling by interconnection and control by damping injection of a fluid-structure system with non-collocated actuators and sensors”. *International Conference on Noise and Vibration Engineering - ISMA 2016*. 2016.

[25] F. L. Cardoso-Ribeiro, D. Matignon, and L. Lefevre. “A structure-preserving Partitioned Finite Element Method for the 2D wave equation”. *IFAC-PapersOnLine* 51 (2018), pp. 119–124.

[26] F. L. Cardoso-Ribeiro, D. Matignon, and L. Lefèvre. “A Partitioned Finite Element Method for power-preserving discretization of open systems of conservation laws”. *arXiv preprint arXiv:1906.05965* (2019).

[27] F. L. Cardoso-Ribeiro, D. Matignon, and V. Pommier-Budinger. “Modeling of a fluid-structure coupled system using port-Hamiltonian formulation”. *IFAC-PapersOnLine* 48 (2015), pp. 217–222.

[28] F. L. Cardoso-Ribeiro, D. Matignon, and V. Pommier-Budinger. “Piezoelectric beam with distributed control ports: a power-preserving discretization using weak formulation.” *IFAC-PapersOnLine* 49 (2016), pp. 290–297.

[29] F.-L. Cardoso-Ribeiro. “Port-Hamiltonian modeling and control of a fluid-structure system”. PhD thesis. University of Toulouse, 2016.

[30] E. Cheynet. *Earthquake simulation*. [accessed 2020-9-12]. Matlab Central File Exchange, 2019.

[31] R. W. Clough and J. L. Tocher. “Finite element stiffness matrices for analysis of plates in bending”. *Int. Conf. on Matrix Methods in Structural Mechanics*. 1965, pp. 515–545.

[32] W. Commons. *File:Taipei 101 Tuned Mass Damper 2010.jpg — Wikimedia Commons, the free media repository*. [accessed 2020-8-6]. 2015.

[33] W. Commons. *File:Pole 3 building seismic base isolator.jpg — Wikimedia Commons, the free media repository*. [accessed 2020-8-6]. 2018.

[34] A. Concha, L. Alvarez-Icaza, and R. Garrido. “Simultaneous parameter and state estimation of shear buildings”. *Mechanical Systems and Signal Processing* 70 (2016), pp. 788–810.

[35] P. Dickerson, C. Guerreiro, T. Keating, J. M. Nzioka, S. H. Chung, S. Reis, B. J. Abiodun, K. J. Bowen, R. Djalante, J. Grellier, et al. “Air-Global Environment Outlook (GEO-6): Healthy planet, healthy people chapter 5”. *Global Environment Outlook (GEO-6): Healthy Planet, Healthy People* (2019).

[36] A. Donaire and S. Junco. "Derivation of input-state-output port-hamiltonian systems from bond graphs". *Simulation Modelling Practice and Theory* 17 (2009), pp. 137–151.

[37] V. Duindam, A. Macchelli, S. Stramigioli, and H. Bruyninckx. *Modeling and control of complex physical systems: the port-Hamiltonian approach*. Springer Science & Business Media, 2009.

[38] R. G. Durán, L. Hervella-Nieto, E. Liberman, R. Rodríguez, and J. Solomin. "Approximation of the vibration modes of a plate by Reissner-Mindlin equations". *Mathematics of Computation* 68 (1999), pp. 1447–1463.

[39] H. Durrant-Whyte and T. C. Henderson. "Multisensor data fusion". In: *Springer handbook of robotics*. Springer, 2016, pp. 867–896.

[40] D. Eberard, B. M. Maschke, and A. J. Van Der Schaft. "An extension of Hamiltonian systems to the thermodynamic phase space: Towards a geometry of nonreversible processes". *Reports on mathematical physics* 60 (2007), pp. 175–198.

[41] M. Encina, J. Yuz, M. Zañartu, and G. Galindo. "Vocal fold modeling through the port-Hamiltonian systems approach". *2015 IEEE Conference on Control Applications (CCA)*. IEEE. 2015, pp. 1558–1563.

[42] G. Escobar, A. J. van der Schaft, and R. Ortega. "A Hamiltonian viewpoint in the modeling of switching power converters". *Automatica* 35 (1999), pp. 445–452.

[43] A. Falaize and T. Hélie. "Passive guaranteed simulation of analog audio circuits: A port-Hamiltonian approach". *Applied Sciences* 6 (2016), p. 273.

[44] A. Falaize and T. Hélie. "Passive simulation of the nonlinear port-Hamiltonian modeling of a Rhodes piano". *Journal of Sound and Vibration* 390 (2017), pp. 289–309.

[45] C. R. Farrar and K. Worden. "An introduction to structural health monitoring". *Philosophical Transactions of the Royal Society A: Mathematical, Physical and Engineering Sciences* 365 (2007), pp. 303–315.

[46] S. Fiaz, D. Zonetti, R. Ortega, J. M. A. Scherpen, and A. J. van der Schaft. "A port-Hamiltonian approach to power network modeling and analysis". *European Journal of Control* 19 (2013), pp. 477–485.

[47] N. R. Fisco and H. Adeli. "Smart structures: part I—active and semi-active control". *Scientia Iranica* 18 (2011), pp. 275–284.

[48] F. Gandhi and S.-G. Kang. "Beams with controllable flexural stiffness". *Smart Materials and Structures* 16 (2007), p. 1179.

[49] M. Géradin and D. J. Rixen. *Mechanical vibrations: theory and application to structural dynamics*. John Wiley & Sons, 2014.

[50] A. H. Ghasemi, J. B. Hoagg, and T. M. Seigler. "Decentralized vibration and shape control of structures with colocated sensors and actuators". *Journal of Dynamic Systems, Measurement, and Control* 138 (2016).

[51] G. Golo, V. Talasila, A. Van Der Schaft, and B. Maschke. "Hamiltonian discretization of boundary control systems". *Automatica* 40 (2004), pp. 757–771.

[52] C. Gomes, C. Thule, D. Broman, P. G. Larsen, and H. Vangheluwe. "Co-simulation: a survey". *ACM Computing Surveys (CSUR)* 51 (2018), pp. 1–33.

[53] D. Gross, W. Hauger, W. Schnell, J. Schröder, and W. A. Wall. *Technische Mechanik*. Vol. 4. Springer, 2009.

[54] F. Guerra, T. Haist, A. Warsewa, S. Hartlieb, W. Osten, and C. Tarín. "Precise building deformation measurement using holographic multipoint replication". *Applied Optics* 59 (2020), pp. 2746–2753.

[55] Y. Guo and A. Kareem. "System identification through nonstationary data using time–frequency blind source separation". *Journal of Sound and Vibration* 371 (2016), pp. 110–131.

[56] R. J. Guyan. "Reduction of stiffness and mass matrices". *AIAA journal* 3 (1965), pp. 380–380.

[57] B. Hamroun, A. Dimofte, L. Lefèvre, and E. Mendes. "Control by interconnection and energy-shaping methods of port Hamiltonian models. Application to the shallow water equations". *European Journal of Control* 16 (2010), pp. 545–563.

[58] M. Henke, J. Sorber, and G. Gerlach. "Multi-layer beam with variable stiffness based on electroactive polymers". *Electroactive Polymer Actuators and Devices (EAPAD) 2012*. Vol. 8340. International Society for Optics and Photonics. 2012.

[59] J. P. Hespanha, P. Naghshtabrizi, and Y. Xu. "A survey of recent results in networked control systems". *Proceedings of the IEEE* 95 (2007), pp. 138–162.

[60] P. Holzwarth and P. Eberhard. "SVD-based improvements for component mode synthesis in elastic multibody systems". *European Journal of Mechanics-A/Solids* 49 (2015), pp. 408–418.

[61] T. J. R. Hughes. *The finite element method: linear static and dynamic finite element analysis*. Courier Corporation, 2012.

[62] M. Ikeda, D. D. Šiljak, and D. E. White. "Decentralized control with overlapping information sets". *Journal of optimization theory and Applications* 34 (1981), pp. 279–310.

[63] Y. Ikeda. "Active and semi-active vibration control of buildings in Japan-Practical applications and verification". *Structural Control and Health Monitoring: The Official Journal of the International Association for Structural Control and Monitoring and of the European Association for the Control of Structures* 16 (2009), pp. 703–723.

[64] S. Jang, S. H. Sim, H. Jo, and B. F. Spencer Jr. "Decentralized bridge health monitoring using wireless smart sensors". *Sensors and Smart Structures Technologies for Civil, Mechanical, and Aerospace Systems 2010*. Vol. 7647. International Society for Optics and Photonics. 2010.

[65] M. Jelali and A. Kroll. *Hydraulic servo-systems: modelling, identification and control*. Springer Science & Business Media, 2012.

[66] D. Jeltsema and A. Doria-Cerezo. "Port-Hamiltonian formulation of systems with memory". *Proceedings of the IEEE* 100 (2011), pp. 1928–1937.

[67] S. J. Julier and J. K. Uhlmann. "General decentralized data fusion with covariance intersection". *Handbook of multisensor data fusion: theory and practice* (2009), pp. 319–344.

[68] B. Khaleghi, A. Khamis, F. O. Karray, and S. N. Razavi. "Multisensor data fusion: A review of the state-of-the-art". *Information fusion* 14 (2013), pp. 28–44.

[69] U. A. Khan and J. M. F. Moura. "Distributing the Kalman filter for large-scale systems". *IEEE Transactions on Signal Processing* 56 (2008), pp. 4919–4935.

[70] S. Korkmaz. "A Review of Active Structural Control: Challenges for Engineering Informatics". *Computers & Structures* 89 (2011), pp. 2113–2132.

[71] P. Kotyczka. *Numerical methods for distributed parameter port-Hamiltonian systems*. 2019.

[72] P. Kotyczka, H. Joos, Y. Wu, and Y. Le Gorrec. "Finite-dimensional observers for port-Hamiltonian systems of conservation laws". *2019 IEEE 58th Conference on Decision and Control (CDC)*. IEEE. 2019, pp. 6875–6880.

[73] P. Kotyczka, G. Koch, E. Pellegrini, and B. Lohmann. "Transparent parametrization of nonlinear IDA-PBC for a hydraulic actuator". *IFAC Proceedings Volumes* 43 (2010), pp. 1122–1127.

[74] P. Kotyczka, B. Maschke, and L. Lefèvre. "Weak form of Stokes–Dirac structures and geometric discretization of port-Hamiltonian systems". *Journal of Computational Physics* 361 (2018), pp. 442–476.

[75] A. Kugi and W. Kemmetmüller. "Energy based modelling of lumped-parameter hydraulic systems". *4th Mathmod*. 2003, pp. 825–834.

[76] A. Kugi and W. Kemmetmüller. "New energy-based nonlinear controller for hydraulic piston actuators". *European journal of control* 10 (2004), pp. 163–173.

[77] N. Kurata, T. Kobori, M. Takahashi, N. Niwa, and H. Midorikawa. "Actual seismic response controlled building with semi-active damper system". *Earthquake engineering & structural dynamics* 28 (1999), pp. 1427–1447.

[78] Y. Le Gorrec, H. Zwart, and B. Maschke. "Dirac structures and boundary control systems associated with skew-symmetric differential operators". *SIAM journal on control and optimization* 44 (2005), pp. 1864–1892.

[79] Y. Lei, D. T. Wu, and Y. Lin. "A decentralized control algorithm for large-scale building structures". *Computer-Aided Civil and Infrastructure Engineering* 27 (2012), pp. 2–13.

[80] X. Ling and A. Haldar. "Element level system identification with unknown input with Rayleigh damping". *Journal of Engineering Mechanics* 130 (2004), pp. 877–885.

[81] C.-H. Loh, J. P. Lynch, K.-C. Lu, Y. Wang, C.-M. Chang, P.-Y. Lin, and T.-H. Yeh. "Experimental verification of a wireless sensing and control system for structural control using MR dampers". *Earthquake engineering & structural dynamics* 36 (2007), pp. 1303–1328.

[82] J. P. Lynch. "Decentralization of wireless monitoring and control technologies for smart civil structures". PhD thesis. Stanford University Stanford, CA, 2002.

[83] A. Macchelli and C. Melchiorri. "Modeling and control of the Timoshenko beam. The distributed port-Hamiltonian approach". *SIAM Journal on Control and Optimization* 43 (2004), pp. 743–767.

[84] A. Macchelli, C. Melchiorri, and L. Bassi. "Port-based modelling and control of the Mindlin plate". *Proceedings of the 44th IEEE Conference on Decision and Control*. IEEE. 2005, pp. 5989–5994.

[85] A. Macchelli, A. J. van der Schaft, and C. Melchiorri. "Multi-variable port Hamiltonian model of piezoelectric material". *2004 IEEE/RSJ International Conference on Intelligent Robots and Systems (IROS)*. Vol. 1. IEEE. 2004, pp. 897–902.

[86] A. Macchelli, A. J. van der Schaft, and C. Melchiorri. "Port Hamiltonian formulation of infinite dimensional systems I. Modeling". *2004 43rd IEEE Conference on Decision and Control (CDC)*. Vol. 4. IEEE. 2004, pp. 3762–3767.

[87] B. M. Maschke and A. J. van der Schaft. "Port-controlled Hamiltonian systems: modelling origins and systemtheoretic properties". *IFAC Proceedings Volumes* 25 (1992), pp. 359–365.

[88] B. M. Maschke, A. J. van der Schaft, and P. C. Breedveld. "An intrinsic Hamiltonian formulation of the dynamics of LC-circuits". *IEEE Transactions on Circuits and Systems I: Fundamental theory and applications* 42 (1995), pp. 73–82.

[89] S. N. McClain, C. P. McMullen, B. J. Abiodun, G. Armiento, R. Bailey, R. Balasubramanian, R. Barra, K. J. Bowen, I. Dankelman, K. DePryck, et al. "Cross-cutting issues-Global Environment Outlook (GEO-6): Healthy planet, healthy people chapter 4". *Global Environment Outlook (GEO-6): Healthy Planet, Healthy People* (2019).

[90] R. D. Mindlin. "Influence of rotatory inertia and shear on flexural motions of isotropic, elastic plates". *Journal of Applied Mechanics* 18 (1951), pp. 31–38.

[91] R. Moulla, L. Lefevre, and B. Maschke. "Pseudo-spectral methods for the spatial symplectic reduction of open systems of conservation laws". *Journal of computational Physics* 231 (2012), pp. 1272–1292.

[92] A. G. O. Mutambara. *Decentralized estimation and control for multisensor systems*. CRC press, 1998.

[93] T. Nagayama, B. F. Spencer Jr, and J. A. Rice. "Autonomous decentralized structural health monitoring using smart sensors". *Structural Control and Health Monitoring: The Official Journal of the International Association for Structural Control and Monitoring and of the European Association for the Control of Structures* 16 (2009), pp. 842–859.

[94] S. Neuhaeuser, M. Weickgenannt, C. Witte, W. Haase, O. Sawodny, and W. Sobek. "Stuttgart SmartShell–a full scale prototype of an adaptive shell structure". *Journal of the International Association for Shell and Spatial Structures* 54 (2013), pp. 259–270.

[95] Y. Niu, C.-P. Fritzen, H. Jung, I. Buethe, Y.-Q. Ni, and Y.-W. Wang. "Online simultaneous reconstruction of wind load and structural responses—theory and application to canton tower". *Computer-Aided Civil and Infrastructure Engineering* 30 (2015), pp. 666–681.

[96] T. Noak, J. Ruth, and U. Müller. "Adaptive hybrid structures". *Proceedings of the International Conference on Adaptable Building Structures*. 2006.

[97] J. O'Callahan and P. Li. "SEREP expansion". *Proceedings of the 14th International Modal Analysis Conference*. Vol. 2768. 1996, p. 1258.

[98] Y. Ohtori, R. E. Christenson, B. F. Spencer Jr, and S. J. Dyke. "Benchmark control problems for seismically excited nonlinear buildings". *Journal of engineering mechanics* 130 (2004), pp. 366–385.

[99] R. Olfati-Saber, J. A. Fax, and R. M. Murray. "Consensus and cooperation in networked multi-agent systems". *Proceedings of the IEEE* 95 (2007), pp. 215–233.

[100] R. Ortega, A. Van Der Schaft, B. Maschke, and G. Escobar. "Interconnection and damping assignment passivity-based control of port-controlled Hamiltonian systems". *Automatica* 38 (2002), pp. 585–596.

[101] H. M. Paynter. *Analysis and design of engineering systems*. MIT press, 1961.

[102] A. Quarteroni and A. Valli. *Numerical approximation of partial differential equations*. Vol. 23. Springer Science & Business Media, 2008.

[103] H. Ramirez, B. Maschke, and D. Sbarbaro. "Irreversible port-Hamiltonian systems: A general formulation of irreversible processes with application to the CSTR". *Chemical Engineering Science* 89 (2013), pp. 223–234.

[104] R. Rashad, F. Califano, A. J. van der Schaft, and S. Stramigioli. "Twenty years of distributed port-Hamiltonian systems: a literature review". *IMA Journal of Mathematical Control and Information* (2020).

[105] F. R. Rofooei, A. Mobarake, and G. Ahmadi. "Generation of artificial earthquake records with a nonstationary Kanai–Tajimi model". *Engineering Structures* 23 (2001), pp. 827–837.

[106] T. E. Saaed, G. Nikolakopoulos, J.-E. Jonasson, and H. Hedlund. "A state-of-the-art review of structural control systems". *Journal of Vibration and Control* 21 (2015), pp. 919–937.

[107] N. Sandell, P. Varaiya, M. Athans, and M. Safonov. "Survey of decentralized control methods for large scale systems". *IEEE Transactions on automatic Control* 23 (1978), pp. 108–128.

[108] A. J. van der Schaft and B. M. Maschke. "Hamiltonian formulation of distributed-parameter systems with boundary energy flow". *Journal of Geometry and Physics* 42 (2002), pp. 166–194.

[109] A. van der Schaft, D. Jeltsema, et al. "Port-Hamiltonian systems theory: An introductory overview". *Foundations and Trends in Systems and Control* 1 (2014), pp. 173–378.

[110] T. M. Scheuermann, P. Kotyczka, C. Martens, H. Louati, B. Maschke, M.-L. Zanota, and I. Pitault. "An object-oriented library for heat transfer modelling and simulation in open cell foams". *arXiv preprint arXiv:2002.03789* (2020).

[111] W. Schnell, D. Gross, W. Hauger, and P. Wriggers. *Technische Mechanik: Band 4: Hydromechanik, Elemente der Höheren Mechanik, Numerische Methoden*. Springer-Verlag, 2006.

[112] B. Schweizer, P. Li, and D. Lu. "Explicit and implicit cosimulation methods: stability and convergence analysis for different solver coupling approaches". *Journal of Computational and Nonlinear Dynamics* 10 (2015).

[113] R. Schwertassek and O. Wallrapp. *Dynamik flexibler Mehrkörpersysteme: Methoden der Mechanik zum rechnergestützten Entwurf und zur Analyse mechatronischer Systeme*. Springer-Verlag, 2017.

[114] C. Secchi, S. Stramigioli, and C. Fantuzzi. *Control of interactive robotic interfaces: A port-Hamiltonian approach*. Vol. 29. Springer Science & Business Media, 2007.

[115] G. Senatore, P. Duffour, and P. Winslow. "Energy and cost assessment of adaptive structures: case studies". *Journal of Structural Engineering* 144 (2018).

[116] G. Senatore, P. Duffour, P. Winslow, and C. Wise. "Shape control and whole-life energy assessment of an 'infinitely stiff'prototype adaptive structure". *Smart Materials and Structures* 27 (2017).

[117] D. D. Siljak. *Decentralized control of complex systems*. Courier Corporation, 2011.

[118] K. Smarsly and K. H. Law. "Decentralized fault detection and isolation in wireless structural health monitoring systems using analytical redundancy". *Advances in Engineering Software* 73 (2014), pp. 1–10.

[119] W. Sobek and P. Teuffel. "Adaptive systems in architecture and structural engineering". *Smart Structures and Materials 2001: Smart Systems for Bridges, Structures, and Highways*. Vol. 4330. International Society for Optics and Photonics. 2001, pp. 36–46.

[120] W. Sobek, P. Teuffel, A. Weilandt, and C. Lemaitre. "Adaptive and lightweight". *Proceedings of the international conference on adaptable building structures, Adaptables2006, Eindhoven, The Netherlands*. 2006, pp. 03–05.

[121] B. F. Spencer and S. Nagarajaiah. "State of the art of structural control". *Journal of structural engineering* 129 (2003), pp. 845–856.

[122] B. F. Spencer Jr. “Benchmark structural control problems for seismic-and wind-excited structures”. *Journal of Engineering Mechanics* 130 (2004), pp. 363–365.

[123] S. S. Stanković, D. M. Stipanović, and D. D. Šiljak. “Decentralized dynamic output feedback for robust stabilization of a class of nonlinear interconnected systems”. *Automatica* 43 (2007), pp. 861–867.

[124] W. Stephan and R. Postl. *Schwingungen elastischer Kontinua*. Springer, 1995.

[125] F. Strehle, M. Pfeifer, L. Kölsch, C. Degünther, J. Ruf, L. Andresen, and S. Hohmann. “Towards port-Hamiltonian modeling of multi-carrier energy systems: A case study for a coupled electricity and gas distribution system”. *IFAC-PapersOnLine* 51 (2018), pp. 463–468.

[126] V. Talasila, G. Golo, and A. J. van der Schaft. “The wave equation as a port-Hamiltonian system and a finite dimensional approximation”. *Proceedings of 15th international symposium mathematical theory of networks and systems (MTNS), South Bend*. 2002.

[127] United Nations Environmental Programme (UNEP). *The 10YFP programme on sustainable buildings and construction*. [accessed 2020-11-20]. United Nations, 2016.

[128] B. Vincent, N. Hudon, L. Lefèvre, and D. Dochain. “Port-Hamiltonian observer design for plasma profile estimation in tokamaks”. *IFAC-PapersOnLine* 49 (2016), pp. 93–98.

[129] N. M. T. Vu, L. Lefevre, and B. Maschke. “Port-hamiltonian formulation for systems of conservation laws: application to plasma dynamics in tokamak reactorss”. *IFAC Proceedings Volumes* 45 (2012), pp. 108–113.

[130] N. M. T. Vu, L. Lefevre, and B. Maschke. “A structured control model for the thermo-magneto-hydrodynamics of plasmas in tokamaks”. *Mathematical and computer modelling of dynamical systems* 22 (2016), pp. 181–206.

[131] J. Wang, Z.-D. Ma, and G. M. Hulbert. “A gluing algorithm for distributed simulation of multibody systems”. *Nonlinear dynamics* 34 (2003), pp. 159–188.

[132] A. Warsewa, M. Böhm, P. Rapp, O. Sawodny, and C. Tarín. “Decentralized and Distributed Observer Design for Large-Scale Structures using Dynamic Condensation”. *2019 IEEE 15th International Conference on Automation Science and Engineering (CASE)*. 2019, pp. 1256–1262.

[133] A. Warsewa, J. L. Wagner, M. Böhm, O. Sawodny, and C. Tarín. “Decentralized LQG control for adaptive high-rise structures”. *Proceedings of the 21st IFAC world congress 2020*. 2020.

[134] A. Warsewa, M. Böhm, F. Guerra, J. L. Wagner, T. Haist, C. Tarín, and O. Sawodny. "Self-tuning state estimation for adaptive truss structures using strain gauges and camera-based position measurements". *Mechanical Systems and Signal Processing* 143 (2020).

[135] A. Warsewa, M. Böhm, O. Sawodny, and C. Tarín. "A port-Hamiltonian approach to modeling the structural dynamics of complex systems". *Applied Mathematical Modelling* 89 (2020), pp. 1528–1546.

[136] A. Warsewa, J. L. Wagner, M. Böhm, O. Sawodny, and C. Tarín. "Networked decentralized control of adaptive structures". *Journal of Communications* 15 (2020).

[137] J. Wauer. *Kontinuumsschwingungen*. Springer, 2014.

[138] S. Weidner, C. Kelleter, P. Sternberg, W. Haase, F. Geiger, T. Burghardt, C. Honold, J. Wagner, M. Böhm, M. Bischoff, et al. "The implementation of adaptive elements into an experimental high-rise building". *Steel Construction* 11 (2018), pp. 109–117.

[139] H. Werkle. *Finite Elemente in der Baustatik: Statik und Dynamik der Stab-und Flächentragwerke*. Springer-Verlag, 2008.

[140] Y. Wu, B. Hamroun, Y. Le Gorrec, and B. Maschke. "Port-Hamiltonian system in descriptor form for balanced reduction: Application to a nanotweezer". *IFAC Proceedings Volumes* 47 (2014).

[141] J. T. Yao. "Concept of structural control". *Journal of the Structural Division* 98 (1972).

[142] H. Zwart and B. Jacob. "Distributed-parameter port-Hamiltonian systems". *CIMPA* (2009).